Local surface environment and degradation processes of degradable magnesium biomaterials under simulated physiological conditions

Dissertation

zur Erlangung des akademischen Grades
Doktor der Ingenieurwissenschaften
(Dr.-Ing.)
der Technischen Fakultät
der Christian-Albrechts-Universität zu Kiel

vorgelegt von

Jorge González de Frutos

Kiel 2020

Erstgutachterin: Prof. Dr. Regine Willumeit-Römer

Zweitgutachter: Prof. Dr. Mikhail Zheludkevich

Oral examination: Monday, 27th of April 2020

Acknowledgements

First of all, I would like to thank Prof. Dr Regine Willumate-Römer for giving me the opportunity to work at the Institute of Metallic Biomaterials in Helmholtz-Zentrum Geesthacht. Her rigorous scientific guidance was essential for the accomplishment of this written scientific work. In addition, I really appreciate the help of Prof. Dr Mikhail Zedludkevic for reviewing my thesis work.

I would also like to thank my colleagues form WZK and especially Dr Sviatlana Lamaka for her crucial scientific input and for being an example of good practice, dedication and enthusiasm. Also, I would like to thank Dr Frank Feyerabend and Dr Thomas Ebel for their support and advises on structuring ideas and translating them into a piece of paper.

I want to put on the record that was a pleasure to be part of the WB institute because of the excellent PhD community that I met. The short meetings and the occasional sweets in the kitchen, the discussed ideas in the office, jokes and laughs in the office, truly helped the daily life during those three years.

Finally, I wanted to thank my father and the rest of my family for their love, help, and understanding, especially my wife Maria and my little girl Isabel who help me to stand firmly during the difficult moments with love and happiness.

Erklärung

Hiermit erkläre ich, dass die beigefügte Dissertation, abgesehen von der Beratung durch die Betreuerin, nach Inhalt und Form meine eigene Arbeit ist.

Die Arbeit, ganz oder zum Teil, wurde nie schon einer anderen Stelle im Rahmen eines Prüfungsverfahrens vorgelegt und ist nie veröffentlicht worden oder zur Veröffentlichung vorgelegt worden.

Außerdem ist die Arbeit unter Einhaltung der Regeln guter wissenschaftlicher Praxis der Deutschen Forschungsgemeinschaft entstanden.

Geesthacht, den

Abstract

The development of high purity Mg alloys and new processing techniques have led to the emergence of the first degradable Mg implants on the market. Those commercially available implants are designed for specific bone fixation and atherosclerosis treatments. Nevertheless, the not well-understood degradation mechanisms of Mg-based materials under physiological conditions is one of the reasons hindering the promising use of those materials for other applications as a degradable biomaterial. Due to the current uncertainties in defining/monitoring the complex corrosive *in vivo* environment, the influence of the different physiological fluid components in the Mg degradation mechanism has to be clarified by *in vitro* studies. However, most of the *in vitro* studies monitor the bulk solution environment, defined by the concentrations and pH, as the only relevant corrosive environment. Only a few *in vitro* studies take into account the mass transfer phenomena at the Mg surface and identify the importance of the local surface environment on Mg degradation mechanisms. However, those studies do not provide insight into the correlation between the solution conditions at the surface and the degradation products layer as a critical degradation rate modifier. Among all the physiological fluids components, the inorganic fraction, and particularly the presence of Ca^{2+} cations, was revealed in previous studies as a critical modifier of the degradation rate of Mg alloys. For this reason, the effect of Ca^{2+} cations presence on the pH at the Mg /degradation solution interface (interface pH) were investigated in this work by Scanning Ion-selective Electrode Technique (SIET) on different magnesium materials (HP-Mg, Mg-1.2Ca, Mg-2Ag and E11). The different corrosive solutions based on the commercial HBSS composition were applied under flow conditions to mimic the *in vivo* homeostasis. Moreover, the influence of the presence of Ca^{2+} cations in the degradation products layer composition was analysed by optical microscopy (OM), backscattered scanning electron microscopy (BSEM), energy dispersive x-rays (EDX), grazing angle x-ray diffraction (GAXRD), micro x-ray fluorescence (µXRF), and Fourier Transform Infrared Spectroscopy Attenuated Total Reflectance (FTIR-ATR). The results show that the presence of Ca^{2+} cations generates a decrease in the degradation rate (26% - 65% depending on the Mg material) and the interface pH (around pH 8 for all the alloys). These effects are attributed to the fast development of an amorphous calcium phosphate (CaPs) compact outer layer. The precipitation/dissolution equilibrium of the products forming the degradation layer generates an extra buffering system at the interface. This local buffering system can absorb the differences in the pH promoted by different materials with significant differences in the degradation rate. Therefore, this study contributes to describe the local surface environment of Mg-based materials under simulated physiological conditions and provides relevant information concerning the importance of the interface pH on the development of the degradation products layer.

Zusammenfassung

Die Entwicklung hochreiner Mg-Legierungen und neuer Verarbeitungsverfahren resultierten in die Markteinführung der ersten abbaubaren Mg Implantate. Diese kommerziell erhältlichen Implantate wurden entwickelt, um Knochen zu fixieren und Atheroskleroseprobleme zu lösen. Dennoch sind die noch nicht ausreichend gutverstandenen Abbaumechanismen von Mg-basierten Materialien unter physiologischen Bedingungen einer der Gründe, die den vielversprechenden Einsatz dieser Materialien für andere Anwendungen verhindern. Aufgrund der aktuellen Unsicherheiten bei der Definition/Überwachung der komplex korrosiven *in vivo* Umgebung, muss der Einfluss der verschiedenen physiologischen Flüssigkeitskomponenten im Mg-Abbaumechanismus durch *In vitro*-Studien geklärt werden. Die meisten *In vitro*-Studien berücksichtigen jedoch nur den Zustand der Bulklösung, definiert durch die Konzentrationen und den pH-Wert, als die einzige relevante korrosive Umgebung. Darüber hinaus berücksichtigen nur wenige In-vitro-Studien die Stoffaustauschphänomene an der Mg-Oberfläche und identifizieren die Bedeutung der lokalen Oberflächenumgebung für die Abbaumechanismen von Mg. Diese Studien geben jedoch keinen Einblick in den Zusammenhang zwischen den Lösungsbedingungen an der Oberfläche und der Abbauprodukte der Schicht als kritische Einflussgröße der Abbaurate. Unter allen Komponenten der physiologischen Medien wurde der anorganische Anteil und insbesondere das Vorhandensein von Ca^{2+}-Kationen in früheren Studien als kritischer Faktor der Abbaurate von Mg-basierten Materialien identifiziert. Aus diesem Grund wurde die Auswirkung des Vorhandenseins von Ca^{2+}-Kationen in der korrosiven Lösung auf den lokalen pH-Wert der Oberfläche in dieser Arbeit durch Scanning Ion-selective Electrode Technique (SIET) auf verschiedene Magnesiummaterialien (HP-Mg, Mg-1.2Ca, Mg-2Ag und E11) untersucht. Die verschiedenen korrosiven Lösungen auf Basis der kommerziellen HBSS-Zusammensetzung wurden unter Strömungsbedingungen eingesetzt, um die *in vivo* Homöostase nachzuahmen. Darüber hinaus wurde der Einfluss des Vorhandenseins von Ca^{2+}-Kationen in der Schicht der Abbauprodukte durch optische Mikroskopie (OM), Rasterelektronenmikroskopie (REM), energiedispersive Röntgenspektroskopie (EDX), Glanzwinkel-Röntgenbeugung (GAXRD), Mikro-Röntgenfluoreszenz (µXRF) und Fourier-Transform-Infrarotspektroskopie – Abgeschwächte Totalreflexion (FTIR-ATR) analysiert. Die Ergebnisse zeigen, dass das Vorhandensein von Ca^{2+}-Kationen eine Abnahme der Abbaurate (26% - 65% je nach Mg-Legierung) und des lokalen pH Wertes in Oberflächennähe (ca.pH 8 für alle Legierungen) bewirkt. Diese Effekte sind auf die schnelle Entwicklung einer kompakten Außenschicht aus amorphem Calciumphosphat (CaPs) zurückzuführen. Das Fällungs-/Lösungsgleichgewicht der Abbauschicht bildenden Produkte erzeugt jedoch ein zusätzliches Puffersystem an der Oberfläche. Dieses lokale Puffersystem kann die Unterschiede im pH-Wert absorbieren, die

durch verschiedene Materialien mit signifikant unterschiedlichen Abbauraten begünstigt werden. Diese Studie trägt dazu bei, die lokale Oberflächenumgebung von Mg-basierten Materialien unter simulierten physiologischen Bedingungen zu beschreiben und liefert relevante Informationen über die Bedeutung des oberflächennahen und lokalen pH Wertes für die Schichtentwicklung der Abbauprodukte.

Contents

1 Introduction

1.1 Biomaterials for bone remodelling

The definition of a biomaterial has been modified progressively over the time according to a paradigm change concerning the favoured interaction between the biomaterial and the biological tissues from an inert to a determining active role, as is detailed in *Table 1*. According to that, a current and agreed definition accepted by the *European Society for Biomaterials* (ESB), defines biomaterials as materials designed to interact with biological systems to assess, treat, enhance or replace any tissue, organ or function of the body.

Table 1 Definitions applied to Biomaterials over time.

Year	Definition	Reference
1975	The material used to replace a part or a function of the body in a safe, reliable, economical, and physiologically acceptable manner	[1]
1980	Materials of synthetic origin as well as of natural origin in contact with tissues, blood and other biological fluids, intended for use in the manufacture of prostheses, diagnostic or therapeutic devices and storage applications without adverse effects on the living organism and its constituents	[2]
1992	The inert material used in medical devices intended to interact with biological tissues	[3]
2003	Materials that constitute parts of medical implants, extracorporeal devices, and disposables that have been utilised in medicine, surgery, dentistry, and veterinary medicine as well as in every aspect of patient healthcare	[3]
2004	Every synthetic material used to replace part of a living system or to function in intimate contact with living tissue	[4]

The variety of biomaterials and their possible applications have significantly expanded during recent decades. Those materials are currently applied for a prosthesis as implants to replace a specific injured or absent tissue, materials used as tools for the implant fixation, for transport and drug delivery, and used as adhesives to stop bleeding. Furthermore, biomaterials can be created by tissue engineering *in vitro* to regenerate living tissues. Also, there is the possibility of modifying and controlling the surface properties of materials, in particular topography and surface chemistry aiming to stimulate specific interactions of materials with the biological environment, like simulating biological responses or improving the osteoconductive capacity [5].

A *biomaterial* should satisfy the following properties; (i) non-toxic for the organism, (ii) chemically stable or with controlled chemical stability, (iii) suitable mechanical properties, (iv) adequate size and design, (v) reproducible in all its characteristics, and (vi) affordable. Given those requirements and the complexity of the interactions between the *biomaterial* and the physiological environment, the development of biomaterials needs the confluence of different disciplines. Material science, biology and physiology, clinical sciences, and more fundamental sciences like chemistry and physics, are therefore required to solve the challenges of a new biomaterial product efficiently.

Despite the high regenerative capacity of bone, bone together with joint pathologies are among the leading causes of chronic pain, physical disability and work absence in both developed and developing countries, affecting millions of people worldwide [5]. Thus, the last two decades (2000-2020) has been declared by the World Health Organization as the Bone and Joint Decade [6]. Currently, over 100 million Europeans and 40 million people over 45 years in the USA suffer musculoskeletal problems. As the average age of the population rises, the USA projections estimate an increase up to more than 60 million persons (22% of the population) by the year 2030. This projection presents a significant impact on patient quality of life, direct medical and indirect costs [5].

New technologies and advances in orthopaedic surgery, like the current gold standard use of *autografting* that involves the bone tissue transplantation from a non-load-bearing site of the patient and transplantation into the traumatised site, have significantly contributed to enhancing bone repair. Despite this, there are still some cases where problems related to improper bone healing need to be resolved; (i) fracture non-unions and delayed-unions, (ii) osteoporosis-related fractures, (iii) fracture/implant infection issues, (iv) maxillofacial reconstruction with augmentation material. Therefore, the need for novel technologies and methods that provide more feasible and efficient therapeutic biomaterial options is apparent.

The predicted significant increase of those pathologies and the deficiencies in the current orthopaedic solutions reinforces the need for novel technologies and methods to provide more feasible and efficient therapeutic biomaterial options. According to those necessities, new biomaterials for the design of structures in tissue engineering are currently under development. Those new biomaterials aim at improved strength, low Young´s modulus, and a correct load distribution fixation capacity. Furthermore, cell/drug delivery systems should be implemented to guide bone repair, to release the adequate dose of osteoinductive signals and to supply or attract cells capable of responding to these signals and differentiating into osteogenic cells.

1.2 Concepts of metallic biomaterials

1.2.1 Permanent metallic biomaterials

The necessity of long bone fracture fixation is the origin of the use of metals as biomaterials in the 19th century [7]. Since then, metallic materials have predominated in temporary (implant has to be removed: e.g. bone plates, pins and screws) and permanent (the implant is intended to stay in the body: e.g. total joint replacements, tooth roots and fillings) bone replacements [8]. New applications, such as vascular stents [9] shows an increase in the application of metals as biomaterials. Besides a large number of metals and alloys generally produced in industry, only a few are classified as biocompatible and can serve as an implant material for a long/temporal necessity. Current metallic biomaterial systems and its applications are mainly stainless steels (e.g. temporary devices and total hip replacements), and titanium-based alloys (e.g. specific parts of hip replacements or nails). However, other metals like cobalt-based alloys (e.g. used for total joint replacements and dentistry castings) and NiTi alloys (e.g. vascular stents, intracranial aneurysm clips, and dental arch-wires) are nowadays applied. Those *traditional* permanent metallic materials present some disadvantages like stress shielding inducing re-fracture, and in many cases, a second surgery will be necessary to remove the implanted device to avoid adverse effects [10]. In the case of young patients, the necessity of implant removal is even more crucial to allow developmental bone growth [11].

1.2.2 Degradable biomaterials

In contrast to the traditional corrosion/degradation resistant materials, the concept of a degradable or absorbable biomaterial emerged aiming a controlled degradation at the *in vivo* environment eliminating the need for a second surgery to remove the implant [12]. This aim requires that the mechanical requirements of the material must remain intact or at least sufficient during the regeneration time of the tissue. According to that, *Figure 1* describes the needs regarding the degradation time the total resorption time of the biomaterial, for orthopaedic and vascular applications.

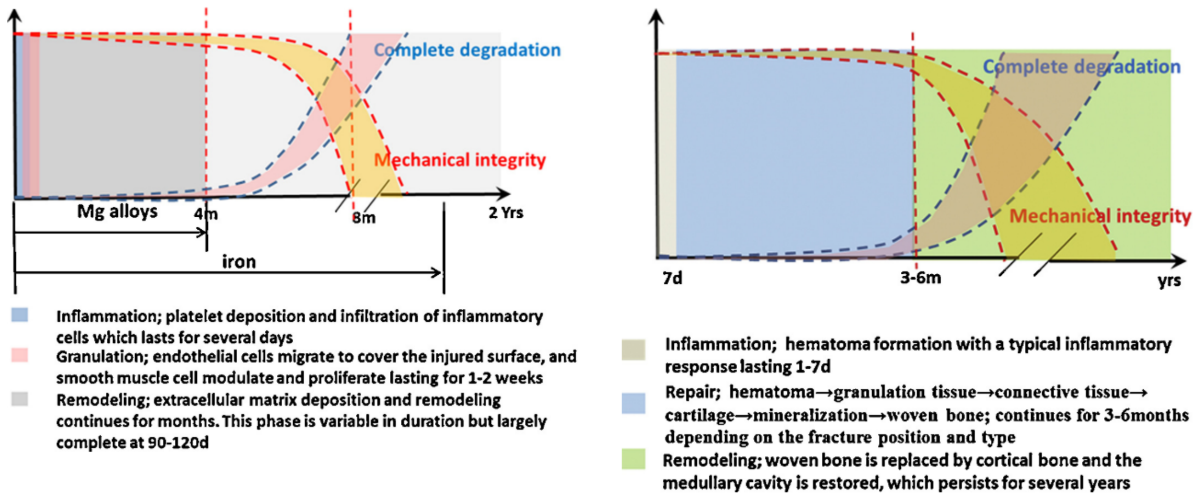

Figure 1: Schematic diagrams that present the mechanical requirements for (left) a degradable metallic stent during the vascular healing process, and (right) a degradable implant during the bone healing process (with permission by Elsevier [13]*).*

Novel materials like degradable polymers have increasingly taken on great importance in low-load bearing fracture sites [14,15]. However, an insufficient mechanical strength or brittleness, long-term inflammatory responses of degradation derived products, and a non-optimal osteoinductivity during the degradation process, have limited the application of current biodegradable polymers. On the other side, certain ceramics with excellent biocompatibility, bioactivity, with a degradation resistant composition, make them good candidates for bone repairing biomaterials. However, the poor fracture toughness, brittleness and stiffness of those materials limit their application [16].

Concerning the disadvantages of degradable polymers and ceramics mentioned above, degradable metals are advantageous due to their mechanical and biocompatibility properties for bone fixation. After completing the mechanical support mission of the implant, the aim of a total dissolution requires that the principal component(s) should be an essential element that can be metabolised by the human body [17]. Among minority systems (e.g. tungsten [18,19], Ca-based [20,21] and Sr-based bulk metallic glasses (BMGs) [22]), current research efforts on biodegradable metals include iron-based [23], zinc-based [24–26], and magnesium-based, the latter being the leading-edge of those biodegradable metals [27].

1.2.3 Degradable magnesium-based biomaterials

Magnesium-based degradable biomaterials are promising in the field of bone remodelling, thanks to the following characteristics:

i) The physiological environment degrades Magnesium-based materials.

ii) Magnesium alloys densities (1.7 – 2.0 g/cm^3) are close to the cortical bone density values (see *Table 2*).

iii) Magnesium-based materials have mechanical properties similar to those of natural bone (see *Table 2*) reducing the problem of stress shielding re-fractures.

iv) The fact that magnesium is the fourth most abundant cation in the human body makes magnesium an essential element that is tolerable in significant amounts in the human body without adverse reactions [28]. Besides, half of the physiological Mg is stored in the bone tissue [29], and it is an essential element involved in numerous metabolic reactions. This fact leads to a physiological absorption and metabolisation of magnesium-based materials degradation products.

v) Magnesium-based materials have been reported to stimulate new bone formation showing positive osteoconductivity [30].

Despite the many advantages of magnesium as a degradable biomaterial, many factors are hampering its broader use. First of all, there is an unmatched strength for implantation sites with load-bearing requirements, like for critical bone defects (CBD). *Table 2* shows with typical UTS values around 45 MPa when cortical bone reaches values as high as 283 MPa. In the second place, magnesium-based materials have too high (initial) degradation rate associated with a high hydrogen release that can lead to gas accumulation, disturbing the bone-implant connectivity [31].

Table 2: Mechanical properties of different materials suitable for bone remodelling implants.

Tissue	**UTS (MPa)**	**E (Gpa)**	**Density (g/cm^3)**
Human cortical bone [32]	35 - 283	5 - 23	1.8 - 2.0
Human cancellous bone [16]	1.5 - 38	10 – 1570 (MPa)	1.0 – 1.4
Ti alloys			
CP-Ti (Grade 4)	550 [33]	103-107 [34]	4.5 [35]
Ti6Al4V (as cast) [32]	830 - 1025	114	4.43
Ti6Al4V (wrought) [32]	896 - 1172	114	4.43
Ti6Al7Nb [36]	900 - 1050	114	4.51
Iron alloys			
Stainless steel 316L [32]	480 -620	193	8.0
Pure Iron (electroformed)	160 - 435	211	7.86
Mg alloys			
Pure Mg	90	44	1.74
AZ91E	165 - 457	45	1.81
WE43	250 - 277	44 - 46	1.84
Mg-10Gd	69.1 – 85.4	-	1.88
Mg-6Zn	277 - 281	42.3	1.84
Mg-1Ca	75 - 240	-	1.73
Polymers			
Polyglocolide (PGA) [16]	55 - 80	5 - 7	1.5 – 1.707 [36]
Polylactide (PLA)- D,L [16]	90 -103	1.9	-
Poly-L-Lactide (PLLA) [16]	45 - 70	2.7	-
Polycaprolatcone (PCL) [16]	10 -35	0.4 – 0.6	-
Chitosan	35 - 75	2 - 18	-
Collagen	50 - 150	0.002 - 5	-
Ceramics			
Hydroxiapatite [16]	40 -200	80 - 110	-
Tri-calcium phosphate (TCP)	-	-	-
DCP brushite	15 - 25	40 - 55	-
DCP monetite	10 - 15	22 - 35	-

* UTS: Ultimate tensile strength, E: Young´s modulus.

Finally, yet importantly, the degradation mechanisms especially under the complexity of physiological conditions, the effect of released ions (e.g. Mg^{2+} and alloying elements) in the tissue healing process (e.g. remodelling process) and their possible physiological accumulation [37] are not well understood. Nonetheless, using high purity magnesium and the recent advances in alloying and material processing tailoring the microstructures, give the possibility to tune adequate corrosion rates and mechanical properties matching the different implantation sites necessities. For these reasons, magnesium implants, like Magmaris® stents

(BIOTRONIK), MAGNEZIX® screws and pins (Syntellix AG) or Resomet® screws and wires (U&i Corporation), have been recently introduced in the market [36,38].

1.3 Magnesium degradation: an interface phenomenon

Although some magnesium-based implants are already used clinically, the chemical environment and the degradation mechanisms under physiological conditions are only sparsely understood. As mentioned before, the promising application of polymer-based resorbable implants has been limited due to the adverse reactions of such materials in the body, including a not optimal osteoinductivity [16,39]. Furthermore, the importance of understanding the degradation mechanism under relevant environments was also identified as necessary for other biodegradable metals like zinc [40] and iron [41], in order to translate *in vitro* degradation tests into *in vivo* performance of the material. Therefore, apart from the necessity of tailoring appropriate mechanical properties, and obtaining the same or proportional accelerated *in vitro* degradation rate compared to *in vivo* conditions, the study of the degradation mechanisms involving magnesium-based materials and the development of reliable investigation methods are essential for the development of those implant materials.

On the other side, the complexity of an implantation site environment and the difficulty of monitoring the *in vivo* degradation process, despite few current early works [42,43], hinders the possibility of direct laboratory mimicking of the *in vivo* conditions [44,45]. Therefore, there is a significant interest in identifying [46,47] and correlating [48–51] differences between the *in vitro* and *in vivo* degradation testing results [52,53]. Moreover, the study of the local processes at the Mg interface under physiological conditions by *in vitro* studies became a valuable tool to reconstruct the overall physiological process.

According to the above, the present section aims to describe how the surface environment influences the Mg dissolution and the formation of the degradation products layer. For this purpose, it is necessary to review how the electrochemical processes, the degradation environment composition, the degradation products layer composition and morphology, the pH, and the *in vitro* testing set-up can affect the alloy degradation rate. The understanding of those individual and synergic effects at the local surface environment is crucial to progress in the establishment of a general mechanism.

1.3.1 Electrochemical processes of Mg corrosion

The capability of magnesium alloys to work as a biodegradable implant resides upon its weak corrosion resistance in the neutral-acidic aqueous environment. The highly negative standard electrode potential of Mg ($E°_{SHE}$ = -2.37 V) shows the high tendency to the dissolution of the metallic atoms (Mg^0) into the aqueous media (Mg^{2+}). This thermodynamic tendency to the dissolution depends on the alloy composition.

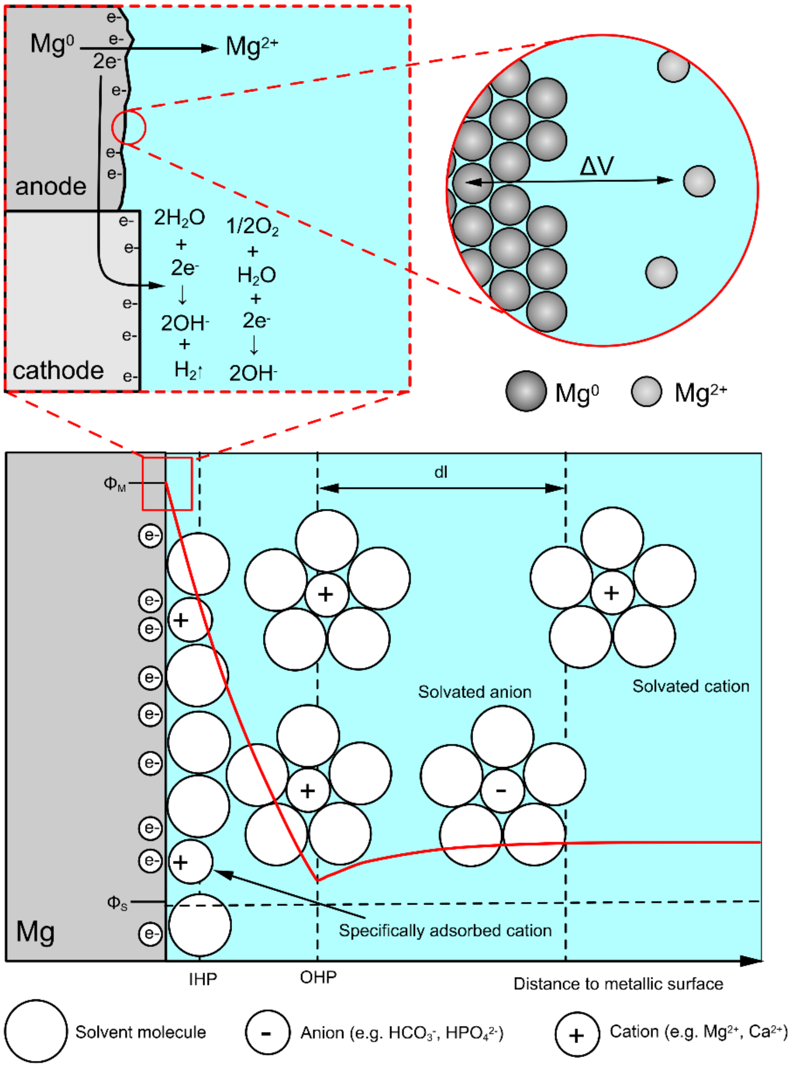

Figure 2: Schematic diagram that presents the electrochemical processes at the Mg surface under immersion in aqueous media and the electrochemical potential developed above the surface. In the anodic area, the oxidation of the metallic atoms takes place while in the cathodic area where the semi-cathodic reaction take place consumes the electrons produced in the anodic area. The resulting negatively charged surface develops the electrical double layer, and an electric potential difference so-called Galvani or inner potential difference ($\Delta\Phi$) is developed across the double layer. [IHP: inner Helmholtz plane or compact layer, OHP: outer Helmholtz plane, Φ_M: Galvani potential at the metallic surface, Φ_S: Galvani potential at the bulk solution, dl: diffusion layer]

The positive charge of dissolved Mg^{2+} atoms in the solution leaves an accumulation of negative charge on the metal surface. Due to the separation of charges, a “capacitor” situation is generated, promoting the arrangement of the ionic species in the solution adjacent to the metal surface named *electrochemical double layer*. This structure, depicted in *Figure 2,* is defined in the literature [54,55] as follows; i) the negatively or positively charged surface, ii) a compact layer of solvent molecules and specifically or contact adsorbed ions with no hydration shell that remove the hydration layer covering the metallic surface that partially compensates the surface charge and which its *locus* of centres define the Inner Helmholtz Plane (IHP), iii) and a not specifically adsorbed layer of solvated ions by long-range electrostatic forces which their *locus* of centres conform the Outer Helmholtz Plane (OHP). Due to the thermal agitation in the solution, the non-specifically adsorbed ions are distributed in a diffuse region between the OHP and the bulk until the bulk solution that is called diffusive layer (dl). This diffusive layer balance completely the charge on the metal surface defining a drop of the electric potential (so-called Galvani potential or inner potential) along with the nearby surface solution which can be described by the theory of Gouy Chapman [55], as is depicted by the red line in *Figure 2.* The extension of this diffusive layer decisively depends on the ionic strength (I). The thickness of the diffusion layer decreases with an increase in the number of charge carriers. Moreover, in the case of a concentrated solution, the diffusion layer can be eliminated. For solutions of around 10^{-2} M, the thickness of this double layer is estimated to be less than 100 Å (0.01 µm). The composition of the double layer and the electric potential gradient change during the formation of the degradation products layer. Those changes influence the kinetics of the surface processes and therefore the metallic dissolution kinetics, since the ion transport across the metal-degradation product layer, the degradation product layer-electrolyte interface and the degradation products layer is governed by the electric potential drop along with those areas [55].

The electrochemical behaviour of magnesium alloys is believed to be similar to pure magnesium [56,57], therefore ruled by the same cathodic and anodic reactions presented in $eq. 2–4$. Despite that, the influence of alloying elements on the electrochemical process cannot be excluded, as numerous electrochemical tests presented significant changes on the corrosion rate (i_{cor}) for different alloy composition [58,59]. Due to the high electronegative potential of magnesium, almost any other phase present in the microstructure (secondary phases, segregated areas, impurities, or noble inclusions) will behave nobler than the α-Mg matrix accelerating the dissolution. Traditional strategies for the improvement of mechanical properties were revealed to improve the degradation rate of the alloy. Those processes improve the homogenous distribution of the potential active cathodic nucleus and therefore generating a lower and more homogeneous degradation [56]. Some of those strategies are the alloy design [60,61], extrusion [62–64], High-Pressure-Torsion (HPT) [65,66], or Equal Channel Angular Pressing (ECAP) [67,68].

Moreover, the metallic dissolution in an aqueous solution is dependent not only on the electrode potential but also on the acidity/basicity level of the solution [69]. The thermodynamic prediction of metallic corrosion was illustrated by Marcel Pourbaix (1966) in the form of potential-pH diagrams, as shown for magnesium–water system depicted in *Figure 3.* The corrosion of metallic magnesium may occur in the potential-pH regions where hydrated Mg^{2+} ions are stable, and no corrosion occurs in the highly negative electrode potential regions where metallic magnesium is thermodynamically stable. In the regions where magnesium hydroxide is stable (pH > 10) a decrease in the corrosion rate is expected due to the slightly soluble $MgO/Mg(OH)_2$ bilayer formed on the surface [59]. As illustrated in *Figure 3*, the physiological environment places magnesium materials in a non-protective area of the E-pH diagram. However, the reduction reaction of water ($eq. 3$) produces an alkalinisation process that cannot be compensated by the hydrolysis of Mg^{2+} due to its low pK_{hyd} [70]. Therefore, the alkalinisation process changes the behaviour of magnesium alloys by stabilising the degradation products layer formed on the surface.

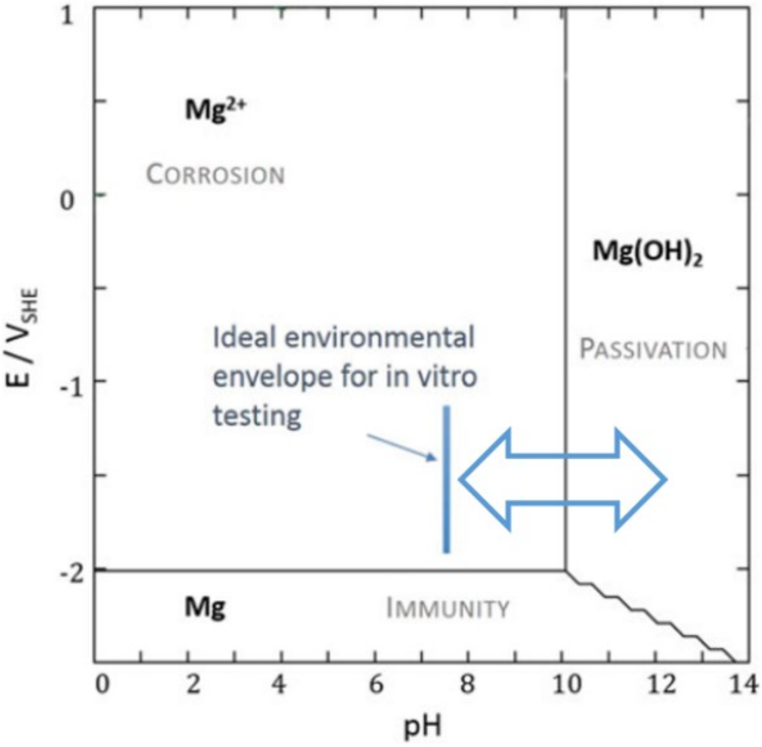

Figure 3: Pourbaix diagram for magnesium immersed in aqueous media at 25 °C, where is presented the physiological pH (with permission by Springer [71]*).*

However, the dissolution rate obtained determined by a corrosion potential (E_{cor}) and a corrosion current (i_{cor}), depends on kinetic factors coming from the surrounding environment affecting both the oxidation and the reduction semireactions. Those factors are, for example, the microstructure of the alloy, the presence of impurities or secondary phases, and the degradation products layer formed on Mg surface. The influence of the environmental factors in magnesium electrochemistry is evidenced when the magnesium standard reduction potential (-2.37 V_{SHE}) is compared to the measured corrosion potential (E_{corr}) with values between -1.7 and -1.4 V_{SHE} for magnesium alloys under immersion in dilute NaCl solutions [72,73].

The variability in the magnesium degradation performance found for different corrosive solutions is attributed to the different composition and morphology of the degradation products layer formed on the magnesium surface. Such differences in layer composition are derived from the composition of the corrosive solution and the alloy. The fact that the E_{corr} is shifted to nobler values and the current densities decrease by increasing the pH of the solution [72,74] points to the significant effect of the pH on the stability of the degradation products layer with protective effects.

In the presence of moisture or under immersion in simple aqueous environments at room temperature, the natural and not entirely covering cubic MgO *halite* film [58] formed on magnesium surface, is transformed via hydroxylation into a MgO/$Mg(OH)_2$ bilayer structure [59,75], as shows $eq. 1$. This bilayer structure is a diffuse mixed oxide/hydroxide film defined by a thin-dense MgO-rich inner-layer and a thick-porous $Mg(OH)_2$-rich outer layer. The change in the compactness from a dense inner to a porous layer is a consequence of a volume change in the crystal structure from the transition from Mg-O to Mg-OH bonds and the continuous dissolution-precipitation process of the bilayer [76].

$$MgO_{(surface)} + H_2O \rightarrow Mg(OH)_{2\,(surface)} \qquad (eq. 1)$$

This bilayer structure is not fully-protective under neutral and acidic aqueous solutions due to the dependency of *brucite* dissolution on the pH shown in previous works [77]. This lead to a not fully-passivated surface that cannot prevent the contact between the metal and the degradation solution; therefore, cannot stop the degradation process from continuing. The oxidation process $(eq. 2)$ where the metallic magnesium (Mg) is transformed to ionic magnesium (Mg^{2+}) in solution is accompanied with at least one reduction reaction which will consume the electrons produced in the anodic reaction. Due to the low magnesium corrosion potential [72], the primary reduction reaction on Mg under neutral and alkaline environments is the water reduction reaction $(eq. 3)$.

$$Mg \rightarrow Mg^{2+} + 2e^- \qquad (eq. 2)$$

$$2H_2O + 2e^- \rightarrow H_2 + 2OH^- \qquad (eq. 3)$$

Contrary to what is traditionally stated for magnesium corrosion mechanism under aqueous media, recent works have shown that the reduction of dissolved oxygen takes place as a secondary reduction reaction $(eq. 4)$. This reduction reaction takes place on the noble alloy impurities particles (e.g. Fe, Cu, Ni and Zn) present in the Mg matrix, segregated on the grain boundaries, and also coming from the corrosive solution [59,70,78,79]. However, other electrochemically active features at the surface like noble secondary phases can generate the oxygen reduction reaction. The importance of the O_2 reduction reaction in the kinetics of magnesium corrosion has to be weighed depending on the corrosive environment [80]. Accordingly, the low partial pressure of oxygen of specific human physiological implantation sites (e.g. bone) predicts a decrease in the rate of *in vivo* degradation compared to the normal aerated conditions of *in vitro* testing [81].

$$O_2 + 2H_2O + 4e^- \rightarrow 4OH^- \qquad (eq. 4)$$

Therefore, the magnesium degradation process under simple deaerated aqueous media leads to the overall reaction presented in $eq. 5$.

$$Mg + 2H_2O \rightarrow Mg(OH)_2 + H_2 \qquad (eq. 5)$$

Therefore, under a simple aqueous solution magnesium dissolution kinetics is modulated by the existence of the not fully-protective MgO/$Mg(OH)_2$ film, and the presence of impurities, secondary phases or noble inclusions (present in any magnesium alloy), that provide efficient cathodic areas that accelerate the corrosion rate [82].

1.3.2 Influence of the physiological environment on Mg degradation

Traditional Pourbaix diagrams, like the one in *Figure 3*, observe the corrosion process in the presence of pure water containing no solutes and a specific Mg^{2+} concentration. However, the presence of other ions (e.g., chlorine, sulfates, carbonates, and phosphates), will significantly affect the structures of the immunity, passivation, and corrosion areas of an E-pH diagram [44]. Under those more complex compositions, the alkalinisation process does not only stabilise the $Mg(OH)_2$, resulting in the precipitation of other insoluble salts that contribute to the degradation products layer formation, e.g. $CaCO_3$ that was found to protect cathodically immersed steel [83].

According to that, the composition of the physiological environment provides a greater complexity on the degradation mechanism of magnesium-based materials compared with the conventional simple *in vitro* corrosive solutions (e.g., 3.5% NaCl). The corrosive physiological fluid can be defined as an aqueous solution containing inorganic electrolytes (e.g., Na^+, K^+, Ca^{2+}, Mg^{2+} Cl^-, HCO_3^-, HPO_4^{2-}), organic substances of low-molecular-weight (e.g., glucose, amino acids) as well as organic polymeric structures (e.g., proteins), and gases dissolved (e.g. CO_2, O_2). All those components, in addition to the pH (pH 7.4), are well balanced by the complex physiological homeostasis. Moreover, the physiological environment of the bone can provide a mechanical solicitation that in combination with the aggressive chemical environment can generate an acceleration of the degradation rate by, e.g. stress corrosion cracking, fatigue corrosion [84–88].

Influence of the Inorganic fraction of physiological fluids on Mg degradation

It has been reported that magnesium corrosion rate depends significantly on the degradation solution applied on *in vitro* testing. Previous studies on the influence of the inorganic components under simulated physiological conditions showed significant differences in degradation rate and the degradation products layer composition/morphology compared with the ones obtained under more simple solutions. The following ions are included in different proportions depending on the physiological fluid compartment: Na^+, K^+, Cl^-, Ca^{2+}, Mg^{2+}, HPO_4^{2-}, HCO_3^-, SO_4^-.

When magnesium is immersed in the presence of Cl^- anions, the dissolution process is accelerated by the reaction of those anions with the $MgO/Mg(OH)_2$ film generating more soluble compounds. Besides that, as exposed by *Williams et al.* [89], the solubility of $Mg(OH)_2$ varies with the chloride ion in the range of 100 and 1000 mM accordingly $eq. 6$, the mechanism by which passive films are disrupted by Cl^- anions is a long-standing issue in corrosion science.

$$K_{sp} = K_{sp}^{1} + 4.8 \times 10^{-11} \log_{10}[Cl^-] \qquad (eq. 6)$$

The commonly addressed mechanism involving the formation of soluble $MgCl_2$ [90,91] seems not to be justified by the thermodynamic of the reaction between the $Mg(OH)_2$ and the Cl^- anion. Alternatively, the role of the detrimental effect of Cl^- anion on the film breakdown has been attributed to the formation of slightly water-soluble hydrated magnesium hydroxy chloride complexes with the general composition $Mg_kCl_l(OH)_m \cdot nH_2O$ [89]. The low-temperature stable phases are the crystalline needlelike 3-1-8 phase or $Mg_2Cl(OH)_3 \cdot 4H_2O$ and the 5-1-8 phase or $Mg_3Cl(OH)_5 \cdot 8H_2O$ [92]. Their solubility was estimated to be lower than the $Mg(OH)_2$, according to *Mazuranic et al.* [93] as is presented in *Table 3.*

Table 3: Approximate solubility products calculations of the 3-1-8 and 5-1-8 magnesium hydroxy chloride complexes, and $Mg(OH)_2$ at variable ionic strengths (I) [93]. *Kw: water autoionization constant, K_{sp}: solubility product of the hydroxy chloride complexes.*

Phase	**pH**	**I (mol dm^{-3})**		**- log K_w (interpolated)**	**- log K_{sp}**
			Log ($K_{sp} \cdot K_w^{-3}$)		
3-1-8	6.12	13.02	20.55	Unknown	
	6.15	12.12	20.53	Unknown	
	6.20	10.44	20.46	Unknown	
	6.30	10.41	20.76	Unknown	
	6.40	6.37	20.44	Unknown	
			Log ($K_{sp} \cdot K_w^{-5}$)		
5-1-8	7.60	5.91	39.41	15.06	35.89
	7.62	5.70	39.46	14.98	35.44
	7.70	5.54	39.78	14.94	34.92
			Log ($K_{sp} \cdot K_w^{-2}$)		
$Mg(OH)_2$	8.40	5.08	17.00	14.78	12.56
	8.50	4.92	17.19	14.72	12.25
	8.50	4.18	17.13	14.50	11.87
	8.70	3.15	17.30	14.22	11.14

The results provided by *Taltavull et al.* [94] on magnesium degradation, support the negative influence of the Cl^- anions but also revealed a dependency of the detrimental effect on the alloy composition and microstructure due to a relation with the galvanic effect between secondary particles and α-Mg matrix. According to *Kirkland and Birbilis* [71], the higher content of Cl^- anions on typical SBF solutions compared with human plasma or interstitial fluids, can be one of the reasons that accelerate the *in vitro* degradation of magnesium-based materials compared with the *in vivo* conditions. However, the difference on the degradation rate caused by an increase on Cl^- anions of about a 40% (from 102.5 to 144.4 mM) is almost non-existent when simulated physiological conditions are applied (composition and buffering system). This fact was justified by *Xin et al.* [95] with an extra compact degradation product layer generated by the presence of Ca, Mg-phosphates that hinder the contact between the Cl^- anions and the metallic surface and that possibly do not react with the Cl^- anions.

Previous works [95–97] stated that magnesium corrosion is accelerated in the presence of SO_4^- ions, showing a lesser trend to pitting but promoting greater mass loss by a general degradation process. However, *Agha et al.* [48] showed this effect with SO_4^- concentrations increased up to the physiological range (200 mg/L), but no influence was observed when Ca^{2+}, HCO_3^- and $HPO4^{2-}$ ions were present.

The degradation of pure magnesium in sulfate/carbonate solutions with HCO_3^- concentrations between 0.7 and 7 mM was studied by *Baril et al.* [96], concluding that under those conditions the HCO_3^- ions increase the rate dissolution fo the $MgO/Mg(OH)_2$ film by forming soluble salts, in accordance with *Gulbrandsen* [98]. On the contrary, according to *Li et al.* [99], the presence of carbonates in SBF with the presence of Ca^{2+} and Mg^{2+} ions showed an increase of a passivation effect until reach a concentration of 27 mM and an increase in the degradation rate when this concentration is exceeded. The passivation effect in the presence of HCO_3^- was justified by a more protective degradation products layer when the HCO_3^- stays bellow 27mM. On the other hand, when an increase in HCO_3^- concentration is not accompanied also by an increase of cations like Ca^{2+} the increase of degradation rate was justified by the ionisation of the bicarbonates that promotes acidification and therefore delaying the alkalinisation process that promotes the saturation of $Mg(OH)_2$. That increment in the degradation rate was later confirmed by *Agha et al.* [48] for HP-Mg immersed in HBSS when the concentration of HCO_3^- ions was increased from 22 to 44 mM. The different effect of HCO_3^- ions presented in previous works lies in the importance of the cations present in solution, pointing to the higher importance of Ca^{2+} cations concerning degradation protection compared with the Mg^{2+} ions. At the same time, *Li et al.* [99] showed how important is the stability of the degradation solution composition and pH during the degradation test. According to that, due to the perfect physiological balance between the cations, anions, and pH, the stability of the degradation solution is essential when *in vivo* degradation predictions are attempted. On the other hand, *Li et al.* [99] omitted the possible influence that other ions present in SBF (e.g. Mg^{2+} or HPO_4^{2-}) may have in the degradation products layer and therefore, in their protective effect.

The contribution of magnesium phosphates and magnesium carbonates to the passivation of magnesium surface has been previously studied. A systematic electrochemical study, performed on AZ91 by *Xin et al.* [95], revealed the synergic protective effect of HPO_4^{2-} and HCO_3^- in the presence of Cl^- and SO_4^{2-} ions. The author identified a robust protective effect of magnesium phosphate precipitated on the surface. When HCO_3^- are included, an initial increase of the degradation is promoted due to its buffer effect. However, as the alkalinisation process continues, the precipitation of magnesium carbonate adds its protective effect decreasing, even more, the degradation rate compared with the only addition of HPO_4^{2-} ions, and suppress localised pitting corrosion. In accordance to the previously presented protective effect of the HPO_4^{2-} ions, *Williams et al.* [100] proposed that HPO_4^{2-} ions are converted into PO_4^{3-} ions on the high alkaline cathodic zones, and together with the Mg^{2+} ions migrated from the anodic zones promote precipitation of magnesium phosphate that hinder the electron transfer to the cathodic surface area and therefore the cathodic reaction. In addition, *Williams et al.* [100] point to the ineffective effect of HPO_4^{2-} ions under high alkaline solutions, due to a massive magnesium phosphate precipitation on the anodic zones that prevent enough migration of Mg^{2+} and HPO_4^{2-} ions to the cathodic zones. Once more, those studies point to the necessity of controlling the environmental pH in order to promote an effective precipitation process that possibly happens under *in vivo* conditions.

Among all synergic influences of the inorganic fraction, the magnesium degradation in the presence of a physiological fluid generates a degradation products layer which significantly modulates the interaction between the magnesium surface and the corrosive solution and in turn the degradation rate. From the results presented in the mentioned works, the presence of Mg^{2+}, Ca^{2+}, HCO_3^- and HPO_4^{2-} ions present a critical role in this protective effect. The presence of those compounds is ruled by the environment (concentration and pH) during the degradation process. Therefore, to understand and predict the behaviour of magnesium-based materials under physiological conditions, it is crucial to define the correct physiological composition and control the pH during the degradation process.

Inorganic precipitation processes and degradation products layer formation

According to mentioned above, the inorganic fraction of the degradation products layer (e.g. $Mg(OH)_2$, Ca,Mg-carbonates/phosphates) modulate the intrinsic degradation rate of a specific alloy composition-microstructure. The presence of those components on the surface is ruled by the heterogeneous precipitation equilibriums based on the following physicochemical conditions:

1. Solution supersaturation
2. Nucleation
3. Crystal growth

The driving force of a heterogeneous precipitation reaction is the *supersaturation* condition. This thermodynamic condition defines a chemical reaction at which the reactants are much more soluble than the formed product. This condition is necessary but not sufficient for the precipitation process, due to the necessary, but difficult to evaluate under the complex physiological conditions, *nucleation* and *crystal growth* processes [101]. Anyhow, the thermodynamic driving force can be evaluated by the change of the Gibbs free energy (ΔG) and its relationship with the constant of the dissolution/precipitation equilibrium, so-called solubility product (K_{sp}). For a general ionic solid, A_nB_m, the equilibrium and its K_{ps} has the following form:

$$A_nB_{m_{(s)}} \leftrightharpoons mA^{n-}{}_{(aq)} + nB^{m+}{}_{(aq)} \qquad (eq.7)$$

$$K_{ps} = \frac{a_{A^-}{}^{m} \cdot \ a_{B^+}{}^{n}}{a_{A_nB_{m_{(s)}}}} = a_{A^-}{}^{m} \cdot a_{B^+}{}^{n} \qquad (eq.8)$$

Where a_{A-} and a_{B+} are the ionic activities, or *effective concentration*, of the species A^{n-} and B^{m+} in the solution when it is saturated in the compound $A_nB_{m_{(s)}}$ for which ionic activity is equal to unity [102]. The relation between the Gibbs free energy change and the K_{sp} for the above general reaction is given by:

$$\ln K_{sp} = \frac{-\Delta G_R^{\circ}}{RT} \qquad (eq.9)$$

Where ΔG_R° is the Gibbs free energy change per mole of the reaction, R is the ideal gas constant, and T is the temperature in Kelvin.

Therefore the *saturation index* (SI) is defined as a variable that quantifies the necessary deviation from the equilibrium to observe the nucleation and growth phenomenon [103].

$$SI = \frac{\Delta G}{RT} = \ln \frac{(a_{A^-}{}^{m} \cdot a_{B^+}{}^{n})_{solution}}{K_{sp}} = \ln \frac{IAP}{K_{sp}} \qquad (eq.10)$$

Where $(a_{A^-}{}^{m} \cdot a_{B^+}{}^{n})_{solution}$ or IAP is the actual product of the free ion species in solution.

Under a situation of a diluted solution, the ionic activity of the dissolved species can be approximated to its concentrations:

$$a_i = \gamma_i \cdot C_i \;\; ; \;\; diluted\ solutions \;\rightarrow\; \gamma_i = 1\,;\; a_i = C_i \qquad (eq.11)$$

Here, γ_i is the activity coefficient, and $\mathrm{C_i}$ is the concentration of the dissolved component. Therefore, the thermodynamic tendency to precipitate can be evaluated according to the following inequalities:

$$SI = \ln\frac{IAP}{K_{sp}} = \ln\frac{[A-]^m[B+]^n}{[A-]^m{}_{eq}[B+]^n{}_{eq}} \qquad (eq.12)$$

$IAP > K_{sp}\ (SI > 0), leads\ to\ precipitation\ (supersaturation)$

$IAP < K_{sp}\ (SI < 0), leads\ to\ dissolution\ (undersaturation)$

$IAP = K_{sp}\ (SI = 0), the\ solid\ is\ in\ equilibrium\ with\ the\ solution\ (saturated)$

According to above, at the first moment of the immersion, the solution in contact with the magnesium material is in unsaturated conditions for the precipitation of the compounds that will form the degradation products layer, and no precipitate is formed. With the progress of magnesium dissolution, a significant amount of Mg^{2+} and OH^- ions are released from the interface. Those changes in composition and the presence of other ions in the solution (e.g. HCO_3^-, HPO_4^{2-}) change the ionic activities and local levels of *supersaturation* for certain chemical stoichiometries are generated. Thus, those stoichiometries are thermodynamically stable and therefore may be part of the degradation products layer. Moreover, the precipitation process itself modify the ionic concentration of the nearby surface aqueous environment due to the ion consumption and the pH change. Therefore, the driving force for the precipitation process is continuously modified during the degradation products layer formation. According to that, if the ionic composition of the bulk corrosive solution is not replaced, the degradation products layer composition will be affected during the degradation process and possibly its protective capacity.

pH influence on the formation of the degradation products layer

The influence of the pH on a heterogeneous inorganic precipitation equilibrium is based on Le Chatelier's principle [104]. As presented schematically in *Figure 4,* if the compound involved in the precipitation equilibrium has a basic anion, changes in the pH can shift the precipitation equilibrium by competing with a secondary acid-base equilibrium (*Figure 4, ii*). Since this basic anions are present for all the relevant compounds found in the degradation products layer of magnesium-based materials under physiological conditions (e.g. OH^-, CO_3^{2-}, PO_4^{3-}), the importance of the local pH in the degradation process is evident. As an example, the precipitation of DCPD or *brushite* ($CaHPO_4{\cdot}2H_2O$), a possible precursor of bioapatite formation, should involve the release of protons lowering the pH value in the vicinity and eventually in the surrounding solution [105].

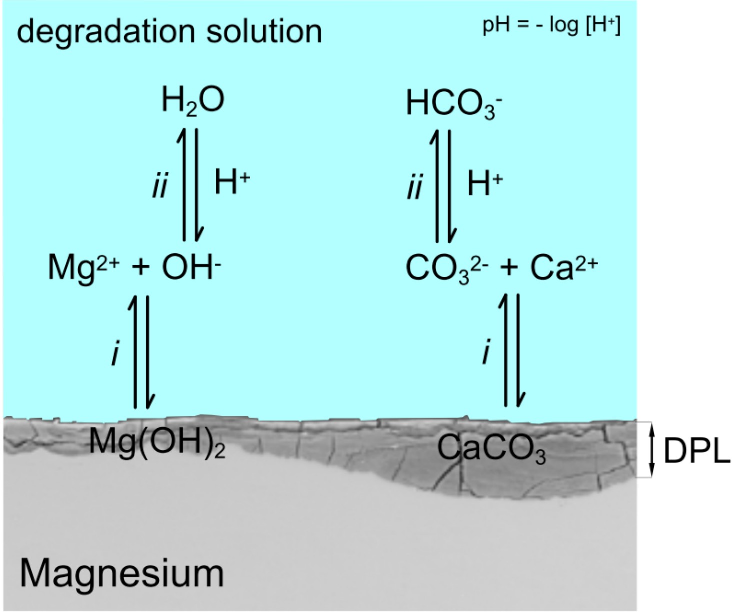

Figure 4: Scheme of (i) heterogeneous precipitation equilibriums for $Mg(OH)_2$ and $CaCO_3$, both often found in the degradation products layer (DPL) of magnesium-based materials under simulated physiological conditions, and (ii) its relationship with the pH of the degradation solution at the interface.

In accordance to the above, *In vitro* experiments performed at different fixed pH [106] or the use of different buffer systems [49,74,107] has linked the degradation rate of different magnesium alloys to the pH at which the *in vitro* test was performed. Therefore, to control the pH inside the physiological pH range during the degradation process, it is crucial to simulate the *in vivo* performance of magnesium-based materials. However, as exposed by *González et al.* [44], different buffering systems currently used for *in vitro* testing has its chemistry and can interfere with the degradation mechanism. According to that, a controlled CO_2 atmosphere in the presence of HCO_3^- (CO_2/HCO_3^- buffering system) is the closest way to mimic the physiological pH regulation system, and its use is preferable to the use of HEPES, Tris, or PBS.

Influence of the organic fraction of physiological fluids and cell influence on Mg degradation

The differences in the degradation process become more complicated with the addition of organic molecules and macromolecules in the simulated physiological fluids. Some of those complex organic influences have been studied on magnesium-based degradable biomaterials under *in vitro* conditions.

According to previous works [108,109], the addition of glucose helps to dissolve the degradation products layer in simple saline solutions, while in more complex solutions promotes a calcium phosphate (CaPs) layer by Ca-chelating and adsorption on the magnesium surface.

The presence of free amino acids in Hank´s balanced salt solution (HBSS) evaluated by *Hou et al.* [110], was found to promote the surface protection possibly by adsorption on the surface and capture of Ca^{2+} and PO_4^{3-} ions. Therefore, the higher concentration of Ca^{2+} and PO_4^{3-} ions promotes higher supersaturation levels of CaPs phases and therefore promoting a higher content of those phases even in the inner part of the degradation products layer. This increased degradation resistance by amino acids addition was also observed for steel and aluminium [111,112].

Apart from contributing to the response of the biological environment to the implant material, proteins have an essential influence on the metallic biomaterials surface behaviour. Many studies were carried out to evaluate the influence of proteins in metallic biomaterials, including magnesium-based materials. However, the effect of proteins remain partially unclear due to the complex conformational changes of proteins in solution and the unclear understanding of the kinetics and thermodynamics ruling the protein adhesion process [113]. However, the initial development of the double electric layer and the established Galvi potential difference along the diffusion layer is modified by the adsorption of lower molecular weight solutes (e.g., amino acids, or glucose), as exposed *Andrade et al.* [114]. Therefore, the adsorption between proteins and the metallic surface can be justified due to the electrostatic interaction between the negatively charged proteins at the physiological pH of 7.4 (e.g., Fibrinogen) [115], and the metallic surface through divalent cations as Ca^{2+} or Mg^{2+} as bridging agents [116]. This bounding could be established by direct interaction via positively charged domains like the ones present in the human plasma fibronectin [114], or by van der Waals and hydrophobic interactions [117]. However, is also controlled by other properties of the substrate and the medium like the roughness, pH, hydrophobicity, and reactivity of the surface [113].

Contradictory results are found in the scientific literature about the protein effect on magnesium degradation. Several authors proposed that the absorption of the proteins into the magnesium surface contribute to generating a denser and more protective degradation products layer delaying the dissolution of the alloy [116,118]. This protein layer was also associated with enrichment in CaPs in the degradation products layer observed both *in vitro* and *in vivo* situations [32,110,115]. Apart of promoting the CaPs layer, the protective character of the presence of the protein layer might be related to a disturbing development of the local pH due to the restricted mass transfer between the metallic surface and the bulk degradation solution [119]. This beneficial effect of proteins was also found for Ti alloy immersed in PBS [120]. The effect was attributed to the capability of the proteins to restrict the metal dissolution by the formation of metal/protein/hydroxide complex surface layer and the capability to prevent harmful effects of the pH change on the degradation products layer. However, the presence of proteins in solution can also delay the crystal growth of the CaPs due to the capacity of the proteins to complex the Ca ions as was exposed by *Höhn et al.* [113].

On the other hand, some authors presented a detrimental effect of protein addition that was explained by differences in the experimental design including differences in the buffering system, the degradation media exchange, or the protein concentration [121]. Furthermore, the protein effect was found to be concentration-dependent when magnesium was electrochemically tested in the presence of NaCl solutions at different concentrations of bovine serum albumin (BSA) [122]. This concentration dependence was also found for steel together with a possible protein-blocking-effect of the cathodic areas presented in iron when those materials were immersed in PBS (Phosphate buffered saline) solution in the presence of different proteins [123]. Besides, a time dependency was also found for the degradation effect of proteins, and possibly amino acids. An initial faster absorption process promotes the protective the protein contribution to the protective layer. With increasing immersion time, the chelation effect of Mg^{2+} and other ions becomes more significant than the adsorption processes increasing the degradation rate of magnesium [109,124,125]. Therefore, leading to higher values of osmolality in the degradation solution, especially when a mixture of free amino acids and proteins is present [110].

The *in vivo* condition implies the presence of cells in direct and indirect contact with the implant material. Therefore, one step forward on simulating a physiological degradation environment is to perform magnesium degradation *in vitro* tests in the presence of relevant cells and study the interaction with the implant material. Most of the studies involving cells on magnesium degradable biomaterials are focussed on the influence of the material on the cells, including cell adherence, cell activity and cytotoxicity [126–132]. Even though the cells in direct contact might influence the material degradation performance, only few studies have analysed this direct interaction due to the high complexity of the necessary testing set-up and the complexity of analysing the local processes involving such interactions. The results of the influence of L929 cells on the degradation of Mg-Ca system provided by *Kannan et al.* [133], suggested that the lactic acid released by the cell metabolic activity can decrease the pH at the interface promoting the destabilisation of the semi-protective degradation products layer and therefore increasing the degradation rate. *Agha et al.* [134] studied the compositional analysis in the cross-sections of the degradation products layer performed by FIB (Focused Ion Beam) milling of different magnesium materials after immersion under cell culture conditions in the presence and absence of human osteoblast and L929 mouse fibroblast. The authors postulated that the presence of osteoblast could alter the magnesium surface actively by; i) an acidification process due to the cell metabolic activity exposed by *Kannan et al.* [133], ii) generating an extra protective effect due to the intrinsic biomineralisation process (Ca and P enrichment of the degradation products layer), that was found near the cells instead of right underneath the attached osteoblasts, but also iii) in a pasive way hindering the interaction between the material and the degradation solution.

According to what is described in this section, due to the complexity of its composition, the influence of the physiological organic fraction and the influence of cell presence in magnesium degradation still needs to be clarified. The controversy on the protein effect is a consequence of the complex physico-chemical properties of proteins and the complex and continuously changing surrounding environment. The type of protein and the domains charge, the metallic surface chemistry, the roughness, the temperature, the pH and the interaction between protein molecules and other ions present in the degradation [135,136], can modify the adsorption or chelation kinetics of the proteins added [137]. However, besides the extra protection that the adsorption of proteins can promote during Mg degradation, *Hou et al.* [115] have recently exposed that this protective effect might be less relevant compared to the single effect promoted by the inorganic electrolyte composition. Nevertheless, the effect of the organic fraction of physiological fluids on the activity of Ca^{2+} and PO_4^{3-} ions and the effect of relevant cells like human osteoblast on contribution to the biomineralisation process at the metallic surface, highlight the crucial role of the inorganic fraction and justify the need of knowing the environmental conditions ruling the inorganic fraction of the degradation products layer.

In vitro testing set-up and hydrodynamic conditions on Mg degradation

The electrochemical processes of magnesium degradation under aqueous conditions require the movement of electrons at the interface and the movement of ions and other species between the metallic surface and the bulk environment of the corrosive solution. Therefore, the degradation process can also be rate-limited by the mass transfer phenomena between the solution at the surface and the bulk solution when the rate of the electrochemical processes and the degradation products layer are much higher than the mass transfer [103]. *Figure 5* shows the different associated phenomena that take place between the surface and the bulk corrosive environment during magnesium dissolution and the formation of the degradation products layer. According to this, the degradation rate generated is determined by the contribution of the following steps:

a. *Electron transfer* at the alloy surface observing the oxidation and reduction reactions.
b. *Adsorption-desorption* reactions on the alloy surface.
c. *Mass transfer* phenomenon through the degradation products layer and between the bulk solution and the solution near the surface.
d. *Chemical reactions* preceding and following the electron transfer reaction, including heterogeneous precipitation and complexation processes.

The formation of a semi-protective degradation products layer on Mg surface promotes a mass transfer rate-limiting process. Therefore, (d) the formation rate of the degradation products layer and (c) the mass transfer through the degradation products layer are responsible for the fact that the electrode potential is modified until it reaches the i_{cor} and E_{cor}. This situation defines a concentration polarisation situation along with the degradation products layer. The corrosion potential reaches a value between the equilibrium potential of the anodic metal dissolution (oxidation) and the cathodic reaction (reduction) [69].

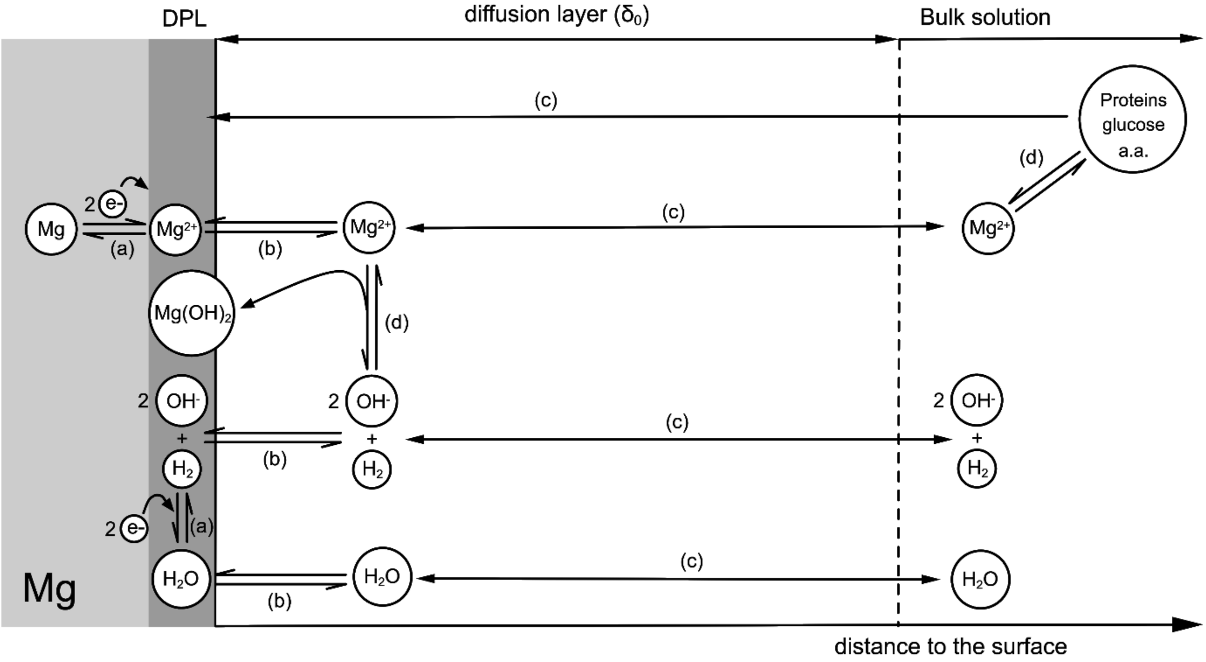

Figure 5: Scheme of the phenomena involved in the magnesium degradation process adapted from Bard and Faulkner [54]. *(a) Electron transfer at the alloy/solution interface, (b) Adsorption-desorption reactions at the interface, (c) mass transfer processes between the surface and the bulk environment, (d) chemical reactions including precipitation and complexation processes following the electron transfer process. [DPL: degradation products layer, a.a: amino acids, (δ_0): diffusion layer].*

Relevant chemical reactions on the degradation products layer formation, depicted as (d) in *Figure 5*, comprise i) heterogeneous inorganic precipitation forming the degradation products layer, but also ii) complexation reactions between organic molecules like proteins or amino acids, which can promote thickening of the degradation products layer or promote the anodic dissolution by complexing Mg^{2+} ions. However, both effects kind will influence the ionic concentration and therefore, the degradation environment during the degradation process.

The mass transfer phenomenon between a reactive surface and the bulk solution involves different driving forces, as explained by *Bard* [54] for an electrode. Those contributions to the mass transfer are generated by migration, diffusion and convection phenomena. Migration and diffusion processes are the main contributions to the mass transfer when a degradation process is performed under static conditions. Migration is the mass transfer generated on charged compounds under the influence of a gradient of an electrical potential, while the diffusion is the mass transfer generated by the movement of species under the influence of a gradient of chemical potential (e.g. concentration gradient). However, the highly reactive surface of magnesium-based materials involving precipitation reactions and therefore promoting significant changes in the concentration of the solution near the surface, and generating hydrogen gas directly on the surface ($eq. 3$), probably result into a mass transfer closer to a natural convection situation. Under those static conditions, the mass transfer can be defined as a “still” bulk solution while a net flow is generated in the solution near the reacting surface with a zero flow is found right on the interface, as *McFarlane* [138] described. However, when a fluid is flowing over a flat surface, as a consequence of the viscous forces, the fluid in contact with the surface is in a stationary velocity and retards the adjacent fluid in the vertical direction. Subsequently, the next adjacent fluid layers are influenced until reaching the edge of a boundary where the velocity equals to the free stream velocity. Within this region, that exists even under very turbulent conditions, the fluid motion is described under laminar conditions, and the component of the fluid velocity normal to the surface is small in comparison with the parallel component that depends on the distance from the surface as depicted in blue in *Figure 6*. This region in the vicinity of an electrode was firstly approximated by Walther Nernst (1916) by assuming a layer with only migration and diffusion contributions to the mass transfer and thickness of δ_N (see *Figure 6*), and total convection contribution after this diffusion layer.

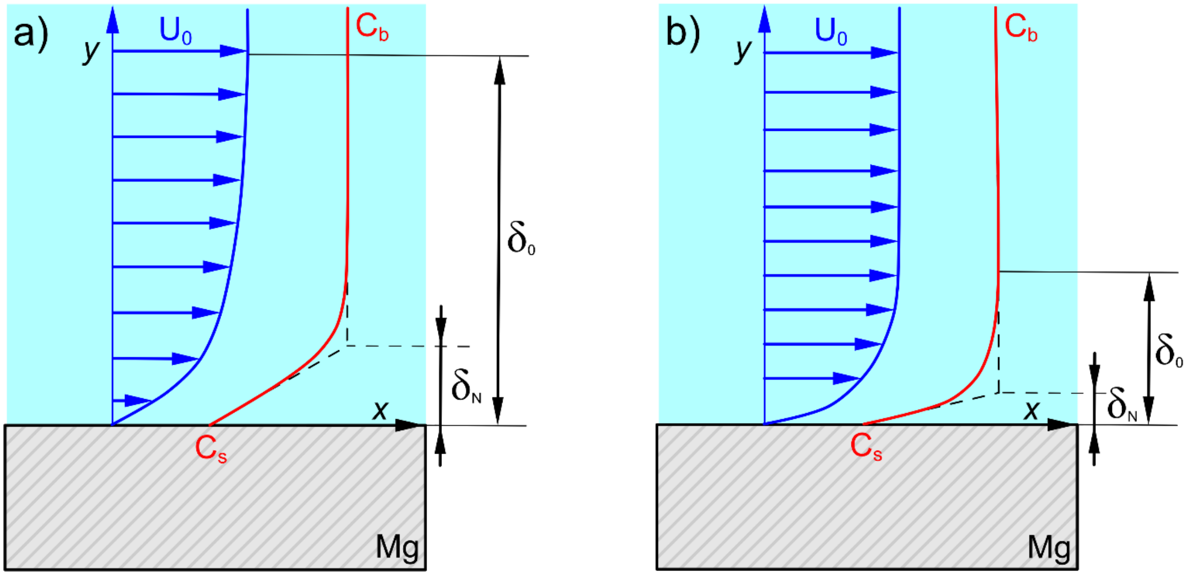

Figure 6: Solution velocity profiles (in blue) and concentration profile of a hypothetical product under a) laminar and b) turbulent flow conditions along a flat surface. δ_0: diffusion layer, δ_N: approximation of the diffusion layer by Nernst, U_0: fluid velocity in the bulk solution, C_b: product concentration in the bulk solution, C_s: product concentration at the interface.

According to this situation, a concentration difference of products and reactants between the surface and the bulk solution is established for a reactive surface. As commented before, this simplified model does not describe the real concentration gradient formed in the normal direction to the surface, depicted in *Figure 6* in red, and therefore the real diffusion layer thickness (δ_0). Even when the diffusion contribution is the responsibility of the solution renewal at the surface (δ_0), a progressive convection contribution inside the diffusion layer and the tangential velocity component cannot be neglected for the mass transport [139]. It should be mentioned that the diffusion layer (δ_0) depends on the diffusion coefficient (D) as presented in $eq. 13$ for static conditions and $eq. 14$ for dynamic conditions under an ideal laminar flow over a vertical plane. Therefore, the same system will find different diffusion layers for different species.

$$\delta_0 = \frac{1}{B}\left(\frac{D\nu x}{\alpha g \Delta c}\right)^{1/4} \qquad (eq. 13)$$

$$\delta_0 \sim 5 D^{1/3} \nu^{1/6} \sqrt{\frac{x}{U}} \qquad (eq. 14)$$

Here α is the density coefficient, g is the acceleration due to gravity, B is a constant estimated between 0.5 and 0.7, ν is the kinematic viscosity of the solvent, D is the diffusion coefficient of the species, x is the distance along the surface, U is the relative fluid velocity, and Δc is the difference of concentration between the surface and the bulk solution.

Such concentration gradients generate two differentiated compositional environments between the solution in direct contact with the surface and the bulk solution. Therefore, the interface environment is the one ruling the degradation products layer formation, and changes on those concentration gradients in products and reactants are the reason for changes in the degradation products layer composition and morphology, and consequently on the degradation rate. Therefore, the progress on defining the local conditions is necessary to understand the chemical mechanisms involved.

As is described later in *section 1.4*, there are be significant differences in the environment (fluid composition, content and exchange rate) found for different implantation sites. Those differences are believed to be one of the reasons for the different degradation rates found by µCT for different implant parts in contact with different tissues [140,141]. Therefore, this finding supports that the hydrodynamic conditions are factors influencing the degradation rate, and therefore, the mechanism involved in the process.

Although those simple considerations about fluid hydrodynamics are useful to describe general influences in different *in vitro* set-ups, they cannot be applied to evaluate the hydrodynamic conditions and to quantify the mass transfer of a complex geometrical configuration like the ones typically applied for *in vitro* magnesium degradation set-ups. Therefore, the complex boundary limits and the concentration profiles generated by the different geometries considered in degradation testing must be analysed by localised measurement methods and *computational fluid dynamic modelling*.

1.3.3 State of the art in magnesium degradation set-ups

A multitude of set-ups has been applied to the degradation of magnesium alloys [44]. However, those set-ups can be divided into two categories; set-ups under (i) *static*, and (ii) *dynamic conditions*.

Under *static conditions*, the degradation test is performed in the same medium during the whole immersion time [50] or is entirely or partially replaced with fresh medium during the immersion process (*semi-static*) [118,142,143]. As described previously, the diffusion layer is relatively thick under static conditions. The mass transfer between the surface region and the bulk medium is mainly controlled by diffusion and by the natural convection generated due to the concentration gradient and the forced convection of the H_2 evolution. Due to the high diffusion contribution and the limited solution volume applied, the mass transfer phenomenon might control the precipitation processes under static conditions. The available standards that researchers can follow [144,145] show notable differences in the volume per sample area (*V/A) ratio* proposed and support the necessity to standardise the *in vitro* set-up. Besides this, the ASTM corrosion evaluation recommendations for engineering materials [144] observe the importance of the solution *V/A ratio* and the immersion time to prevent possible distortions on the test conditions and therefore on the corrosion evaluation. Concerning degradable magnesium biomaterials, the *V/A ratio* seems to be even more relevant than for traditional corrosion-resistant engineering alloys. The high tendency of magnesium materials to degrade leads to significant changes in the environment due to the alkalinisation process and a high Mg^{2+} ions release (see $eq.2$ and $eq.3$). Previous authors tested the influence of the *V/A ratio* on magnesium degradation revealing an influence in the bulk pH developed [146] and the resultant *in vitro* degradation rate [71]. This phenomenon might be explained by the linked effect of the alkalinisation process and the prompted protective precipitation process that is stabilised at high pH. Despite this fact, an alloy subjected to the same buffer concentration by applying different V/A ratios leads to different pH evolutions. Moreover, a limit in the *V/A ratio* above which the corrosion rate is independent of the *V/A ratio* was previously identified [147]. This is due to the fact that the buffer capacity (β) depends not only on the buffer concentration but also on its volume [148]. Therefore, increasing the *V/A ratio* will lead simultaneously to an increase of β. The $Mg(OH)_2$ *brucite* compound have been found as the main degradation component for magnesium *in vitro* tests under simple degradation solution compositions [149]. For more complex *in vitro* solution compositions and for *in vivo* conditions [150,151], *brucite* was found together with other compounds like $MgCO_3$, $CaCO_3$, $Mg_3(PO4)_2$, $Ca_5(PO4)_3(OH)$ [48,132,142]. According to the previously described relationship between the pH and the solubility, higher pH values shift the heterogeneous equilibriums to the precipitation side and thus stabilising their presence in the degradation product layer. The pE - pH diagram shown in *Figure 3*, depicts this dependency regarding the $Mg(OH)_2$ phase. The dependency of the formation of phosphate-based phases on the pH is also shown in previous studies [152,153]. Therefore, when the buffer capacity of the degradation solution is not high enough to absorb the alkalinisation process, the saturation index (*SI)* of the products forming the degradation products layer compounds increases. This fact generates a more protective layer and the contact between the metallic surface, and the electrolyte is more restricted modulating the corrosion kinetics by a diffusion-controlled rate process through the degradation products layer. The implementation of the buffering system provided by cell culture conditions (CO_2/HCO_3^-) and the application of the so-called *semi-static* methodology was applied by previous authors [98] to mimic the fluid exchange and the buffer capacity in the implantation site. Those modifications lead to more comparable results to the ones obtained under *in vivo* conditions due to less influence of the set-up methodology. However, it is necessary to take into account the differences in the dissolution kinetics of different Mg-based materials in order to face specific semi-static conditions.

Dynamic conditions involve the immersion of the material at a constant or intermittent flow rate in a recirculating closed-loop or an open circulating set-up of the degradation solution [154]. The mass transfer between the surface region and the bulk solution is accelerated by an increase in the forced convective participation due to the applied flow, that results in a thinner diffusive limit layer (δ_0), as depicted in *Figure 6(b)*. Several previous works have shown the relevance of dynamic conditions in magnesium *in vitro* testing [155–159]. However, the influences of the dynamic conditions are not entirely understood, and therefore, the degradation mechanism of magnesium-based materials under dynamic conditions continues to be unclear. The different performance of magnesium-based materials under dynamic conditions compared to the static ones is currently attributed to (i) a higher *V/A ratio* and (ii) higher mass transfer phenomena. As discussed above, this leads to higher buffer capacity and lower possibilities for reaching saturation or depletion of relevant components, with what is possible a better mimic of the physiological homeostasis of the body fluid compositions. Under dynamic conditions, the degradation solution volume enclosed in the testing chamber/cell has much lower relevance than observed under static conditions, while the total volume circulated through the testing chamber and the possibility of the fresh recirculating medium, become more relevant. Due to the application of a flow rate, the testing chamber configures specific boundary conditions that define the mass transfer phenomena between the surface and the bulk solution. By reducing the diffusion layer thickness (δ_0) and increasing the fluid velocity, the mass transfer is increased, and therefore, the kinetics of the electrochemical process are not limited, as was revealed by polarisation measurements in a rotatory disc electrode at different rotation speeds by *Marco and Van der Biest* [155].

According to that, experiments on dynamic testing point to the idea that the applying a specific flow rate is not enough to describe the hydrodynamic conditions surrounding the sample, mainly when high flow speeds are generated over the material surface. Therefore it is necessary to evaluate the mass transfer and the mechanical effects on the sample surface, as was highlighted by previous authors [160–162]. Despite to the difficulty of evaluating the mass transfer in a complex geometry, the latest results indicate that the evaluation of the hydrodynamic pressure generated over the surface of the sample is a consequence of the flow applied, and the geometry of the set-up, and possibly can be correlated with the mass transfer generated between the surface and the bulk solution. To measure this hydrodynamic pressure, those authors have analysed the flow-Induced shear stress (FISS) generated by the fluid over the sample´s surface by *computational fluid dynamic modelling*. Their results suggest that an increase of the FISS increases the degradation rate when dynamic conditions are applied compared to static conditions at equal *V/A ratio* [158]. Moreover, the degradation products layer composition and the degradation morphology were also affected by those dynamic conditions, which might suggest that mass transfer also influences the kinetics of the precipitation processes that govern the degradation products layer formation. In contrast to the hydrodynamic conditions presented for the BEF, the high blood flow of blood vessels might have a significant impact on the FISS generated on a degradable metallic stent. The generated FISS, that is possibly increased with the presence of the stent itself, accelerate the overall degradation rate due to the increase of mass transfer, an enhanced capacity to maintain the pH around the physiological value, and mechanical forces generated on the surface [163].

1.4 Bone as implantation site

As mentioned above, degradable magnesium implants are currently aimed for orthopaedic applications and angioplasty treatment of atherosclerosis processes. Those two implantation sites present a different environment which is supposed to affect the performance of a magnesium-based biomaterial differently. Furthermore, as commented before, differences in magnesium-based materials degradation rate were found by µ-CT volume loss analysis for different areas of the same implant when is in contact with different tissues like muscle, cortical bone and bone marrow cavity [140,141,164]. This fact, remarks the importance of not only the general implantation target (bone or artery environments) but also taking into account the different local environments of an implantation site.

1.4.1 Bone as a tissue

Bone is a specialised conjunctive tissue that can be defined as a porous composite material made up of cells, vessels, organic, and inorganic molecules. These organic and inorganic phases are configured in a hierarchical and complex architecture classified from the organ level to the nanostructured level as depicted in *Figure 7.* This organisation varies according to the anatomical location and type of the bone. Bone is classified by two types of bone tissue: *cortical* and *trabecular* bone.

Cortical bone, which comprises 80% of the skeleton, is a dense tissue that provides the mechanical strength and protection transmitting mechanical forces from the musculature. The *cortical* bone is organised in structural units called osteons. Osteons consists of concentric bone layers called *lamellae,* as schematised in *Figure 7*, which surround hollow channels containing small blood vessels called *Haversian channels*. *Trabecular* bone tissue, also known as *cancellous* or *spongy bone,* is a highly porous structure that represents approximately 20% of the skeleton mass. The *trabecular* bone tissue is organised into a network of interconnected rods and plates that surround pores filled with bone marrow. This porous structure does not have the strength of cortical bone. However, it contributes to the mechanical role of bone by providing internal support distributing the load and absorbing energy, particularly in the vicinity of joints [5].

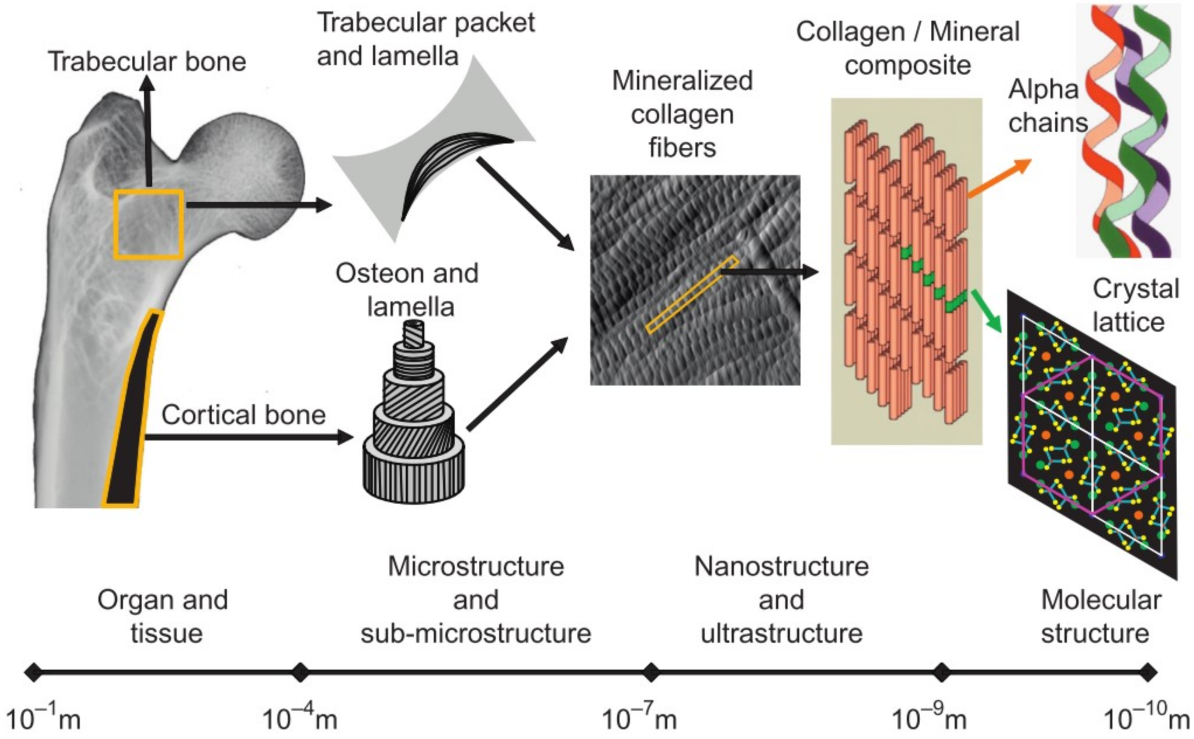

Figure 7: Hierarchical structure of cortical and trabecular bone (with permission by Elsevier [165]*).*

Bone is a living organ with the capacity of adapting its shape, mass and microstructural architecture throughout life by the processes of bone *modelling* and *remodelling*. Those processes are regulated by the activity of *osteoclast*, *osteoblast* and *osteocytes*. Bone *modelling* involves growth and adaptation of bones to produce a mechanically functional architecture. In contrast, bone r*emodelling* is a process whereby bone is continuously renewed so that it continues to maintain strength throughout life and collaborate in the complex *mineral homeostasis*, as described in detail by *Burr et al.* [165]. Bone *modelling* facilitates the growth and change in the shape of bones and predominantly occurs during childhood and adolescence, but also occurs in the adult skeleton and serves to regulate overall changes in bone morphology in response to altered mechanical loading. This process is generated by the simultaneous bone resorption by *osteoclast*s cells and bone formation by *osteoblast* cells, acting on different surfaces of the bone, to alter the overall bone shape or dimensions.

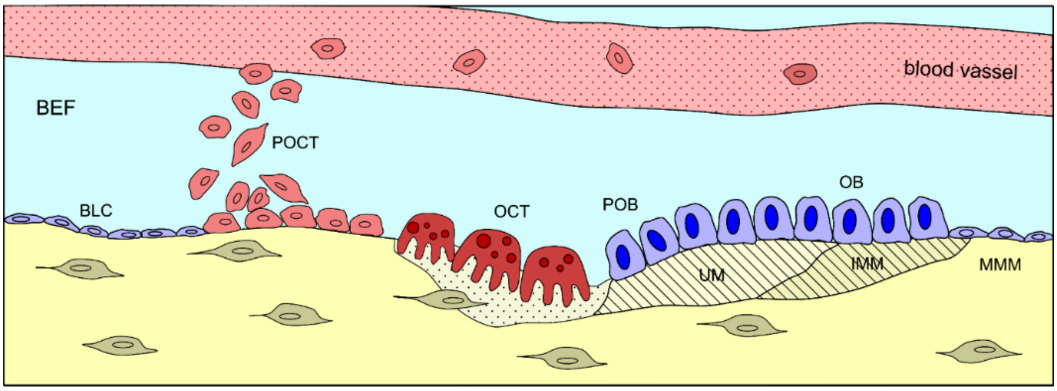

Figure 8: Scheme that presents the bone remodelling cycle and the basic multicellular units (BMU). The typical aged or damaged resting bone surface is lined with bone-lining cells (BLC). Signals (morphogenetic or physical) received directly or indirectly by bone-lining cells shift these cells from resting (neutral) to an osteoid destruction state, secretion of collagenase, change in shape followed by detachment from bone surface, and attraction of pre-osteoclasts (POCT) coming from the blood vessels and thus help initiate osteoclast (OCT) bone resorption. The resorption cavity is then filled by the osteoblast (OB) with unmineralised extracellular matrix (UM) by the osteoblast. After maturation of the extracellular matrix, the mineralisation is promoted ending in fully functional mineralised extracellular matrix (MMM). Based on the text published by Cowin [166].

Bone *remodelling* is a coordinated physiological process in which the digestion process of aged or damaged bone tissue takes place by *osteoclast* and the osteoblast that fills the resorption cavity with new bone tissue. In contrast to the bone *modelling*, *osteoclast* and *osteoblast* operate concurrently on the same surfaces and are known collectively as basic multicellular units (BMUs) [165], as it is shown in *Figure 8.* The organisation of the BMUs in cortical and trabecular bone differs more morphologically than biologically. The mechanism controlling the equilibrium between bone resorption and formation is not yet fully understood since it requires interaction between different cell phenotypes and is regulated by a variety of biochemical and mechanical factors [165,167].

1.4.2 Bone biomineralisation

As mentioned before, one of the promising characteristics of Mg-based biomaterials applied for orthopaedic applications is the enhanced formation of bone tissue shown in animal trials. Current *in vivo* experiments [31] show an initial fibrous and bone tissue encapsulation in close contact with the implant. The degradation process observed showed simultaneous material resorption and bone formation until the bone can remodel entirely after the complete degradation of the magnesium implant. A necessary process to generate the new bone tissue is the mineralisation of the collagen bone matrix. Those exceptional osteoconductive properties of Mg-based materials can be partially attributed to the compositional similarities between the degradation products layer formed on the metallic surface under physiological conditions and the mineralised structure of the bone.

Although macroscopically and microscopically different, the two areas of bone tissue (*cortical* and *trabecular*) are similar in their chemical composition [166]. The nanostructure level of organisation involves the same structure of the organic and mineral phases presented in *Figure 7*. The *organic phase* provides the necessary elasticity and flexibility and comprises approximately 35% of the total mass of the bone. The *mineral phase* is critical for the mechanical integrity of the skeleton, providing stiffness and load-bearing strength and comprises around 60% of the total bone mass. This mineral phase consists of small, poorly crystalline, no-stoichiometric, and largely impure hydroxyapatite (HA, $Ca_{10}(PO_4)_6(OH)_2$), that is bound within and between the collagen fibrils in an ordered manner (see *Figure 7*).

According to the scheme presented in *Figure 8*, the generation of new bone tissue by the *remodelling* process starts with the resorption of the damaged or old bone by the osteoclast. Then the osteoblast produces a non-mineralised extracellular matrix, mainly consisting of collagen type I. After the production and maturation of this extracellular matrix, the mineralisation process starts. The physicochemical principles ruling crystal formation from a solution are three: solution supersaturation, nucleation, and crystal growth, as explained in *section 1.3.2*. However, in the case of the bone biomineralisation, these steps are not the only ones determining the *primary mineralisation* and further maturation, due to the different interfaces present in the biological environment. A schematic representation of the many factors currently considered to influence the mineral deposition/resorption process is presented in *Figure 9*.

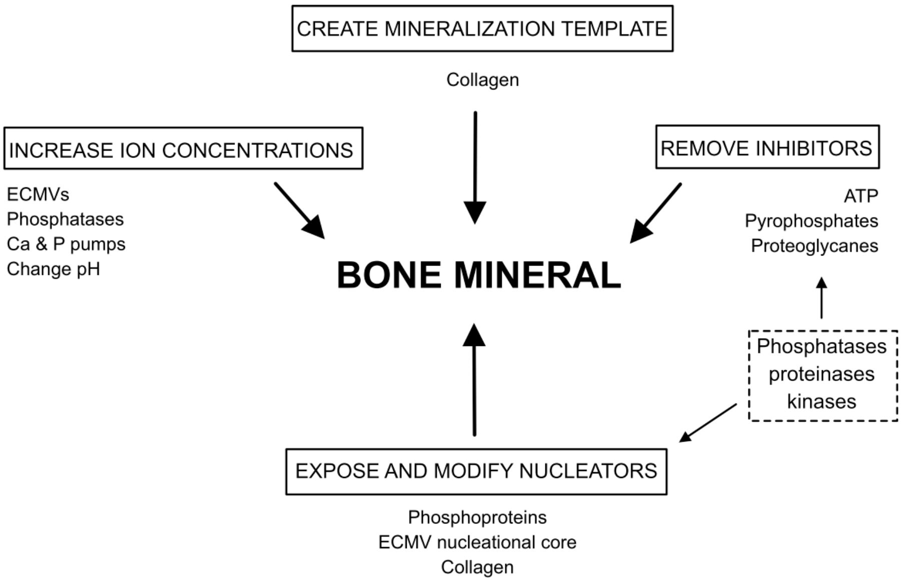

Figure 9: Ionic sources and inhibitors for the bone biomineralisation process (adapted with permission by CTC press [166]*). [ATP: Adenosine triphosphate, ECMVs: extracellular matrix vesicles]*

Among all the factors ruling the *primary mineralisation*, the extracellular collagen protein matrix presents a leading role contributing with a supramolecular framework to support, delimit and control the apatite formation (see *Figure 7*). In all cases, bone tissue formation begins with the extracellular deposition of a collagen matrix (Type I) that exhibits a specific arrangement resulting parallel aligned fibrils, and periodic hole zones (about 40 nm long and 5 nm wide) between the aligned fibrils. This collagen arrangement acts as a template for the mineral formation that takes place in the hole zone of the collagen fibrils, and crystal growth is extended progressively to the inter- and intrafibrillar space [168]. Therefore, the mineralised crystals in bones (45 - 20 nm in size and 3 nm thickness) are aligned along the main loading axis to resist the mechanical loads [105]. This protein matrix promotes the binding to specific surfaces, possibly by a specific charge distribution of collagen fibrils near the gap that promote the charge-based attraction of anionic mineral precursor-additive complexes, blocking the potential nucleation sites and thereby decreasing the crystal length [168]. However, the regulation mechanism is still unclear, with no consensus on how collagen and mineral are secreted.

One of the most recurrent hypotheses of bone mineral formation is the one based on the transformation of precursors phases. *In vitro* studies in simulated body fluid suggest that calcium phosphate can proceed by surface-controlled aggregation, forming an amorphous phase that is subsequently nucleated to crystalline apatite [169]. Three main precursor phases have been proposed historically for the initiation of bone tissue; amorphous calcium phosphate (ACP), octacalcium phosphate (OCP), and dicalcium phosphate dihydrate (DCPD or *brushite*). On the contrary, other studies point to the mineralisation inhibitors promoting the infiltration of amorphous liquid-like precursors and nucleation of hydroxyapatite within the collagen fibrils [170,171]. Although such experiments address the inorganic phase transformations during bone formation, the *in vivo* scenario is more complex, and there is no clear association between the mineral phase and organic phases like polysaccharides and non-collagenous proteins during the mineralisation process. Also, changes in the local ionic concentration of calcium and phosphates varying the saturation levels, possibly regulated by the extracellular matrix vesicles (ECMVs) produced by osteoblasts, can be involved in the mineralisation process, or directly by the generation of HA mineral crystals within the matrix vesicle membrane [172,173]. Other possible driving forces in the rate of mineral deposition/resorption are the activity of *alkaline phosphatase* that hydrolyses the organic phosphate substrates releasing free inorganic phosphate, the decrease of the local pH-regulated by the osteoclast activity for bone resolving, or the presence of anionic proteins that help to maintain a basic environment to facilitate apatite deposition [166].

As mentioned above, the apatite mineral conforming the bone tissue contains a large number of impurities. Those impurities include carbonates, citrates, magnesium, fluoride and strontium incorporated in the crystal lattice or absorbed on the surface [166]. Despite that the structure of this mineral phase is still under investigation, biomineralised bone apatite crystals have been proposed to be formed of nanocrystals nucleus (apatitic domain) covered by a hydrated and rather labile but structured surface layer (non-apatitic domain) that contains relatively mobile ions (mainly bivalent anions and cations: Ca^{2+}, HPO_4^{2-}, CO_3^{2-}). This labile surface layer minimises the surface energy of the nanocrystals [168]. It has been proposed that the apatite substitution of the phosphate groups (e.g. *HA type B* by carbonates, and *HA type A* by hydroxyl groups) or Ca^{2+} cations (e.g. by Mg^{2+}, Na^+), allow the mineral to be more easily resorbed, by distorting the shape and the size of the crystals and reducing the stability of the mineral lattice.

Bone mineralised crystals are formed and remain immersed in the extracellular bone fluid (BEF), which composition is challenging to analyse with precision due to separation difficulties and the constant evolution of the bone mineral crystals [105]. Nevertheless, it is generally considered that the ion concentrations in BEF are similar to those in blood, with differences in some ions concentration, as shown in *Table 6*. Considering the concept of supersaturation for heterogeneous precipitation reactions exposed in *section 1.3.2*, BEF composition is supersaturated in Octacalcium Phosphate (OCP) and stoichiometric Hydroxyapatite (HA), even when those phases have been not observed, while Amorphous Calcium Phosphate (ACP) and Dicalcium Phosphate Dihydrate or *brushite* (DCPD) are under-saturated (see *Table 4*).

Table 4: Supersaturation levels of bone extracellular fluid (BEF), concerning the main calcium phosphates of biological interest [105]. *[DCPD: Dicalcium phosphate dihydrate or brushite, Triclinic OCP: Octacalcium phosphate with triclinic structure, ACP: Amorphous calcium phosphate, HA: Hydroxyapatite]*

Calcium phosphates	Solubility product (pK)	Ionic product in the bone extracellular fluid (pK$_i$)
DCPD (Brushite) $CaHPO_4 \cdot 2H_2O$	6.62	12.9
Triclinic OCP: $Ca_8H_2(PO_4)_6 \cdot 5H_2O$	96.6	93.9
ACP: $Ca_3(PO_4)_2$	24 – 26	27.5
HA: $Ca_{10}(PO_4)_6(OH)_2$	117.2	98.3

1.4.3 The hydrodynamic environment of the bone

As exposed in *section 1.3.2*, the degradation rate is dependent on the fluid content, composition and fluid exchange. Therefore, an accurate description of the implantation site is necessary to define the *in vitro* set-up and will help to obtain results closer to the ones obtained *in vivo* and to interpret the mechanisms behind. However, little about hydrodynamics in bone is known. The compiled data presented in *Table 5* compares the fluid content and the blood flow of tissues that can be in contact with a bone repairing implant material.

Table 5: Comparison of water content and blood flow (per 100 g of tissue) of relevant human tissues for the implantation of magnesium-based materials. Data extracted from [32].

Tissue	Water content (%)	Blood flow (mL / min·100 g)
Heart	71.2 – 80.3	1000
Muscle	76.0	38
Brain	76.0 – 78.0	560
Liver	72.9 – 77.3	1000
Spleen	76.5 – 81.1	1200
Intestine	71.0 – 72.7	1000
Adipose	-	28
Skin	67.8 – 75.8	120
Bone	43.9	120

The hydrodynamic conditions presented by the interstitial fluid are more relevant for an implant aiming bone remodelling, but less is known about such conditions in the BEF compartment. The fluid in the interstitial compartment contains the characteristics detailed in *Table 6* that are slightly different from the blood plasma composition.

Table 6: Composition and characteristics of human interstitial fluid and blood plasma.

Component	Interstitial fluid [174–176]	Blood Plasma [51,107,118,174,175,177,178]
Na^+	136 - 146	142
K^+	4.0	5.0
Ca^{2+}	1.2 – 1.5	2.5 (1.3)
Mg^{2+}	0.5 – 0.7	1.5 (1.0)
Cl^-	115	103
HCO^{3-}	26	22 – 30
HPO_4^{2-}, $H_2PO_4^-$	0.6 - 1.7	1.0
SO_4^{2-}	0.7	0.5
Glucose	1.0	3.6 – 5.2
Amino acids	unknown	0.25 – 0.40
Protein (g/L)	20.6	63 - 80
Vitamins	unknown	µg-mg
Osmolality (mOsm/L)	281.0	282.0
Density (g/cm^3)	1.0	1.024 – 1.030

Note. All concentrations in mM unless otherwise stated. The values in brackets correspond to the ionic concentrations not bound to proteins.

The human blood serum contains a well-regulated concentration of calcium around 2.5 mM. However, only 1.3 mM is free and not bound to proteins, that is a similar concentration to the one found in BEF. The estimated pH of mature BEF is considered to be slightly more acidic than the physiological pH in adults. However, this estimation has to be taken with caution, due to the constant release of protons from the bone mineral phase related with their maturation

[105]. The interstitial fluid is derived by filtration and diffusion from the capillaries in a state of near-equilibrium along the capillary membrane. It contains almost the same constituents as plasma except for significant lower concentrations of proteins, that cannot pass outward through the pores of the capillaries easily.

The high metabolic activity of bone requires constant transport of nutrients, ions, proteins, glycolipids, and cells. The nutrients are transported from the blood flow into the BEF compartment surrounding the vessels and from there to be absorbed interstitially or drained through the lymphatic system. The interstitial fluid conforming the BEF is entrapped in the spaces among the interstitial connective tissue vertebrate by proteoglycan filaments (collagen). As schematised in *Figure 10,* the extracellular or interstitial fluid is generated by the hydrostatic pressure generated by the hart, pushing water and its dissolved substances through the capillary pores into the interstitial spaces. The difference in proteins concentration, as one main factor, between the vessels and the extracellular compartment, induces osmosis pressure, that drives the water back into de vessels. Also, the lymphatic system returns to the circulation the small amounts of excess protein and fluid that leak from the blood into the interstitial spaces. These combined factors generate a net flux across the BEF compartment (J_v) that at steady state can be described by Starling´s equation depicted in $eq. 15$.

$$J_v = J_L = L_p \cdot S \cdot [(P_c - P_i) - \sigma(\Pi_c - \Pi_i)] = k_f \cdot NFP \qquad (eq. 15)$$

Where J_L is the lymphatic flow L_p is the hydraulic permeability, S is the surface area for filtration, P_c and P_i are capillary and interstitial hydrostatic pressures, Π_c and Π_i are the capillary and interstitial colloid osmotic pressures, σ represents the osmotic reflection coefficient, k_f is the capillary filtration coefficient (mL/min), and NFP present the net filtration pressure (mmHg). In normal conditions, NFP is slightly positive, resulting in a net filtration of fluid across the capillaries into the interstitial space in most organs. This slight imbalance between the inward and outward fluid movement along the capillary membrane, about 0.3 mmHg, is translated in a small amount of fluid that is eventually returned by the lymphatic system.

As exposed by *Rutkowski et al.* [179], the interstitial flow is difficult to measure due to the low value of the flow rate, to the heterogeneity of those values along with different physiological areas, and the possible artefacts created by the selected flow tracer. For this reason, just a few works performed direct measurements of the interstitial flow. Moreover, those measurements were performed only close to the surface by fluorescence recovery after photobleaching (FRAP) or nuclear magnetic resonance (NMR), and on anaesthetised animals, in which the interstitial fluid velocities are likely to be substantially different from those in an awake animal due to changes in blood pressure and lymphatic pumping. Those values were reported to vary between 0.1 and 4.0 µm/s. In accordance, the regular rate of net filtration in the entire body exposed by *Guyton and Hall* [174] is only about 2 mL/min. The heterogeneity of the interstitial flow resides in the different number and size of pores in each capillary and the number of capillaries in which the blood is flowing between the different capillary tissue system. Because of the large number of proteoglycan filaments, it is difficult for the fluid to flow smoothly through the *interstitium*. However, due to the short distances between the capillaries and the tissue cells, this diffusion allows rapid transport through the *interstitium* of, e.g. water molecules, electrolytes, small molecular weight nutrients, cellular excreta, and gases like oxygen and carbon dioxide.

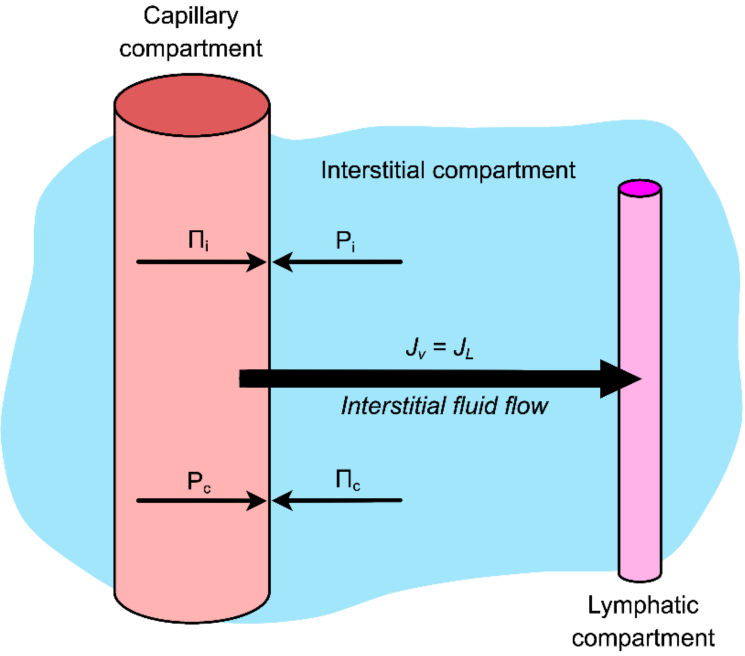

Figure 10: Driven forces on the movement of fluid and substances between the intravascular, interstitial and lymphatic compartments, that generates the homeostasis of the Interstitial fluid. Π_i*: Interstitial colloid osmotic pressure,* Π_c*: Capillary colloid osmotic pressure,* P_i*: Interstitial hydrostatic pressure,* P_c*: Capillary hydrostatic pressure,* J_V*: Net flux across the interstitial compartment,* J_L*: Lymphatic flow.*

Therefore, the implantation environment concerning orthopaedic applications should be defined by the absence of a mechanical influence generated by the fluid flow (in the range of µ-fluids), but with active transport of nutrients that keep constant the fluid composition. Therefore, *in vitro* set-ups aiming a bone implantation site simulation should be defined according to the previous considerations.

2 Motivation and objectives

The previous introduction presents some of the influences affecting the degradation mechanism of magnesium-based materials under *in vivo* conditions. Due to the difficulty of monitoring the *in vivo* degradation process, magnesium degradation mechanism under physiological conditions remain unclear. This missing information contributes to hinder the use of those materials from being extended to other applications apart from those currently on the market.

The composition and morphology of the degradation products layer derive from the alloy composition and form the corrosive environment (including inorganic, organic and cell presence). Among all the compounds present in the degradation product layer, the inorganic fraction is responsible for most of the resistance to degradation provided by the degradation products layer. The condition triggering the precipitation of the inorganic compounds present in the degradation products layer is the thermodynamic condition of *supersaturation.* This condition depends on the ionic activity of the species involved in the precipitation process, on the pH, and the presence of organic molecules and cells that can modify the concentration of specific ions. Moreover, the reactive magnesium surface and the mass transfer restrictions defined by the hydrodynamic conditions of the testing set-up might generate a concentration profile of products (e.g., Mg^{2+}, OH) and reactants (e.g., HCO_3^-, HPO_3^{2-}) that differentiate the composition of the bulk solution and the solution next to the degradation interface. Therefore, the local surface environment must be the most relevant for the degradation products layer formation and therefore modulates the degradation rate indirectly.

The natural alkalinisation process generated by magnesium degradation in aqueous media has been reported in numerous previous *in vitro* studies [146]. Subsequently, a interface pH as high as 12 has been traditionally inferred from this observed alkalinisation process and the presence of $Mg(OH)_2$ in the degradation products layer in simple NaCl aqueous solutions [106]. On the contrary, the efficient physiological pH homeostasis that ensures a correct biological activity [180], point to the interface pH levels as more relevant in the degradation products layer formation compared with the measurement of bulk pH during magnesium dissolution. Therefore, a reliable local *in situ* values of pH in addition to relevant ionic concentrations can help to predict the composition of the degradation products layer. Only recently with the application of local potentiometric techniques, an interface pH around 10 units has been revealed during *in situ* magnesium degradation processes in NaCl aqueous solutions [181–183], as well as in a more complex degradation media like Ringer's solution [184] and SBF [185]. However, those values were used to explain microstructural effects or to describe the behaviour of cathodic and anodic zones and were not correlated with the alloy composition, the degradation solution composition, and the degradation products layer formed on the metallic surface.

Therefore, the present work aims to correlate the interface pH values with the inorganic fraction of a simulated body fluid composition and the degradation products layer composition. This correlation will help to understand the interface phenomena that justify the degradation products layer composition during *in vitro* magnesium-based materials degradation. Accordingly, the following questions were defined:

- Do the electrochemical reactions of magnesium degradation promote a significant increase in the interface pH under immersion in physiological conditions? How does the inorganic fraction of a simulated body fluid influence the interface pH? Moreover, is this assumed high pH the one ruling the compounds forming the degradation products layer?
- Does the interface pH of degraded magnesium depend on the alloy composition, and therefore, the degradation process for different alloys promote different degradation products layer composition?
- Are the hydrodynamic conditions affecting the interface pH, and therefore influencing the mechanism and the degradation performance of the alloy?

SIET measurements were used to study the *in situ* interface pH on high purity magnesium (HP-Mg) and different alloying systems under current study as potential degradable biomaterial systems (Mg-Ag, Mg-Nd-Gd, and Mg-Ca). The degradation solutions applied, based on Banks´ Balanced Salt Solution (HBSS), observed the inorganic fraction composition of simulated body fluid. Dynamic conditions at a rate of 1.5 mL/min, were applied in order to keep constant the degradation solution composition and to avoid a mechanical effect of the flow on the degradation surface. Those conditions were defined in the Introduction to mimic a general implantation site for an orthopaedic purpose. Additionally, the degradation products layer composition was characterised in order to correlate the interface pH, the degradation solution composition, and degradation performance of the alloy.

3 Material and methods

3.1 Material production

The magnesium alloys involved in this study were supplied by Magnesium Innovation Center (MagIC) in Helmholtz-Zentrum Geesthacht (HZG). The chemical compositions of as-cast high purity Magnesium (HP-Mg), extruded and T4 heat-treated Mg-2Ag, as cast Mg-10Gd-1Nd-0.1Ca (E11) and as-cast Mg-1.2Ca are shown in *Table 7*. Such variety of materials was considered in order to provide different surface conditions, in composition and microstructure, but observing compositional systems that are currently under study due to its potential use as degradable implant biomaterials. The as-cast HP-Mg was considered as a material reference that is commonly used in *in vitro* studies [45,186–189], and provide no additional influence of secondary phases and solid solution alloying elements influences on the corrosion kinetics. The Mg-Ca system is currently under consideration as degradable biomaterial [190–193] due to the cytocompatibility of Ca as an alloying element (major component of human bone and also essential in cell chemical signalling), and its capacity to improve the mechanical properties of magnesium by grain refinement [194], with a good density compromise (Ca density 1.54 g/cm^3). Besides, the Mg-Ca system was also chosen to evaluate the influence on the degradation process of the Ca coming from the alloy dissolution and not from the degradation solution. For this reason, an as-cast microstructure with a higher content than 1% Ca content was selected to ensure a fast degradation rate and therefore a high Ca^{2+} cations release. The Mg-Ag system has been recently revealed as a potential degradable material with potential long-term antibacterial properties with a good degradation performance between 2% and 6% of Ag when a T4 solution treatment is performed to avoid harmful secondary phases [195,196]. Therefore, due to the capacity of the total solution of a 2% Ag, the as-extruded and T4 treatment was selected to provide a grain refined with solid solution influenced microstructure. As *Hort et al.* [197] exposed, Mg-10Gd alloy brings a good compromise between an improvement in the mechanical properties due to solution strengthening and precipitation strengthening, with acceptable toxicity despite contradictory results in the literature, and an improvement in the degradation resistance. Besides, *Mayer et al.* [198] revealed that the addition of 1% of Nd with an adequate heat treatment could improve the elongation (T4) and strength (T6), in addition to its re-passivation properties of the system. Moreover, the degradation of as-cast E11 system was compared to the as-cast WE43 system (Mg-4Y-0.5Gd-2Nd-0.5Dy) by *Feyerabend et al.* [199], showing similar levels of Mg^{2+} ion release and increase of osmolality, that can be correlated with similar degradation rates. The as-cast microstructure was selected to see the influence of well defined noble secondary phases in the microstructure.

Table 7: Chemical composition of tested magnesium alloys. The composition is expressed in ppm or wt.% when indicated.

Element	**Hp-Mg**	**Mg-1.2Ca**	**Mg-2Ag**	**E11**
Ag[1]	0.5	<1[1]	1.99%	-
Al	34	0.10%	340	370
Ca[2]	3	1.10%[2]	-	0.19%[2]
Cu	<1	44	13	49
Fe	50	35	27	15
Gd[3]	n/a	n/a	n/a	9.25%[3]
La	<5	<13	-	134
Mn	8	440	-	462
Ni	<2	12	35	>180
Nd	-	-	-	1.36%
Si	2	220	-	8
Zn	36	28	n/a	53
Zr	5	58	n/a	22
Mg	99.98%	98.71%	97.97%	88.74%
Pr	-	-	-	0.33%

[1] Ag: AAS, Agilent Technologies 240FS AA, λ=328.1 nm.
[2] Ca: AAS, Agilent Technologies 240FS, Matrix standardised method (Gd, Nd, Mg), λ=422.7 nm.
[3] Gd: µXRF M4 Tornado (Bruker), 25 µm spot analysis (Rh K), 20x20 mm area analysed, 8 ms/pixel.

All the alloys were produced by permanent mould direct-chill casting from the pure materials, magnesium (99.99%, Xinxiang Jiuli Magnesium Co., Ltd, Xinxiang, China), silver (99.99%, ESG Edelmetall-Handel GmbH. & Co. KG, Rheinstetten, Germany), gadolinium (99.5 wt. %, Grirem, China), neodymium (99.5 wt. %, Grirem, China) and calcium (99.51 wt. %, Alfa Asear, Germany). A protective atmosphere of argon containing 2 wt% of sulfur hexafluoride (SF_6) was used during the melting process. The melt was placed into a preheated Ni-free steel mould coated with boron nitride (BN) as a mould-release agent to prevent the direct contact between the melt and the mould. The mould was placed in a holding furnace at 680°C for 15 minutes. After the holding time, the mould was slowly immersed in running water to solidify the ingot.

Table 8: Applied parameters for the hot extrusion process of Mg-2Ag samples.

Diam. (mm) Ingot	T (°C) Ingot	Diam. (mm) Container	T (°C) Container	Diam. (mm) Die	T (°C) Die	Extrusion ratio	Punch speed (mm/s)
100	285	125	300	12	300	108	0.7

All the alloys except the Mg-2Ag system were used in as-cast conditions. The as-cast Mg-2Ag material was homogenised at 450°C in a resistance furnace (Linn Elektro Therm AK 40. 06, Bad Frankenhausen, Germany) for at least 8 hours with a protective argon atmosphere. After the homogenisation period, the alloy was quenched by dipping into a cold water bath. The resultant homogenised ingot was machined into a Ø 100 x 200 mm cylinder for the extrusion process. The machined ingots were heated up to 285°C and processed by indirect hot extrusion (*Table 8*), and the rods were cooled down under atmospheric conditions. After removal of the top and the bottom of extruded rods to get rid of defects and impurities, the rods were heat-treated in a steel box under argon atmosphere in a resistant furnace (Vulcan™ A-550, DENTSPLY CERAMCO, USA) at 450°C for 8 hours. After the T4 heat treatment, the rods were quenched in water and machined into Ø 9 x 1.5 mm discs.

3.2 Metallographic preparation

To reveal the microstructure of the alloys and the morphology and composition of the degradation products layer cross-sections, the samples were embedded in Demotec 30 (Demotec metallographic, Nidderau, Germany) methyl methacrylate-based resin. After the resin solidification, the surface was ground with sandpaper down to P2500. Then the samples were polished in the presence of water-free oxide polishing suspension (OPS). The residual OPS and ground material was removed with 100% ethanol in an ultrasonic bath, and the samples were analysed by optical microscopy and scanning electron microscopy. To reveal the grain size and microstructure distribution, the polished surfaces were etched by in a picric acid solution dissolved in water (17%), ethanol (79%), glacial acetic acid (4%, all chemicals by VWR International), for few seconds depending on the alloy. After the etching time, the samples were rinsed in 100% ethanol and dried by compressed hot air.

3.3 Degradation tests

3.3.1 Sample preparation

The discs corresponding to the different alloys were ground with P2500 grade silicon carbide paper and cleaned in an ultrasonic bath in n-hexane (20 minutes), acetone (20 minutes), and 100% ethanol (3 minutes). After the cleaning process, the weight of the samples was measured with an analytical balance (SBC 31, Scaltec Instruments, Göttingen) and afterwards sterilised ultrasonically in 70% ethanol for 20 minutes. Then the samples were dried in sterile multi-well plates at 50°C in a drying oven and stored under vacuum at 200 mbar (Vacucenter, SalvisLAB) until the experiments were performed.

3.3.2 Degradation testing solutions

The alloys were tested in different degradation solutions based on Hank's Balanced Salt Solution (ThermoFisher Scientific, ref. 14175053) at room temperature and during different immersion times between the first moments until 24 hours of immersion. The exact compositions of those solutions are compared with the body fluid plasma composition in *Table 9,* according to the additions of NaCl (Sodium chloride ≥ 99%, Sigma Aldrich), KCl (Potassium chloride, ≥ 99.5% Merck, Darmstadt, Germany), $MgCl_2 \cdot 6H_2O$ (Magnesium chloride hexahydrate, ≥ 98.0%, Merck), $CaCl_2 \cdot 2H_2O$ (Calcium chloride dihydrate, ≥ 99% Fluka, Germany), $NaHCO_3$ (Sodium hydrogen carbonate, ≥ 99.5%, Merck), Na_2SO_4 (Sodium sulphate, Merck, Darmstadt, Germany), $MgSO_4$ (Magnesium sulphate, Merck), $Na_2HPO_4 \cdot 2H_2O$ (di-sodium hydrogen phosphate, ≥ 99.5%, Merck), KH_2PO_4 (potassium dihydrogen phosphate, ≥ 99.5% Merck), $C_6H_{12}O_6$ (D(+)-glucose, >99%, Fluka BioChemika) and HEPES (4-(2-hydroxyethyl)-1-piperazineethanesulfonic acid, ≥99%, Merck).

Table 9: Comparison between the degradation solutions (I – VIII) applied in the local pH measurements detailed in the present work and the composition of the inorganic fraction of the blood plasma. The concentrations are specified in a dissociated form in mM.

Solution	**Na^+**	**Mg^{2+}**	**Cl^-**	**K^+**	**Ca^{2+}**	**SO_4^{2-}**	**HCO_3^-**	**HPO_4^{2-}**	**D-glucose**	**HEPES**
Blood plasma [44]	142	1.5 (1.0)	103	5.0	2.5 (1.3)	0.5	22-30	1.0	3.6-5.2	-
I	142.8	-	143.3	5.8	-	-	4.2	0.8	5.5	-
II	142.8	1.5	146.3	5.8	-	-	4.2	0.8	5.5	-
III	142.8	-	148.3	5.8	2.5	-	4.2	0.8	5.5	-
IV	143.8	1.5	151.3	5.8	2.5	0.5	4.2	0.8	5.5	-
V	137.9	-	148.2	5.3	2.5	-	-	-	5.5	-
VI	138.7	-	148.2	5.7	2.5	-	-	0.8	5.5	-
VII	142.1	-	148.2	5.3	2.5	-	4.2	-	5.5	-
VIII	142.8	-	148.3	5.8	2.5	-	4.2	0.8	5.5	75.1

Note: The values in brackets correspond to the ionic concentrations not bound to proteins.

I. HBSS (ThermoFisher Scientific, ref. 14175053) + 5.5 mM glucose

II. HBSS + 1.5 mM $MgCl_2 \cdot 6\ H_2O$ + 5.5 mM glucose

III. HBSS + 2.5 mM $CaCl_2 \cdot 2\ H_2O$ + 5.5 mM glucose

IV. HBSS + 1.5 mM $MgCl_2 \cdot 6\ H_2O$ + 2.5 mM $CaCl_2 \cdot 2\ H_2O$ + 0.5 mM Na_2SO_4 + 5.5 mM glucose
V. 137.9 mM NaCl + 5.3 mM KCl + 2.5 mM $CaCl_2 \cdot 2\ H_2O$ + 5.5 mM glucose
VI. 137.9 mM NaCl + 5.3 mM KCl + 2.5 mM $CaCl_2 \cdot 2\ H_2O$ + 0.4 mM $Na_2HPO_4 \cdot 2H_2O$ + 0.4 mM KH_2PO_4 + 5.5 mM glucose
VII. 137.9 mM NaCl + 5.3 mM KCl + 2.5 mM $CaCl_2 \cdot 2\ H_2O$ + 4.2 mM $NaHCO_3$ + 5.5 mM glucosa
VIII. HBSS + 2.5 mM $CaCl_2 \cdot 2\ H_2O$ + 5.5 mM glucose + 75.1 mM HEPES

The above compositions allowed to evaluate the influence of Ca^{2+} Mg^{2+}, HCO_3^{-}, HPO_4^{2}, SO_4^{2-} ions, and the influence of HEPES as a complementary buffering system, in the interface pHand the degradation products layer under dynamic degradation conditions (1.5 mL/min).

3.3.3 Immersion tests under flow conditions

Analogous to the immersion tests performed for the SIET measurements, immersion tests under dynamic conditions were performed to analyse the degradation products layer composition and morphology after 3 and 6 hours and the mass loss after 24 hours. For this purpose, three samples of each alloy were prepared according to *section 3.3.1* and immersed in HBSS (*solution I*) and HBSS with the addition of 2.5 mM of $CaCl_2 \cdot 2\ H_2O$ (*solution III*) to reproduce the two differentiated interface pH conditions revealed in the SIET measurements. The samples were immersed in an in-house made flow chamber (see *Figure 11*) manufactured from medical-grade polyether ether ketone (PEEK, Arthur Krüger, Barsbüttel, Germany) with a chamber volume of about 18 cm^2.

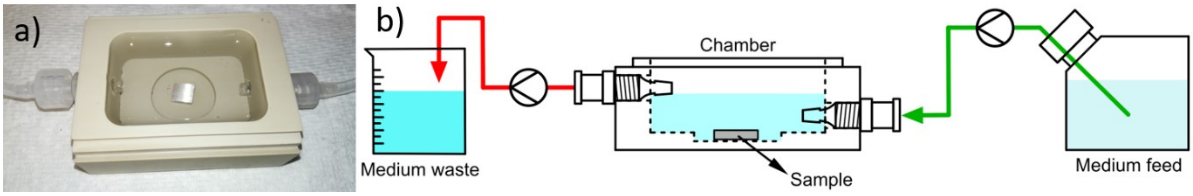

Figure 11: a) Image of the in-house bioreactor chamber, and b) scheme of the dynamic set-up assembled, applied to the immersion tests performed to evaluate the mass loss and the characterisation of the degradation product layer on the Mg alloys.

The immersion time was selected in order to generate enough thickness of the degradation products layer to avoid a significant error in the mass measurement. A TL15E peristaltic pump (Medorex, Nörten-Hardenberg, Germany) provided permanent fresh degradation solution at a flow rate of 1.5 mL/min flow rate, which was distributed by Versilic® silicone tubes (Saint Gobain, IDEX Health & Science GmbH, Wertheim, Germany) and Norpren A-60-G tubes (Saint Gobain, IDEX Health & Science GmbH, Wertheim, Germany) used for the pumping process. The flow rate was selected in order to keep constant the composition of the degradation solution according to the considerations for a better mimicking of an orthopaedic implantation site simulation exposed in *section 1.3.2*. The set-up was permanently open to the atmosphere, therefore equilibrated with the air composition, to mimic the conditions applied in the SIET measurements. Previously to every test, the complete set-up was cleaned during 30 minutes in distilled water under ultrasound bath and sterilised by pumping 70% ethanol for 30 min, and then the system was rinsed with HBSS.

3.3.4 Mass loss calculations

The measure of the mass loss (ML) is possibly the simplest *in vitro* method to estimate the degradation rate of magnesium-based materials [71]. Even when the set-up applied for the immersion test highly vary between groups [44], the system is based on measuring the mass loss of the sample due to its conversion into degradation products layer, at different immersion times. However, the data obtained do not reveal any information on mechanisms, and a certain degree of degradation and multiple replicates are needed to avoid systematic errors [71].

After the 24 hours of dynamic immersion at 1.5 mL/min the degradation products were removed by immersing the sample into chromic acid (200 $g \cdot L^{-1}$) for 5 minutes. The mass loss was obtained from subtraction between the mass sample after the cleaning process (m_1) and the mass sample after degradation products layer removal (m_2), as depicted in $eq. 16$.

$$\Delta m_t = m_1 - m_2 \quad [g] \qquad (eq. 16)$$

3.3.5 Hydrogen evolution measurements

According to the cathodic reaction presented in $eq. 3$, one atom of Mg will generate one hydrogen gas molecule. Consequently, measuring the hydrogen produced in an immersion test is equivalent to the mass loss happening in the sample. These measurements allow taking multiple time points for the same immersion test. However, they are not suitable for the earliest stages of degradation or for highly resistant alloys/coating systems that release low hydrogen volumes. Despite there are some additional influences difficult to estimate, like possible secondary cathodic reactions (e.g. oxygen reduction), or solubility of H_2 in the degradation solution, this technique has been widely used in corrosion studies of magnesium alloys [71].

Hydrogen evolution tests were performed according to the set-up presented in previous work [200]. The eudiometers (art. 2591-10-500 from Neubert-Glass, Germany) was used to exclude the contact of the degradation solution with the atmosphere in the laboratory.

Therefore, only the gases initially dissolved in the electrolyte can participate in the chemical equilibria in the degradation process.

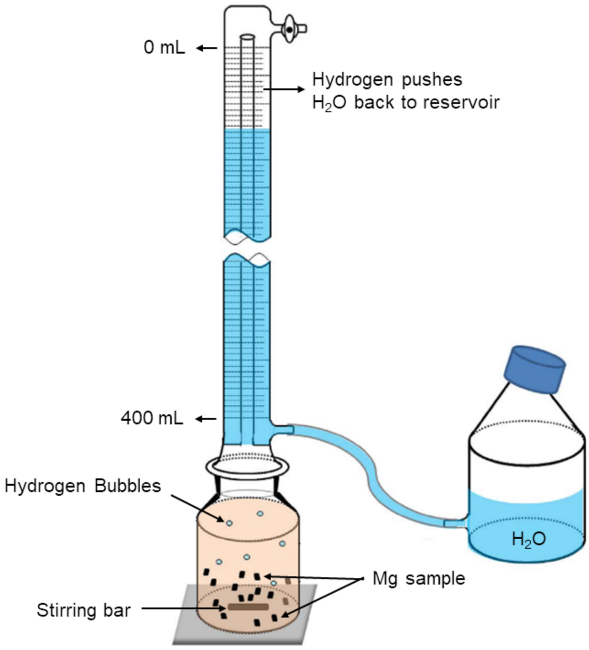

Figure 12 Schematic representation of the eudiometer used for the H_2 evolution measurements (with permission by Elsevier [200]*).*

The necessary number of samples to reach a surface area higher than 30 cm^2 for each alloy, were placed in 500 mL of degradation solution for 80 hours under constant stirring at 300 r.p.m. Due to the critical influence of Ca^{2+} cations in the interface pH values identified in the SIET measurements when HCO_3^- and HPO_3^{2-} are present, the degradation solution compositions applied were HBSS (*solution I*) and HBSS with the addition of 2.5 mM of $CaCl_2 \cdot 2H_2O$ (*solution III*). Previous to the immersion test, the samples were cleaned in 0.1 M H_2SO_4 for 3 minutes and thoroughly rinsed with deionised water and dried in the stream of hot air, to remove possible contaminations introduced during the processing and cutting processes. The values of hydrogen evolved presented are the result of two parallel immersion tests and normalised to the initial material surface area immersed.

3.4 Local pH measurements by Scanning Ion-selective Electrode Technique (SIET)

Scanning Ion-selective Electrode Technique (SIET) is a potentiometric Scanning Electrochemical Microscopy (SCEM) composed by an electrochemical cell, consisting of a reference electrode and an Ion-selective microelectrode as a working electrode under zero current conditions, as shown in *Figure 13(a)*. The Ion-selective microelectrode consists of a glass micropipette that includes a liquid membrane selective to the target ion. SIET technique is based on how the substrate (e.g., metallic surface) in the presence of a solution, perturb the electrochemical response of the microelectrode that is held or moved over the substrate. A cell potential, under zero current conditions, observes the sum of a series of local potential differences generated at the different interfaces of the cell *Figure 13(b)*. However, only the potential difference between the liquid membrane and the sample solution depends on the ionic activity of targeted ion in the solution, and all other potential contributions should be constant [201]. Therefore a change of potential between the working electrode and a reference electrode in the cell, after being amplified and digitalised, is used to determine the activity or concentration of the selected ion in the solution upon calibration according to Nernst equation [201]. As *Taryba* [202] highlighted in her work, the signal from an ion-selective electrode is directly dependent on an activity that is the ”effective concentration” of the ion of interest, but not on the total concentration in the solution, according to the Nernst equation ($eq. 17$). Due to the microscopic size of the electrode, the change of potential provides information about the local environment of the substrate (local ion activity). Also, the movement of the microelectrode is usually carried out by motors driven by piezoelectric elements bringing high spatial resolution measurements.

$$E_i = E_i^0 + \frac{RT}{z_i F} \ln a_i \qquad (eq. 17)$$

Nowadays there is a different kind of Ion-selective microelectrodes, depending on the nature of the ion-selective membrane (Glass Membrane Electrodes, Liquid Ion-selective membrane electrodes, and solid-state electrodes) or the shape and size of the electrode [201,203]. Liquid Ion-selective membranes are based on an internal filling solution composed of several organic components, so-called cocktail, and an internal reference electrode. A typical chemical cocktail consists of a solution of an *ionophore* and lipophilic additives on an organic solvent. The main functional part of the chemical cocktail is the *ionophore* compound providing the controlled permeability to the liquid membrane. It consists of a selective and reversible complexing compound that is capable of transporting the target ion (e.g. Mg^{2+}, Ca^{2+}, Ag^{+}, Cl^{-}, H^{+}) across the membrane excluding the rest of the species. The *ionophore* compound can be an ion exchanger, a neutral carrier or a charged carrier. The solvent content should be carefully controlled due to its effects on the dielectric constant and the mobility of the ionophore molecules affecting the selectivity and stability of the membrane [204]. The main tasks of the solvent are the solubilisation of high ionophore concentrations and the lipophilic salts, to moderate the viscosity and adequate the lipophilicity. The lipophilic additives (alkali salts with lipophilic anions) help to improve the selectivity of the membrane by preventing the interaction of lipophilic ions from the sample with the ionophore compound, but also reduce the electrode response time and lower the membrane electrical resistance [201]. By varying the composition of the cocktail, a good electrode performance can be achieved in order to provide the direct identification and quantification of the target species during the progress of the corrosion process. Different chemicals and some ready membranes are commercially available for particular applications [205], and the performance of different of those chemical components are reviewed in previous works [203,206].

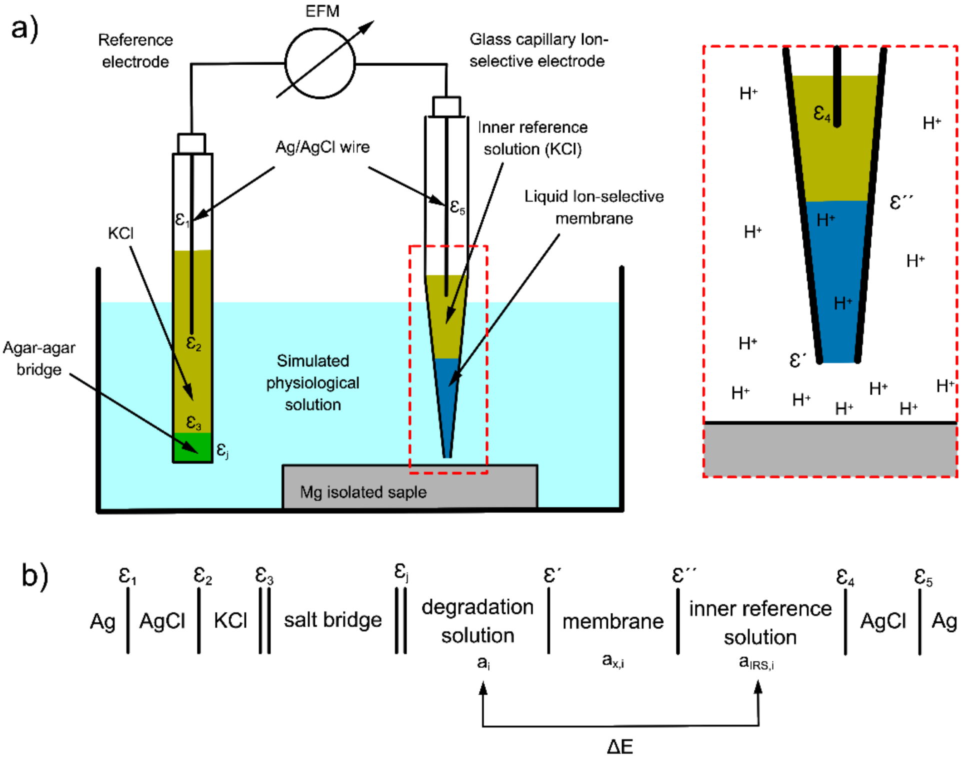

Figure 13: a) Schematic representation of the Scanning Ion-selective electrode assembly and the glass-capillary microelectrode used in the present work for the in situ local pH measurements on Mg surfaces, and b) series of the local potential differences established at the different interfaces present in the SIET components. ε_1: potential difference at the Ag/AgCl interface, ε_2: potential difference at the AgCl/KCl interface, ε_3: potential difference at theKCL/salt bridge interface, ε_j: liquid junction potential formed at the salt bridge/degradation solution interface, ε': potential difference at the degradation solution/liquid membrane interface, ε'': potential difference at the liquid membrane/inner reference solution,$a_{IRS,i}$: activity of the ion i in the inner reference solution of the glass microelectrode, a_i: activity of the ion i in the degradation solution next to the glass microelectrode tip, $a_{x,i}$: activity of the ion i within the liquid membrane, ΔE: cell potential difference.

Liquid membrane glass micropipette electrodes are micropipettes created from glass capillaries that are coated internally and externally with silane. The tip is filled with the membrane chemical cocktail generating a column between 10 and 100 µm, and an internal Ag/AgCl wire is introduced inside like an internal reference electrode. The shape of the micropipette tip is generated by a special pulling machine, and its diameter varies typically between 0.1 µm to 5 µm [201,207]. Despite the variety of H^+-sensitive ionophores developed till now, most of the current works applying a pH-sensitive microelectrode on local corrosion studies are based on the only commercial H^+-sensitive chemical cocktail available (Hydrogen ionophore I cocktail B, Sigma-Aldrich) [208]. Such commercial cocktail does not cover the entire pH range occurring during the degradation processes, including those of magnesium under simulated body fluids. Therefore, the development of H$^+$-sensitive microelectrodes with an optimised working pH range [208] and its application in combination with other local techniques (e.g. SVET) [181,204,207,209] bring essential information to describe the localised physicochemical processes during the progress of magnesium.

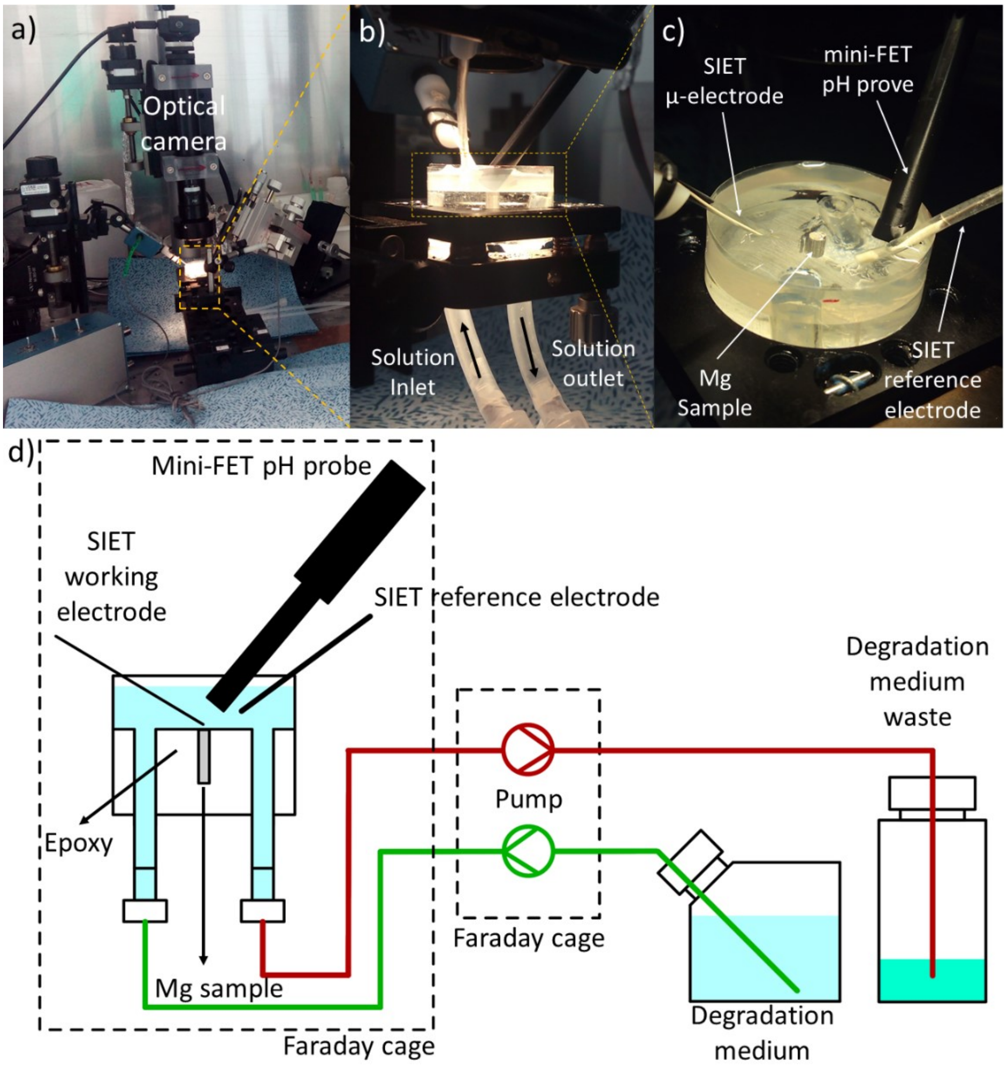

Figure 14: a) Image of the Scanning Ion-selective Electrode set-up (SIET) applied on the in situ local pH measurements; b) and c) details of the mounted Mg sample and flow the chamber included in the set-up; d) scheme of the dynamic conditions applied during the local pH measurements by SIET.

The local pH measurements presented in this work were performed with a commercial SVET/SIET/DVIT system from Applicable Electronics controlled by LV4 software (ScienceWares, New Haven, USA) [208]. Samples of the alloys were machined up to approximately 1 - 2 mm diameter and embedded in epoxy resin configuring a home-made flow cell (5 mL) as depicted in *Figure 14(c)* and *(d)*. The samples were subsequently polished to generate a surface free of imperfections that would prevent the free movement of the microelectrode at 10 – 45 μm above the surface, allowing to use the same embedded sample of each alloy for all the experiments presented in this work. A TL15E peristaltic pump was applied to induce a constant flow rate of 1.5 mL/min. The local pH measurements were performed using a glass-capillary microelectrode with a tip orifice diameter of 1.8 ± 0.2 μm. The tip of the was filled with a non-commercial chemical cocktail based on *0.06 mol* kg^{-1} of the ionophore *benzyldioctadecylamine,* 0.03 mol kg^{-1} additive (ion-exchanger) potassium *tetrakis*(4-chlorophenyl) borate (KTClPhB, Sigma-Aldrich Ref. 60591), 33.0 w/w % of poly(vinyl chloride) (PVC, Sigma-Aldrich, ref. 81392) and up to 100.0 w/w % of 2-nitrophenyl octyl ether (NPhOE, Sigma-Aldrich, ref. 73307) as a solvent, according to previous studies [208]. The glass-capillary microelectrode was calibrated in HBSS solutions with 6, 8 and 10 pH by addition of NaOH and HCl, in order to prevent interferences from harmful components of conventional pH standard solutions and to favour the conditioning of the microelectrode membrane. The potential drift over the time of the glass-capillary microelectrode was corrected based on the bulk pH measured by the mini-FET electrode (Sentron-SI, mini-FET 9202-010 electrode).

After levelling the sample, the microelectrode was calibrated and positioned above the sample. At this time, the scans were defined in the software. Finally, the flow-cell was filled with the degradation solution, and the pump was connected. This procedure ensures that the first moments of the degradation process were recorded. Under those conditions, the glass-capillary microelectrode performed parallel and perpendicular to the sample surface 500 point-by-point steps of 0.6 milliseconds reading time and 0.8 seconds of resting time, generating a measuring time of 40 minutes for every individual line scan. Each of the scan-line started and finished 1000 μm away from the edge of the Mg sample to reach the bulk solution conditions. The scanning distance to the sample surface was established *post factum* after concluding the horizontal scans, 3 – 24 hours of immersion, by breaking the probe over the sample surface at the final steps of the point-by-point perpendicular line scan.

3.5 Difference Viewer Imaging Technique (DVIT)

DVIT systems are based on a fast CCD digital video camera with high magnification, a stable light source, a video frame grabber board and software that contains a video subtraction algorithm developed to discern specific sites on the sample that change with time, giving a clear display of changes with time. This system can perform non-invasive observations of minor changes in the appearance of the surface and adjacent environment. The processed image reveals only differences between the reference and the consecutive images and eliminates the background “noise” caused by the visible static features in the processed images. This technique requires a stable light source, a stable liquid surface without vibration or air currents, and no dust particles in the solution.

In the present work, a DVIT system (AOE, Applicable Electronics) with the LV4 software [210,211], was used to study minor changes in the appearance of the magnesium surface and adjacent electrolyte. For this purpose, a reference image was taken at the very first moment when the degradation solution containing 0.5 wt% phenolphthalein solution in the water-ethanol mixture (v/v 1:0.4) was introduced into the cell in contact with the magnesium sample. Consecutive images were taken at 60 to 30 images per minute, and the difference image was obtained by digitally subtracting the reference image from each consecutive image. The DVIT observations were performed at room temperature of 22 ± 2°C maintained by the lab climate control system, for less than 7 minutes in static conditions to prevent the loss of focus caused by an unbalanced solution fed.

3.6 Alloys and degradation products characterisation

3.6.1 Scanning electron microscopy (SEM) and energy dispersive x-ray (EDX)

Between the multiple interactions between the electron beam and the specimen atoms, the *primary electrons* can interact with the atomic nucleus of the atoms present in the sample, being backscattered (or reflected) from the sample. Those backscattered electrons possess higher energy than the secondary electrons and have a definite direction travelling in straight lines. Besides, those electrons possess information of the interacted material of the sample since as bigger the size of the interacted nucleus is the number of backscattered electrons increases, producing images with a high degree of atomic number contrast.

When the primary electrons ionise the atoms of the sample, those atoms can relax generating electron transitions emitting x-ray emission, between other energies, as a result of the energy conservation principle. The x-rays emitted are characteristic of the elements [212] and are identified via a detector using their unique energies or wavelengths to ascertain the composition of the sample. In EDX, a solid-state detector collects and counts all emitted x-rays at once, divides the energy spectrum into different channels or ranges, and displays it on the computer screen creating a spectrum formed by peaks corresponding to the energies of elements present in the sample.

A backscattered scanning electron microscope Phenom PRO-X (Phenom-World BV, Eindhoven, Netherlands) with a thermionic Cerium Hexaboride (CeB_6) source and an x-ray Silicon-drift detector (SDD), was used to evaluate the morphology of the degradation products layer from the front view and the cross-sections generated from the immersed samples at 15 kV of acceleration voltage.

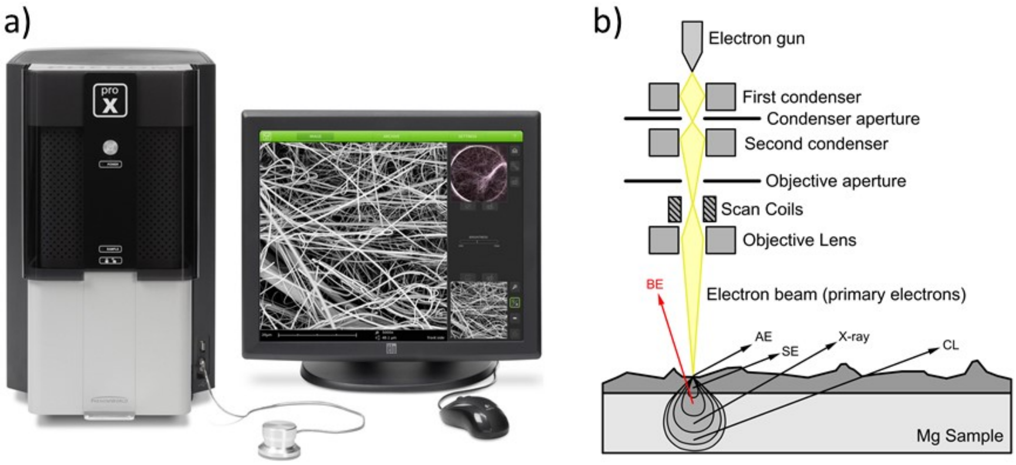

Figure 15: a) Image of Phenom Pro-X BSE-SEM used for the characterisation of the degradation product layer; b) general scheme of a scanning electron microscope and the resulting interaction between the electron beam and the sample: (BE) Backscattered electrons, (SE) Secondary electrons, (AE) Auger electrons, (x-ray) Characteristic electrons, (CL) Cathodoluminescence.

3.6.2 Grazing Angle X-ray Diffraction (GAXRD)

The interaction of an incident monochromatic x-ray beam of a fixed wavelength (λ) with a crystal sample results in a characteristic diffraction pattern that is described by the Bragg equation, as described in *Figure 16*. This diffraction pattern can be used to determine the structural properties of the sample. Therefore with information like the incident wavelength (λ) and the diffraction pattern, is possible to measure the lattice dimensions of a crystalline sample, and therefore identify and differentiate between compounds.

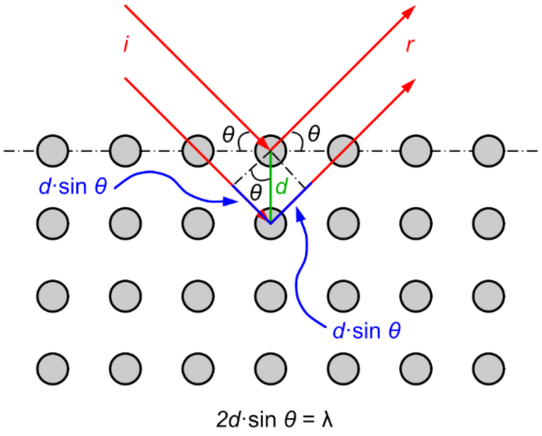

Figure 16: Scheme showing the interaction of the incident x-ray radiation (i) with a crystal lattice (grey regular structure), the reflected x-rays (r), and the Bragg´s law equation. θ: incidence angle, d: distance between two consecutive atomic planes, λ: incident wavelength.

GAXRD is a diffractive x-ray method to obtain compositional and thickness information regarding the crystalline phases present in superficial areas or thin layers [213]. The conventional Bragg-Brentano reflection geometry, where large grazing angles of incidence provide information of several hundred micrometres inside the material, The GAXRD scattering configuration (*Figure 17*) is designed to minimise the substrate contribution on the diffraction response and therefore optimising the surface signal modifying the Bragg-Brentano geometry to provide an "asymmetric" diffraction result by varying the incidence angle [214]. A monochromatic x-ray beam hits the sample at a fixed small-angle α, larger than the critical angle for total reflection, α_c, but usually smaller than 10°. Moreover, the diffraction profile is registered by a detector. By changing the incident angle, different depth can be reached, and a compositional profile can be determined.

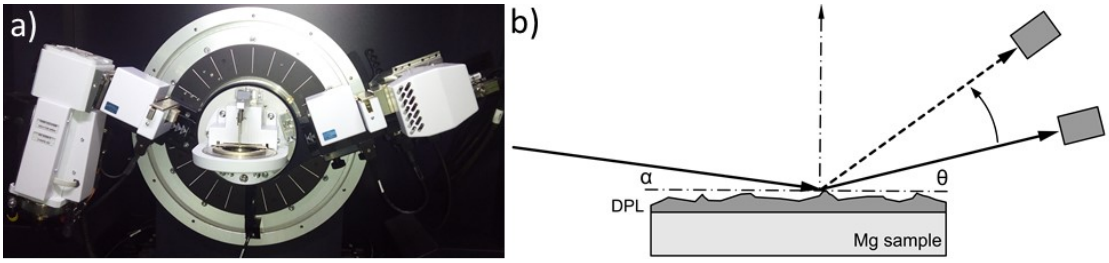

Figure 17: Image of A) Bruker D8 Advance x-ray diffraction set-up used in the present work, and B) scheme presenting the grazing angle diffraction configuration. [α: angle of the x-ray incidence, and θ: angle of the diffracted beam, with respect to the inspected surface]

The surfaces of degraded samples generated during immersion tests were analysed by a Bruker D8 Advance (Bruker, Karlsruhe, Germany) in a grazing incidence geometry of 1 degree. The generator was set for 40 kV and 40 mA, and the data was collected between 15 and 80 degrees of 2θ at intervals of 0.02 degrees. The cutting time was 2 s per data point. The data analysis was carried out by BrukerEVA and PDF-2 (Release 2015 RDB) analysis software.

3.6.3 Micro X-ray fluorescence (µXRF)

X-ray fluorescence analysis is a spectrochemical analytical tool that allows the analysis of a wide number of chemical elements. The basis of the X-ray fluorescence analysis is an excitation and relaxation process within the atomic electron shell. The X-ray source radiation hits the analyte atoms inducing the ionisation of the inner shell electrons by the photoelectric effect and therefore generating electron vacancies in the inner shells (K, L, M). The creation of the vacancy in a particular shell result in a cascade of electron transitions, all correlated with the emission of X-ray photons with a well-defined energy corresponding to the difference of energy between the atomic shells involved (*Figure 18c)*. One characteristic of X-ray fluorescence in comparison to optical fluorescence is that the excitation occurs with distinctly higher energies and that the emitted fluorescence radiation lies within the X-ray range. Because inner atom shells are involved, this process is predominantly specific to elements and not specific to molecules. For this reason, conclusions about the chemical bonds cannot be made this way directly. The possible excitation states and shell transitions are subject to the atomic physics laws and result in a spectrum line, which is characteristic of each element. Depending on the ionised shell, the radiation is labelled K-, L-, M-radiation and, depending on the refilling shell, and additional indication, e.g. Kα1, 2, Kβ1, Lα1, describes the relative intensity of the lines of one line series and depends on the level where the electrons come. Fluorescence lines can only be excited with energy lines that are higher than the fluorescence line itself. The emitted x-ray radiation of the sample hits the detector, where they are absorbed and generate charges. These charges are collected by the electrical field and then amplified and filtered to reduce the different noise contributions. To facilitate the element identification and quantification, the number of X-ray quanta measured by the detector must be converted into a digital spectrum. For a better spectrum evaluation, the electronics generate a signal at exactly energy zero that can be used for energy calibration, but also for the calibration of energy resolution and of dead time determination. The natural width of fluorescence lines is typically < 10 eV and variations depending on the type of lines (K, L, M) and the chemical bond type of the atom are negligible.

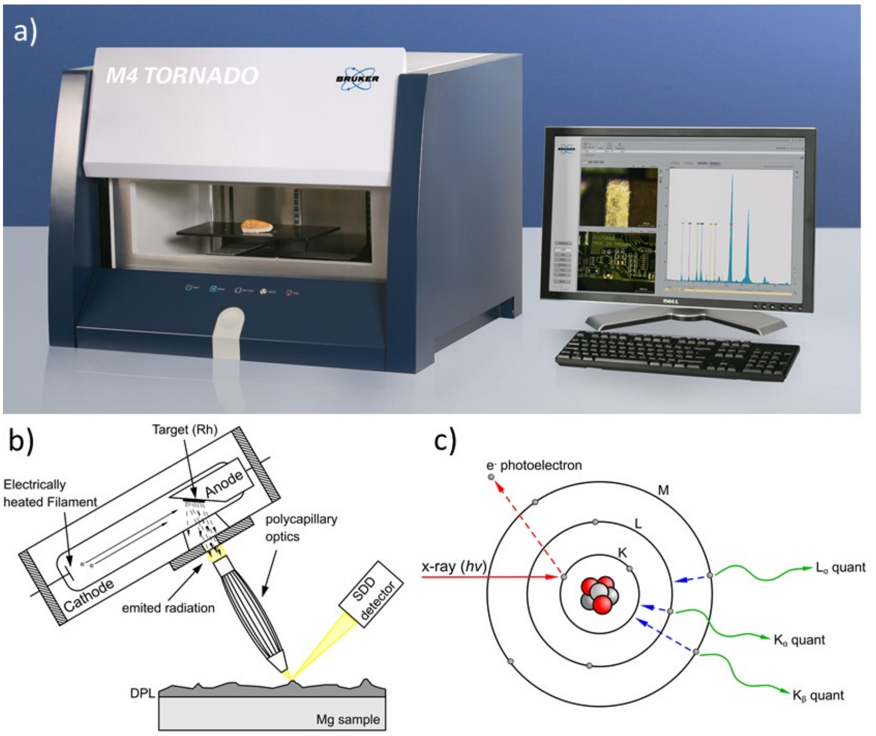

Figure 18: a) Image of the µXRF M4 Tornado (Bruker), b) components of the µXRF M4 Tornado and c) the schematic process of the atomic phenomena involving the x-ray fluorescence emission. A high-energetic x-ray photon ionises an inner energy level, e.g. the K-shell of an atom. After the ionisation, a fast cascade of electrons refills the gap with electrons from a higher energy level. The energy difference between the two states is emitted as an x-ray photon, the so-called x-ray fluorescence.

A 2D energy dispersive (EDXRF) X-ray spectrometer µXRF M4 TORNADO (Bruker, Ettlingen, Germany) was used for elemental analysis and relative quantification of the degradation products layer after the degradation processes. The X-ray source anode material selected was Rhodium (Rh) that with the help of a poly-capillary optics generate a spot size down to 25 µm with a high excitation intensity. The energy dispersive silicon drift detector (SDD) of 30 mm^2 offers a high-count rate with a stable energy resolution < 145 eV for Mn Kα. The X-ray tube settings used for the analysis were a tube voltage of 50 kV and a current of 600 µA. The measurements were conducted under vacuum at 20 mbar to improve the identification of elements with an atomic number lower than 16. A 12.5 µm aluminium foil was applied as a primary filter to cut off the excitation radiation scattered from the sample material absorbing the photons of ~12 keV, and reducing the diffraction peaks of possible crystalline materials. The average spectra of 3 cycles over a sample area of 1.5 cm^2 were analysed with a 25 µm distance between analysed points. The standards quantification method was based on a fundamental parameter (FP) quantification algorithms. Those algorithm derives the net peak intensities and then calculates the sample composition, but based on the assumed sample composition; the resulting µXRF spectra are simulated (forward calculated). These simulated spectra are compared with the measured spectra and matched by iterating the sample properties. This approach incorporates multiple physical effects like self-absorption and secondary excitations, strong peak overlaps, and pronounced absorptions effects are treated to the best of knowledge, providing more robust results due to a larger set of fluorescence lines that can be used for the quantification.

3.6.4 Fourier Transform Infrared Spectroscopy Attenuated Total Reflectance (FTIR-ATR)

Most molecules absorb light in the infrared region of the electromagnetic spectrum due to the activation of different vibration or stretching modes between the different atoms present in the molecule. According to this, infrared spectroscopy is a well-established technique that can be applied to analyse the compounds developed on the sample surface as a result of the degradation process. The FTIR-ATR is based on the phenomenon of total internal reflection of IR radiation at the boundary between two media with different refraction index [215]. The IR radiation is transmitted under total internal reflection through a medium in an optically dense medium (ATR crystal, n_1) when the angle of incidence (θ) is greater than the critical angle ($\theta_c = sin^{-1} n_{2,1}$). The close contact generated by the pressure applied between the ATR crystal and an optically rare medium (sample, n_2) generate an orthogonal evanescent wave into the rare medium (sample) in each reflection point, that decays exponentially with the distance from the interface [216], as shown in *Figure 19*. Some of the energy of the evanescent wave is absorbed by active vibrational modes of the atoms present in the sample and reflected radiation return to the detector, registering an attenuation of the incident compared with the reflected beam intensity ($I_0 > I$). The resultant attenuated radiation as a function of the wavelength produces the ATR spectrum.

An estimation of the analysis depth (evanescence wave penetration) in an ideal homogeneous solution is given by $eq. 19$. This value has been estimated in previous works [5], according to the decay of the 95% of the electric field from the evanescent field presented in $eq. 18$ [218]. However, the penetration of the evanescent wave across an oxy-hydroxide film is more complicated to determine, and studies on the absorption of ions onto layers of particles deposited on ATR crystals have confirmed a sampling depth around 4-7 microns [215].

$$E = E_0 \cdot exp\left[-\frac{2\pi}{\lambda_1}\left(\sin^2\theta - n_{2,1}^2\right)^{1/2} \cdot Z\right] \qquad (eq. 18)$$

$$d_p = \frac{\lambda_1}{2\pi}\left(\sin^2\theta - n_{2,1}^2\right)^{-1/2} = \frac{3}{\gamma} \qquad (eq. 19)$$

Where λ_1 is the wavelength of the radiation in the denser medium, λ the wavelength in free space, θ the angle of incidence with respect to the normal. The parameter $n_{1,2}$ is defined as the ratio of the refractive indices, $n_{2,1} = {}^{n_2}/_{n_1}$, where n_1 and n_2 are respectively, the refractive indices of the optically denser and less dense media, and Z is the distance from the surface.

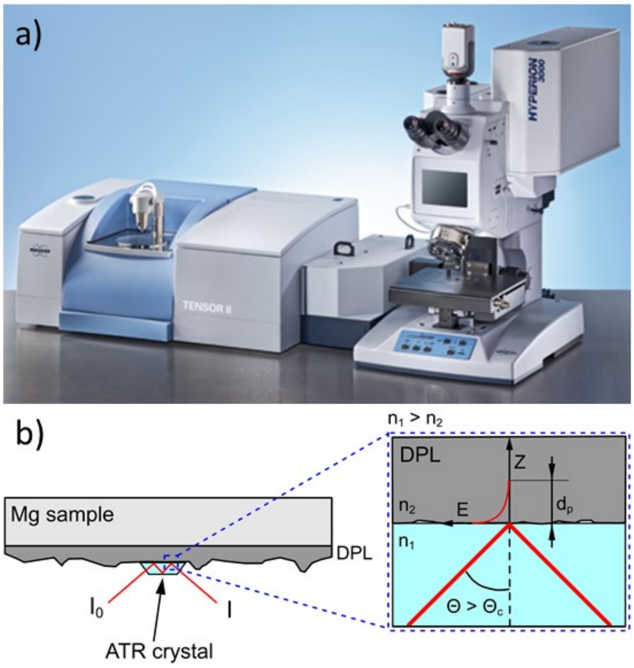

Figure 19: a) Image of the FTIR-ATR Tensor 27 (Bruker), and b) scheme of the sample-ATR crystal coupling in a multi-bounce ATR system, and the generated evanescent wave into the DPL on the surface of the Mg alloy. DPL: degradation product layer, n_1, n_2: refractive indices of the ATR crystal and the DPL respectively, Θ, Θ_c: angle of incidence and the critical angle of incidence of the IR radiation, d_p: penetration of the evanescent wave across the DPL, Z: distance within the DPL in which the evanescent wave is established.

The samples after immersion tests were rinsed in 100% ethanol and stored under vacuum until analysed by in the FTIR-ATR equipment Tensor 27 (Bruker, Ettlingen, Germany) to measure the IR spectra of the degradation products formed on the surface. Every spectrum is the result of an average of 512 scans with a resolution of 2 cm^{-1}. The data evaluation was performed by OPUS software version 7.5.18 (Bruker, Ettlingen, Germany).

3.6.5 Solubility modelling and prediction of the degradation products layer composition

The *Medusa-Hydra* chemical equilibrium modelling software developed by I. *Puigdomenech* [219] was used to evaluate the thermodynamic stability of the possible compounds present in the degradation products layer under the conditions presented during the immersion tests. The *Hydra* software contains a database with the log K_{sp} at 25°C for several compounds formation reaction with its stoichiometry, and *Medusa* module is capable of performing thermodynamic stability diagrams based on different algorithms applied to the computation of aqueous multicomponent, and calculating the activity coefficients. Therefore for each heterogeneous equilibrium contained in the *Hydra* database can be established the relation between the ionic activity and the K_{sp}. The ionic activity or “effective concentration” is estimated by a mathematical approximation applied to calculate the activity coefficient $(eq.21)$. This approximation depends typically on the ionic strength of the solution $(eq.20)$, and *Medussa* module corrects the ionic activity according to the Helgeson equation $(eq.22)$, that is also useful for diluted solutions in the similar range as Davies equation. According to that, *Medussa* software calculates the activity coefficients and with the K_{sp} calculate the concentration for each aqueous and solid phases.

$$I = {}^{1}\!/_{2} \sum m_i \cdot Z_i^2 \qquad (eq.20)$$

$$\gamma_i = a_i \,/\, m_i \qquad (eq.21)$$

$$\log \gamma_i = -Z_i^2 A\sqrt{I} / \left(1 + B\sqrt{I}\right) - \log(1 + 0.018 I) + bI \qquad (eq.22)$$

where I corresponds to the concentration of electric charge in a solution, m_i is the molality of an aqueous species "i" with charge Z_i in mol / (kg of water). γ_i is the activity coefficient for an aqueous species "i", a_i is the activity of the aqueous species "i", and m_i corresponds to the concentration. And the coeficients A, B and b are temperature dependant parameters.

4 Results

4.1 Alloys microstructure and intermetallic phases

Apart from the different composition of the alloying systems presented in Table 7, *Figure 20* shows the different microstructure derived from the different composition and processing routes.

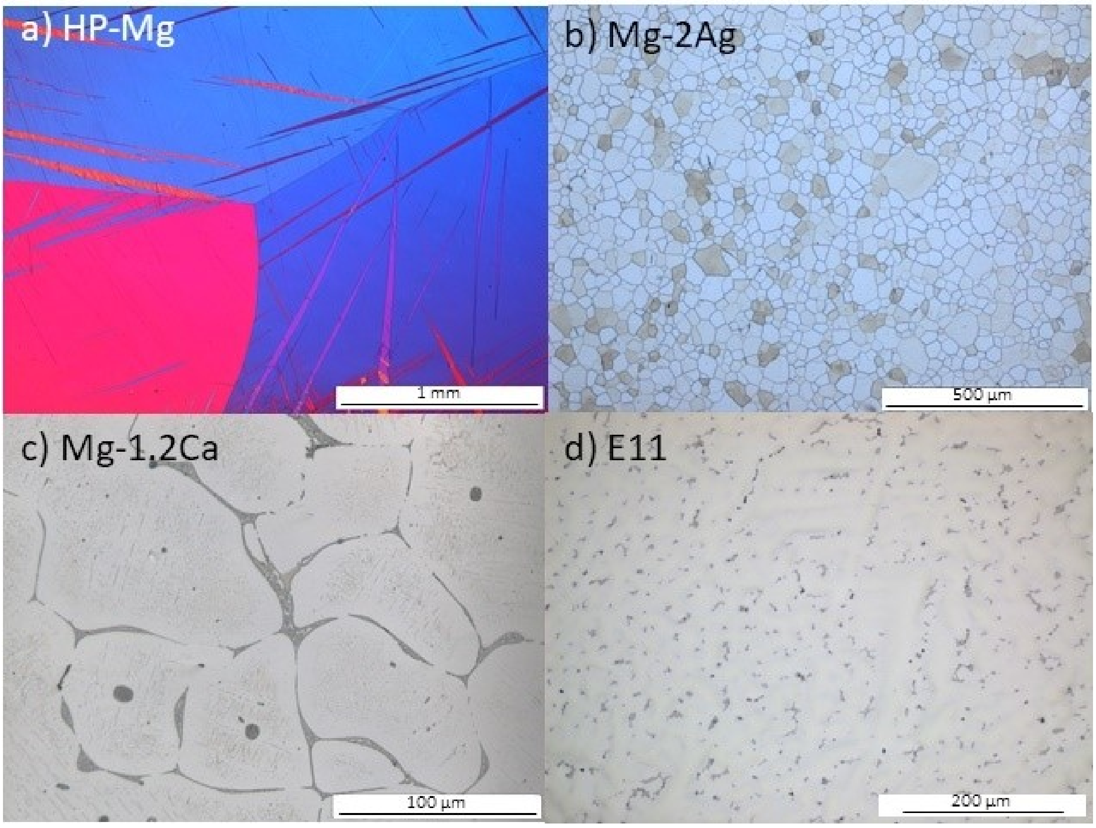

Figure 20: Microstructure of the composition and processes of the alloy described in section 3.1 revealed by optical microscopy. a) As cast High purity magnesium (polarised light), b) extruded and T4 heat-treated Mg-2Ag, c) as cast Mg-1.2Ca, and d) as cast E11 (Mg-10Gd-1Nd-0.1Ca). The microstructures presented in c) and d) were revealed without the final etching procedure, to not affect the highly reactive microstructural features.

The HP-Mg (*Figure 20a*) shows a microstructure entirely formed by equiaxial grains of α-Mg matrix between 0.7 and 4 mm in diameter. In the case of the Mg-2Ag alloy, *Figure 20(b)* shows equiaxial grains (between 25 and 15 µm diameter). The T4 heat treatment performed before and after the extrusion process avoid the presence of degradation detrimental secondary phases (Mg_4Ag or $Mg_{54}Ag_{17}$) that can be found in a typical as-cast microstructure [220,221]. The high purity of the HP-Mg samples and the big grain size made it impossible to detect any relevant microstructural feature by SEM/EDX. In the same way, the SEM/EDX analysis for the Mg-2Ag samples brings no extra information than the one obtained by optical microscopy (grain size and morphology), due to the fully solubilised silver by the T4 heat treatment.

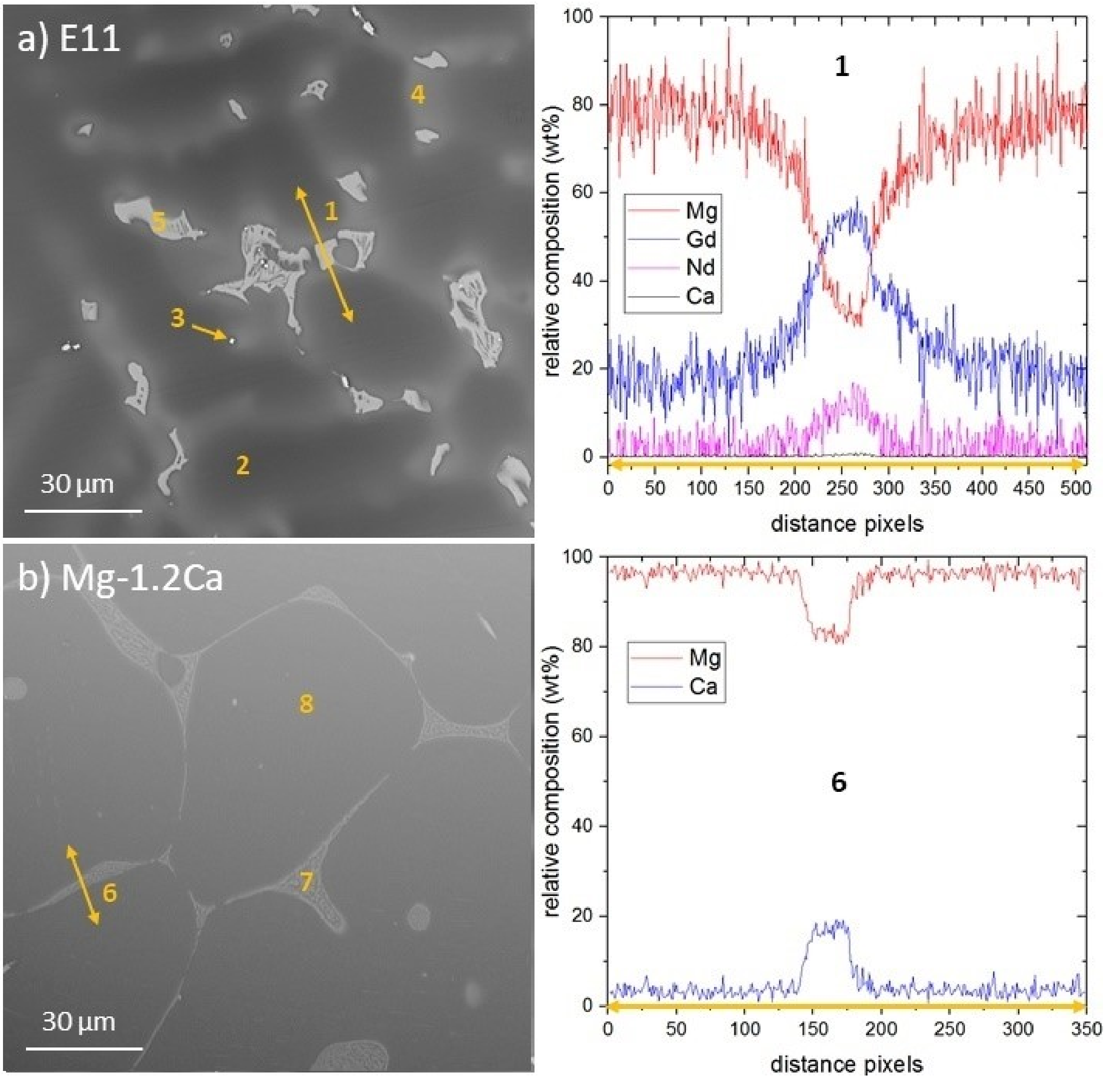

Figure 21: Microstructural and relative chemical analysis of the phases present in the a) E11, and b) Mg-1.2Ca alloys, by BSE and EDX.

The course as-cast structure identified by optical microscopy for the Mg-1.2Ca samples present dendritic areas between 60 and 270 μm diameter of the α-Mg matrix (*Figure 24b, point 8*), which are surrounded by a eutectic structure formed by α-Mg and a Ca-rich intermetallic phase (see *Figure 24b, point 7* and *scan line 6*). This phase, identified as Mg_2Ca in previous works [192,193], was also localised among the grain boundaries. In the case of the E11 alloy, the optical image in *Figure 20(d)* shows a dense secondary phase network in a darker colour than the matrix. The BSE-SEM and the EDX analysis revealed a dendritic as-cast microstructure formed by the primary Mg dendrites with Gd, Nd and Ca in solid solution (*Figure 21a, point 2*), and well defined cellular net of Gd, Nd-rich secondary phases around dendrite arms (*Figure 24a*, point 5). Those phases with pseudo-eutectic morphology, are probably composed of β-Mg_5(Gd, Nd), as was identified previously [198,222]. High level of segregation on Gd and Nd was revealed by the brighter areas surrounding the secondary phases (see *Figure 21a*, *point 4 and line scan 1*). Also, bright cuboidal particles between 0.5

and 5 µm (*Figure 24a, point 3)*, identified previously as [Gd, Nd, Mg]-hydrides (REH_2/REH_3) [223,224], were found to be associated with the secondary phase or the Gd/Nd segregated areas in the α-Mg matrix.

Table 10: Relative chemical analysis performed by EDX of the microstructural features identified in Figure 21. The compositions are given in wt.%.

	Mg	Gd	Nd	Ca	O
2	94.33	3.88	0.35	0.13	1.31
3	63.44	29.70	2.56	0.90	3.40
4	88.12	9.61	0.77	0.11	1.39
5	73.14	18.97	4.55	0.90	2.44
7	85.58	-	-	11.41	3.01
8	98.30	-	-	0.46	1.24

4.2 *In situ* measurement of interface pH of Mg

4.2.1 Solution influence on the interface pH of Mg

The SIET set-up under dynamic conditions was applied to evaluate the influence of the relevant inorganic electrolytes on the surface local pH during the degradation process. *Figure 22* shows the influence of the addition of Mg^{2+} cations to the local pH along the E11 surface. The four consecutive scans performed along the first 119 min of immersion in HBSS (*solution I*) revealed a surface local pH between 9.75 and 10, at 10 µm above the surface (*Figure 22a*). The values obtained for the different scans showed no apparent change tendency within such immersion time. With the addition of 1.5 mM $MgCl_2$ (*solution II*), the interface pH at 45 µm above the surface was decreased down to 9.25 - 9.5. Besides the influence of Cl^- anions on the degradation rate discussed in *section 1.3.2*, the $MgCl_2$ addition did not promote a higher interface pH as a consequence of a higher degradation rate. This fact, support a stronger influence of the Mg^{2+} cations contribution, than the harmful effect generated by such increment in Cl^- anions. However, the slight decrease of pH might be related to the lower bulk pH of *Figure 22(b)* in contrast with the one presented in *Figure 22(a).* The orange arrow depicted in *Figure 22(b)* showed how after approximately 76 min of immersion this area behave less active showing a lower pH in contrast with the behaviour found for earlier immersion times (black and red lines) and the subsequent one (blue line). The pink arrows in *Figure 22* revealed how the direction of the flow rate applied, depicted with a red arrow on the *in situ* optical image of the sample, generates a shoulder shape for every profile. The optical images included in

Figure 22, showed how the addition of Mg^{2+} ions did not generate appreciable differences in the degradation morphology revealed on the microstructure. In both degraded surfaces, well-defined bright and dark areas that can be assimilated to the features revealed in *Figure 21(a)* for the E11 microstructure. Besides, a high hydrogen development with big size bubbles was generated during the whole immersion time.

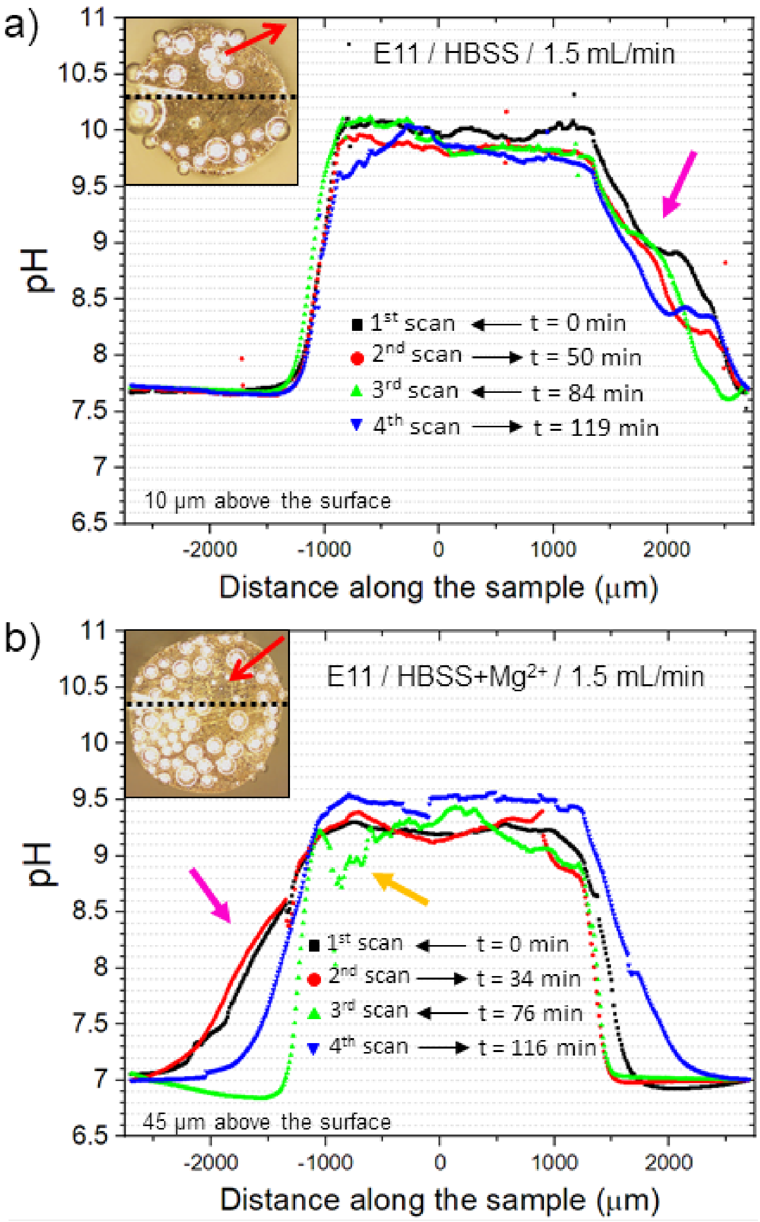

Figure 22: Influence of the presence of Mg^{2+} cations in the Hank´s balanced salt solution (HBSS) composition on the in situ interface pH developed on the E11 alloy under the first 2 hours of dynamic immersion (1.5 mL/min). The figure presents in a) four consecutive SIET parallel line scans at 10 µm above the surface under immersion in Hank´s balanced salt solution (HBSS, solution I), and b) four consecutive parallel line scans at 45 µm under immersion in Hank´s balanced salt solution (HBSS) with the addition of 1.5 mM of $MgCl_2{\cdot}6H_2O$ (solution II). The direction of the flow rate is indicated by the red arrow placed on the in situ obtained digital images. The orange arrow identifies an area on the surface with a lower interface pH than the rest of the scanned surface. The pink arrow shows a shoulder-shaped artefact on the pH profile generated by the solution flow.

The effect of the presence of Ca^{2+} cations (*solution III*) on the interface pH was studied by the SIET parallel scanned lines on the E11 surface that are presented in *Figure 23*. With the addition of 2.5 mM of $CaCl_2 \cdot 2H_2O$ (*Figure 23b*) four consecutive scans within the first 360 min of immersion at 30 µm above the surface, showed a interface pH between 7.8 and 8.2 units, with high active zones indicated by orange arrows. The presence of Mg^{2+} and SO_4^{2-} ions in addition to the Ca^{2+} cations showed in *Figure 23(a)* a interface pH between 7.6 and 8.1 units within the first 94 min of immersion. A high pH zone on the interface between the sample and the resin was revealed and indicated by an orange arrow.

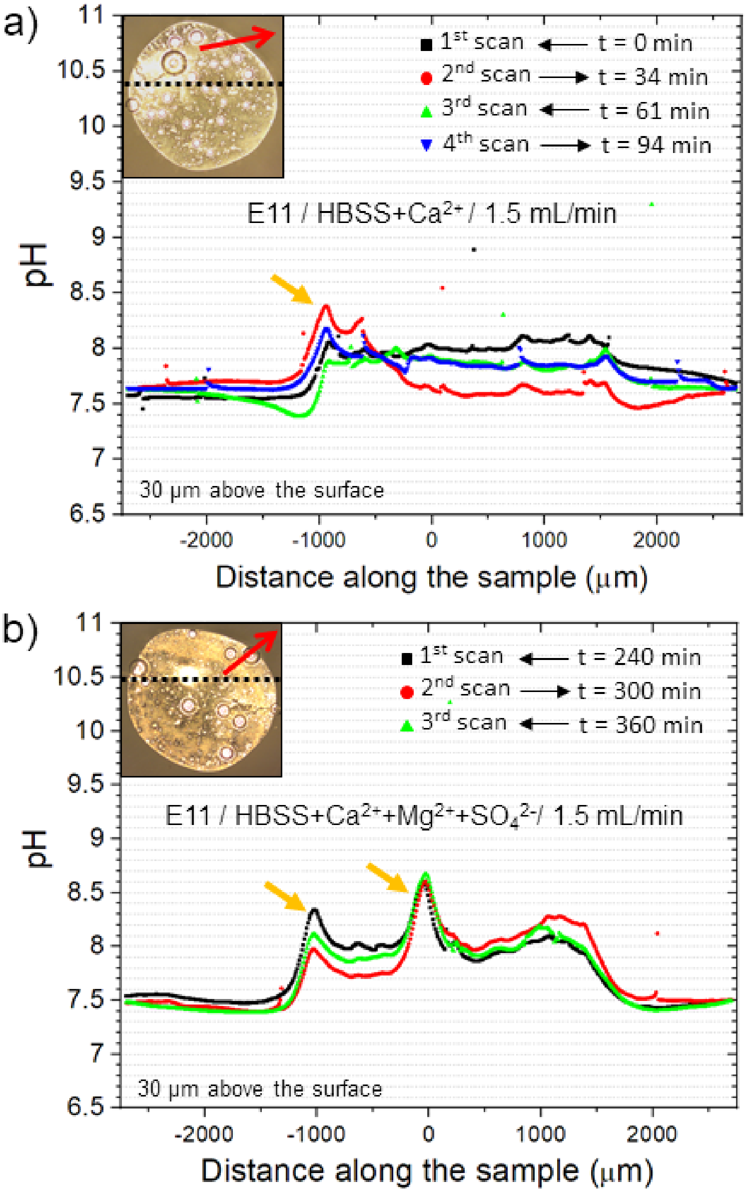

Figure 23: Influence of the presence of Ca^{2+}, Mg^{2+} and SO_4^{2-} ions in the Hank´s balanced salt solution (HBSS) composition on the in situ interface pH developed on the E11 alloy under dynamic immersion (1.5 mL/min). The figure presents in a) four consecutive SIET parallel line scans at 30 µm above the surface during the first 1.6 hours of immersion in Hank´s balanced salt solution (HBSS) with the addition of 2.5 mM of $CaCl_2 \cdot 2H_2O$ (solution III), and in b) three consecutive SIET parallel scans at 30 µm above the surface between 4 - 6 hours of immersion in Hank´s balanced salt solution (HBSS) with the addition of 2.5 mM of $CaCl_2 \cdot 2H_2O$, 1.5 mM of $MgCl_2 \cdot 6H_2O$, and 0.5 mM of

Na_2SO_4 (solution IV). The direction of the Flow rate is indicated by the red arrow placed on the in situ digital images. The orange arrows point to higher interface pH areas that were connected with high hydrogen evolution.

As well as for the scans presented in *Figure 22,* the consecutive scans presented in *Figure 23* did not reveal a tendency on the interface pH over the immersed time. All the abrupt increments in the interface pH values presented in the figures above with orange arrows were associated with a high localised hydrogen evolution. Due to the well-distributed network of secondary phases along with the whole material, those highly active zones can be supposedly attributable to zones with a higher concentration of impurities levels. In contrast to the optical images presented in *Figure 22*, the ones presented in *Figure 23* showed a homogeneous bright appearance were no microstructure features can be identified. This fact can be seen later in *Figure 33*. Concerning the hydrogen evolution in the presence of Ca^{2+} cations, the degradation process generated small bubbles that were fast detached.

The immersion of the E11 surface, used previously for the SIET measurements, was used to study the first stages of the alkalinisation process. The sample was immersed under static conditions in the presence of HBSS (*solution I*) and HBSS with the addition of 2.5 mM $CaCl_2 \cdot 2H_2O$ (*solution III*) in the presence of phenolphthalein as a pH indicator. The optical changes were digitally monitored by DVIT. As a result, the image sequence presented in *Figure 24* shows the first 6 minutes of immersion in the mentioned solutions. *Phenolphthalein* dissociation constant (pK_{In}) is 9.4 ± 0.5, and the pH range for the colour change is between 8.2 and 10.0 from a transparent form (H_2Ph) to an intense pink (In^{2+}). Therefore the pink colouration reveals the alkalinisation of the solution.

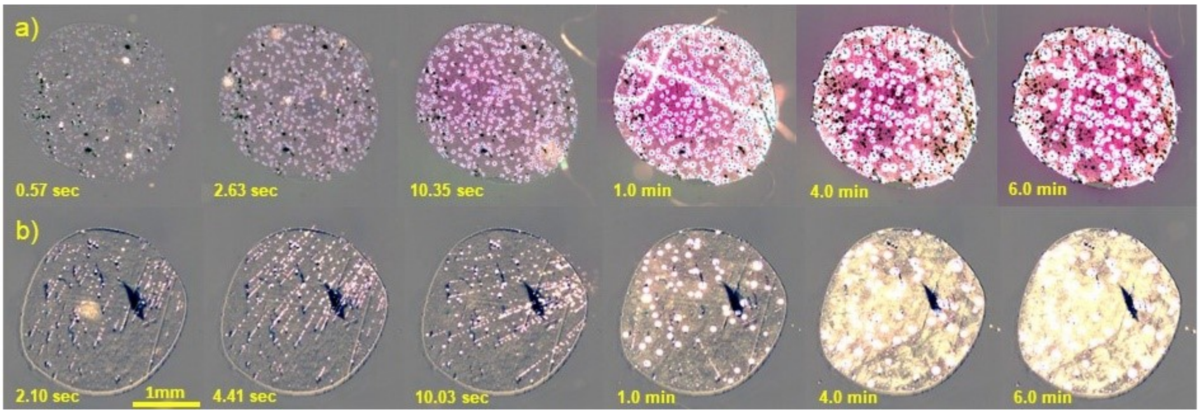

Figure 24: DVIT in situ investigations of the general alkalinisation generated on the degradation solution by the immersion of the same E11 sample used in previous SIET scans (Figure 22 and Figure 23) during the first 6 minutes of immersion in a) Hank´s balanced salt solution (HBSS, solution I) with the addition of phenolphthalein, and in b) Hank´s balanced salt solution (HBSS) with the addition of 2.5 mM of $CaCl_2 \cdot 2H_2O$ (solution III) and phenolphthalein. The change into a pink colour of the solution is generated by a shift in the pH between 8.2 and 10.0 due to the pK_{In} of 9.4 ± 0.5 of the phenolphthalein.

The DVIT analysis for the immersion in HBSS (see *Figure 24a*) shows that the accumulation of small, static and homogeneously distributed hydrogen bubbles on the surface of the alloy is accompanied by a very slight and local pink colouration within the first second.

After two seconds of immersion, the size of the hydrogen bubbles increase, and the pink colour becomes more evident and generalised on the whole sample surface. After the first 10 seconds of immersion, the hydrogen bubbles continue increasing their size and the indicator colour intensity increases. After one minute, the pink colouration starts to propagate in the solution surrounding the sample surface. In contrast, in the presence of HBSS with the addition of 2.5 mM of $CaCl_2 \cdot 2H_2O$ (*Figure 24b*) shows the formation of localised hydrogen bubble streams from the first two seconds with an apparent slight pink colouration surrounding the bubbles. This situation remains until the first ten seconds of immersion. After this point, the sample begins to show a brighter surface becoming intensively brighter with the immersion time, and the hydrogen bubbling becomes less active, showing an increment of the bubbling size. At the same time, the pink colour from the indicator persists only surrounding the bubbles.

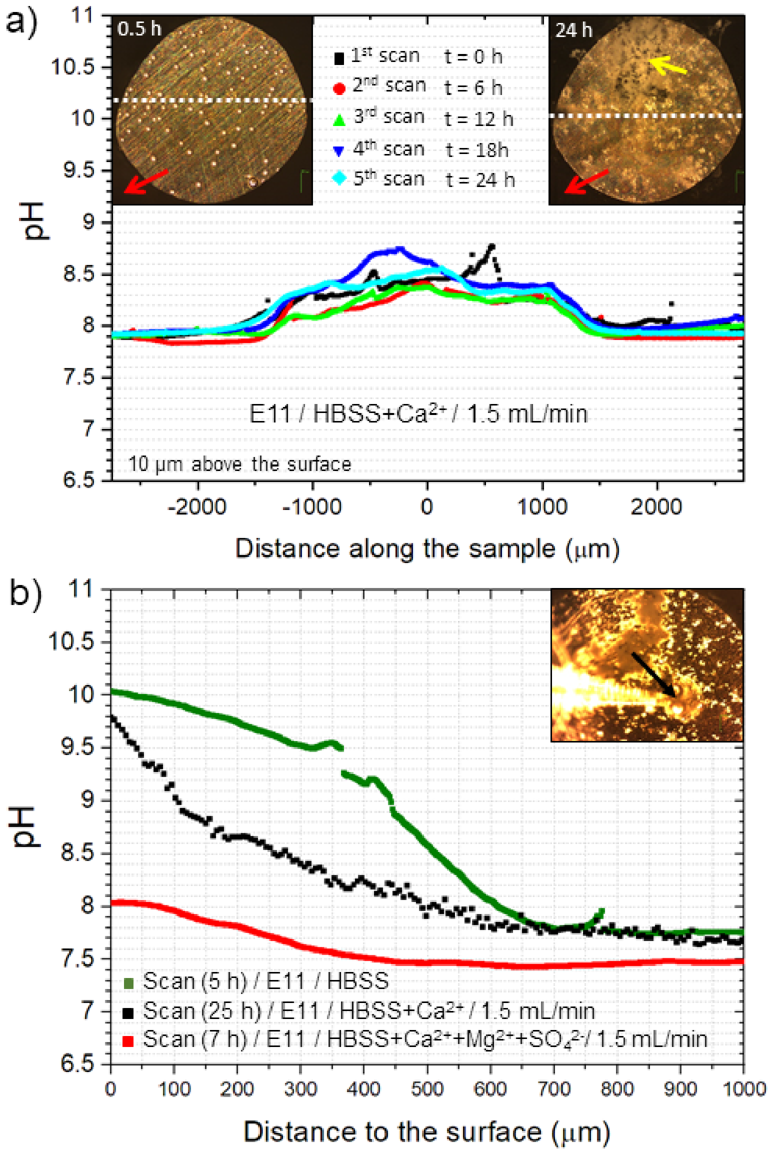

Figure 25: a) Variation of the in situ interface pH of the E11 sample within the first 24 hours of immersion revealed by 5 parallel SIET scans at 10 µm above the surface under Hank´s balanced salt solution (HBSS) with the addition

of 2.5 mM of $CaCl_2 \cdot 2H_2O$ (solution III). b) Three perpendicular SIET scans performed from 1 mm above the surface under dynamic immersion (1.5 mL/min), in (green line scan) Hank´s balanced salt solution (HBSS, solution I) , in (black line scan) Hank´s balanced salt solution (HBSS) with the addition of 2.5 mM of $CaCl_2 \cdot 2H_2O$ (solution III), and in (red line scan) Hank´s balanced salt solution (HBSS) with the addition of 2.5 mM of $CaCl_2 \cdot 2H_2O$, 1.5 mM of $MgCl_2 \cdot 6H_2O$, and 0.5 mM of Na_2SO_4 (solution IV). The direction of the Flow rate for the scans presented in (a) is indicated by the red arrow placed on the in situ digital images.

The same immersion test in the presence of phenolphthalein was applied for the rest of the alloys but in the absence of the DVIT system. The same fast alkalinisation process was found for all surfaces in the absence of Ca^{2+} cations in the HBSS composition, and in contrast, the presence of Ca^{2+} cations generated no colour change of the phenolphthalein, revealing a lower pH than the range 8.2 – 10.0.

The parallel SIET scans performed within the first 24 hours of immersion over the E11 surface alloy presented in *Figure 25(a)*, revealed that the lower interface pH environment in the presence of Ca^{2+} cations persists at least during the 24 hours of immersion. The slight differences in the interface pH shown in *Figure 25(a)* (pH 7.8 – 8.2) and *Figure 23(b)* (pH 8.1 – 8.4) can be explained by: a) After every degradation test and the subsequent surface preparation, the surface can present new non-homogeneous areas or differences in the impurity levels exposed that can generate slight differences in the activity of the surface, b) the manual preparation of the SIET electrode (membrane cocktail and capillary morphology) can bring differences in the sensitivity of the system, and c) a difference in the scanning high of the electrode between 10 and 30 µm can also bring a slight difference. However, those slight differences do not mask the lower pH environment promoted by the presence of the Ca^{2+} cations.

Moreover, with the presence of Ca^{2+} cations a higher amount of precipitates were found in the surface (*Figure 25a*, optical image after 24 h on the right corner), and a continuous localised filiform degradation process (yellow arrow in *Figure 25a*), often starting in the interface resin/sample, was found. The perpendicular line scan performed on the head of the active degradation filiform process (black line scan of *Figure 25(b)* revealed a significantly higher local pH than the areas were this filiform degradation is not present (red line scan of *Figure 25b*).

The perpendicular SIET scans performed from 1 mm above to the surface shows again both differentiate behaviours in the presence and absence of Ca^{2+} cations. The scans performed for the E11 surface under degradation in HBSS (green line scan in *Figure 25b*) shows an increase from pH 7.5-7.7 in the bulk solution up to pH 10 – 10.2 on the surface. While with the addition of $CaCl_2 \cdot 2H_2O$, including the presence of Mg^{2+} and SO_4^{2-} ions (red line scan in *Figure 25b)* this increment is less pronounced reaching an interface pH up to 8.0. Those pH profiles provide information concerning the mass transfer between the surface/interface area and the bulk solution. Establishing this limit for the H^+/OH^- species at

700 µm under the immersion in HBSS (green line scan in *Figure 25b*), and a diffusion layer around 500 µm under the immersion in HBSS with the addition of Ca^{2+} cations.

Therefore, the presence of Ca^{2+} cations in the corrosive solution leads to a significantly lower interface pH that is developed since the first seconds of immersion and persists until at least 24 hours of immersion. Consequently, lower differences between the interface pH and the bulk pH were found in the presence of Ca^{2+} cations in solution. However, the additional presence of Mg^{2+} in the corrosive solution in the physiological range seems to not promote significant changes on the interface pH. The stability of the local surface environment is interrupted by local active areas where a high interface pH is reached companied with high hydrogen evolution.

4.2.2 Alloy influence on the interface pH of Mg

In order to show the influence of the dissolution kinetics, promoted by differences in the alloy composition and microstructure, in the *in situ* local pH, SIET scans were performed over the surface of the HP-Mg, Mg-2Ag and Mg-1.2Ca samples within the first 3 hours of immersion in HBSS (*solution I*) and HBSS with the addition of 2.5 mM $CaCl_2{\cdot}2H_2O$ (*solution III*). The SIET scans were performed between 30 and 50 µm above the surface assuring that all the measurements were performed inside the diffusion layer, and therefore the interface pH values can be comparable. By comparing *Figure 26, Figure 27, and Figure 28*, the effect of the addition of the $CaCl_2{\cdot}2H_2O$ on the interface pH was consistent with the ones presented in *Figure 22(a)* and *Figure 23(b)*.

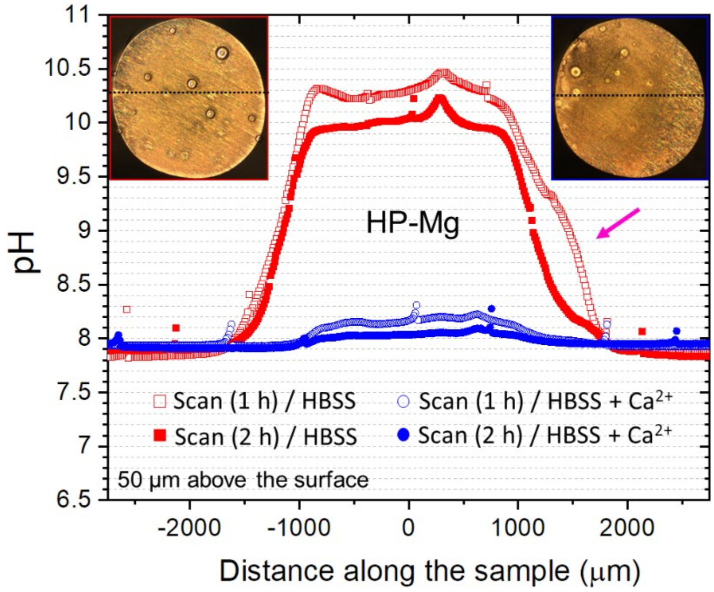

Figure 26: Effect of the addition of 2.5 mM of $CaCl_2{\cdot}2H_2O$ in Hank´s balanced salt solution (HBSS) composition on the in situ interface pH developed on the HP-Mg sample. The figure shows two consecutive parallel SIET scans above 50 µm above the surface within the first 2 hours of immersion in (red scans) Hank´s balanced salt solution (HBSS, solution I), and in (blue scans) Hank´s balanced salt solution with the addition of 2.5 mM of $CaCl_2{\cdot}2H_2O$ (solution III). The pink arrow shows a shoulder-shaped artefact on the pH profile generated by the solution flow.

The values of the interface pH along the scans show a similar behaviour between the HP-Mg and the Mg-2Ag, without significant abrupt pH values. A pH between 9.9 and 10.4 in HBSS and around pH 8.1 when Ca^{2+} cations were included in the degradation solution. In the case of the as-cast Mg-1.2Ca alloy, high local pH areas associated with intense hydrogen evolution were identified all along the surface and at the interface sample/resin. Those active zones seem to mask a slightly lower interface pH when the sample was immersed in HBSS (*solution I*), that seems to be between 9.8 and 10.2 pH units.

On the other hand, when the as-cast Mg-1.2Ca surface was immersed in the presence of Ca^{2+} cations (*solution III*), the interface pH showed similar values to the HP-Mg and Mg-2Ag (T4) surfaces but with a higher number of highly active zones. Those zones reached pH levels above 8.5 units, and its magnitude differed between the first and the second hour of immersion. The more homogeneous interface pH found for the HP-Mg and Mg-2Ag is probably related to the high homogeneity of the systems in composition and microstructure and the absence of secondary phases and impurities in a significant amount.

Despite the substantial differences in degradation rates presented for all Mg-based materials tested in later *section 4.3.2*, small differences in the absolute local pH values and the substantial differences in the composition and microstructures, the presence of Ca^{2+} cations generated a similar depletion of the local pH environment up to 8.0 – 8.2 units for all the materials. The differences in the number of highly active zones can be explained by differences in the presence of the impurities or secondary phases, that depending on its distribution along the surface might be an essential source for the differences in the absolute interface pH values.

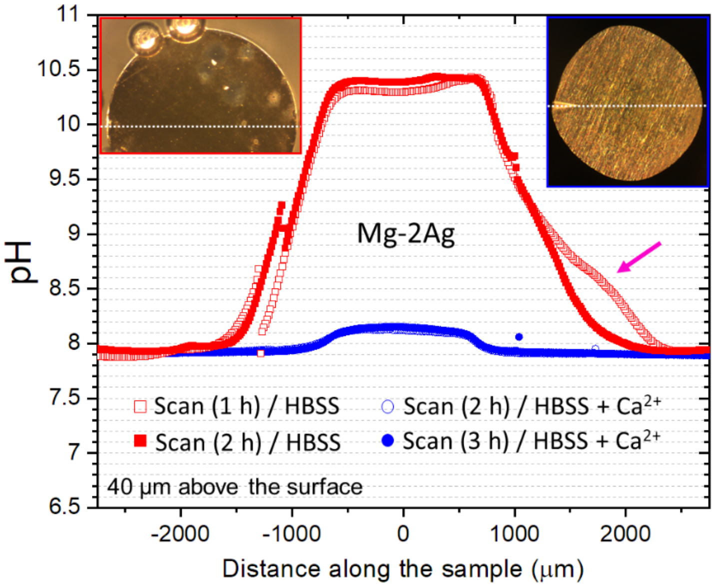

Figure 27: Effect of the addition of 2.5 mM of $CaCl_2\cdot 2H_2O$ in Hank´s balanced salt solution (HBSS) composition on the in situ interface pH developed on the Mg-2Ag sample. The figure shows two consecutive parallel SIET scans above 50 µm above the surface within the first 3 hours of immersion in (red scans) Hank´s balanced salt solution

(HBSS, solution I), and in (blue scans) Hank´s balanced salt solution with the addition of 2.5 mM of $CaCl_2 \cdot 2H_2O$ (solution III). The pink arrow shows a shoulder-shaped artefact on the pH profile generated by the solution flow.

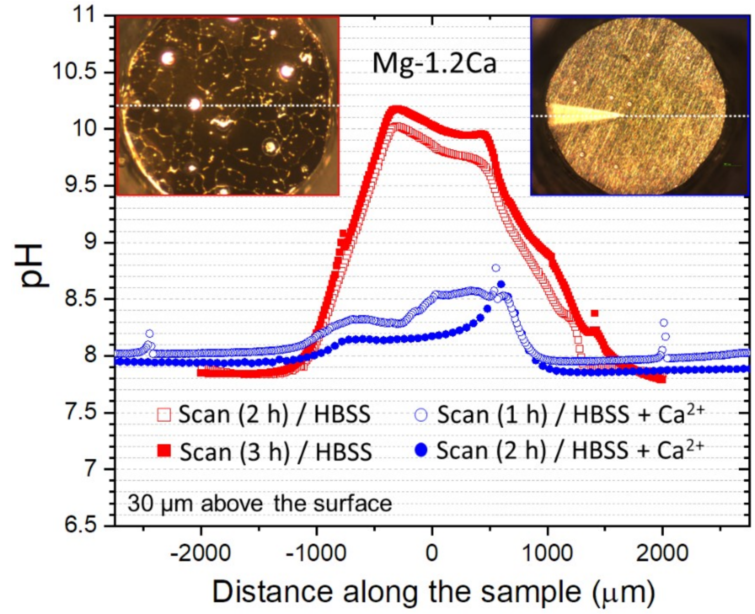

Figure 28: Effect of the addition of 2.5 mM of $CaCl_2 \cdot 2H_2O$ in Hank´s balanced salt solution (HBSS) composition on the in situ interface pH developed on the Mg-1.2Ca sample. The figure shows two consecutive parallel SIET scans above 50 µm above the surface within the first 3 hours of immersion in (red scans) Hank´s balanced salt solution (HBSS, solution I), and in (blue scans) Hank´s balanced salt solution with the addition of 2.5 mM of $CaCl_2 \cdot 2H_2O$ (solution III). The pink arrow shows a shoulder-shaped artefact on the pH profile generated by the solution flow.

As in previous observations was noticed, the optical appearance of the surface also points to differences in the processes happening on the surface. In the case of Mg-2Ag and Mg-1.2Ca samples, as well as was pointed before for the E11 system, a darker surface was revealed with the degradation in HBSS, while in the presence of Ca^{2+} cations the surface remains closer to the initial bright metallic appearance. The Mg-2Ag sample showed a homogeneous dark surface under the immersion in HBSS while for the Mg-1.2Ca the dark surface included bright features that can be identified with the microstructural characteristics presented in *Figure 21(b).* In the case of the HP-Mg (*Figure 26*), this fact is not observable, showing similar bright surfaces under both degradation conditions. The importance of the presence of Ca^{2+} cations in the interface environment can also be inferred from the effect of the calcium included in the as-cast Mg-1.2Ca system. On one side, the dissolution of the alloy seems to provide enough calcium to the local environment to generate the same precipitation effect, but in lower magnitude, lowering the interface pH under immersion in HBSS (*solution I*). Moreover, with the presence of Ca^{2+} cations in the corrosive solution composition, the Ca^{2+} cations originated from the alloy dissolution seems to contribute to the passivation process that promoted a higher filiform effect.

According to all described above, the substantial differences in the dissolution kinetics coming form the differences the composition and microstructures analysed, do not have significant influences on the interface pH in contrast to the strong influence of the presence of Ca^{2+} cations in solution.

4.2.3 Influence of solution exchange on interface pH of Mg

Due to the faster degradation rate (detailed later in *section 4.3.2*) and therefore its possible faster influence on the local pH environment, the E11 alloy was chosen to show the influence of the degradation solution exchange on the interface pH. The surface of the E11 sample was immersed in HBSS (*solution I*) and HBSS with the addition of $CaCl_2 \cdot 2H_2O$ (*solution III*) under static conditions with a 5 mL solution limited by the degradation cell enclosed volume (*Figure 14*), and under dynamic conditions of 1.5 mL/min of flow rate. Under those conditions, four consecutive SIET local pH measurements were performed in parallel to the sample surface within approximately the first 120 min of immersion, which translates to around 225 mL of degradation solution when dynamic conditions were applied.

Figure 29 showed the influence of the fluid exchange on the interface pH while the surface is immersed in HBSS. The *in situ* static conditions (*Figure 29a*) revealed an interface pH between 10.0 and 10.8 units. Moreover, the bulk pH presented a shift along the immersion time that goes between approximately 7.6 to 8.1 units, highlighted by a dashed black arrow in *Figure 29(a)*. In addition, the orange arrow in *Figure 29(a)* highlights how the edges of the sample were revealed as highly active zones with a high local pH. Possibly, this effect is potentiated by the static conditions that are not able to absorb the alkalinisation process and therefore, the edges of the sample are faded in the pH profile. Moreover, this effect seems to affect the expected progression of the bulk pH after every scan. On the other hand, by exchanging the HBSS solution with a rate of 1.5 mL/min (*Figure 29b*), the interface pH dropped to 9.8 and 10.0 Under those dynamic conditions, the edge of the sample is better defined as showed on the left side of the profiles in *Figure 29(b)*, and the bulk pH is maintained stable around 7.6 units. As in previous figures, the effect of the flow direction in the local pH profile (highlighted in the microscopy image by a red arrow) fade the right edge of the sample, as highlighted by the pink arrow in *Figure 29(b)*.

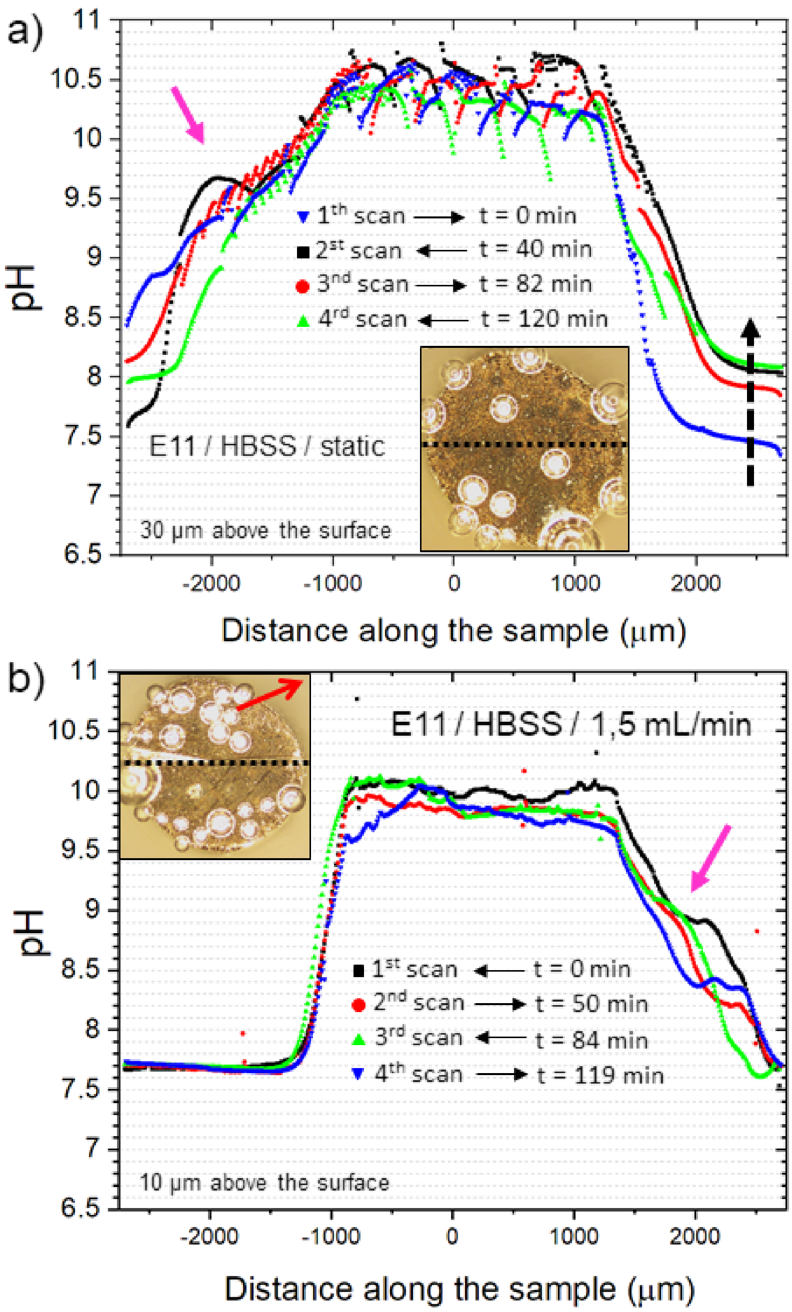

Figure 29: Comparison of the in situ interface pH developed on the E11 sample under immersion in Hank´s balanced salt solution (HBSS, solution I) within the first two hours of immersion revealed by four consecutive parallel SIET scans under a) static conditions in a chamber with an approximate volume of 5 mL at 30 µm above the surface and b) dynamic conditions with a flow rate of 1.5 mL/min at 10 µm above the surface. The direction of the flow for the scans presented in (b) is indicated by the red arrow placed on the in situ digital image. The pink arrow shows a shoulder-shaped artefact on the pH profile generated by the solution flow. The black dashed arrow in (a) the increase of the bulk pH over the immersion time.

When the E11 surface was exposed to the presence of Ca^{2+} cations (*solution III)*, the interface pH showed no apparent differences when the static (*Figure 30a*) and the dynamic conditions (*Figure 30b*) were applied. However, an increase in the bulk pH was noticed between the first scan, performed within the first 40 min, and the subsequent ones, when the static conditions were applied (black dashed line in *Figure 30a*). On the contrary, under the dynamic conditions presented in *Figure 30(b)*, the bulk solution pH remains stable at around 7.6 units within the immersion time.

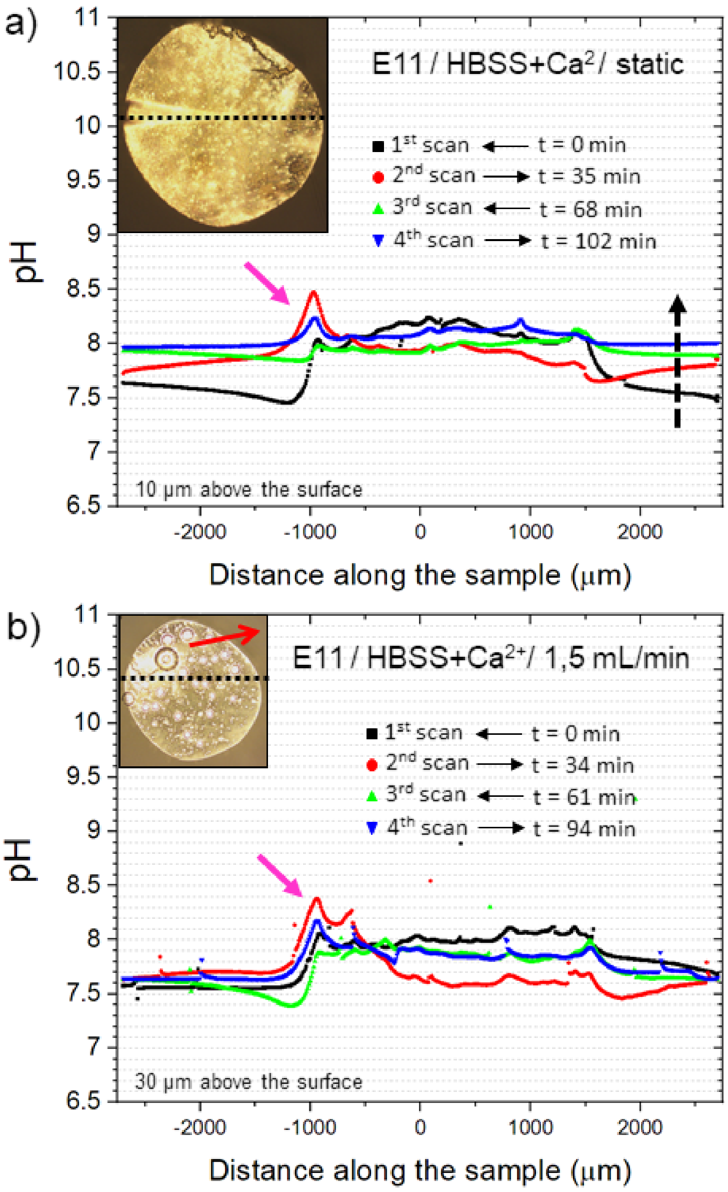

Figure 30: Comparison of the in situ interface pH developed on the E11 sample under immersion in Hank´s balanced salt solution (HBSS) with the addition of 2.5 mM of $CaCl_2 \cdot 2H_2O$ (solution III) within the first two hours of immersion revealed by four consecutive parallel SIET scans under a) static conditions in a chamber with an approximate volume of 5 mL at 10 µm above the surface and b) dynamic conditions with a flow rate of 1.5 mL/min at 30 µm above the surface. The direction of the flow for the scans presented in (b) is indicated by the red arrow placed on the in situ digital image. The orange arrows point to higher interface pH areas that were connected with a high hydrogen evolution. The black dashed arrow in (a) the increase of the bulk pH over the immersion time.

Figure 31 shows two perpendicular SIET profiles performed from a distance of 1000 µm down to the surface during the *in situ* degradation of an E11 sample in HBSS (*solution I*). The profiles depicted show the difference between the local pH between static conditions and the dynamic conditions of 1.5 mL/min described previously. The revealed profile under static conditions (red profile in *Figure 31*) was performed within the first 2.5 hours of immersion, revealing a final interface pH of 10.8 units. The high local pH value on the surface decreases progressively until reaching the stable pH of the bulk solution at around 8.9 units along with a diffusion layer that extends 700 µm over the surface. When a flow rate of 1.5 mL/min was applied (blue profile in *Figure 31*), the local pH profile performed within the first 3.5 hours of immersion revealed lower pH values along with the whole profile and reaching a final interface pH of 10.0 units. In the same way, as under static conditions, the value of the local pH decreases from the surface until the bulk conditions (pH 7.8) along with a diffusion layer of 700 µm. It should be noted that in the closest part to the surface, the pH values presented a plateau that is not mentioned when the diffusion layer is described in the literature. Traditionally, the mass transfer at the nearest volume of the surface is ruled by the diffusion processes describing a linear behaviour as presented in *Figure 6*. This plateau can be described as a volume of the solution where the pH is stabilised or saturated by possibly the precipitation/dissolution process generated on the surface and the buffer capacity of the solution. Therefore, is possibly a portion of the solution in which exist a particular supersaturation situation. However, the necessary processes of nucleation and crystal growth do not promote the net precipitation process, that is only favoured at the surface.

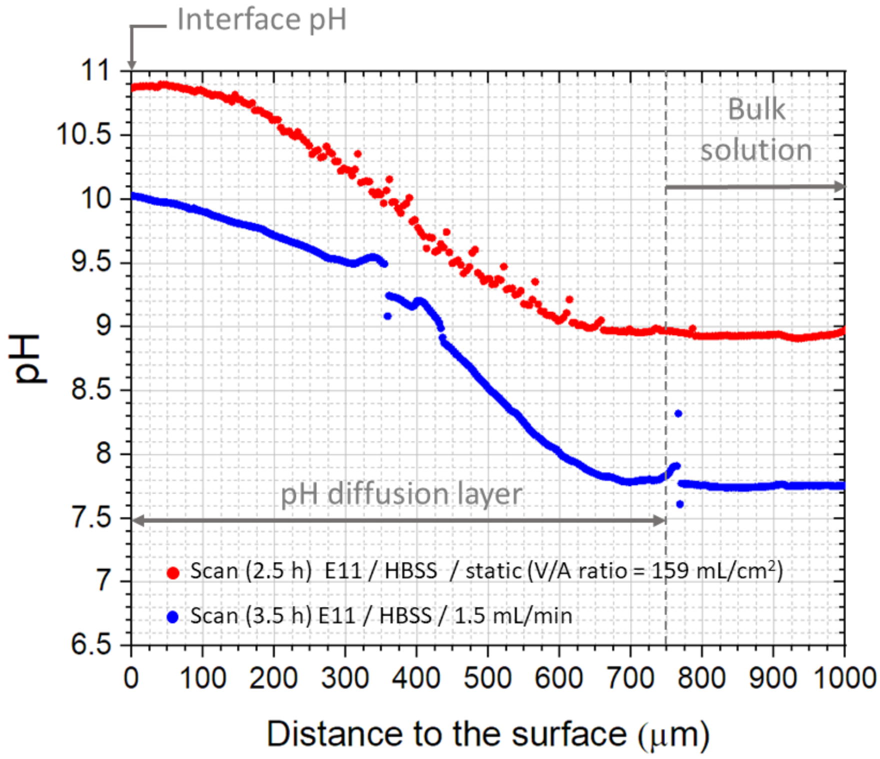

Figure 31: Comparison of two perpendiculars in situ local pH profiles performed from 1 mm above the E11 surface until crashing the microelectrode on the surface. Both profiles were performed within the first three hours of immersion (the immersion time referenced in the figure corresponds to the moment when the microelectrode crashed the surface) in Hank´s balanced salt solution (HBSS, solution I) under (red profile) static conditions in a chamber with an approximate volume of 5 mL, and (blue profile) under dynamic conditions with a flow rate of 1.5 mL/min. The figure identifies three different areas above the surface with different pH environment: the interface pH, the pH diffusion layer, and the bulk pH.

Therefore, the renewal of the corrosive solution has a direct impact on the bulk solution pH and therefore can better mimic the physiological homeostasis that can be extended also to the ionic composition of the relevant ions (e.g. Ca^{2+}, Mg^{2+}, HCO_3^-, HPO_4^{2-}). The increased mass transfer also affected the pH profile in the diffusion layer and the interface pH value, revealing that the local surface environment is also modified by the flow applied. Under static conditions, the lower alkalinisation generated by the presence of the Ca2+ cations is absorbed by the mass transfer and the V/A ratio applied. This situation promotes the same interface pH values than under dynamic conditions.

4.2.4 Current status of the interface pH measurements on Mg degradation

Apart from the few recent works defining the local surface environment, the results presented in those works differ with the ones presented in the previous sections even though those degradation test were also performed under Ca^{2+}-containing simulated body fluids. The degradation of high-pressure torsion deformed (HPT) Mg-0.6Ca and Mg-0.9Ca in no-buffered Ringer's solution (NaCl, KCl and $CaCl_2$) by *Mareci et al.* [184], showed similar interface pH values just an initial period of lower local interface pH within the first 200 minutes of immersion and just for the Mg-0.6Ca system. However, longer immersion times showed a significant increase in the interface pH between 10 and 11.2 units. The absence of the HCO_3^- and HPO_4^{2-} in the Ringer´s solution, fully justify the higher interface pH values found in the cited work. Besides, the static conditions applied generate a limited buffer capacity and therefore promote the increasing alkalinisation of the bulk solution that with the immersion time can affect the interface pH. Also, the limited degradation solution volume and the constant degradation products layer formation can generate a drop in the solution dissolved CO_2 coming from the atmosphere that initially can provide a carbonate source for the degradation products layer.

The results of interface pH reported by *Jamali et al.* [225] on the degradation of AZ31 under static conditions in SBF containing Ca^{2+}, HCO_3^- and HPO_4^{2-} with HEPES (4-(2-Hydroxyethyl)piperazine-1-ethane sulfonic acid) as a buffering agent, showed slight differences with the local pH value observed in the present work. The values up to 11.9 pH units found by *Jamali et al.* [225] is in agreement with the highly active zones showed in *Figure 25*. However, the local pH values corresponding with no especially active zones presented by S. Jamali revealed a pH of 9.6 -9.8 that differ in more than one pH unit with the values measured in the present work in the presence of Ca^{2+} cations (*Figure 25*). Those discrepancies are unlikely resulting from differences in the scanning surface distance since the perpendicular profiles presented in *Figure 31* presents a difference of less than 0.1 pH unit between scanning distances of 10 and 50 µm above the surface.

Therefore, the higher interface pH values found in the literature in the presence of Ca^{2+} cations can be explained by the following factors:

i) A substantially bigger electrode diameter like the Ir/IrOx probe (195 µm) used by *Jamali et al.* [225], in contrast with the 2 µm diameter microelectrode used in the present work, can obstruct the local diffusion/convection processes, leading to a local OH^- ion accumulation and therefore reveal higher interface pH values.

ii) The potential dependency of the Ir/IrOx probe on the local concentration of O_2 and H_2 could affect the pH values measured in [185].

iii) The SCEM measurements conducted by *Jamali et al.* [225] were performed under static conditions in contrast to the measurements performed under dynamic conditions in the present work. As is presented in *section 4.2.3*, the influence of dynamic conditions leads to a difference of 0.8 pH units at the interface when a flow rate of 1.5 mL/min is applied in comparison with the static conditions. Therefore, the limited mass transfer between the surface and the bulk medium generated by the static conditions, lead to higher levels of alkalinisation at the interface, which is aggravated with the immersion time due to the dependency of the buffer capacity with the volume [148].

iv) As later developed in *section 5.2*, due to the limited amount of Ca^{2+}, HCO_3^- and HPO_4^{2-} of a static immersion set-up, the solution concentrations can decrease during the degradation products layer formation leading to different precipitation process on the surface that can generate a less protective degradation products layer with a composition that provide different buffering capacity.

v) Moreover, finally, but no less critical, the buffer activity provided by the addition of HEPES has been reported to actively alter the process of magnesium degradation under physiological conditions [118,226,227]. The addition of HEPES actively suppresses the local alkalinisation process from the beginning of the degradation process, promoting a faster magnesium degradation. The increase of the ionic strength by the HEPES addition [228,229] decrease the ionic activities of the electrolytes inhibiting or delaying the phosphates and carbonates formation and therefore limiting the protective degradation formation [230]. A possible reactivity with $Mg(OH)_2$ decreasing the effectiveness of the protection of this compound on the surface, and the possibility of an Mg^{2+}-HEPES complexation at the high local Mg^{2+} concentrations [107] might also be responsible for an enhancing of the degradation rate and end to a higher pH environment at the interface. Therefore, the additional fast absorption of the alkalinisation process in the surface environment and the destabilisation of the degradation products layer will promote higher degradation rates that might be reflected in a higher interface pH.

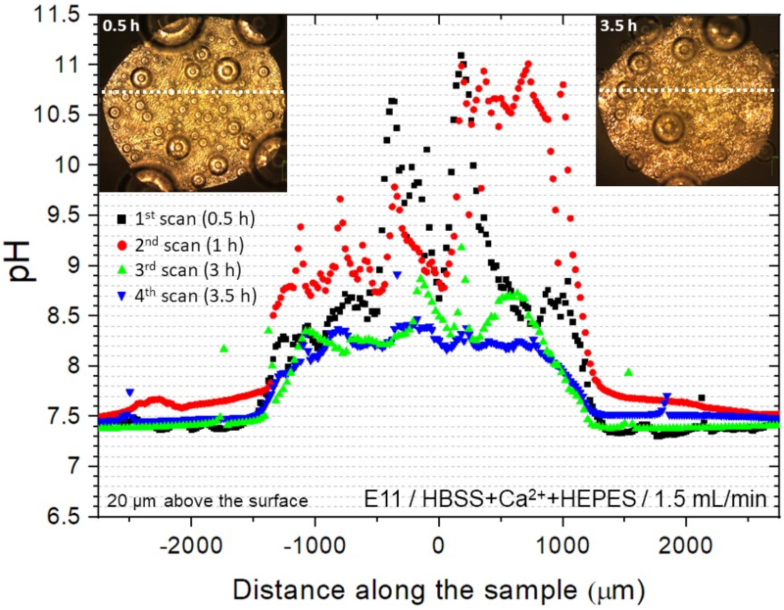

Figure 32: Influence on the in situ local interface pH developed on the E11 sample under immersion in Hank´s balanced salt solution with the addition of 2.5 mM of $CaCl_2·2H_2O$ and 75.1 mM of HEPES as a buffering system (solution VIII). The figure presents four consecutive parallel SIET scans performed under dynamic conditions (1.5 mL/min) at 20 µm above the surface within the first 3.5 hours of immersion.

To evaluate the influence of HEPES on the interface pH by the SIET set-up used in the present work, SIET parallel scans were performed on the same E11 sample under immersion in HBSS with the addition of $CaCl_2·2H_2O$ and the same flow rate previously applied (1.5 mL/min) but with the addition of HEPES (*solution VIII*). The results, shown in *Figure 32*, reveal that HEPES generate slightly lower bulk pH values (around pH 7.5) in contrast with the pH close to 8 presented in *Figure 25*.

On the other hand, the addition of HEPES shows a dynamic effect on the interface pH over the immersion time, that does not show up in its absence. Initially, until 1 hour of immersion, the interface pH shows values between 8.8 and 11.0, with an irregular surface activity revealed by high hydrogen evolution. After 1 hour of immersion, the interface pH becomes progressively lower and more regular along the surface until reach homogeneous values all over the surface around pH 8.3 after 3.5 hours of immersion, that are in agreement with the values presented in *Figure 25*.

Therefore the addition of HEPES seems to partially inhibit the precipitation process revealed in *Figure 24* by DVIT that promote the low interface pH in the presence of Ca^{2+} cations. Under dynamic conditions where the solution concentrations exposed to the sample are constant, longer immersion times allows a slower building up of the protective degradation products layer during the immersion time. In contrast, under static conditions, a limited amount of relevant ions (e.g., Ca^{2+}, HPO_4^{2-}) that can build up the protective degradation products layer, and the constant alkalinisation process that might consume part of the HEPES buffer capacity, promotes a higher interface pH. Therefore, the presence of HEPES distorts precipitation mechanisms that are expected to happen under physiological conditions.

4.3 Influence of Ca^{2+} cations on the degradation products layer and degradation rate

Previous results pointed to the critical influence of the presence of the Ca^{2+} cations in the degradation solution modifying the interface pH environment significantly. Therefore, the characterisation of the degradation products layer composition under those conditions is necessary to describe an essential part of the degradation mechanism under simulated physiological conditions.

4.3.1 Microstructural considerations and degradation products layer

The microstructure of the E11 alloy with nobler (Gd, Nd-rich secondary and segregated areas) and less noble areas (α-Mg) is ideally suitable to observe changes in the degradation microstructure on the microscale, that cannot be readily observable for a refined, fully solubilised alloying or for pure Mg microstructures. According to that, the optical images included in *Figure 33* revealed the differences in the degraded microstructure of E11 sample after the degradation process which took place during the *in situ* SIET measurements under HBSS in *Figure 22(a)* and under HBSS with the addition of $CaCl_2 \cdot 2H_2O$ in *Figure 23(b)*.

Under dynamic degradation in HBSS (*solution I*), the E11 surface (*Figure 33a*) revealed a degradation morphology defined by two different areas. According to the microstructure analysis exposed in *section 4.1* and the SEM/EDX analysis presented in *Figure 34*, the heterogeneous morphology shows an apparent not degraded and well-defined cathodic areas (Gd, Nd-rich intermetallics / Gd, Nd-segregated areas) and highly degraded dark areas that revealed an anodic behaviour (primary α-Mg dendrites) areas. The addition of $CaCl_2 \cdot 2H_2O$ to the HBSS composition (*Figure 33b*) led to fewer differences between the degradation of the cathodic and anodic features of the E11 microstructure. Those changes were only visible under polarised light due to the differences in the reflected light between the flat metallic surface and the precipitates on the surface. Under this polarised light, the primary α-Mg dendrites showed a slight degradation process and were covered with a precipitate that appears in green tones (*Figure 33b)*. On the other side, the presence of Ca^{2+} cations led to the promotion of a filiform degradation process, marked with a blue arrow in *Figure 33b.* This filiform degradation morphology was observed for all the alloying systems, as presented later in *Figure 36* for the Mg-2Ag system.

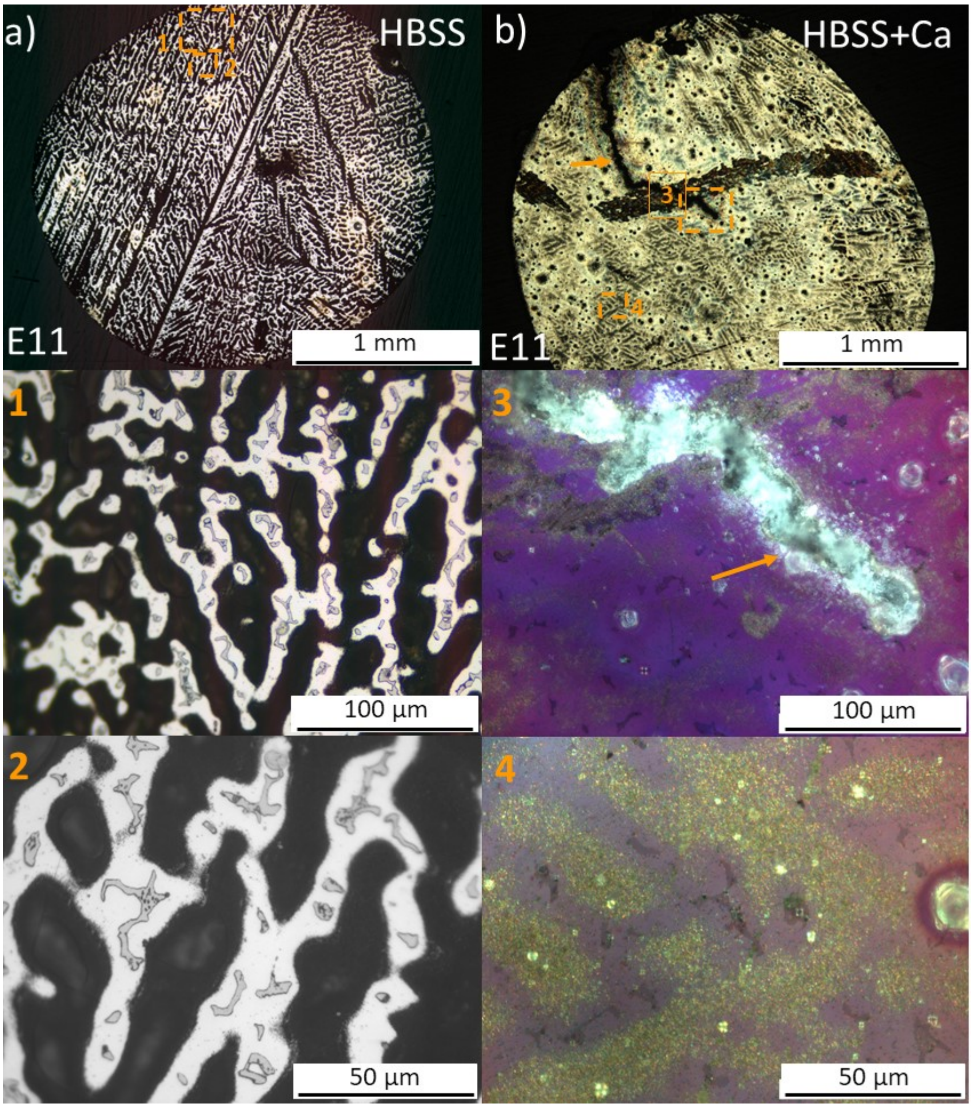

Figure 33: Changes in the degradation morphology revealed on the E11 surface as a result of the dynamic immersion (1.5 mL/min) in a) Hank´s balanced salt solution (HBSS, solution I) and b) Hank´s balanced salt solution with the addition of 2.5 mM of $CaCl_2 \cdot 2H_2O$ (solution III). Subsequent images (1 - 4) show the magnification of the highlighted areas in images a) and b).

To investigate in detail the degradation products layer morphology and composition, BSE-SEM/EDX analysis was performed on the degradation product layers generated on an E11 sample after 3 hours of dynamic immersion in HBSS and HBSS with the addition of Ca^{2+} cations (see *Figure 34*). The degradation of the E11 in HBSS *(Figure 34a-c*) showed the cracked morphology of the degradation products layer generated on the α-Mg dendrites due to the drying process after immersion, and the apparently no degradation process on the Gd, Nd-rich areas involving secondary phases and surrounding segregated zones. The composition of the degraded α-Mg areas shown in the *point 1* and *3* in (see *Table 11*), revealed an enrichment on Gd, O, and P of the degradation products layer, with respect to the α-Mg composition presented in the *point 2* of *Table 10*. Besides the apparent non-degradation of the areas with a more cathodic behaviour, the EDX analysis performed on *point 2 (see Table*

11) revealed an increased composition in O and P with a significant accumulation of Gd, compared to the relative composition presented in *point 4* (*Table 10*). This analysis point to a possible slight degradation/dealloying process of the anodic element content (e.g. Mg) and the accumulation of cathodic elements (e.g. Gd) as was presented for the intermetallic phase in the Mg-Zn-Ca system by *Cihova et al.* [231].

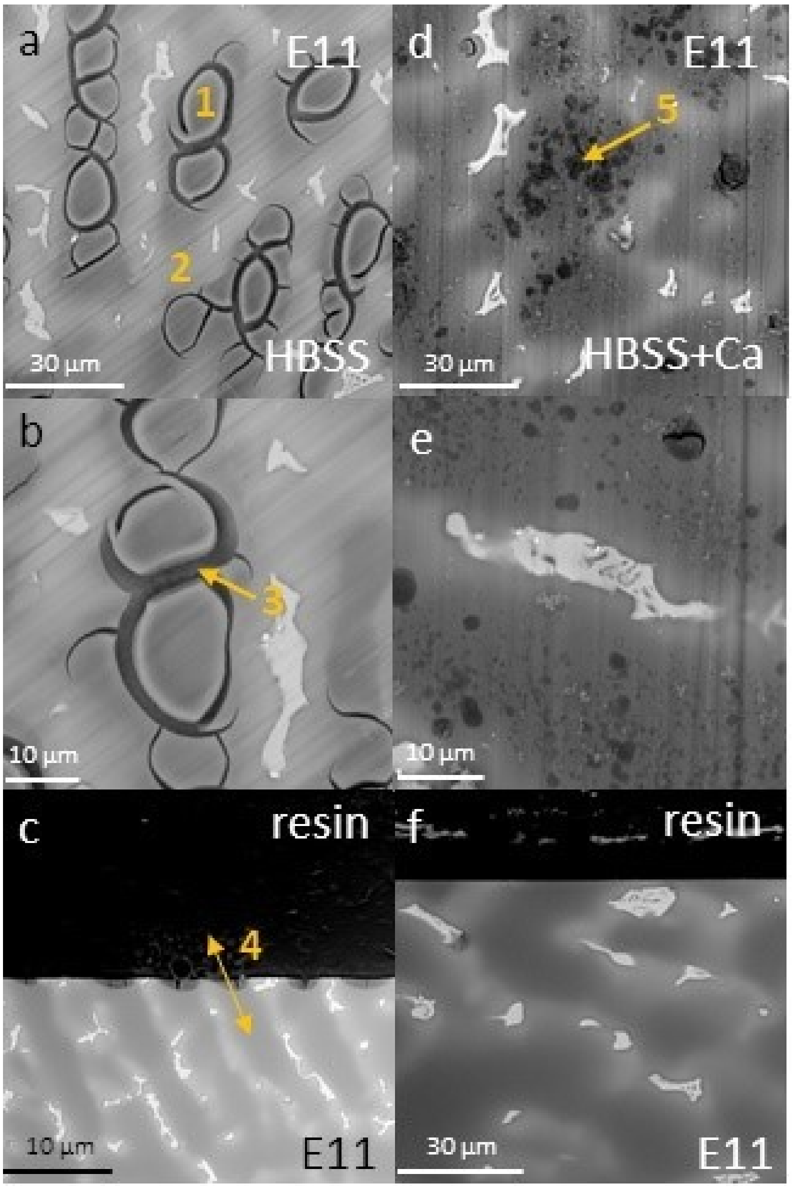

Figure 34: Change in the degradation morphology revealed by backscattered scanning microscopy (BSE) on the E11 alloy as a result of three hours of dynamic immersion (1.5 mL/min) in (a – d) Hank´s balanced salt solution (HBSS, solution I) and in (e – h) Hank´s balanced salt solution (HBSS) with the addition of 2.5 mM of $CaCl_2 \cdot 2H_2O$ (solution III). The areas highlighted in orange were analysed by energy dispersive x-ray spectroscopy (EDX) and the relative chemical composition is detailed in Figure 35 and Table 11.

The results of the EDX analysis *4* are shown in *Figure 35*. The relative compositional profiles revealed the enrichment in Gd, P, and O of the degradation products layer with regards to the α-Mg matrix composition again.

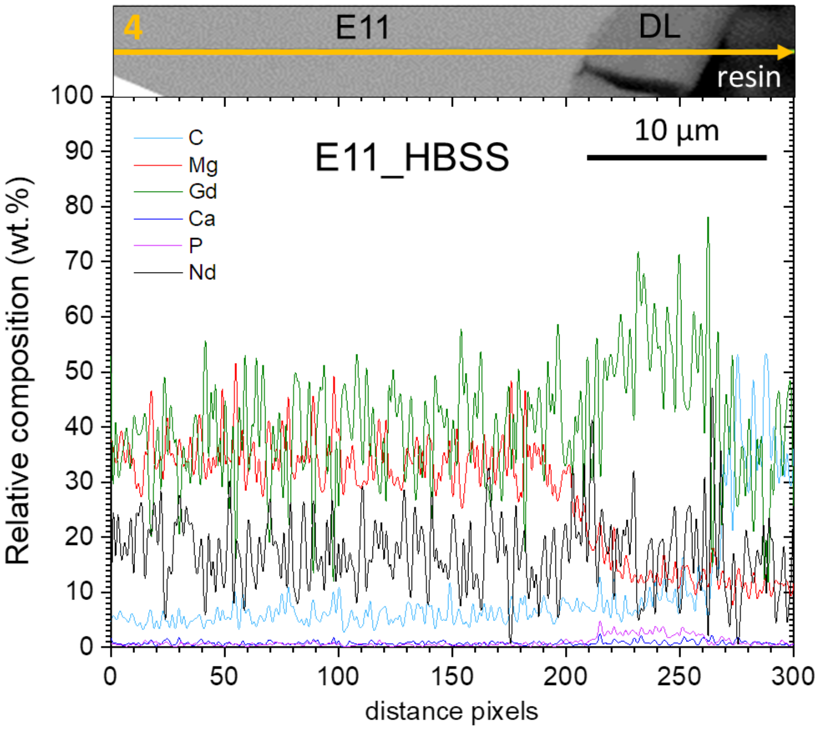

Figure 35: Chemical analysis performed by energy-dispersive x-ray spectroscopy (EDX) on the cross-section (4) presented in Figure 35 (c) of the E11 sample after 3 hours of immersion in Hank´s balanced salt solution (HBSS, solution I)

With the presence of Ca^{2+} cations in the HBSS composition (see *Figure 34d-f*), the primary α-Mg dendrites showed a lower degradation process. The analysis of the degradation products layer (*analysis 5*, *Table 11*) revealed an enrichment on Gd and O but and Ca content respective to the alloy composition. The relative proportion of P precipitated was decreased concerning the degraded α-Mg matrix in HBSS. Moreover, the degradation products layer formed after 3 hours of immersion in the presence of Ca^{2+} cations was not thick enough to be able to investigate the cross-section by conventional BSEM or by EDX.

Table 11: Relative chemical analysis in wt.% by energy-dispersive x-ray spectroscopy (EDX), of the scanned points indicated in Figure 34.

	Mg	**Gd**	**Nd**	**Ca**	**P**	**O**	**Na**	**C**	**Cl**	**Si**
1	42.3	15.1	0.4	0.2	6.1	29.8	-	6.0	-	-
2	70.6	20	-	0.2	1.1	7.0	1.0	0	0.1	-
3	63.9	10.1	-	0.2	2.0	17.0	1.2	5.5	0	-
5	66.5	10.9	-	1.0	1.6	15.5	0.7	-	1.4	1.4

The inspection of the Mg-2Ag surface after 3 hours of immersion in HBSS (*solution I*) and HBSS with the addition of $CaCl_2{\cdot}2H_2O$ (*solution III*) under dynamic conditions, is shown in *Figure 36*. The surface morphology was optically identified as a homogeneous dark surface under the immersion in HBSS and a brighter surface with dark filiform degraded regions in the case of the immersion in HBSS with the addition of $CaCl_2{\cdot}2H_2O$ (*solution III*). This homogeneity of the degraded surface can be easily associated with the homogeneous microstructure exposed in *Figure 20*, in which no secondary phases were present in contrast to the E11 system.

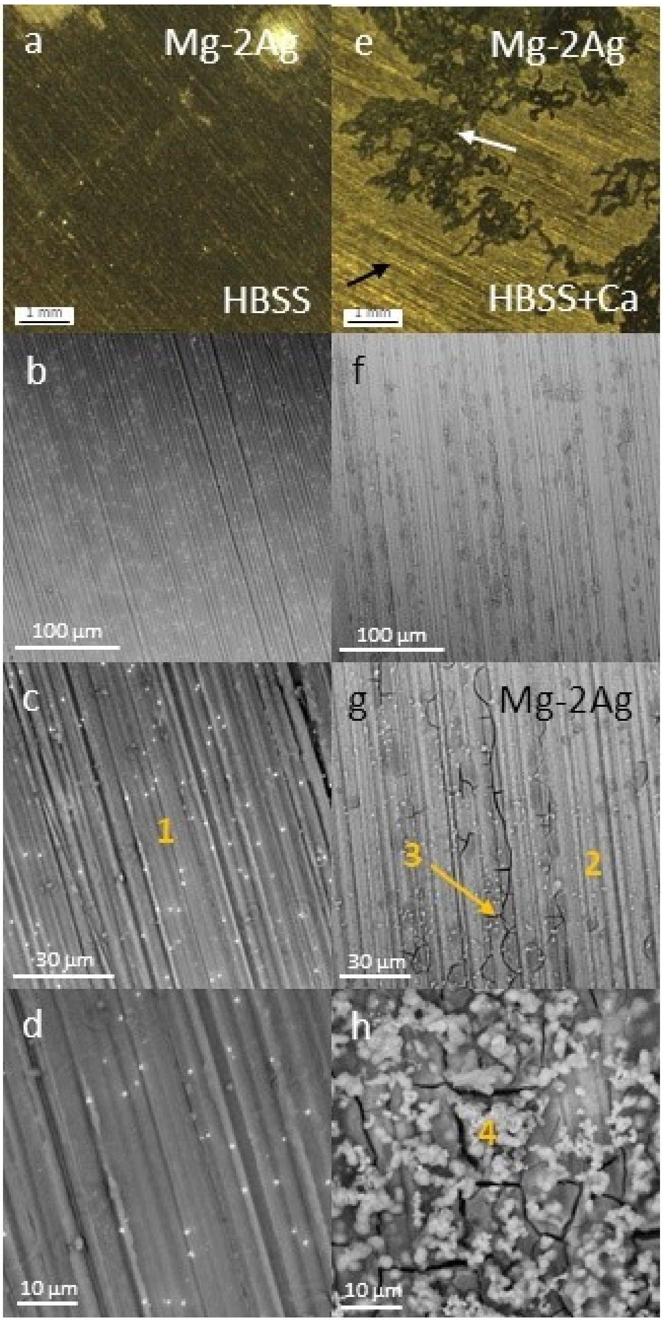

Figure 36: Change in the degradation morphology revealed by backscattered scanning microscopy (BSE) on the Mg-2Ag alloy as a result of three hours of dynamic immersion (1.5 mL/min) in (a – d) Hank´s balanced salt solution (HBSS, solution I) and in (e – h) Hank´s balanced salt solution (HBSS) with the addition of 2.5 mM of $CaCl_2{\cdot}2H_2O$ (solution III). The areas highlighted in orange were analysed by energy-dispersive x-ray spectroscopy (EDX), and the relative chemical composition is detailed in Table 12.

The details revealed by SEM showed the remaining marks from the surface preparation by the grinding process. The EDX analysis performed over the surface (*point 1* in *Table 12*) revealed precipitation of O, P, and C. Moreover, a concentration of Ag was also denoted in the degradation products layer concerning the composition given for this alloy (see *Table 7*), possibly related with the 0.5 – 1.5 µm star-like bright precipitates disseminated all over the surface.

After immersion in HBSS with the addition of $CaCl_2 \cdot 2H_2O$ ions, the bright surface shows under the BSEM two areas with different degradation morphology on which globular precipitates were present in different density. Areas with a general degradation process pointed with a black arrow in *Figure 36(e)*, can be described as areas with some zones aligned in parallel to the cutting marks that present a higher degradation process (see *Figure 36f, g*). Those areas present an increased relative composition in O, Ca, P and Ag, as was revealed by a comparison between the analysed points 7 and 8 in *Table 12*. The second degradation feature corresponds to areas undergone an aggressive filiform process and are pointed by a white arrow in *Figure 36(e)*. Those areas, as denoted in previous dynamic immersion tests of the E11 surface, present a rough morphology characterised by a high density of the globular precipitates and a significant increase of Ca, P, O, C relative composition and for this alloy also in Ag, in contrast with other areas of the sample, as shows the analysis of *point 4* (see *Table 12*).

Table 12: Relative chemical analysis in wt.% by energy-dispersive x-ray spectroscopy (EDX), of the scanned points indicated in Figure 36.

	Mg	**Ag**	**Gd**	**Nd**	**Ca**	**P**	**O**	**Na**	**C**	**Cl**	**Si**	**K**
1	57.0	3.3	-	-	-	1.1	27.8	1.2	9.5	0.1	0.2	-
2	64.2	1.5	-	-	1.3	1.3	18.9	1.0	11.3	0.3	0.1	-
3	34.6	3.8	-	-	4.3	3.1	33.9	0.8	17.9	0.9	0.4	0.2
4	14.9	0.5	-	-	9.9	5.2	43.8	0.9	23.4	0.4	0.7	0.1

In order to quantify in a more extensive way, the differences in the composition of the degradation products layer, a relative quantification and elemental distribution mapping were performed by µ-XRF, on the whole surface of the E11 (see *Figure 37*) and Mg-2Ag (see *Figure 38*) samples after 3 hours of dynamic immersion. The results presented in *Figure 37* (up) under immersion in HBSS shows the previously denoted increase in the concentration of Gd on the degradation products layer. On the other hand, the P relative concentration, besides a not perfectly homogeneous distribution, possibly points to a phosphate-based degradation products layer. This inhomogeneity in the P distribution might be associated with differences in the degradation degree in the sample since the areas with a higher concentration in P can be correlated with the visible more degraded upper part of the sample in the optical image. The homogeneity Ca distribution corresponds to the Ca included in the alloy composition and its integration in the degradation products layer. In the presence of Ca^{2+} cations *Figure 37* (down), the homogeneity of a lower degraded appearance surface is interrupted by the filiform degraded areas. The pattern showed by the elemental distribution of Ca, P and Mg show the co-precipitation process with a Ca/P ratio of 0.8.

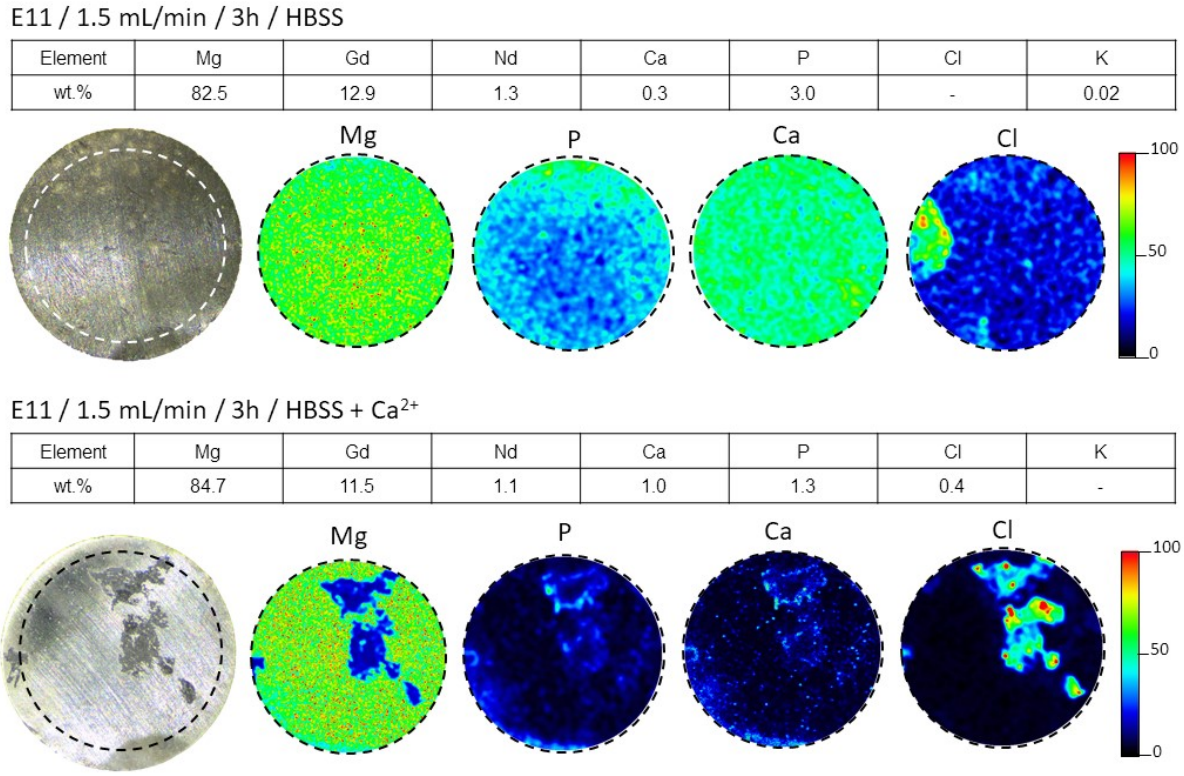

E11 / 1.5 mL/min / 3h / HBSS

Element	Mg	Gd	Nd	Ca	P	Cl	K
wt.%	82.5	12.9	1.3	0.3	3.0	-	0.02

E11 / 1.5 mL/min / 3h / HBSS + Ca^{2+}

Element	Mg	Gd	Nd	Ca	P	Cl	K
wt.%	84.7	11.5	1.1	1.0	1.3	0.4	-

Figure 37: Chemical element distribution and elemental relative quantification in wt.% of the degradation products layer generated on an E11 alloy after 3 hours of dynamic immersion (1.5 mL/min) in (up) Hank´s balanced salt solution (HBSS, solution I) and (down) HBSS with the addition of 2.5 mM of $CaCl_2{\cdot}2H_2O$ (solution III), performed by µ-XRF.

The µ-XRF analysis performed on the Mg-2Ag degraded surface showed the same precipitation characteristics. Under the degradation in HBSS, the degradation products layer is characterized by correlation of the areas with a high relative concentration of P and the low Mg concentration areas. Therefore, pointing as in the case of the E11 alloy to degradation products layer based on P. The presence of Ca is associated with the content coming from the primary magnesium production [232]. In the case of the degradation under HBSS with the presence of Ca^{2+} cations, the areas with a higher degree of degradation identified with a lower concentration of Mg can be correlated in this case with areas in which there is a higher concentration of P and Ca. In the case of this alloy, the precipitation process shows a Ca/P ratio of 0.6.

Mg-2Ag / 1.5 mL/min / 3h / HBSS

Element	Mg	Ag	Ca	P	Cl	Na
wt.%	93.2	1.3	0.03	2.2	-	0.3

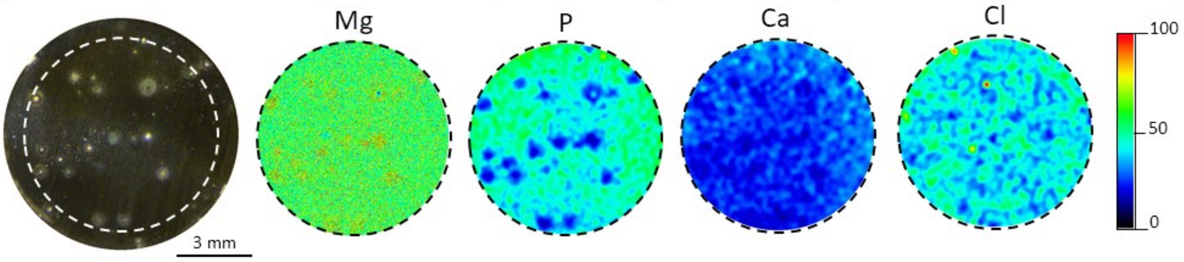

Mg-2Ag / 1.5 mL/min / 3h / HBSS + Ca^{2+}

Element	Mg	Ag	Ca	P	Cl	Na
wt.%	94.6	1.3	1.3	2.2	0.3	0.2

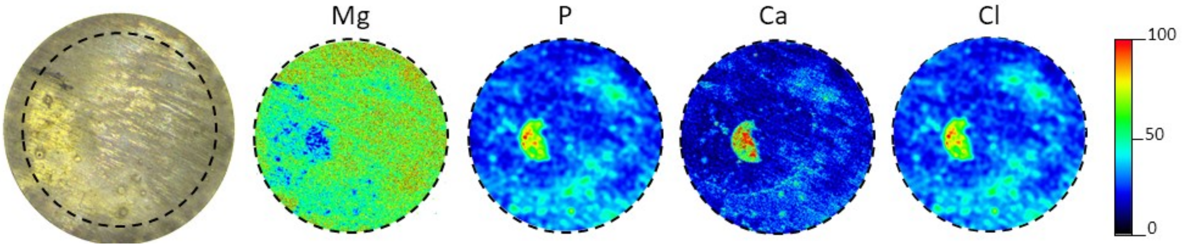

Figure 38: Chemical element distribution and elemental relative quantification in wt.% of the degradation products layer generated on an Mg-2Ag alloy after 3 hours of dynamic immersion (1.5 mL/min) in (up) Hank´s balanced salt solution (HBSS, solution I) and (down) HBSS with the addition of 2.5 mM of $CaCl_2 \cdot 2H_2O$ (solution III), performed by µ-XRF.

According to the previous characterisation results, different precipitation phenomena involving precipitation of P or Ca-P "co-precipitation" have been identified for the degradation under HBSS (*solution I*) and HBSS with the addition of $CaCl_2 \cdot 2H_2O$ (*solution III*) respectively. Since the precipitation phenomena were found to be similar for the degradation of two entirely different systems like the E11 and the Mg-2Ag, this process can be assumed for the rest of the alloys except for the accumulation of the respective alloying elements.

In order to reveal the composition and structure of the degradation products responsible of the different precipitation mechanism in the presence or absence of Ca^{2+} cations the analysis of the degradation products layer by glancing angle X-ray diffraction analysis were performed at $\alpha = 1°$ on the degradation products layer generated on the HP-Mg, Mg-1.2Ca, E11 and Mg-2Ag surfaces. The degradation products layer analysed was generated on the samples after 3 hours of immersion under dynamic conditions (1.5 mL/min) in HBSS (*solution I*) and HBSS with the addition of $CaCl_2 \cdot 2H_2O$ (*solution III*). The glancing angle x-ray diffraction patterns presented in *Figure 39* reveals differences in the crystalline compounds precipitated on the surface between the different alloys. However, no differences in the crystalline products were found by comparing the same alloy system in the presence or absence of Ca^{2+} cations in the HBSS composition.

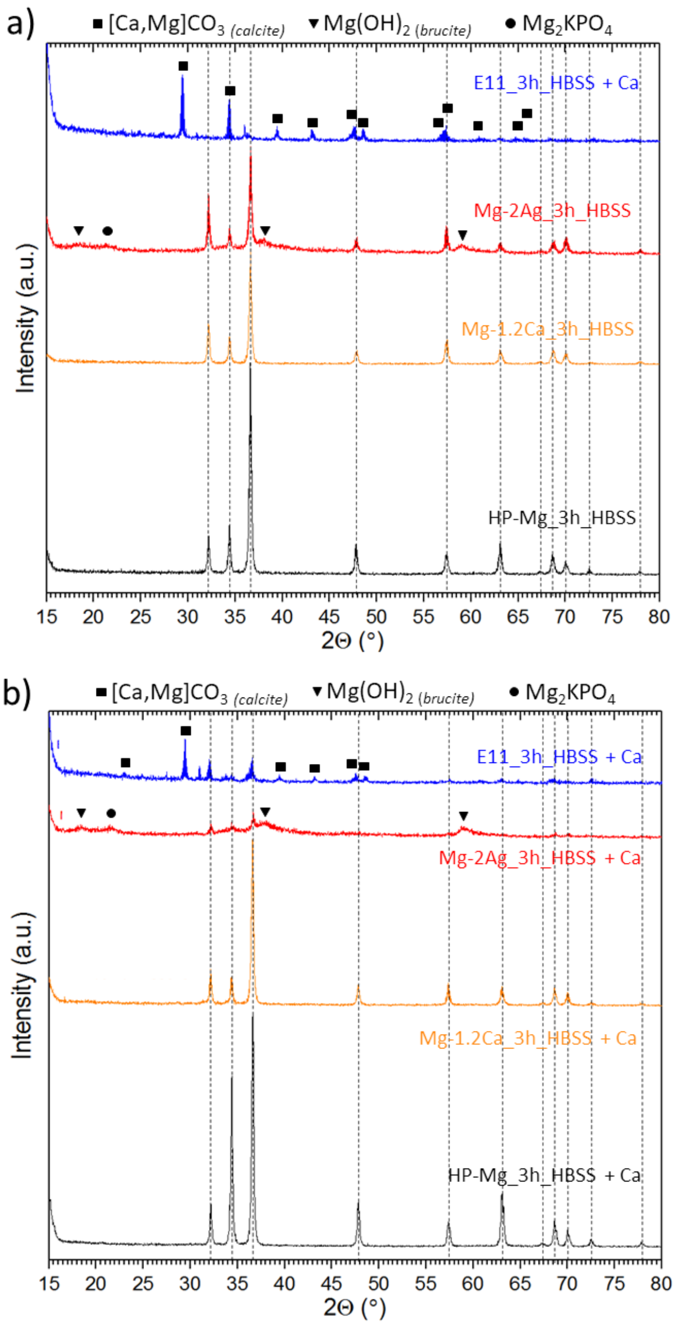

Figure 39: Grazing angle x-ray diffraction (GAXRD) patterns performed at 1° of incidence on the degraded surfaces of the HP-Mg, Mg-2Ag, Mg-1.2 Ca and E11 samples, after 3 hours of dynamic immersion (1.5 mL/min) in a) Hank´s balanced salt solution (HBSS, solution I), and b) HBSS with the addition of 2.5 mM of $CaCl_2 \cdot 2H_2O$ (solution III). The segmented lines correspond to the diffraction lines of pure Mg, that were the only ones identified on the HP-Mg and the Mg-1.2Ca samples.

The diffraction patterns generated by the HP-Mg and Mg-1.2Ca surfaces under HBSS or HBSS with the addition of $CaCl_2 \cdot 2H_2O$ did not confirm the presence of any crystalline compound apart from the diffraction peaks that correspond to the crystalline Mg structure. The degradation products layer generated on E11 under both corrosive solution compositions (HBSS and HBSS with Ca^{2+} cations) shows a diffraction pattern matching a *calcite* structure, possibly with calcium (Ca) atoms partially substituted by magnesium [Ca, Mg]CO_3. Moreover, the degradation products layer generated on Mg-2Ag shows broad peaks pointing to the presence of $Mg(OH)_2$ with *brucite* structure, and a peak about θ = 21.4° that possibly can be assigned to a magnesium phosphate with stoichiometry Mg_2KPO_4. It is worth mentioning that the relative intensity between the magnesium diffraction peaks and the ones corresponding the precipitated crystalline compounds ($Mg(OH)_2$, [Ca, Mg]CO_3 and Mg_2KPO_4) is not the same under both corrosive environments (HBSS and HBSS with Ca^{2+} cations), possibly due to differences in the degradation products layer thickness.

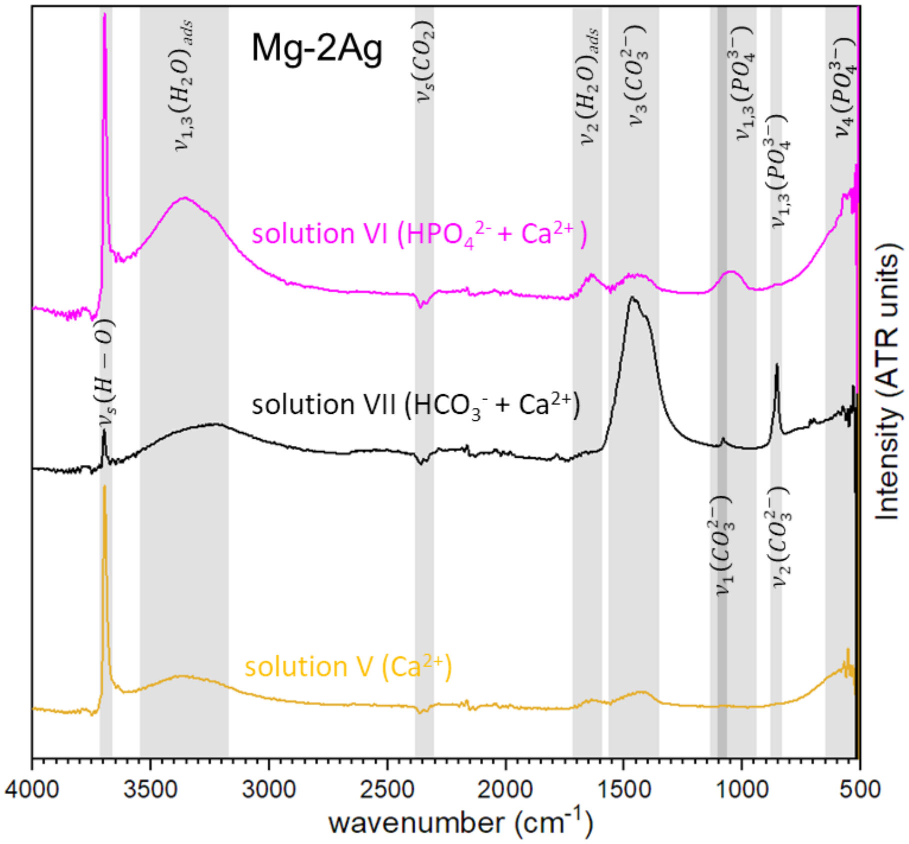

Figure 40: FTIR-ATR analysis of the degradation product layer (DPL) of Mg-2Ag generated after 3 hours of dynamic immersion (1.5 mL/min) in different degradation solutions with different composition in Ca^{2+}, HCO_3^- and HPO_4^{2-} according the labels next to each spectra and which full composition is presented in Table 9. The figure presents the FTIR-ATR spectra under immersion in solution VI (Pink spectra: NaCl, KCl, $CaCl_2 \cdot 2H_2O$, Na_2HPO_4, KH_2PO_4, glucose), under solution VII (Black spectra: NaCl, KCl, $CaCl_2 \cdot 2H_2O$, $NaHCO_3$, glucose), solution V (Yellow spectra: NaCl, KCl, $CaCl_2 \cdot 2H_2O$, glucose).

The absence of crystalline compounds in the degradation products layer found on as-cast HP-Mg and as-cast Mg-1.2Ca and the differences in the crystalline compounds found for the E11 and Mg-2Ag suggest that the precipitation process that promotes the decrease in the interface pH is generated by different compounds than the ones identified by glancing angle X-ray diffraction. As exposed in *section 1.4.2*, under BEF fluid compositions, amorphous phases like ACP can be present in the first moments of the biomineralisation process and be precursors for subsequent crystalline phases. Therefore, the analysis of the degradation products layer by FTIR-ATR can provide information about precipitation of amorphous or nanostructured phases, that might be the key to the precipitation mechanism under study.

In order to identify the contribution to the degradation products layer composition of the presence of Ca^{2+}, HCO_3^- and HPO_4^{2-}, the degradation of Mg-2Ag samples was performed under simplified degradation solutions based on the HBSS composition (*solution V, VI, and VII* in *Table 9*) under 3 hours of dynamic conditions (1.5 mL/min). Due to the presence of glucose in the HBSS composition (*solution I*), this component was added in all degradation solutions as the only organic phase present. Considering the same contribution of the glucose in the IR signal for all the degradation solutions, the presented infrared spectra will bring information about the inorganic polyatomic ions present in the degradation products layer.

The degradation under *solution V* (yellow spectra) containing Cl^-, Na^+, K^+, Ca^{2+} ions and glucose, present a very low relative intensity of the $\nu_3(CO_3^{2-})$ and $\nu_2(CO_3^{2-})$ absorption bands, compared with the $\nu(O-H)$ band at 3696 cm^{-1}. The presence of the $\nu_3(CO_3^{2-})$ and $\nu_2(CO_3^{2-})$ bands might be related to the presence of the glucose and the reaction between the CO_2 dissolved and the Ca^{2+} cations in solution. The intense and sharp band at 3696 cm^{-1} might be associated to the O-H bonds present in glucose molecules, but can also result of the contribution of the A_{2u} infrared active mode of $Mg(OH)_2$ [233,234]. The broadband between 3200 and 3500 cm^{-1} and the band at 1640 cm^{-1} can be assigned to absorption bands associated with the O-H stretching and H-O-H bending bands of hydrated phases [235]. The double band presented at 2360-2336 cm^{-1}, belongs to the difference between the atmospheric CO_2 in the background and the one adsorbed onto the sample.

The black spectra obtained under degradation in *solution VII* in the presence of Cl^-, Na^+, K^+, Ca^{2+}, and HCO_3^- ions. The significant increment in the intensity of the $\nu_3(CO_3^{2-})$ mode at 1462 cm^{-1}, as well as the presence of the low intensity $\nu_1(CO_3^{2-})$ mode at 1083 cm^{-1}, and the sharp $\nu_2(CO_3^{2-})$ band at 854 cm^{-1} point to the influence of the HCO_3^- ions in the degradation products layer. Those bands have been previously identified as characteristic bands belonging to the vibrational modes of the carbonate molecule in amorphous and anhydrous $MgCO_3$ [236]. In addition, the less relative intensity of the sharp band at 3696 cm^{-1} in comparison with the (CO_3^{2-}) corresponding bands, points to the importance of the presence of Mg and Ca carbonates on the outer part of the degradation products layer.

The pink colour spectra generated under immersion in *solution VI* present the influence of the presence of Cl^-, Na^+, K^+, Ca^{2+}, and HPO_4^{2-} ions. In contrast to the bands previously presented, broadband appears around 1033 cm^{-1} corresponding to the combination of the $\nu_3(PO_4^{3-})$ and $\nu_1(PO_4^{3-})$ modes, as described in [237–240]. The corresponding $\nu_3(CO_3^{2-})$ and $\nu_2(CO_3^{2-})$ bands appear with considerably lower relative intensity comparing with the $\nu(O-H)$ sharp band at 3696 cm^{-1}, possibly due to a small presence of glucose and perhaps to low precipitation of carbonates due to the atmospheric CO_2 dissolved in the solution in the outer part of the degradation products layer.

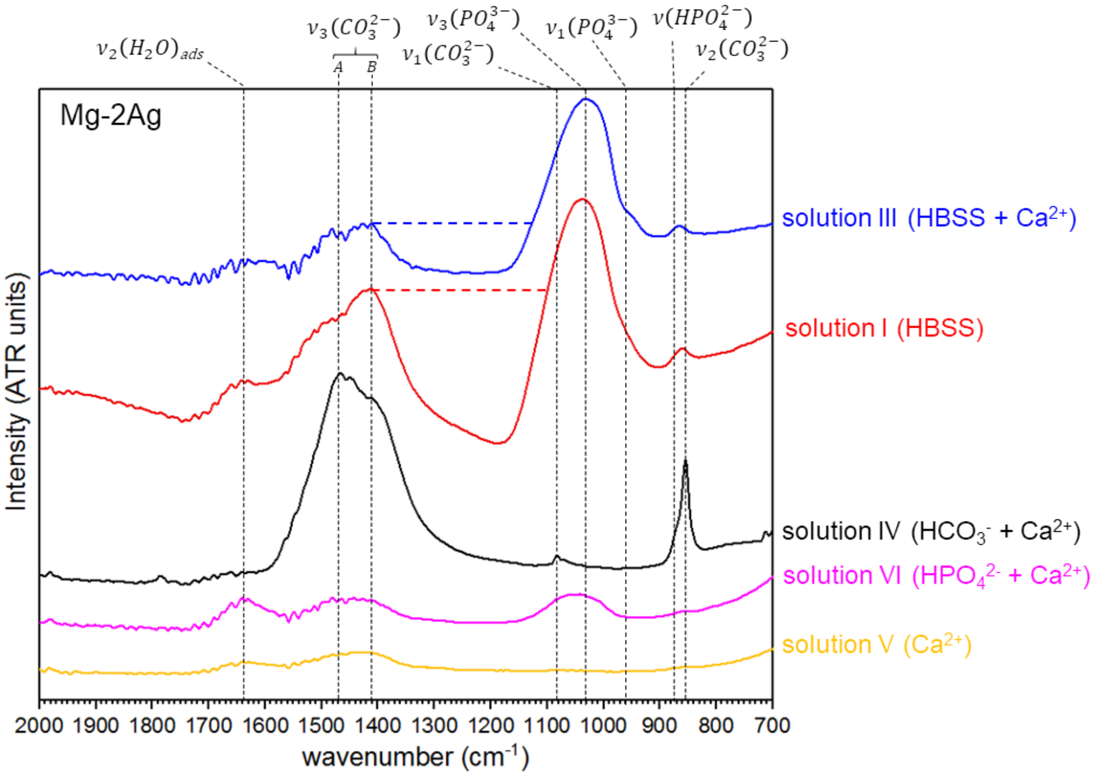

Figure 41: FTIR-ATR analysis between 2000 and 700 cm^{-1} of the degradation product layer (DPL) of Mg-2Ag generated after 3 hours of dynamic immersion (1.5 mL/min) under (red spectrum) HBSS (solution I) composition, and (blue spectrum) HBSS with the addition of 2.5 mM $CaCl_2 \cdot 2H_2O$ (solution III). The figure highlight with dashed lines the relative intensity between the $\nu_3(CO_3^{2-})_B$ and the combination of the $\nu_1(PO_4^{3-})$ and $\nu_3(PO_4^{3-})$ vibrational bands, showing the influence of the addition of $CaCl_2 \cdot 2H_2O$ to the HBSS composition on the composition of the outer part of the degradation product layer. In addition, the figure includes the spectra presented in Figure 40.

To identify the influence of the addition of $CaCl_2 \cdot 2H_2O$ to the degradation solution in the presence of HCO_3^- and HPO_4^{2-}, *Figure 41* presents a magnification of the spectra presented in *Figure 40* between 2000 and 700 cm^{-1}. By comparison of the red spectra corresponding to the degradation process under HBSS *(solution I*), and the blue spectra under HBSS with the addition of $CaCl_2 \cdot 2H_2O$ (*solution III*), an increase of the relative intensity of the $\nu_3(PO_4^{3-})$ with respect to the $\nu_3(CO_3^{2-})$ absorption bands is visible with the presence of Ca^{2+}. This point to a higher presence of phosphate-containing phases, at least in the outer part degradation products layer, due to the limited depth of this analysis technique.

To compare the effect of the presence of the Ca^{2+} cations on the phosphates-carbonates relative precipitation between two different alloying systems, the FTIR-ATR analysis presented in *Figure 42* were performed on the degradation products layer of E11 and Mg-2Ag after 3 hours of immersion in HBSS (*solution I*) and HBSS with Ca^{2+} cations (*solution III*) under dynamic conditions (1.5 mL/min).

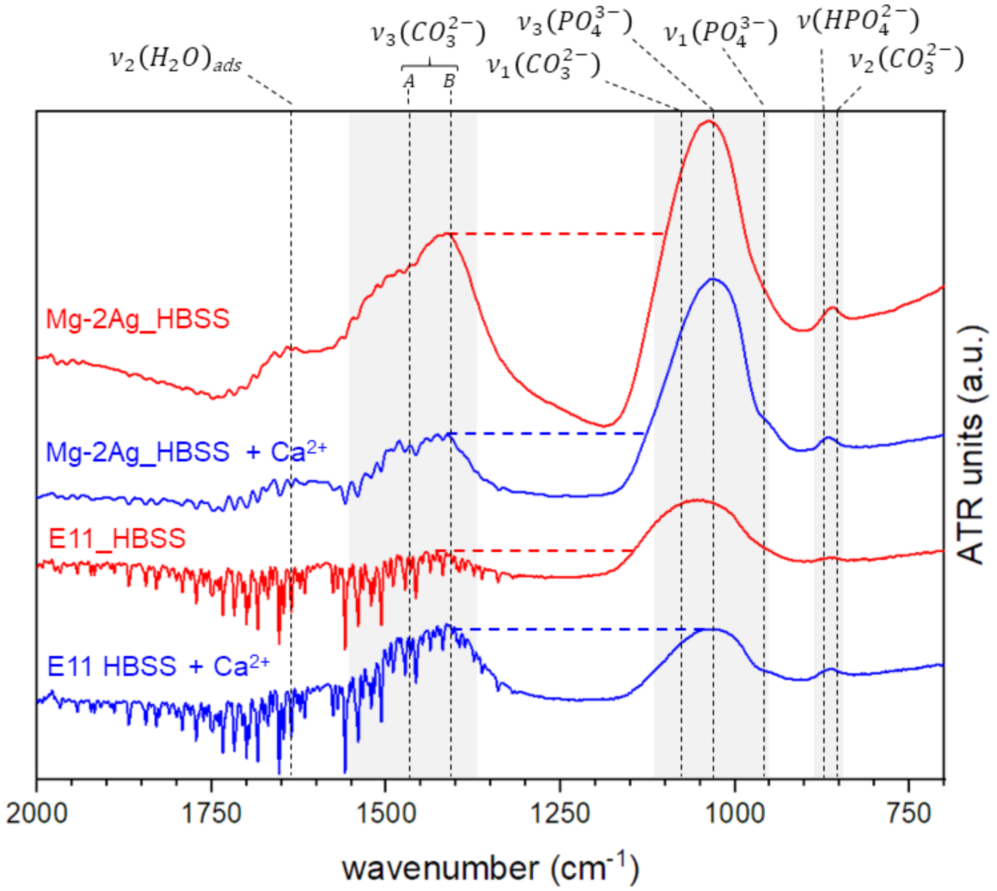

Figure 42: Compositional differences of the outer part of the degradation product layer generated on the E11 (blue) and the Mg-2Ag (red) after 3 hours of dynamic immersion (1.5 mL/min) in (solid lines) Hank´s balanced salt solution (HBSS, solution I) and (dashed lines) HBSS with the addition of 2.5 mM $CaCl_2 \cdot 2H_2O$ (solution III).

The previous higher relative intensity of the $\nu_3(PO_4^{3-})$ band with respect to the $\nu_3(CO_3^{2-})$ band showed for the Mg-2Ag alloy when Ca^{2+} cations are present, is presented in the red coloured spectra in *Figure 42.* On the contrary, the degradation products layer on the E11 surface (blue spectra), revealed the opposite situation with a higher relative intensity of the $\nu_3(CO_3^{2-})$ band with respect to the $\nu_3(PO_4^{3-})$ band in the presence of Ca^{2+} cations. The high noise level presented between 3500 and 4000 cm^{-1} and between 1750 and 1500 cm^{-1} corresponds to the signal of water vapour that comes up if the concentration of the compounds is very low and the thickness of the degradation products layer is below the penetration depth of the IR system.

According to the results presented in *Figure 42*, the degradation products layer on E11 presents a different composition that results in the same lower interface pH than for the Mg-2Ag and the rest of the alloys. To investigate this complex precipitation process, the progress of the relative intensity of between the $\nu_3(PO_4^{3-})$ and $\nu_3(CO_3^{2-})$ bands were monitored on E11 samples after 10 minutes, 1 hour, and 3 hours of immersion in HBSS (*solution I*) and HBSS with the addition of $CaCl_2 \cdot 2H_2O$ (*solution III*). After 10 minutes of immersion in HBSS (*solution I*) the degradation products layer shows the same relative intensities between the $\nu_3(PO_4^{3-})$

and $\nu_3(CO_3^{2-})$ bands. After 1 hour of immersion, the relative intenstity of the $\nu_3(PO_4^{3-})$ band showed a strong increase that remain until 3 hours of immersion. Under immersion in HBSS in presence of Ca^{2+} cations (*solution III*), from the first 10 minutes until 1 hour of immersion the $\nu_3(PO_4^{3-})$ band shows a significant higher relative intensity compared with the $\nu_3(CO_3^{2-})$ band. But after 3 hours of immersion, the relative intensities of both bands $\nu_3(PO_4^{3-})$ and $\nu_3(CO_3^{2-})$ reach the same intensity.

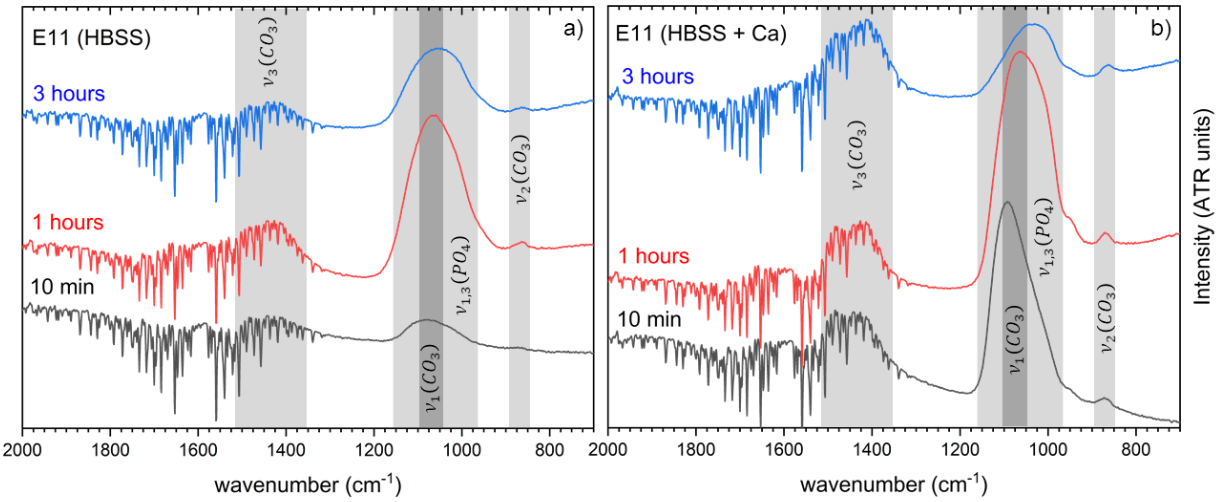

Figure 43: FTIR-ATR analysis of the degradation product layer (DPL) generated at different immersion times (10 minutes, 1 hour and 3 hours) on the E11 surface generated after 3 hours of dynamic immersion (1.5 mL/min) in a) Hank´s balanced salt solution (HBSS, solution I) and b) HBSS with the addition of 2.5 mM $CaCl_2 \cdot 2H_2O$ (solution III).

According to the results described above, the immersion of E11 in HBSS (*solution I*) generates an initial precipitation process based on carbonates and phosphates, then follows a phosphates dominant precipitation process that continues at least until 3 hours of immersion. The immersion in HBSS with the addition of $CaCl_2 \cdot 2H_2O$ (*solution III*), generates a fast-initial phosphates dominant precipitation that lasts at least between the first and the third hour of immersion and leads to later carbonates dominant precipitation process. This phosphate precipitation phenomena in the presence of Ca^{2+} cations can be correlated with the precipitation responsible for the low interface pH identified by SIET, and that is developed from the beginning of the immersion as revealed by the DVIT investigations. According to what was exposed in *section 1.3.2,* those precipitation processes depend on the concentration and pH developed on the surface environment. Therefore, magnesium-based materials with different degradation kinetics (different degradation rates) might promote the changes in the precipitation process exposed in *Figure 43* in different times of the immersion. This may be the reason that justifies the differences shown in *Figure 42* between E11 and Mg-2Ag (T4) for the $\nu_3(PO_4^{3-})$ and $\nu_3(CO_3^{2-})$ bands relative intensity.

4.3.2 Degradation rate by mass loss and Hydrogen evolution

The previous results showed a strong difference in the interface pH environment when Ca^{2+} cations are present in the degradation media. Moreover, *section 1.3.2* exposed the influence of the Ca^{2+} cations on the degradation rate of magnesium-based materials. To evaluate the magnitude of the effect of the addition of the Ca^{2+} cation on the degradation rate, hydrogen evolution (*Figure 44*) and mass loss (*Figure 45*) were measured for HP-Mg, Mg-2Ag, Mg-1.2Ca and E11. The critical effect of the presence of the Ca^{2+} cations in the simulated body fluids composition on the interface pH and the differences in the degradation products layer composition is the reason why the degradation rate was evaluated for the Mg-based materials under immersion in HBSS (*solution I*) and HBSS with the addition of $CaCl_2{\cdot}2H_2O$ (*solution III*).

The presence of Ca^{2+} cations in the HBSS composition (*solution III*) shows a considerable decrease in the accumulated hydrogen over the whole immersion time for all the systems (see *Figure 44*, blue values). The decrease in the hydrogen developed in the presence of Ca^{2+} cations was revealed to be about 1.2 times for the E11 system, 2 times for the Mg-2Ag and Mg-1.2Ca systems, and 1.4 times for the HP-Mg. On the other side, the presence of Ca^{2+} cations in the corrosive solution was found to influence the error presented by the standard deviation for the hydrogen evolution levels. The significantly higher degradation rate generated by the as-cast microstructure of the E11 in comparison with the rest of the materials is justified by the inhomogeneity of its microstructure. The nobler composition of the secondary phases and segregated zones described in *section 4.1* due to the higher concentration of Gd and Nd (Nd E_{she} = -2.30 V, Gd E_{she} = -2.28 V) generate large and well defined cathodic areas in the range of the microscopic scale. This promotes the fast dissolution of the αMg-matrix with anodic behaviour, as described in *section 4.3.1*. Also, the higher content in Cu and Ni, shown in *Table 7*, contribute to the high degradation rate of the E11 system. The inhomogeneity in the microstructure and possibly in the impurity distribution is reflected in the significant error of the hydrogen evolution values, that are masked in the graph by the much larger scale in comparison with the rest of the alloys. The significant increment of that error when the system was degraded in HBSS with the addition of $CaCl_2{\cdot}2H_2O$ could be justified by the high susceptibility to the aggressive filiform degradation process when the passivation promoted by the Ca^{2+} cations meet such inhomogeneous microstructure.

The homogeneous structure of the Mg-2Ag obtained by the extrusion and the heat treatment dissolving all the silver content into the α-Mg matrix (see *Figure 20*), mitigates the strong capacity of the silver to accelerate the degradation process due to its noble reduction potential (Ag E_{she} = +0.80 V). Despite this, the solubilised silver in the αMg-matrix accelerates the degradation rate due to a homogeneous galvanic corrosion process generated in the nano-scale or simply modifying the thermodynamic tendency to dissolve the alloy. Therefore, this microstructure and the content of silver justify a higher hydrogen evolution than for the Mg-1.2Ca and HP-Mg alloys, but less production than for the E11 alloy. Moreover, the homogeneous microstructure and composition of this system seem to reduce the sensitivity of the local filiform degradation process, since the error of the hydrogen evolution values is lower under degradation in HBSS with the addition of $CaCl_2 \cdot 2H_2O$ (*solution III*) than in HBSS (*solution I*).

Despite the non-homogeneous microstructure of the Mg-1.2Ca system, a low degradation rate comparable to the HP-Mg system can be justified by the less harmful addition of calcium as (E_{SHE} = -2.80 V), in contrast to the previously described alloying systems. The calcium released in the environment coming from the alloy dissolution might have an effect decreasing the degradation rate, as in the same way the SIET local pH measurements shown in *section 4.2.2* revealed a slightly lower interface pH during Mg-1.2Ca degradation in contrast to the rest of the alloys. This released calcium might be not enough to switch the environment to a lower pH, like the one generated by the 2.5 mM $CaCl_2 \cdot 2H_2O$ addition in the degradation solution, but possibly enough to provide extra protection of the surface. Therefore, it contributes to a lower degradation rate. This low Ca^{2+} ionic environment might be the reason why the hydrogen evolution values under immersion in HBSS (*solution I*) show significant lower errors in comparison with the rest of the systems, including as cast HP-Mg. The increase of this error under degradation in HBSS with the addition of $CaCl_2 \cdot 2H_2O$ is justified, as for the E11 system, by the inhomogeneity of the microstructure and the impurity levels in a passivated surface.

The absence of alloying elements and the higher purity of the as-cast HP-Mg system at least in Cu and Ni (see *Table 7*), justify the lowest hydrogen evolution of all systems analysed. The lower impurity levels and the absence of secondary phases, also presented for the Mg-2Ag alloy, might also lead to a lower sensitivity to the localised degradation like the filiform morphology presented previously in the presence of Ca^{2+} cations. This fact could explain the lower scattering of the hydrogen evolution values presented by the as-cast HP-Mg and the extruded (T4) Mg-2Agsystems under immersion in HBSS with the addition of $CaCl_2 \cdot 2H_2O$ (*solution III*). But in addition, this scattering is lower than when those material are tested under HBSS (*solution I*).

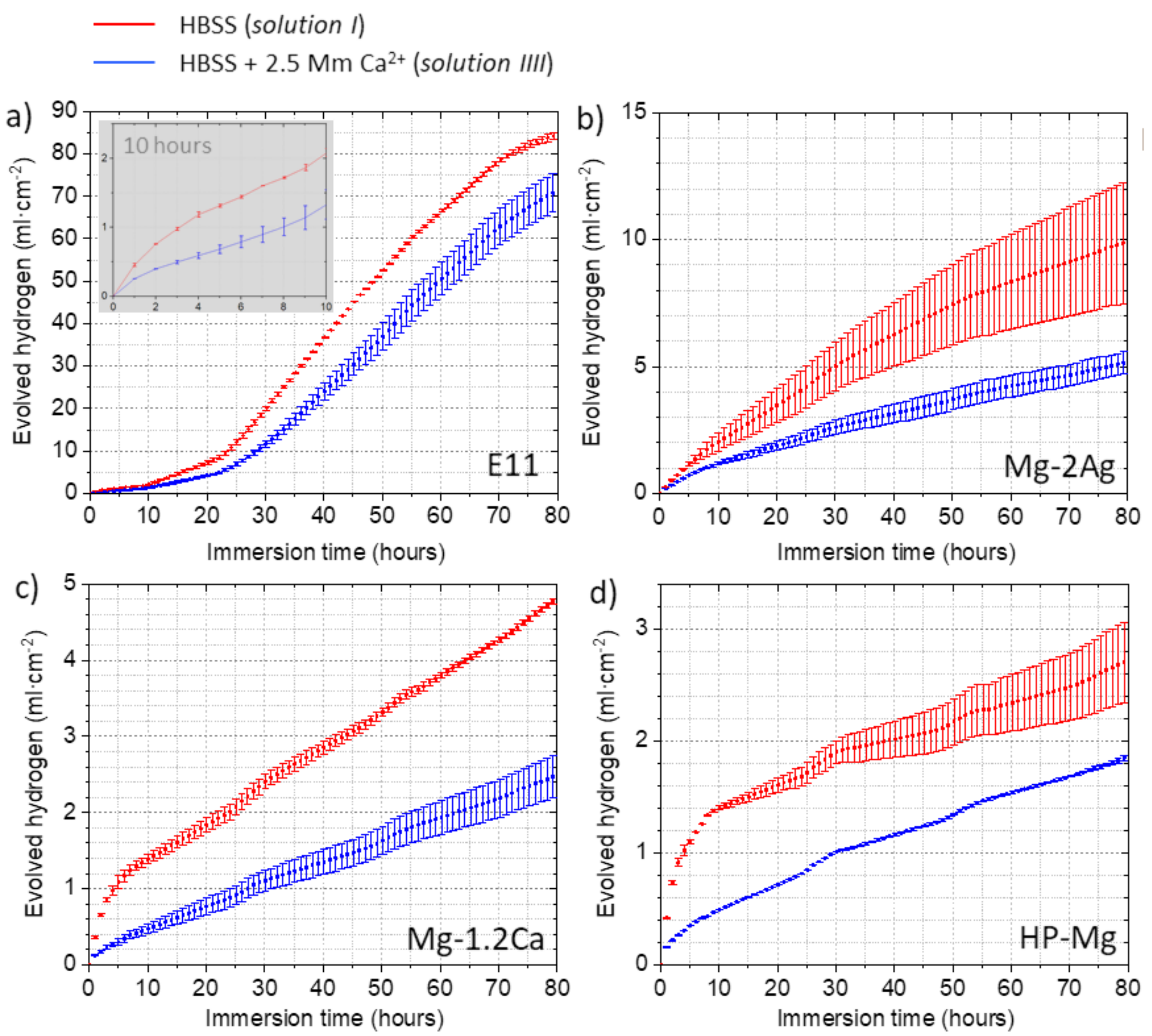

Figure 44: Comparison of the degradation kinetics by the normalised hydrogen evolution curves for the a) E11, b) Mg-2Ag, c) Mg-1.2Ca and d) HP-Mg obtained during 80 hours of stirred immersion in (red) Hank´s balanced salt solution (HBSS, solution I) and (blue) HBSS with the addition of 2.5 mM $CaCl_2 \cdot 2H_2O$ (solution III).

Due to the fact that the hydrogen evolution was collected at constant intervals of the degradation process, the degradation kinetics can be evaluated, and changes in the degradation rate can be identified by changes in the slope. Those changes were revealed to happen at the same immersion time for both the immersion in HBSS and in HBSS with the addition of $CaCl_2 \cdot 2H_2O$ in every alloy tested. In contrast to the stationary values of interface pH revealed by SIET between at least the first 24 hours of immersion, all the alloys show changes in the degradation rate over the immersion time. The Mg-2Ag, Mg-1.2Ca and HP-Mg systems, showed an initial high degradation rate within the first 6 – 10 hours of immersion, possibly related to the establishment of a stationary state of the degradation products layer. This stationary state leads to a stationary degradation rate characterised by a constant slope. The Mg-2Ag system shows around 50 hours of immersion a slight drop in the slope developed under immersion in HBSS while in the presence of Ca^{2+} cations the accumulated hydrogen remains with constant slope until the 80 hours of immersion. On the other side, the E11 alloy undergoes successive increases in the degradation rate at 2, 10, 22, and 70 hours of immersion approximately.

The mass loss values after 24 hours of immersion under dynamic degradation test (1.5 mL/min) are presented in *Figure 45.* The same significant differences, as for the hydrogen evolution measurements, were found for the mass loss values between the E11 and the rest of the alloys, with a mass loss difference of at least five times higher. The addition of $CaCl_2 \cdot 2H_2O$ led to a lower mass loss compared to simple HBSS, but with different relative ratio than the one obtained in the hydrogen evolution experiments. A low scattering was observed for those measurements except for the case of the E11 alloy that again shows a higher scattering for the samples immersed in Ca^{2+}-containing HBSS.

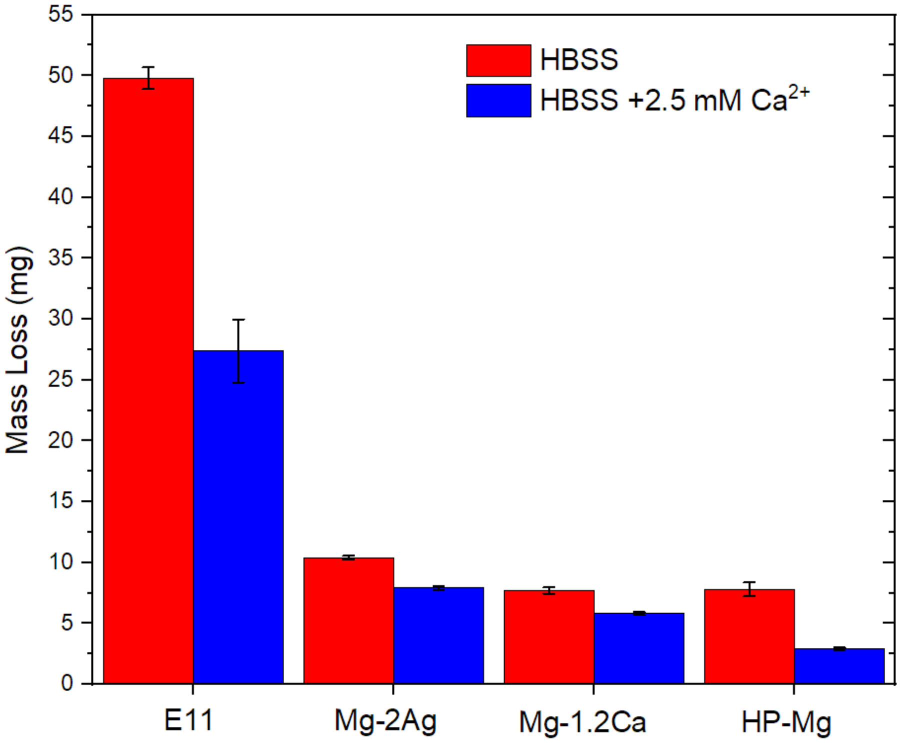

Figure 45: Mass loss for all the Mg alloys after 24 hours of dynamic immersion (1.5 mL/min) in simple (red columns) Hank´s balanced salt solution (HBSS, solution I) and (blue columns) HBSS with the addition of 2.5 mM $CaCl_2 \cdot 2H_2O$ (solution III).

5 Discussion

5.1 Degradation solution composition and degradation products layer on Mg

The performance of a metallic degradable biomaterial in a physiological environment can be defined by the sum of the dissolution rate of the material, the formation of the degradation products layer, and the modification of the near-surface corrosive environment. As previously discussed in the Introduction, the physiological environment of an implantation site should be described by the physiological fluid composition with its inorganic and organic fraction, its volume, the exchange rate of the fluid, and the tissue/cell presence, among the mechanical solicitation influences. Among all those contributions, the inorganic fraction of a physiological fluid is of vital importance since its contribution to the formation of the degradation products layer constitutes the main element delaying the degradation process. According to the time scale described by *Willumeit-Römer* [241], the inorganic fraction is also the first fraction interacting with the metallic surface. This interaction starts at the first nanoseconds of immersion and is ruled by the hydrophobic, hydrophilic, electrostatic interactions and the electrochemistry of magnesium under aqueous solutions.

Therefore, the inorganic compounds present in the degradation products layer are the result of the local environment generated by the dissolution of the alloy, with mainly an increase of the pH and Mg^{2+} ions concentration, and the composition of the physiological fluid surrounding the material. This environment rules the heterogeneous precipitation equilibriums by the temperature, ionic activities of reagents and products, and the pH, defining the thermodynamic condition of saturation that predicts the stability of the different inorganic solid phases forming the degradation products layer. Moreover, the kinetic considerations concerning the necessary energy of nucleation and crystal growth processes determine the final presence of a precipitated phase and also affects its stoichiometry. With the formation of the degradation products layer, defined by its duality of composition and morphology, the kinetics of magnesium dissolution is modulated by hindering the interaction between the degradation solution and the metallic surface.

5.2 Local pH: Surface and bulk solution environments on Mg

The dissolution of a magnesium-based material together with the formation of the degradation products layer on the surface are phenomena that promote variations in the ionic environment of the corrosive solution. These variations originated at the surface (see *Figure 5*), in addition with the limitations of the mass transfer between the bulk solution and the surface (exposed in *section 1.3.2*), promote different concentration profiles for different species (products and reactants) in the perpendicular direction to the magnesium surface, as schematised in *Figure 6*.

Considering the alkalinisation process generated by the production of OH^- ions in the cathodic reaction $(eq. 3)$, the *in situ* local pH profiles measured in perpendicular to the degraded E11 surface (*Figure 30)*, proved this differentiated environment between the local surface and the bulk solution environments. Since this situation is confirmed for a species with a high diffusivity as OH^- anions ($D_{OH-} = 5.28 \cdot 10^{-9}$ m^2 s^{-1}), those concentration profiles can be assumed for species with lower diffusivity like the Mg^{2+} ions ($D_{Mg2+} = 0.71 \cdot 10^{-9}$ m^2 s^{-1}), HCO_3^- ($D_{HCO3-} = 1.105 \cdot 10^{-9}$ m^2 s^{-1} [242]), CO_3^{2-} ($D_{CO32-} = 0.92 \cdot 10^{-9}$ m^2 s^{-1} [242]), HPO_4^{2-} ($D_{HPO42-} = 8.8 \cdot 1^{-10}$ m^2 s^{-1}[243]), or PO_4^{3-} ($D_{PO43-} = 5.8 \cdot 10^{-10}$ cm^2 s^{-1} [243]) but in a different extension along the perpendicular profile to the surface.

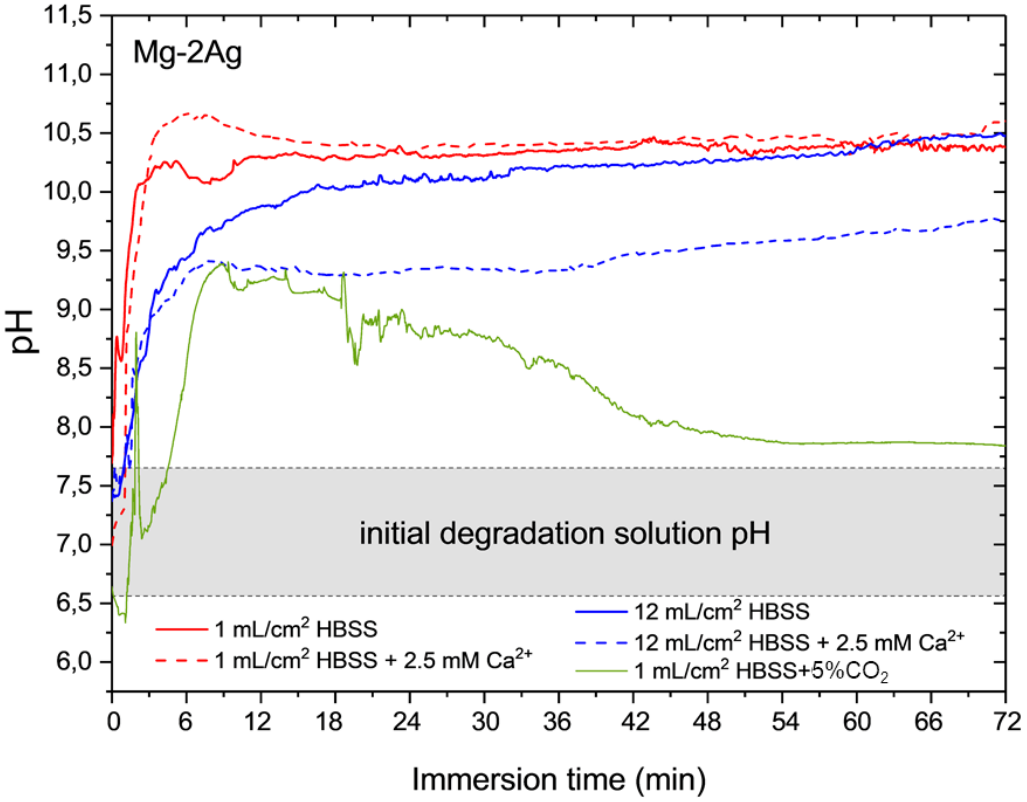

Figure 46: In situ monitor of the bulk pH (mini-FET pH-meter probe at least 5 mm away from the sample) during 72 hours of static immersion of Mg-2Ag samples under atmospheric conditions at different volume per sample area (V/A) ratios of 1 mL/cm^2 (red lines) and 12 mL/cm^2 (blue lines) in (solid lines) Hank´s balanced salt solution (HBSS, solution I) and (dashed lines) HBSS with the addition of 2.5 mM $CaCl_2 \cdot 2H_2O$ (solution III). In addition, the bulk pH was monitor under immersion at 1 mL/cm^2 and a controlled atmosphere of 5 % CO_2 (solid green line).

The constant alkalinisation process accompanying the dissolution of magnesium-based materials can be defined by a constant release OH^- ions from the surface. This alkalinisation process shows a fast rate even for high V/A ratios in the absence of an efficient buffering system. *In situ* pH measurements of the bulk degradation solution presented in *Figure 46*, revealed how fast the degradation process of Mg-2Ag can affect the bulk degradation solution under static conditions. This effect is evaluated at different V/A ratios of 1 and 12 mL/cm^2 in HBSS and HBSS with the addition of $CaCl_2 \cdot 2H_2O$ at room conditions (21°C, 21%O_2, 0.03% CO_2). In the case of a low V/A ratio like 1 mL/cm^2, the system reaches the total alkalinisation within the first 6 hours of immersion even in the presence of Ca^{2+} cations. For a ratio of 12 mL/cm^2, the initial fast increase of the pH is damped by the higher buffer capacity of the higher volume, and for the immersion in HBSS the total alkalinisation is reached around 24 hours of immersion. This total alkalinisation value is reached around a pH of 10.5 units, value that is similar to the interface pH obtained by SIET for immersion in HBSS. The lower alkalinisation values generated in the interface by the addition of Ca^{2+} cations coupled with a high V/A ratio present the same fast initial degradation process, but reaching a lower value of total bulk alkalinisation of about 9.5 after 72 hours of immersion that can be linked to the interface pH measured by SIET under dynamic conditions.

The presence of a buffering system strongly modulates the local pH profile during the degradation process, as demonstrates the pH profile presented in *Figure 46* for HBSS under controlled CO_2 atmosphere (21°C, 21%O_2, 5% CO_2). However, the CO_2/HCO_3^- buffering system generated by the CO_2 atmosphere cannot avoid high levels of alkalinisation of the solution at least for the first 54 hours of immersion. In consonance with those measurements, *Agha et al.* [134] presented a similar bulk pH profile for the degradation of Mg-2Ag under cell culture conditions in a semi-static set-up over 300 hours. The authors present a constant decrease in the bulk pH that is altered by increments of the pH generated by the new solution. However, those pH alterations are gradually less severe with the degradation solution exchange over the immersion time, due possibly to the progressive stabilisation of the degradation products layer.

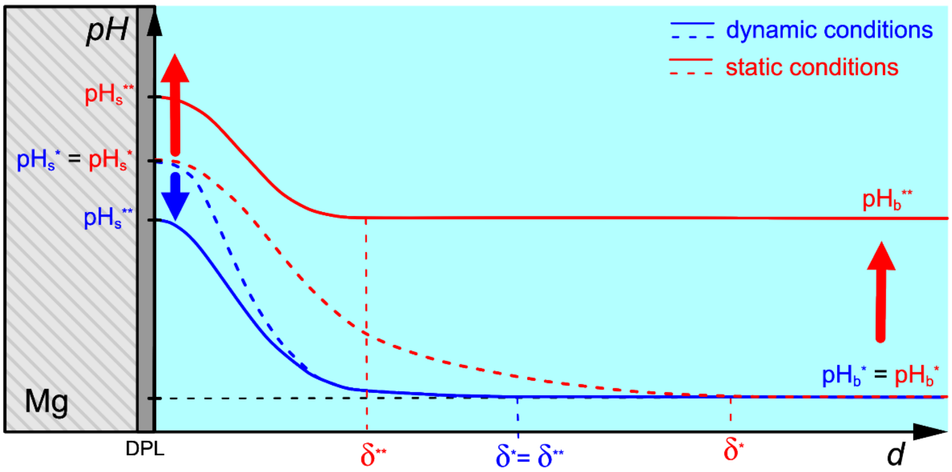

Figure 47: Interpretation of the evolution over the immersion time of the local pH profiles over magnesium surface during the immersion under static conditions (blue), and under dynamic conditions (red), according to the results presented in Figure 31. pH_{int}: pH at the interface, pH_b: pH at the bulk solution, δ: length of the diffusion layer generated over the magnesium surface, at the initial stage of the immersion (*) and after a certain time of immersion (**).

Due to the limitations of the SIET set-up to include a controlled CO_2 atmosphere as a buffering system, the bulk pH was controlled by the flow conditions. The values of the bulk pH measured by the SIET electrode during 24 hours of immersion (see *Figure 25*), proved that the dynamic conditions applied in combination with the volume of the degradation flow chamber were enough to avoid the alkalinisation process in the bulk solution.

Moreover, the degradation solution exchange might also affect the local surface environment. The use of dynamic conditions increases the mass transfer phenomena between the bulk degradation solution and the surface. This is reflected in the value of the interface pH presented in *Figure 30* (blue profile), that presents a significantly lower pH value than the one obtained for the static conditions. The limited mass transfer presented by the static conditions, red profile in *Figure 30*, also with a not effective buffering system, shows how the alkalinisation process generated a high interface pH in comparison than when dynamic conditions are applied. With the immersion time, the alkalinisation effect is extended to the bulk solution as proposed in *Figure 47*. With the limited V/A ratio applied in static conditions, the alkalinisation of the bulk solution can progress to the surface by reducing the difference in pH between the two zones and therefore masking the diffusion layer (δ). The proposed evolution of the local pH profiles in *Figure 47* might explain how the higher convection factor under dynamic conditions shows the same diffusion layer thickness at the immersion time analysed. Accordingly, differences in the diffusion layer thickness between 250 and 1000 µm were found by *Mareci et al.* [184] within the first 26 hours of immersion.

However, the formation of the degradation products layer can also control the interface pH by two effects. i) The degradation products layer act as a barrier that against the diffusion of the products and reactants involved in the electrochemical process of magnesium, therefore hinders the diffusion of the H_2O and OH^- ions involved in the cathodic reaction so reducing the interface pH. ii) The heterogeneous precipitation processes that generate the different compounds present in the degradation products layer involve basic anions that are linked to the interface pH, as is presented in *Figure 48*. The contact between the degradation products layer and the degradation solution, the mass transfer and the buffering system, generates a constant dissolution/precipitation equilibrium that provides an extra buffering system damping the value of the interface pH.

The established low alkaline environment under the presence of Ca^{2+}, HCO_3^- and HPO_4^{2-} in addition to the active physiological pH homeostasis, points to the possible lower significance of an alkalinisation process under *in vivo* conditions. This premise questions the proposed negative effect of an alkaline environment in the implantation site proposed by *Song* [244], but also in the positive stimulation of the callus formation effect proposed by *Zhao et al.* [10]. However, a limited fluid exchange or limited renewal of the ionic composition, similar to the static conditions shown in *Figure 30(a)*, will promote the alkalinisation of the physiological fluid at the interface but possibly also in the bulk fluid environment.

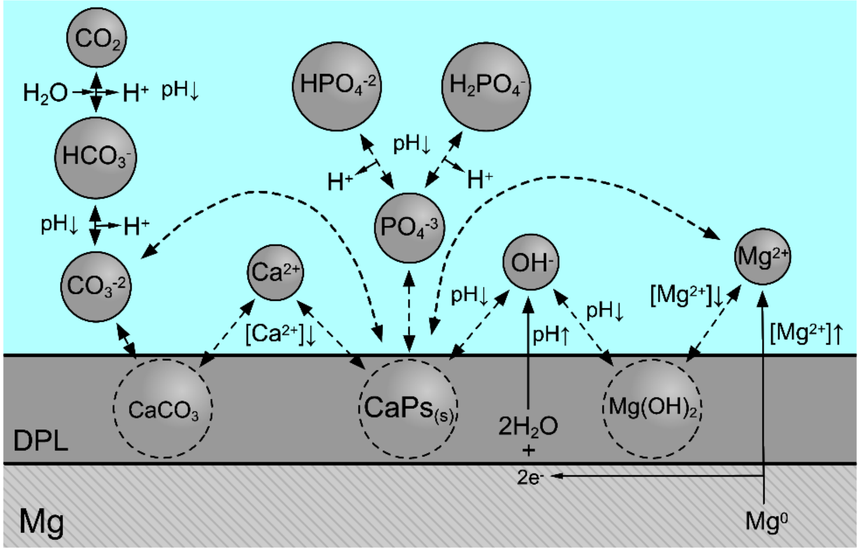

Figure 48: Chemical reactions between relevant inorganic ions present in simulated physiological solutions on the degradation products layer formation and their relationship with the interface pH, according to Ferreira et al. [153]. *CAPs: Calcium phosphates; DPL: Degradation products layer.*

According to the relationship between the pH, the ionic activities and the degradation products layer formation, the differences between the bulk solution and the surface environment highlight the importance of the local measurements for a reliable description of the mechanisms involving magnesium degradation. However, due to the mass transfer between the surface and the bulk environment, both solution compartments (surface and bulk) are interconnected, and they can influence each other. Accordingly, the static or semi-static *In vitro* degradation set-ups might have disadvantages for the study of magnesium degradation mechanisms or for a realistic *in vivo* simulation of the degradation process and rates of Mg-based implant materials. However, the use of static and semi-static set-ups is widely spread due to its simplicity and its capability for reliable material screening testing.

5.3 Alloy influence on the degradation products layer formation on Mg

As discussed in *section 1.3,* the non-fully protective character of the degradation products layer generated on the surface can only modulate the natural tendency of the alloy dissolution. This fact is supported by comparing the degradation rate generated by immersion in HBSS and HBSS with the addition of $CaCl_2 \cdot 2H_2O$. According to that, higher dissolution kinetics should lead to a faster and possibly higher alkalinisation in addition to a faster increase in the Mg^{2+} ions concentration at the surface environment. In contrast, the same interface pH was found under HBSS and HBSS with the addition of $CaCl_2 \cdot 2H_2O$ for all magnesium-materials tested, according to the results presented in *section 4.2.2*. This phenomenon may be justified by hampering the diffusion of products and reagents diffusion and the extra buffering capacity generated by the degradation products layer described in the previous section.

On the other hand, the similar interface pH values obtained under the same degradation solution composition predicts the presence of the same composition of the degradation products layer. In contrast, substantial differences in the crystalline phases present in the degradation products layer (see *Figure 39)*, and differences in the relative intensity of the $\nu_3(PO_4^{3-})$ and $\nu_3(CO_3^{2-})$ IR vibrational bands (see *Figure 43*), were found between the degradation products layer generated on the E11 and Mg-2Ag alloys. In the absence of a local system that can absorb the excess production of Mg^{2+} ions generated by a fast dissolution kinetic, the Mg^{2+} ionic concentration is only modulated by the degradation products layer formation and the diffusion and convection effects. This fact promotes a local accumulation of this and other ions coming from the alloy dissolution, changing in the ionic activities that are responsible for the supersaturation condition of different inorganic phases and changing the kinetic conditions that rule the stoichiometries of the carbonates and phosphates phases, as described in *section 5.4.1*.

In summary, the alloy composition and microstructure define the intrinsic dissolution rate that generates the alkalinisation and the change in the ionic activities that trigger the formation of the degradation products layer. In turn, once the degradation products layer starts to develop, a modulation effect on the electrochemical process gives the degradation products layer the control of the kinetics of corrosion. This situation is generated by restricting the inward solution flow and therefore the ions exchange between the *metal/degradation products layer* interface and the *degradation products layer/degradation solution* interface [75]. However, it also modulates the pH value at the interface as an extra local buffering system. Therefore, the differences in the degradation rate between different magnesium-based materials can generate changes in the concentrations at the interface material/degradation solution that promote changes in the degradation products layer composition and morphology.

5.4 Interface pH, corrosive solution and degradation products layer on Mg

5.4.1 Degradation of Mg-based materials in the absence of Ca^{2+} cations in solution

The degradation of magnesium-based materials under simple solutions like the ones based on NaCl predict a high interface pH at the interface of around 11 units or above due to the constant release of OH^- ions by the primary cathodic reaction ($eq. 3$) and the presence of $Mg(OH)_2$ [75]. The immersion under dynamic conditions on commercial HBSS that ensures a constant solution composition over the immersion time shows a slight decrease on the interface pH which is found around 10 units, on the surfaces of HP-Mg, Mg-2Ag, Mg-1.2Ca, and E11 (see *section 4.2*). This local pH is the result of the formation of a specific degradation products layer that modulates the pH at the interface, as described in *section 5.2*.

The formation of the degradation products layer under dynamic immersion in HBSS is schematised in *Figure 51*. The initial moments of the immersion, due to the direct contact between the bare metallic surface and the degradation solution, are the most reactive moments of the degradation process. Therefore, the fast initial alkalinisation presented in *Figure 49* by the arrow *(a)*, promotes the formation of MgO/$Mg(OH)_2$ on the surface. This partially passivated surface, as described in *section 1.3.1*, should modulate the degradation rate and in turn, the alkalinisation process leading to a lower interface pH around 10 units, as indicated in *Figure 49* by the arrow (*b)*. This shift stabilises the presence of magnesium carbonates, (e.g. $MgCO_{3\ (s)}$). The Mg^{2+} ion concentration released in the local surface environment by the degradation process must be taken into account in order to predict the degradation products layer composition accurately. Therefore, the calculations presented in *Figure 49* include the amount of 0.8 mM Mg^{2+} ions according to the local concentration. This concentration was measured by *Lamaka et al.* [209] directly 10 µm above the anodic areas generated on AZ31B magnesium-based alloy coated with a thin sol-gel film in a 0.05 M NaCl solution.

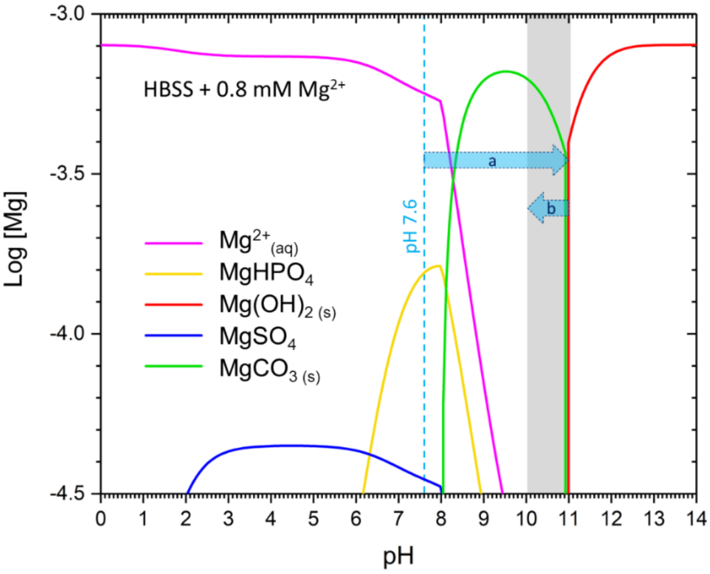

Figure 49: Concentration (M) in logarithmic scale (Log [Mg^{2+}]) for the predicted Mg-containing phases on magnesium surface and its dependency with the interface pH under degradation in Hank´s balanced salt solution (HBSS, solution I) with the addition of 0.8 mM Mg^{2+} ions based on the values obtained by Lamaka et al. [209]. *The dashed blue line presents the initial pH value of the degradation solution, and the grey band shows the interface pH measured by SIET. The blue arrows suggest the shift of the interface pH generated by the degradation process (a) from the first moment to the immersion and (b) with the formation of the degradation products layer.*

The fact that the presence of $Mg(OH)_2$ *brucite* can be identified after several hours of immersion (*Figure 39*) when the interface pH is stabilised at 10 units, can be justified by the following arguments:

i) A higher concentration than 0.8 mM of Mg^{2+} ions can be expected for the alloys tested in the present work in comparison with the anticorrosive coated AZ31B tested by *Lamaka et al.* [209]. This higher concentration on Mg^{2+} ions can shift the stability of the $Mg(OH)_2$ *brucite* phase to lower pH values. But in addition, a higher concentration of Mg^{2+} in the solution was also justified in a previous work by *Mei et al.* [245] by the content of Mg^{2+} ions in BEF (1.5 mM Mg^{2+} ions) in addition to the increment resulting from the degradation process estimated from the hydrogen volume released, according to $eq. 3$. Following that, *Figure 50* shows how an increase of Mg^{2+} ions of (a) 5 and (b) 10 mM in the local surface environment might justify the presence of $Mg(OH)_2$ *brucite* on the surface of a magnesium-based material immersed in HBSS.

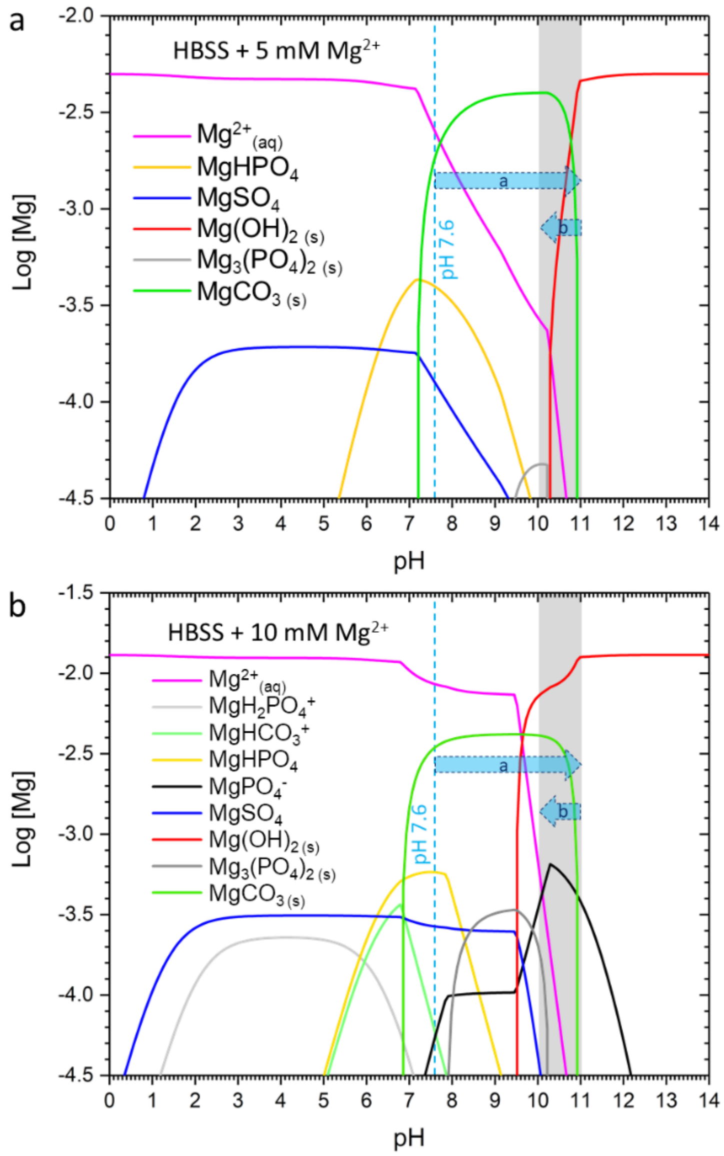

Figure 50: Concentration (M) in logarithmic scale (Log [Mg^{2+}]) for the predicted phases and its dependency with the interface pH in a solution with a composition of a) Hank´s balanced salt solution (HBSS) with the addition of 5 mM Mg^{2+} cations and b) HBSS with the addition of 10 mM Mg^{2+} cations, according to a higher increase of the Mg^{2+}

concentration at the interface due to the dissolution of the alloy. The dashed blue line presents the initial pH value of the degradation solution, and the grey band shows the interface pH measured by SIET. The blue arrows suggest the shift of the interface pH generated by the degradation process (a) from the first moment to the immersion and (b) with the formation of the degradation products layer.

ii) The precipitation of the carbonates phases and the growth of a porous degradation products layer generates a restricted mass transfer of ions between the metallic surface and the corrosive solution. Therefore, as depicted in *Figure 51* with a dashed red line, different concentration profiles might be established along the portion of the solution that leaks along with the degradation products layer. Under those considerations, significantly high Mg^{2+} concentration and higher pH levels will be achieved at the interface metal/degradation products layer or even at the inner parts of the degradation products layer, and therefore stabilising $Mg(OH)_2$ *brucite*.

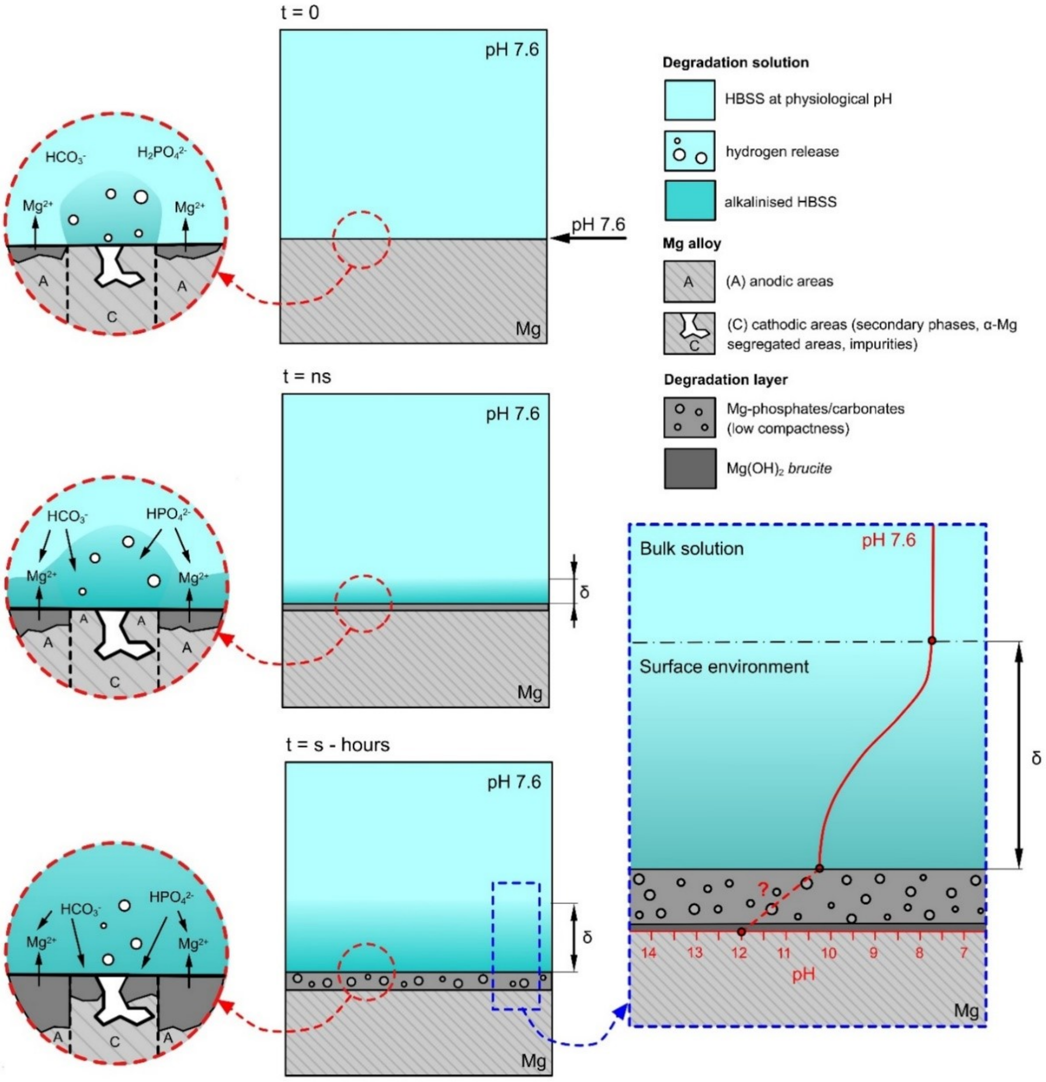

Figure 51: Scheme of the degradation mechanism for magnesium-based materials under simple degradation solution like Hank´s balanced salt solution (HBSS) without the presence of Ca^{2+} cations. The Scheme observes (left) the evolution of the degradation products layer, and (right) the development of the pH above the magnesium surface and the unknown pH environment along the degradation products layer (dashed red line). (δ: diffusion layer).

The presence of crystalline Mg-phosphates phases like the possible Mg_2KPO_4 phase found for the E11 degradation products layer, or the amorphous phosphates phases identified by FTIR-ATR for the Mg-2Ag, is only thermodinamically justified under high Mg^{2+} concentrations at the interface according to the calculations shown in *Figure 50* that predict the presence of $Mg_3(PO_4)_{3(s)}$ and $MgPO_4^-$ and $Mg_3(PO_4)_{2(s)}$ under those circumstances.

According to the results, the degradation layer formation under dynamic conditions in HBSS can be defined as a diffused bilayer structure with an inner layer where $Mg(OH)_2$ *brucite* predominates and an outer layer with the central presence of amorphous and crystalline phases of Mg-carbonates and Mg-phosphates. The discrepancies concerning the stoichiometry and crystallinity of Mg-carbonates and phosphates found in the present work and with other author results are discussed in the next section.

The high degradation rate revealed by the mass loss and the hydrogen evolution values (see *Figure 44 and Figure 45*) and the high interface pH, reveal that the composition, and morphology of the degradation products layer generated under HBSS do not promote significant passivation of the surface. This fact, in agreement with the higher degradation rates for different simulated body fluids in the absence of Ca^{2+} cations found by *Mei et al.* [245]. This fact is reflected in the aggressive dissolution observed in the α-Mg matrix phase present in the E11 microstructure (see *Figure 33 and Figure 34*), induced by the cathodic behaviour of the Gd,Nd-rich intermetallic particles and the Gd-segregated areas in the α-Mg matrix.

Mechanisms of Mg-carbonate/phosphates formation on the degradation products layer

The degradation products layer composition presented by previous authors is in partial agreement with the description above due to a similar general composition but presenting different crystalline Mg-carbonates and phosphates phases. *Kieke et al.* [151] analysed the degradation products layer of Pure-Mg under static immersion in HBSS (solid/liquid ratio of 0.2 g/mL) and cell culture conditions by XRD finding the presence of $Mg(OH)_2$ *brucite* and $Mg(HCO_3)OH\cdot 2H_2O$ *nesquehonite*. *Tie et al.* [246] studied the degradation products layer of Pure-Mg under static conditions in HBSS by XPS, and he identified the presence of MgO, $Mg(OH)_2$, $MgCO_3$ and $Mg_m(PO_4)_n$. Moreover, the presence of $Mg_2CO_3(OH)_2\cdot 3H_2O$ and $Mg_3(PO_4)_2\cdot 2H_2O$ was identified after immersion of pure-Mg in SBF containing HCO_3^-, HPO_4^{2-}, and SO_4^{2-} by *Mei et al.* [245]. Due to the similarity of the degradation solution compositions presented in above-cited works with the HBSS applied in the present work, the same interface pH around 10 units is expected. Therefore, the discrepancies in the Mg-carbonates/phosphates stoichiometry found in the literature and the present work, cannot be just analysed from the thermodynamic point of view.

Christ and Hostetler [247] analysed the geochemical behaviour of $MgCO_3$ *magnesite* defining the precipitation of Mg-carbonates as an actively kinetically controlled process. The appearance of thermodynamically unstable phases (more hydrated) in comparison with the higher thermodynamic stability of *magnesite* is explained by the high ratio between the electrical charge and the ion surface area of the Mg^{2+} ion. This condition generates strong bonds to the water dipoles that creates very strongly bonded layers of water molecules surrounding the magnesium ion ($\Delta H°_{hyd}(Mg^{2+})$ = -672 kcal·mol^{-1}). Those layers have been described as a first solvation shell with six water molecules and 12 water molecules in the case of the second solvation shell, as described by *Hänchen et al.* [248]. Under those circumstances, only the second solvation shell is affected by changes in the temperature and concentrations of the solution. However, with increasing the salinity (e.g., with the addition of NaCl or KCl), the activity of the water in the solution is decreased. Therefore the proportion of less-strongly hydrated Mg^{2+} ions in solution is increased, generating less hydrated forms. According to that, even though $MgCO_3$ *magnesite* is the most stable Mg-carbonate phase; no *magnesite* is found under aqueous media in standard temperature and pressure conditions (STP). In contrast, $Mg(HCO_3)OH \cdot 2H_2O$ *nesquehonite* is mostly the phase precipitated under STP conditions, and therefore justifying that this Mg-carbonate was found by *Kieke et al.* [151] and *Hou et al.* [110] after degradation tests in HBSS under cell culture conditions.

However, the kinetically stabilised *nesquehonite* structure can be affected by the solution environment generating a phase transformation involving more thermodynamic stable phases. Concerning the temperature, *Dong et al.* [249] reported that the solubility of *nesquehonite* in pure water decreased when the temperature increases between 25 and 40°C, and between 50 and 70°C *nesquehonite* experienced a complex phase transformation that includes amorphous phases. The author observed that the phase transition from *nesquehonite* to an Mg-carbonate amorphous phase persisted in the presence of NaCl at 40°C, or by the increasing addition of $MgCl_2$. On the other hand, the addition of Mg^{2+} ions in the presence of NaCl generates a higher ionic strength that means higher salinity, therefore as exposed by *Yoo et al.* [250], a higher concentration of Mg^{2+} ions promote a higher fraction of less hydrated phases like the basic carbonate $(MgCO_3)_4 \cdot Mg(OH)_2$ *hydromagnesite*. Besides, the author exposes that an alkaline environment favours the formation mechanism of *hydromagnesite.* With the increase of the temperature above 40°C, *Hänchen et al.* [248] exposed that *hydromagnesite* is mostly the precipitated phase due to the influence of the temperature on the secondary hydration number. However, the transformation from *hydromagnesite* to *magnesite* under aqueous conditions is a slow process that often requires days at high temperatures (60 – 100°C) and moderate partial pressure of CO_2 (pCO_2). However, other factors can accelerate the transition to *magnesite*. As commented before the increase of the salinity reduce the activity of the water and therefore favour the dehydration by reducing the thickness of the second hydration layer of Mg^{2+} ions. The increase of CO_3^{2-} ions that have a large radius and not completed surrounded by water molecules, can be adsorbed on the crystal surface easier and therefore a low Mg^{2+}/CO_3^{2-} ratio, might help to keep water molecules away from the crystal surface and therefore hindering the formation of *nesquehonite* [250].

Concerning how those phase transformations overcome the kinetic barrier, *Yoo et al.* [250] proposed an Mg-carbonate amorphous structure as the precursor of the later crystalline hydrated Mg-carbonates like *nesquehonite*, and the consumption of OH^- by a low pH, will promote the generation of extra OH^-, affecting the formation of the crystalline Mg-carbonate structures. *Yang et al.* [251] observed a complex phase change at 37°C and 100% RH that was not observed at 25°C, from amorphous Mg-carbonates nanoparticles aggregates to *hydromagnesite*. *Harrison et al.* [252] exposed that multiple hydrated carbonate phases often co-exist, and this is explained due to the more-hydrated phases act as precursors of less hydrated phases. *Davies and Bubela* [253] argument that the transformation between *nesquehonite* and *hydromagnesite* takes place by an amorphization/recrystallization process that involves a poorly-ordered proto-hydromagnesite structure supported by *Lanas and Alvarez* [254] at 115°C, but this precursor is missing at higher temperatures as 460°C.

As detailed in the Introduction, not many works on magnesium-based biomaterials dealt with the degradation process under dynamic conditions (*section 1.3.2*). Within all these works most of them focus of the effect of the flow on the degradation rate and degradation morphology and provide limited information about the degradation products layer composition, most of the times providing relative elemental composition by EDX measurements. However, in agreement with the amorphous phases found in the present work, the dynamic degradation studies on porous commercially pure Mg specimens performed by *Saad et al.* [156,162], presented $Mg(OH)_2$ as the only crystalline precipitate while different morphology precipitates, including different Ca and P quantities, were found on the surface. On agreement with this degradation products layer composition under dynamic conditions, *Li et al.* [188] tested WE43 in HBSS under static, stirred and flowing conditions, concluding that variations on the surface Mg^{2+} and OH^- ion concentrations generated by the different set-ups influence the crystallinity of the products formed on the degradation products layer. Moreover, *Marco et al.* [155] pointed to the formation of crystalline $Mg_2P_2O_7$ only when high rotation speeds were applied to a rotational electrode disc during polarisation measurements, and only crystalline $Mg(OH)_2$ was identified under static conditions.

Similar considerations should be made concerning the stoichiometry of Mg-phosphates. Due to the high affinity of Mg^{2+} ions to bind oxygen-containing ligands, a high number of hydration molecules can also be found in Mg-phosphates phases. According to the precipitation studies of *Tamimi et al.* [255], an abrupt reduction of the water molecules was found when the temperature is increased up to 37°C. For 10 times higher concentrations of

Mg^{2+} than the ones found in the body, $Mg_3(PO_4)_2 \cdot 8H_2O$ and $Mg_2PO_4OH \cdot 4H_2O$ were identified for a pH of 7.4 while for a pH between 8 and 10 the phase $Mg_3(PO4)_2 \cdot 5H_2O$ was stabilised. Therefore, and considering the similarities with the Mg-carbonate formation, the presence of hydrated Mg-phosphate phases, including the amorphous condition, can be justified under the immersion conditions presented in this work.

According to exposed above, seems to be clear that differences in the degradation set-up and the magnesium-based material under degradation, are sources of multiple variations in the local degradation environment. This effect might explain the differences between the different crystalline Mg-carbonates found under static conditions and the amorphous phases found under progressive degradation in the present work:

i) A static or semi-static degradation set-up, especially under low V/A ratios, increase the Mg^{2+} and a decrease in the HCO_3^- ions concentration that might stabilise hydrated products like *nesquehonite*. On the contrary, dynamic conditions provide a constant supply of HCO_3^- ions generating higher carbonate precipitation, as *Knigge and Glasmacher* [256] exposed. Moreover, also the increase in the mass transfer can absorb better the local surface increments of Mg^{2+} and OH^- ions, that might promote the precipitation of amorphous Mg -carbonates.

ii) Moreover, those differences in the degradation set-up can also promote changes in the interface pH as a consequence of the alkalinisation process of the bulk solution, as was revealed by *Mareci et al.* [184] and the *Figure 31*. According to exposed in *section 1.3.2*, the alkalinisation of the local surface environment will increase the solubility of phases like *nesquehonite,* according to $eq. 23$ and favour the presence of $Mg(OH)_2$ [249].

$$s = \frac{K_{sp} \cdot (m_{H+}\gamma_{H+})^2}{K_1 \cdot K_2 \cdot a_{H2O}^4 \cdot P_{CO2} \cdot \gamma_{Mg2+}} \qquad (eq. 23)$$

iii) Differences in the kinetics of the alloy dissolution can affect the local Mg^{2+} ions environment. For a defined set-up in which the mass transfer and the degradation solution composition is fixed, a higher degradation rate promotes an increase of Mg^{2+} ions in the local surface environment.

In conclusion, since those Mg-carbonates/phosphate phases are in constant equilibrium with the ions in solution, different phases are established according to variations in the local concentrations of the electrolyte and the immersion time. Also, the multiple potential hydrated phases, complicate the prediction of Mg-carbonates/phases stoichiometry formation. Therefore, the study of accurate *in situ* local measurements of local ionic concentrations could help to elucidate the mechanisms of the degradation products layer formation under different set-up conditions for different degradation rate magnesium-based materials, and then assimilate such conditions to the ones found in a specific implantation site.

5.4.2 Degradation of Mg-based materials in the presence of Ca^{2+} cations in solution

By including a physiologically relevant concentration of Ca^{2+} cations (e.g., 2.5 mM) was revealed a less aggressive degradation process with less dissolved anodic areas, as showed for the E11 microstructure in *Figure 34*. Besides, the local surface environment is shifted to significantly lower pH values around a pH of 8, and a less aggressive environment results to a significant reduction of the degradation rate for all magnesium alloys tested in comparison with the immersion in HBSS (see *Figure 44* and *Figure 45*).

Under those conditions, the local surface processes involving the degradation mechanism under dynamic immersion in HBSS in the presence of Ca^{2+} cations is characterised by the following steps, that are schematised in *Figure 53*.

i) The initial moments of the immersion expose the direct contact between the metallic surface. Therefore we should expect the most reactive moments of the surface as well as under immersion in HBSS. However, in the presence of Ca^{2+} cations, the DVIT analysis revealed (see *Figure 24*), a low surface pH developed from the first seconds of the immersion. According to the thermodynamic predictions in *Figure 52* for different concentration of Mg^{2+} ions (from 0.8 to 10 mM), from the initial pH of 7.6 until the final local pH developed on the surface (grey band between 8.0 and 8.8 pH units), different compounds are predicted to precipitate on the surface. Those phases are $Ca_5(PO_4)_3OH_{(s)}$ (Hydroxyapatite, HA), crystalline Ca, Mg-carbonate $CaMg(CO_3)_{2(cr)}$, $CaCO_{3(s)}$, among other more soluble phases like $NaHCO_3$ and $MgSO_4$, and $MgCO_{3(s)}$ when the concentration of Mg^{2+} is increased above the physiological value of 1.5 mM. Due to the complicated precipitation process involved at the interface pH in the presence of Ca^{2+} cations, it is not possible to estimate any sequence of precipitation without *in situ* characterisation methods.

   However, according to *Figure 43*, the higher relative intensity of the $\nu_3(PO_4^{3-})$ band with respect to the $\nu_3(CO_3^{2-})$ band within the first 10 minutes of immersion, in comparison with the relative intensity of both bands under immersion in HBSS. This point to the probability that those phases play the leading role on the low initial surface pH revealed by DVIT (*Figure 24*). According to the thermodynamic prediction in *Figure 52,* this influence might be associated with the precipitation of amorphous CaPs. Previous *in vitro* studies by *Agha et al.* [48] on HP-Mg under similar compositions to the HBSS with the addition of $CaCl_2{\cdot}2H_2O$ tested in the present work, support the presence of amorphous CaPs phases. Those amorphous CaPs phases are fundamentally found in the outer part of the degradation products layer. Therefore, it is plausible that a fast initial amorphous CaPs precipitated layer, possibly with a minor fraction of Mg, Ca-carbonates generates the fast initial passivation of the surface.

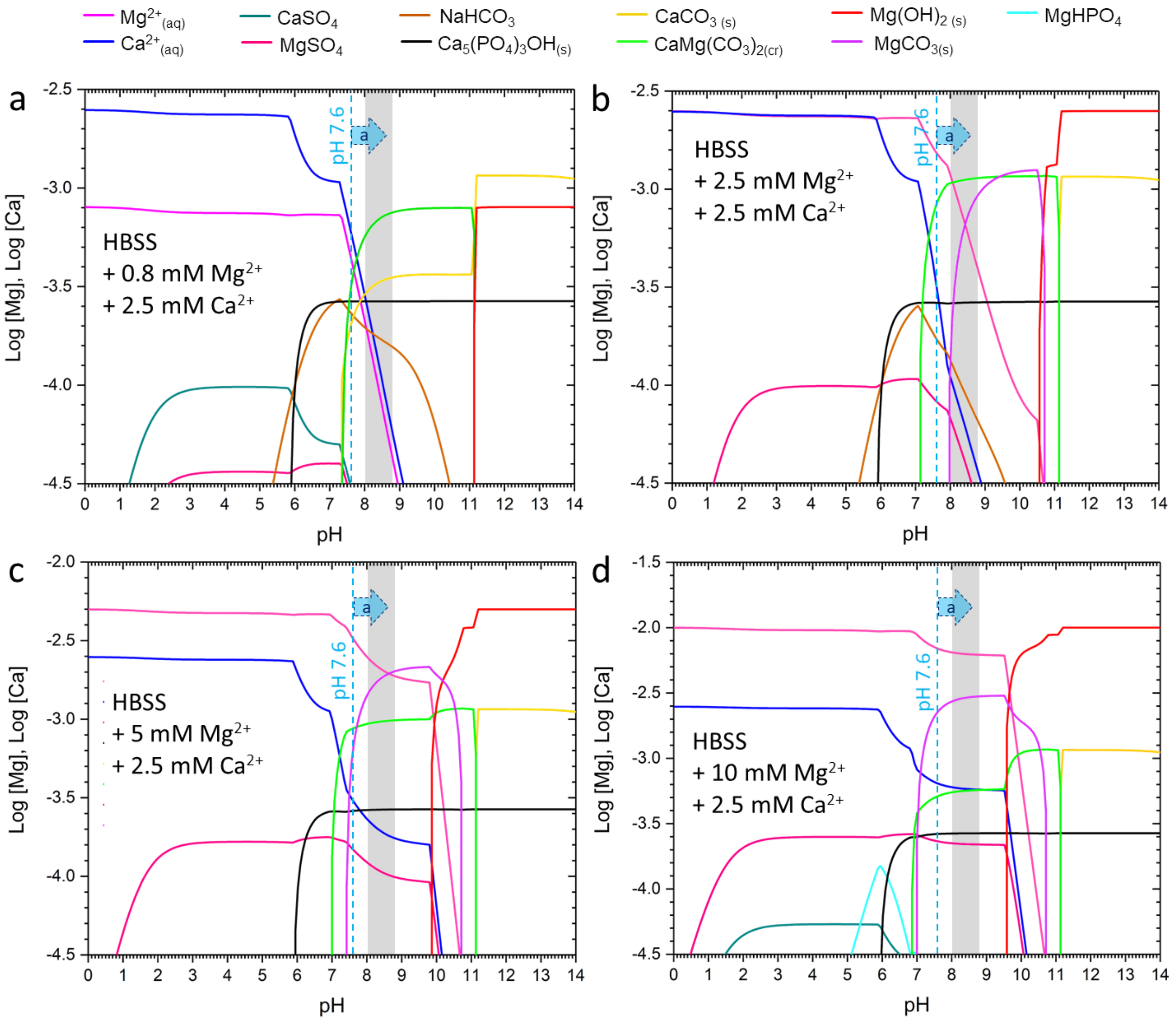

Figure 52: Concentration (M) in logarithmic scale (Log [Mg^{2+}], log[Ca^{2+}]) for the predicted phases and its dependency with the interface pH in Hank´s balanced salt solution (HBSS) with the presence of 2.5 mM Ca^{2+} cations and the presence of a) 0.8 mM Mg^{2+} cations, b) 2.5 mM Mg^{2+} cations, c) 5 mM Mg^{2+} cations, and d) 10 mM Mg^{2+} cations, according to a higher increase of the Mg^{2+} concentration at the interface due to the dissolution of the alloy. The dashed line presents the initial pH value of the degradation solution, and the grey band shows the interface pH measured by SIET under HBSS with the addition of $CaCl_2 \cdot 2H_2O$.

However, the high protective effect of the degradation products layer generated in the presence of Ca^{2+} cations cannot be exclusively attributed to the CaPs. According to previous works [48,245], the contribution of Ca, Mg-carbonates and Mg-phosphates to the degradation products layer in the presence of Ca^{2+} cations showed a synergic effect between the Ca^{2+} HCO_3^- and HPO_4^{2-} ions on the formation of an additional semi-protective layer that generates an of significant reduction on the hydrogen evolution. The synergic precipitation effect of $MgCO_3$ and $Mg(OH)_2$ and $CaCO_3$ *calcite* crystals over the cathodic areas was the postulated mechanism responsible for decreasing the degradation rate of magnesium in the presence of salt solutions in combination with the atmospheric CO_2 [257,258]. In addition, this effect was also manifested for more complex degradation solutions like the ones applied currently for *in vitro* testing [48,259]. On the other side, according to what was exposed in *section 5.2*, the higher amount of inorganic phases precipitated involving several basic anions like the case of $Ca_5(PO_4)_3OH_{(s)}$ or the most realistic amorphous phase $Ca_{10-x}(PO_4)_{6-x}(HPO_4 \text{ or } CO_3)_x(OH \text{ or } ½\ CO_3)_{2-x}$ with $0 \leq x \leq 2$, are the responsibility of the significant drop in the interface pH.

ii) After precipitation of the dense but still not fully protective CaPs phases, a different microenvironment might be established along with the degradation products layer growth, from the metallic surface where the cathodic reaction takes place and the surface of the degradation products layer with a pH of 8.0 – 8.5 units. In this suggested local environment gradient, schematised in *Figure 53* by a red dashed line, a high Mg^{2+} ion concentration and high pH can be assumed. Those conditions will decrease the fraction of amorphous CaPs and $Ca,Mg(CO_3)_{2(cr)}$, and the increase the fraction of Mg-carbonates, according to the thermodynamic prediction of *Figure 52(d)*. This internal microenvironment developed along the degradation products layer will justify the presence of $Mg(OH)_2$, confirmed in *Figure 39(b)*. This increase in the Mg, Ca-carbonates precipitation is supported by the drop of the $\nu_3(PO_4^{3-})$ band relative intensity with rispect to the $\nu_3(CO_3^{2-})$ band over the immersion time exposed in *Figure 43* for the E11 surface.

iii) On the other hand, *Figure 36* confirms that the degradation products layer formed under HBSS with the addition of $CaCl_2 \cdot 2H_2O$ was always accompanied by a localised degradation process with filiform morphology that in occasions has the interface metal/resin as initiation site. Those highly localised degraded areas present higher calcium and chlorine ions precipitation (see *Figure 37* and *Figure 38*). A local degradation process is often justified by surfaces with a high proportional area under cathodic behaviour and smaller areas with anodic behaviours, like the ones found on passivated or coated metallic surfaces. *Gahli* [260] defined the crevice and filiform corrosion in magnesium alloys as a process that typically happens on coated metal surfaces where the trigger is a pitting process. Then the corrosion process happened at a slower rate on radial directions than the one on the direction of the filiform head. With the progress of the filiform head, the body immediately behind is passivated. Due to the low influence of the oxygen reduction reaction in magnesium degradation, the reason why is progressing the head of the filiform structure and the presence of crevice phenomenon under aqueous solution is still unclear. However, this phenomena possibly follow an “autocatalytic” process [261] via interconnection of active galvanic cells formed by noble impurities across the surface generally starting from an anodic spot in the edge of the specimen, and progressing under the internal cathodic sites by the anodic dissolution of the surrounding matrix. This effect could also be associated with the migration of Cl^- anions that compensate the positive charge generated by high Mg^{2+} cations concentration on the head of the filiform morphology, and a possible depletion in ions like Ca^{2+}, HCO_3^- or HPO_4^{2-} suppressing the protective synergic effect. Therefore, the presence of those local degradation processes is justified by the highly protective degradation products layer generated by the addition of $CaCl_2{\cdot}2H_2O$ to the HBSS.

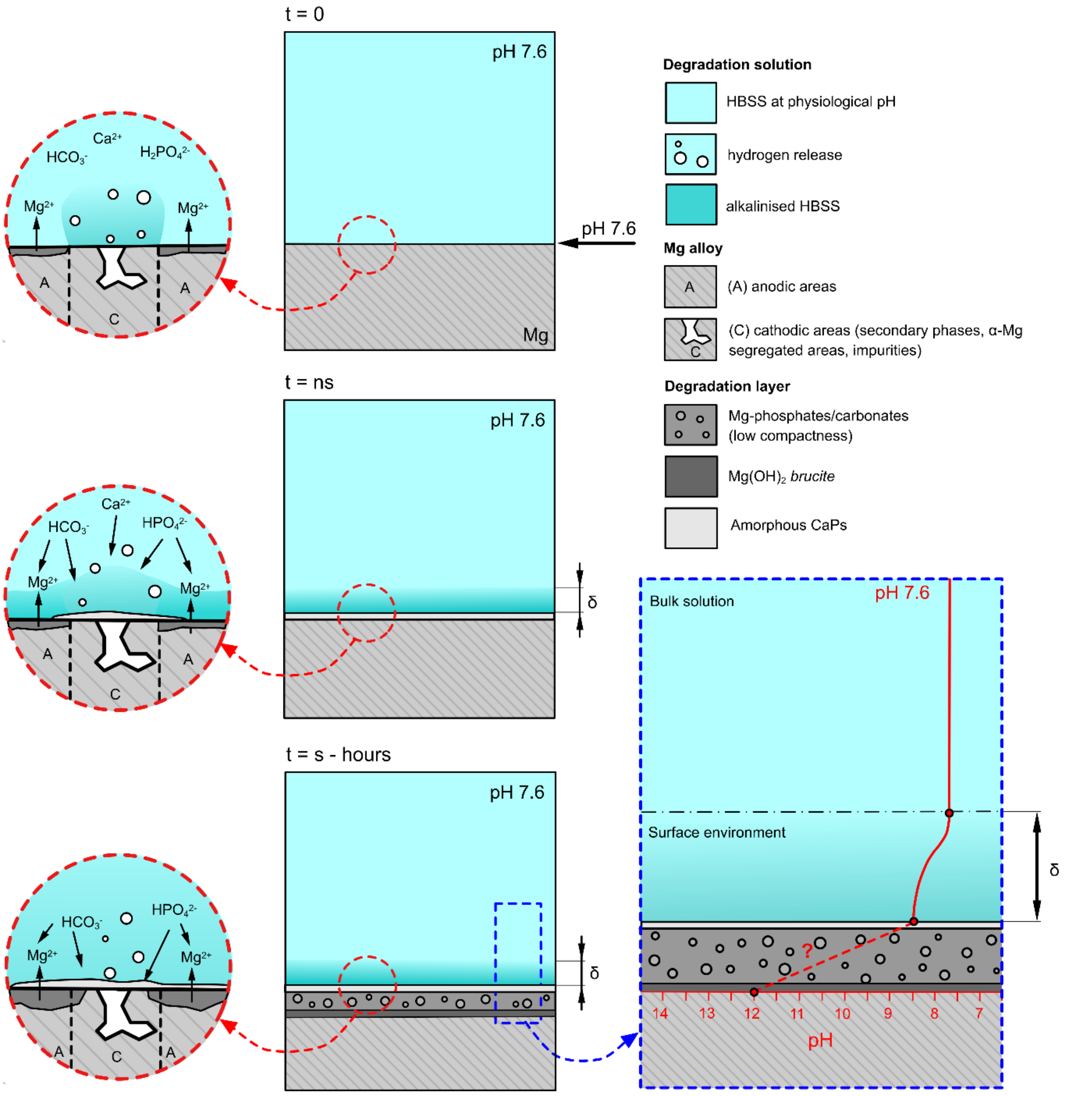

Figure 53: Scheme of the degradation mechanism for magnesium-based materials under Hank´s balanced salt solution (HBSS) with the addition of 2.5 mM of $CaCl_2{\cdot}2H_2O$. The scheme observes (left) the evolution of the degradation products layer, and (right) the development of the pH above the magnesium surface and the unknown pH environment along with the degradation products layer (dashed red line). (δ: diffusion layer).

Mechanisms of Ca-carbonates and CaPs formation on the degradation products layer

The degradation products layer composition generated in HBSS in the presence of Ca^{2+} cations is in agreement with the observations presented by previous authors. *Kalb et al.*

[189] presented a degradation products layer generated on WE43 after 18 hours of immersion in SBF with a bilayer structure. This structure was formed by an internal layer with low concentration in Ca and P and High content of O and Mg, while the external layer presented higher content of P and Ca with lower proportional content of Mg. Moreover, the dynamic conditions applied by *Lévesque et al.* [159], showed again a bilayer structure generated on AM60B-F discs tested in modified HBSS, including Ca^{2+}, Mg^{2+} HCO_3^- and HPO_4^{2-} ions. The author presented a Ca, P-rich outer layer and an inner layer with high content in Mg, O, and P. In addition, *in vivo* experiments presented by *Bowen et al.* [262] showed how pure Mg wires implanted in the arterial adventitia of the abdominal aorta generated presented the same basic structure with a Ca, P-rich outer layer, with an Mg, O-rich inner layer with significant penetration of P and small amounts of C.

Concerning the presence of Ca-carbonate phases, approximately 79 $kcal \cdot mol^{-1}$ more is required to remove the water molecules shell from an Mg^{2+} ion that from a Ca^{2+} ion [247], pointing to a lower kinetic control influence in Ca-carbonates precipitation. Therefore, according to *Zhang et al.* [263] even when the binding free energy between the Mg^{2+} and the CO_3^{2-} ions is higher than between the Ca^{2+} and the CO_3^{2-} ions and the solubility products of both carbonates are rather small in water, the formation of the calcium carbonate nucleation cluster is not thermodynamically preferred but kinetically faster due to the much lower dehydration free energy barrier [263]. According to *Berninger et al.* [264], the presence of Ca^{2+} cations in the environment promotes its incorporation to the *magnesite* structure but without affecting significantly to the *magnesite* growth kinetics. This effect contrasts with the well documented [265–267] inhibiting effect of Mg^{2+} ions in the growth kinetics of calcium carbonate stabilises ACC forms generating a so-called Mg-stabilised amorphous calcium carbonate (Mg-ACC). Also, depending on the Mg: Ca ratio in solution, the stability of Mg-ACC varies, and high Mg content Mg-AAC might crystalise in high-Mg-calcites, together with other hydrated Ca-carbonate phases as exposed by *Loste et al.* [265].

Moreover, *Myszka et al.* [268] and *Lassin et al.* [269] pointed to the importance of amorphous calcium carbonate (ACC), a highly hydrated metastable form, in the biomineralisation process as a precursor to a crystalline Ca-carbonate species like *calcite*. The author highlights the importance of different molecules that acts as crystallisation inhibitors and point to HPO_3^-/PO_3^{2-} ions as an inhibitor of the predicted steps of the Ostwald-Lussac law in the transformation between ACC and $CaCO_3$ *calcite* [263].

Concerning the CaPs phases, the designation of those phases as amorphous is supported by a characteristic broad IR absorption band indicating a relatively significant amount of vibrational freedom [262], and the non-presence or very week presence of phosphates (in the case of degraded Mg-2Ag surface) under crystalline form revealed by XRD diffraction in *Figure 39(b).* The presence of the more stable CaP phase, $Ca_5(PO_4)_3OH$ (HA) can be less favoured due to a faster nucleation process of more soluble CaPs including octacalcium phosphate (OCP) or amorphous Ca-phosphate $Ca_3(PO_4)\cdot nH_2O$. Also, the presence of Mg^{2+} ions shows an inhibition effect on HAP growth despite other CaPs. This effect is possibly justified by competing for the Ca^{2+} structural sites, and the presence of CO_3^{2-} ions that can block the phosphate nucleation sites and therefore reduce the crystallinity or induce the $CaCO_3$ precipitation [270].

6 Summary and conclusions

Scanning Ion-selective Electrode Technique (SIET) was applied to monitor the *in situ* local pH above the surface of different degradable magnesium-based biomaterials (as-cast HP-Mg, as-cast Mg-1.2Ca, as-cast E11, and extruded (T4) Mg-2Ag) under different degradation solutions based on HBSS. Those results were correlated with the degradation rate, the characterisation of the degradation products layer, and the thermodynamically calculated phases, leading to the following findings:

- The SIET scans established a pH profile over the magnesium surface distinguishing a progressive higher pH environment near the surface in contrast with a lower pH of the bulk solution. Under the dynamic conditions applied in this work (1.5 mL/min), the pH varies within the 700 µm above the surface, that defines the diffusion layer for the OH^-/H^+ system. Those differences in the surface environment can be qualitatively equivalent to the concentration of Mg^{2+} ions, and in decreasing direction towards the surface for species that comes from the degradation solution like HCO_3^- or HPO_4^{2-}, due to their higher diffusion coefficients. Therefore, the interface environment is the one that controls the precipitation/dissolution equilibriums of the degradation products layer formation.

- The pH profile above the magnesium surface is affected by the following factors:
    i) The degradation solution exchange affects the mass transfer between the local surface environment and the bulk solution. The dynamic conditions applied in this work (1.5 mL/min) provide a stable bulk composition and pH, avoiding artefacts (e.g. abnormal alkalinisation) presented by the limited volume and limited mass transfer under static or semi-static circumstances. Therefore, a dynamic set-up presents a better capacity of mimicking the *in vivo* results given its potential capacity of mimicking the homeostasis capacity of a specific implantation site condition.

    ii) The buffering system can affect the bulk and the local pH environment. However, widely use buffering systems like HEPES also alter the local surface chemistry. Therefore, the use of buffering systems that simulate the physiological pH homeostasis (e.g., HCO_3/CO_2) is required when an experiment aims the study of degradation mechanisms.

    iii) The *alloy composition/microstructure* has an intrinsic degradation rate that is translated into a specific OH^- and Mg^{2+} ions release. The releasing rate of those products is the source of the alkalinisation process at the surface.

iv) The ionic composition of the corrosive solution at the surface promotes a specific degradation products layer composition and compactness. The compactness of this products layer modulates the kinetics of the magnesium dissolution and therefore the OH^- and Mg^{2+} released to the surface.

v) The precipitation/dissolution equilibriums involving the degradation products layer formation generate a local buffering system at the surface. Those precipitation/dissolution processes modulate the OH^- releasing promoting the same interface pH for significant differences in the dissolution rates. (e.g., between the E11 and HP-Mg systems).

- The immersion of magnesium-based materials under simple solutions like HBSS leads to the formation of a degradation products layer formed by a bilayer structure of an inner layer $MgO/Mg(OH)_2$ *brucite* and an outer layer of amorphous Mg-carbonates and phosphates. This degradation products layer revealed a low protective capacity that promotes an interface pH between 10 and 10.5 units and high degradation rates.
- The addition of the physiologically relevant quantity of Ca^{2+} cations (2.5 mM) to the HBSS composition, generates fast initial precipitation of highly protective amorphous CaPs compounds. The compactness of the CaPs layer hinders actively the diffusion between the solution and the metallic surface, generating different environments at the interface *metal/degradation products layer* and the interface *degradation products layer/surface solution*. Those conditions promote the inward growth of the degradation products layer through the precipitation of Mg,Ca-carbonates that in synergic effect with the amorphous CaPs layer promote a significant decrease in the interface pH (between 8 and 8.5 units) and degradation rate.

Future studies correlating *in situ* interface pH, with local relevant ion concentrations (e.g., Ca^{2+}, Mg^{2+}, HCO_3^-, HPO_4^{2-}), and *in situ* degradation products layer characterisation for different magnesium-based systems and different fluid exchange rates, will bring valuable information to conform a better image of magnesium-based degradation mechanisms under specific implantation sites.

7 References

[1] L.L. Hench, E.C. Ethridge, Biomaterials - The interfacial problem, in: Adv. Biomed. Eng., Elsevier, 1975: pp. 35–150. doi:10.1016/B978-0-12-004905-9.50007-4.

[2] S.D. Bruck, Properties of Biomaterials in the Physiological Environment, CRC Press (Reissued), Boca Raton, 2019. doi:10.1201/9780429279584.

[3] J. Black, Biological Performance of Materials: Fundamentals of Biocompatibility, 4th ed., CRC Press, New York, 2006. doi:10.1002/jbm.820170313.

[4] B. Ratner, A. Hoffman, F. Schoen, J. Lemons, Biomaterial Science: An Introduction to materials in medicine, 2nd ed., Academic Press, 2013. doi:10.1016/C2009-0-02433-7.

[5] J.A. Planell, S.M. Best, D. Lacroix, A. Merolli, Bone repair biomaterials, 1st ed., Woodhead Publishing, 2009. doi:10.1016/B978-1-84569-385-5.50021-0.

[6] P.C. Salgado, P.C. Sathler, H.C. Castro, G.G. Alves, A.M. de Oliveira, R.C. de Oliveira, M.D.C. Maia, C.R. Rodrigues, P.G. Coelh, A. Fuly, L.M. Cabral, J.M. Granjeiro, Bone Remodeling, Biomaterials And Technological Applications: Revisiting Basic Concepts, J. Biomater. Nanobiotechnol. 02 (2011) 318–328. doi:10.4236/jbnb.2011.23039.

[7] Q. Chen, G.A. Thouas, Metallic implant biomaterials, Mater. Sci. Eng. R Reports. 87 (2015). doi:10.1016/j.mser.2014.10.001.

[8] B.D.B. Joseph DeAngelis, M.W.M. Andrew E. Caputo, Jeffrey W. Mast, Principles of Internal Fixation, in: Skelet. Trauma, 4th ed., Saunders, 2008: p. 2784. https://www.elsevier.com/books/skeletal-trauma/cotler/978-1-4160-2220-6.

[9] S. Garg, P.W. Serruys, Coronary stents: Current status, J. Am. Coll. Cardiol. 56 (2010) S1–S42. doi:10.1016/j.jacc.2010.06.007.

[10] D. Zhao, F. Witte, F. Lu, J. Wang, J. Li, L. Qin, Current status on clinical applications of magnesium-based orthopaedic implants: A review from clinical translational perspective., Biomaterials. 112 (2017) 287–302. doi:10.1016/j.biomaterials.2016.10.017.

[11] Z. Zhang, J.T. Egaña, A.K. Reckhenrich, T.L. Schenck, J.A. Lohmeyer, J.T. Schantz, H.G. MacHens, A.F. Schilling, Cell-based resorption assays for bone graft substitutes, Acta Biomater. 8 (2012) 13–19. doi:10.1016/j.actbio.2011.09.020.

[12] R. Mittal, J. Morley, H. Dinopoulos, E.G. Drakoulakis, E. Vermani, P. V. Giannoudis, Use of bio-resorbable implants for stabilisation of distal radius fractures: The United Kingdom patients' perspective, Injury. 36 (2005) 333–338. doi:10.1016/j.injury.2004.09.015.

[13] Y.F. Zheng, X.N. Gu, F. Witte, Biodegradable metals, Mater. Sci. Eng. R Reports. 77 (2014) 1–34. doi:10.1016/j.mser.2014.01.001.

[14] I. Vroman, L. Tighzert, Biodegradable polymers, Materials (Basel). 2 (2009) 307–344. doi:10.3390/ma2020307.

[15] B. Laycock, M. Nikolić, J.M. Colwell, E. Gauthier, P. Halley, S. Bottle, G. George, Lifetime prediction of biodegradable polymers, Prog. Polym. Sci. 71 (2017) 144–189. doi:10.1016/j.progpolymsci.2017.02.004.

[16] Z. Sheikh, S. Najeeb, Z. Khurshid, V. Verma, H. Rashid, M. Glogauer, Biodegradable materials for bone repair and tissue engineering applications, Materials (Basel). 8 (2015) 5744–5794. doi:10.3390/ma8095273.

[17] Y.F. Zheng, X.N. Gu, F. Witte, Biodegradable metals, Mater. Sci. Eng. R Reports. 77 (2014) 1–34. doi:10.1016/j.mser.2014.01.001.

[18] M. Peuster, C. Fink, P. Wohlsein, M. Bruegmann, A. Günther, V. Kaese, M. Niemeyer, H. Haferkamp, C. V. Schnakenburg, Degradation of tungsten coils implanted into the subclavian artery of New Zealand white rabbits is not associated with local or systemic toxicity, Biomaterials. 24 (2003) 393–399. doi:10.1016/S0142-9612(02)00352-6.

[19] M. Knuf, Biodegradation of tungsten embolisation coils used in children, Pediatr. Radiol. 32 (2002) 839–843. doi:10.1007/s00247-002-0825-1.

[20] Y.B. Wang, X.H. Xie, H.F. Li, X.L. Wang, M.Z. Zhao, E.W. Zhang, Y.J. Bai, Y.F. Zheng, L. Qin, Biodegradable CaMgZn bulk metallic glass for potential skeletal application, Acta Biomater. 7 (2011) 3196–3208. doi:10.1016/j.actbio.2011.04.027.

[21] W. Jiao, H.F. Li, K. Zhao, H.Y. Bai, Y.B. Wang, Y.F. Zheng, W.H. Wang, Development of CaZn based glassy alloys as potential biodegradable bone graft substitute, J. Non. Cryst. Solids. 357 (2011) 3830–3840. doi:10.1016/j.jnoncrysol.2011.08.003.

[22] K. Zhao, J.F. Li, D.Q. Zhao, M.X. Pan, W.H. Wang, Degradable Sr-based bulk metallic glasses, Scr. Mater. 61 (2009) 1091–1094. doi:10.1016/j.scriptamat.2009.08.042.

[23] F. Zivic, S. Affatato, M. Trajanovic, M. Schnabelrauch, N. Grujovic, K.L. Choy, Biomaterials in Clinical Practice, Springer International Publishing, 2018. doi:10.1007/978-3-319-68025-5.

[24] G. Katarivas Levy, J. Goldman, E. Aghion, The Prospects of Zinc as a Structural Material for Biodegradable Implants—A Review Paper, Metals (Basel). 7 (2017) 402. doi:10.3390/met7100402.

[25] J.J.D. Venezuela, S. Johnston, M.S. Dargusch, The Prospects for Biodegradable Zinc in Wound Closure Applications, Adv. Healthc. Mater. 1900408 (2019) 1–15. doi:10.1002/adhm.201900408.

[26] J. Venezuela, M.S. Dargusch, The influence of alloying and fabrication techniques on the mechanical properties, biodegradability and biocompatibility of zinc: A comprehensive review, Acta Biomater. 87 (2019) 1–40. doi:10.1016/j.actbio.2019.01.035.

[27] H. Li, Y. Zheng, L. Qin, Progress of biodegradable metals, Prog. Nat. Sci. Mater. Int. 24 (2014) 414–422. doi:10.1016/j.pnsc.2014.08.014.

[28] N.E.L. Saris, E. Mervaala, H. Karppanen, J.A. Khawaja, A. Lewenstam, Magnesium: An update on physiological, clinical and analytical aspects, Clin. Chim. Acta. 294 (2000) 1–26. doi:10.1016/S0009-8981(99)00258-2.

[29] L.A. Martini, Magnesium supplementation and bone turnover, Nutr. Rev. 57 (1999) 227–9. doi:10.1111/j.1753-4887.1999.tb06948.x.

[30] F. Witte, V. Kaese, H. Haferkamp, E. Switzer, A. Meyer-Lindenberg, C.J. Wirth, H. Windhagen, In vivo corrosion of four magnesium alloys and the associated bone

response, Biomaterials. 26 (2005) 3557–3563. doi:10.1016/j.biomaterials.2004.09.049.

[31] T. Kraus, S.F. Fischerauer, A.C. Hänzi, P.J. Uggowitzer, J.F. Löffler, A.M. Weinberg, Magnesium alloys for temporary implants in osteosynthesis: In vivo studies of their degradation and interaction with bone, Acta Biomater. 8 (2012) 1230–1238. doi:10.1016/j.actbio.2011.11.008.

[32] F. Witte, N. Hort, C. Vogt, S. Cohen, K.U. Kainer, R. Willumeit, F. Feyerabend, Degradable biomaterials based on magnesium corrosion, Curr. Opin. Solid State Mater. Sci. 12 (2008) 63–72. doi:10.1016/j.cossms.2009.04.001.

[33] F.A. Shah, M. Trobos, P. Thomsen, A. Palmquist, Commercially pure titanium (cp-Ti) versus titanium alloy (Ti6Al4V) materials as bone anchored implants - Is one truly better than the other?, Mater. Sci. Eng. C. 62 (2016) 960–966. doi:10.1016/j.msec.2016.01.032.

[34] C.N. Elias, J.H.C. Lima, R. Valiev, M.A. Meyers, Biomedical applications of titanium and its alloys, Jom. 60 (2008) 46–49. doi:10.1007/s11837-008-0031-1.

[35] M. Mccracken, Dental Implant Materials: Commercially Pure Titanium and Titanium Alloys, J Prosthod. 8 (1999) 40–43. doi:10.1111/j.1532-849X.1999.tb00006.x.

[36] B.J.C. Luthringer, F. Feyerabend, R.W. Römer, Magnesium-Based Implants: A Mini-Review, Magnes. Res. 27 (2014) 142–154. doi:10.1684/mrh.2015.0375.

[37] A. Sato, Y. Shimizu, Y. Imai, T. Mukai, A. Yamamoto, C. Miura, K. Muraki, Y. Sano, N. Ikeo, M. Tachi, Initial organ distribution and biological safety of Mg2+ released from a Mg alloy implant, Biomed. Mater. 13 (2018). doi:10.1088/1748-605X/aaa9d5.

[38] H.S. Han, S. Loffredo, I. Jun, J. Edwards, Y.C. Kim, H.K. Seok, F. Witte, D. Mantovani, S. Glyn-Jones, Current status and outlook on the clinical translation of biodegradable metals, Mater. Today. 23 (2019) 57–71. doi:10.1016/j.mattod.2018.05.018.

[39] R.J. Kroeze, M.N. Helder, L.E. Govaert, T.H. Smit, Biodegradable Polymers in Bone Tissue Engineering, Materials (Basel). 2 (2009) 833–856. doi:10.3390/ma2030833.

[40] K. Törne, M. Larsson, A. Norlin, J. Weissenrieder, Degradation of zinc in saline solutions, plasma, and whole blood, J. Biomed. Mater. Res. - Part B Appl. Biomater. 104 (2016) 1141–1151. doi:10.1002/jbm.b.33458.

[41] E. Mouzou, C. Paternoster, R. Tolouei, P. Chevallier, C.A. Biffi, A. Tuissi, D. Mantovani, CO2-rich atmosphere strongly affects the degradation of Fe-21Mn-1C for biodegradable metallic implants, Mater. Lett. 181 (2016) 362–366. doi:10.1016/j.matlet.2016.06.017.

[42] H.T. Abbas, Q.H. Abbasi, L.N. Aljihmani, Y. Boudjemline, Z. Hijazi, Remote Monitoring of Absorbable Cardiovascular Stents using Millimetre Waves, 2019 16th Int. Symp. Wirel. Commun. Syst. (2019) 450–451. doi:10.1109/ISWCS.2019.8877268.

[43] I. Bartsch, E. Willbold, B. Rosenhahn, F. Witte, Non-invasive pH determination adjacent to degradable biomaterials in vivo, Acta Biomater. 10 (2014) 34–39. doi:10.1016/j.actbio.2013.08.047.

[44] J. Gonzalez, R.Q. Hou, E.P.S. Nidadavolu, R. Willumeit-Römer, F. Feyerabend, Magnesium degradation under physiological conditions – Best practice, Bioact. Mater.

3 (2018) 174–185. doi:10.1016/j.bioactmat.2018.01.003.

[45] A. Myrissa, N.A. Agha, Y. Lu, E. Martinelli, J. Eichler, G. Szakács, C. Kleinhans, R. Willumeit-Römer, U. Schäfer, A.-M. Weinberg, In vitro and in vivo comparison of binary Mg alloys and pure Mg, Mater. Sci. Eng. C. Mater. Biol. Appl. 61 (2016) 865–74. doi:10.1016/j.msec.2015.12.064.

[46] N.T. Kirkland, N. Birbilis, M.P. Staiger, Assessing the corrosion of biodegradable magnesium implants: A critical review of current methodologies and their limitations, Acta Biomater. 8 (2012) 925–936. doi:10.1016/j.actbio.2011.11.014.

[47] S. Johnston, M. Dargusch, A. Atrens, Building towards a standardised approach to biocorrosion studies: a review of factors influencing Mg corrosion in vitro pertinent to in vivo corrosion, Sci. China Mater. 61 (2017) 475–500. doi:10.1007/s40843-017-9173-7.

[48] N.A. Agha, F. Feyerabend, B. Mihailova, S. Heidrich, U. Bismayer, R. Willumeit-Römer, Magnesium degradation influenced by buffering salts in concentrations typical of in vitro and in vivo models, Mater. Sci. Eng. C. Mater. Biol. Appl. 58 (2016) 817–25. doi:10.1016/j.msec.2015.09.067.

[49] S. Johnston, Z. Shi, A. Atrens, The influence of pH on the corrosion rate of high-purity Mg, AZ91 and ZE41 in bicarbonate buffered Hanks' solution, Corros. Sci. 101 (2015) 182–192. doi:10.1016/j.corsci.2015.09.018.

[50] I. Marco, F. Feyerabend, R. Willumeit-Römer, O. Van Der Biest, Degradation testing of Mg alloys in Dulbecco's modified eagle medium: Influence of medium sterilization, Mater. Sci. Eng. C. 62 (2016) 68–78. doi:10.1016/j.msec.2016.01.039.

[51] I. Marco, F. Feyerabend, R. Willumeit-Römer, O. Van der Biest, Influence of Testing Environment on the Degradation Behavior of Magnesium Alloys for Bioabsorbable Implants, TMS2015 Suppl. Proc. (2015) 497–506. doi:10.1002/9781119093466.ch63.

[52] A.H.M. Sanchez, B.J.C. Luthringer, F. Feyerabend, R. Willumeit, Mg and Mg alloys: How comparable are in vitro and in vivo corrosion rates? A review, Acta Biomater. 13 (2015) 16–31. doi:10.1016/j.actbio.2014.11.048.

[53] P.K. Bowen, J. Drelich, J. Goldman, A new in vitro-in vivo correlation for bioabsorbable magnesium stents from mechanical behavior., Mater. Sci. Eng. C. Mater. Biol. Appl. 33 (2013) 5064–70. doi:10.1016/j.msec.2013.08.042.

[54] A.J. Bard, L.R. Faulkner, Electrochemical Methods - Fundamentals and Applications, 2nd ed., John Wiley & Sons, Inc., 2001. doi:10.1016/B978-0-12-381373-2.00056-9.

[55] Hans-Henning Strehblow, P. Marcus, Fundamentals of Corrosion, in: Corros. Mech. Theory Pract., 3rd ed., CRC Press, Boca Raton, 2012. doi:10.1201/b11020.

[56] G. Song, A. Atrens, M. Dargusch, Influence of microstructure on the corrosion of diecast AZ91D, Corros. Sci. 41 (1998) 249–273. doi:10.1016/S0010-938X(98)00121-8.

[57] M.-C. Zhao, M. Liu, G. Song, A. Atrens, Influence of the β-phase morphology on the corrosion of the Mg alloy AZ91, Corros. Sci. 50 (2008) 1939–1953. doi:10.1016/j.corsci.2008.04.010.

[58] K. Gusieva, C.H.J. Davies, J.R. Scully, N. Birbilis, Corrosion of magnesium alloys: the role of alloying, Int. Mater. Rev. 60 (2014) 1743280414Y.000.

doi:10.1179/1743280414Y.0000000046.

[59] M. Esmaily, J.E. Svensson, S. Fajardo, N. Birbilis, G.S. Frankel, S. Virtanen, R. Arrabal, S. Thomas, L.G. Johansson, Fundamentals and advances in magnesium alloy corrosion, Prog. Mater. Sci. 89 (2017) 92–193. doi:10.1016/j.pmatsci.2017.04.011.

[60] E. Koç, M.B. Kannan, M. Ünal, E. Candan, In fluence of zinc on the microstructure , mechanical properties and in vitro corrosion behavior of magnesium e zinc binary alloys, J. Alloys Compd. 648 (2015) 291–296. doi:10.1016/j.jallcom.2015.06.227.

[61] H.R.B. Rad, M.H. Idris, M.R.A. Kadir, S. Farahany, Microstructure analysis and corrosion behavior of biodegradable Mg-Ca implant alloys, Mater. Des. 33 (2012) 88–97. doi:10.1016/j.matdes.2011.06.057.

[62] L. Hou, Z. Li, H. Zhao, Y. Pan, S. Pavlinich, X. Liu, X. Li, Y. Zheng, L. Li, Microstructure, Mechanical Properties, Corrosion Behavior and Biocompatibility of As-Extruded Biodegradable Mg–3Sn–1Zn–0.5Mn Alloy, J. Mater. Sci. Technol. 32 (2016) 874–882. doi:10.1016/j.jmst.2016.07.004.

[63] P.-R. Cha, H.-S. Han, G.-F. Yang, Y.-C. Kim, K.-H. Hong, S.-C. Lee, J.-Y. Jung, J.-P. Ahn, Y.-Y. Kim, S.-Y. Cho, J.Y. Byun, K.-S. Lee, S.-J. Yang, H.-K. Seok, Biodegradability engineering of biodegradable Mg alloys: tailoring the electrochemical properties and microstructure of constituent phases., Sci. Rep. 3 (2013). doi:10.1038/srep02367.

[64] J. Harmuth, B. Wiese, J. Bohlen, T. Ebel, R. Willumeit-Römer, Wide Range Mechanical Customization of Mg-Gd Alloys With Low Degradation Rates by Extrusion, Front. Mater. 6 (2019). doi:10.3389/fmats.2019.00201.

[65] C.Z. Zhang, S.J. Zhu, L.G. Wang, R.M. Guo, G.C. Yue, S.K. Guan, Microstructures and degradation mechanism in simulated body fluid of biomedical Mg-Zn-Ca alloy processed by high pressure torsion, Mater. Des. 96 (2016) 54–62. doi:10.1016/j.matdes.2016.01.072.

[66] E. Mostaed, M. Hashempour, A. Fabrizi, D. Dellasega, M. Bestetti, F. Bonollo, M. Vedani, Microstructure, texture evolution, mechanical properties and corrosion behavior of ECAP processed ZK60 magnesium alloy for biodegradable applications., J. Mech. Behav. Biomed. Mater. 37 (2014) 307–22. doi:10.1016/j.jmbbm.2014.05.024.

[67] E. Mostaed, M. Vedani, M. Hashempour, M. Bestetti, Influence of ECAP process on mechanical and corrosion properties of pure Mg and ZK60 magnesium alloy for biodegradable stent applications, Biomatter. 4 (2014) e28283. doi:10.4161/biom.28283.

[68] M. Alvarez-Lopez, M.D. Pereda, J.A. Del Valle, M. Fernandez-Lorenzo, M.C. Garcia-Alonso, O.A. Ruano, M.L. Escudero, Corrosion behaviour of AZ31 magnesium alloy with different grain sizes in simulated biological fluids, Acta Biomater. 6 (2010) 1763–1771. doi:10.1016/j.actbio.2009.04.041.

[69] N. Sato, Basics of Corrosion Chemistry, in: Green Corros. Chem. Eng. Oppor. Challenges, 2011: pp. 1–32. doi:10.1002/9783527641789.ch1.

[70] D. Snihirova, M. Taryba, S. V. Lamaka, M.F. Montemor, Corrosion inhibition synergies on a model Al-Cu-Mg sample studied by localized scanning electrochemical techniques, Corros. Sci. 112 (2016) 408–417. doi:10.1016/j.corsci.2016.08.008.

[71] N.T. Kirkland, N. Birbilis, Magnesium Biomaterials Design, Testing, and Best Practice, Springer, 2014. doi:10.1007/978-3-319-02123-2.

[72] T. Cain, L.G. Bland, N. Birbilis, J.R. Scully, A compilation of corrosion potentials for magnesium alloys, Corrosion. 70 (2014) 1043–1051. doi:10.5006/1257.

[73] G.L. Song, A. Atrens, Corrosion mechanisms of magnesium alloys, Adv. Eng. Mater. 1, Issue 1, Sept. , Pages . 1 (1999) 11–33.

[74] W.F. Ng, K.Y. Chiu, F.T. Cheng, Effect of pH on the in vitro corrosion rate of magnesium degradable implant material, Mater. Sci. Eng. C. 30 (2010) 898–903. doi:10.1016/j.msec.2010.04.003.

[75] G. L. Makar, J. Kruger, Corrosion of magnesium, Int. Mater. Rev. 38 (1993). doi:10.1179/imr.1993.38.3.138.

[76] J.A. Yuwono, N. Birbilis, C.D. Taylor, K.S. Williams, A.J. Samin, N. V. Medhekar, Aqueous electrochemistry of the magnesium surface: Thermodynamic and kinetic profiles, Corros. Sci. 147 (2019) 53–68. doi:10.1016/j.corsci.2018.10.014.

[77] O.S. Pokrovsky, J. Schott, Experimental study of brucite dissolution and precipitation in aqueous solutions: Surface speciation and chemical affinity control, Geochim. Cosmochim. Acta. 68 (2004) 31–45. doi:10.1016/S0016-7037(03)00238-2.

[78] D. Mercier, J. Swiatowska, S. Zanna, A. Seyeux, P. Marcus, Role of segregated iron at grain boundaries on Mg corrosion, J. Electrochem. Soc. 165 (2018) C42–C49. doi:10.1149/2.0621802jes.

[79] E. Michailidou, H.N. McMurray, G. Williams, Quantifying the role of transition metal electrodeposition in the cathodic activation of corroding magnesium, J. Electrochem. Soc. 165 (2018) C195–C205. doi:10.1149/2.0251805jes.

[80] L. Wang, T. Shinohara, B.P. Zhang, Influence of deaerated condition on the corrosion behavior of AZ31 magnesium alloy in dilute NaCl solutions, Mater. Trans. 50 (2009) 2563–2569. doi:10.2320/matertrans.M2009191.

[81] E.L. Silva, S. V. Lamaka, D. Mei, M.L. Zheludkevich, The Reduction of Dissolved Oxygen During Magnesium Corrosion, ChemistryOpen. 7 (2018) 664–668. doi:10.1002/open.201800076.

[82] G. Song, a. Atrens, Understanding Magnesium Corrosion—A Framework for Improved Alloy Performance, Adv. Eng. Mater. 5 (2003) 837–858. doi:10.1002/adem.200310405.

[83] Y. Yang, J. Scantlebury, E. Koroleva, A Study of Calcareous Deposits on Cathodically Protected Mild Steel in Artificial Seawater, Metals (Basel). 5 (2015) 439–456. doi:10.3390/met5010439.

[84] X. Li, C. Chu, P.K. Chu, Effects of external stress on biodegradable orthopedic materials: A review, Bioact. Mater. 1 (2016) 77–84. doi:10.1016/j.bioactmat.2016.09.002.

[85] X.N. Gu, Y. Lu, F. Wang, W. Lin, P. Li, Y. Fan, The effect of tensile and fluid shear stress on the in vitro degradation of magnesium alloy for stent applications, Bioact. Mater. 3 (2018) 448–454. doi:10.1016/j.bioactmat.2018.08.002.

[86] B. Denkena, J. Köhler, J. Stieghorst, A. Turger, J. Seitz, D.R. Fau, L. Wolters, N.

Angrisani, J. Reifenrath, P. Helmecke, Influence of stress on the degradation behavior of Mg LAE442 implant systems, Procedia CIRP. 5 (2013) 189–195. doi:10.1016/j.procir.2013.01.038.

[87] Y. Koo, H.B. Lee, Z. Dong, R. Kotoka, J. Sankar, N. Huang, Y. Yun, The Effects of Static and Dynamic Loading on Biodegradable Magnesium Pins in Vitro and in Vivo, Sci. Rep. 7 (2017) 1–9. doi:10.1038/s41598-017-14836-5.

[88] P.B. Srinivasan, C. Blawert, W. Dietzel, K.U. Kainer, Stress corrosion cracking behaviour of a surface-modified magnesium alloy, Scr. Mater. 59 (2008) 43–46. doi:10.1016/j.scriptamat.2008.02.032.

[89] G. Williams, H. Dayfydd, R. Subramanian, Chloride Ion Concentration Effects on Passivity Breakdown in Magnesium, ECS Trans. 58 (2014) 23–34. doi:10.1149/05831.0023ecst.

[90] Y. Song, D. Shan, R. Chen, F. Zhang, E.-H. Han, Biodegradable behaviors of AZ31 magnesium alloy in simulated body fluid, Mater. Sci. Eng. C. 29 (2009) 1039–1045. doi:10.1016/j.msec.2008.08.026.

[91] R.-C. Zeng, X.-T. Li, S.-Q. Li, F. Zhang, E.-H. Han, In vitro degradation of pure Mg in response to glucose, Sci. Rep. 5 (2015) 13026. doi:10.1038/srep13026.

[92] M. Pannach, S. Bette, D. Freyer, Solubility Equilibria in the System Mg(OH)2-MgCl2-H2O from 298 to 393 K, J. Chem. Eng. Data. 62 (2017) 1384–1396. doi:10.1021/acs.jced.6b00928.

[93] C. Mazuranic, H. Bilinski, B. Matkovic, Reaction Products in the System MgC12-NaOH-H20, J. Am. Ceram. Soc. 65 (1982) 523–526. doi:10.1111/j.1151-2916.1982.tb10346.x.

[94] C. Taltavull, Z. Shi, B. Torres, J. Rams, A. Atrens, Influence of the chloride ion concentration on the corrosion of high-purity Mg, ZE41 and AZ91 in buffered Hank's solution, J. Mater. Sci. Mater. Med. 25 (2014) 329–345. doi:10.1007/s10856-013-5087-y.

[95] Y. Xin, K. Huo, H. Tao, G. Tang, P.K. Chu, Influence of aggressive ions on the degradation behavior of biomedical magnesium alloy in physiological environment, Acta Biomater. 4 (2008) 2008–2015. doi:10.1016/j.actbio.2008.05.014.

[96] G. Baril, N. Pébère, Corrosion of pure magnesium in aerated and deaerated sodium sulphate solutions, Corros. Sci. 43 (2001) 471–484. doi:10.1016/S0010-938X(00)00095-0.

[97] L. jing Yang, Y. hui Wei, L. feng Hou, D. Zhang, Corrosion behaviour of die-cast AZ91D magnesium alloy in aqueous sulphate solutions, Corros. Sci. 52 (2010) 345–351. doi:10.1016/j.corsci.2009.09.020.

[98] E. Gulbrandsen, Anodic behaviour of Mg in HCO3-/CO2- buffer solutions. Quasi-steady measurements, Electrochim. Acta. (1992) 1403–1412. doi:doi.org/10.1016/0013-4686(92)87014-Q.

[99] Z. Li, G.L. Song, S. Song, Effect of bicarbonate on biodegradation behaviour of pure magnesium in a simulated body fluid, Electrochim. Acta. 115 (2014) 56–65. doi:10.1016/j.electacta.2013.10.131.

[100] G. Williams, H.N. McMurray, R. Grace, Inhibition of magnesium localised corrosion in

chloride containing electrolyte, Electrochim. Acta. 55 (2010) 7824–7833. doi:10.1016/j.electacta.2010.03.023.

[101] R. Zauner, Scale-Up of Precipitation Processes, University College London - Ramsay Memorial Laboratory of Chemical Engineering, 1994. http://hdl.handle.net/10068/615643.

[102] J.E. McMurry, R.C. Fay, J.K. Robinson, Applications of Aqueous Equilibria, in: Chemistry (Easton)., 4th ed., Pearson, 2003.

[103] W. Stumm, J.J. Morgan, Aquatic Chemistry. An Introduction Emphasizing Chemical Equilibria in Natural Waters, 2nd ed., John Wiley & Sons, Inc., 1981. doi:https://doi.org/10.1002/aheh.19730010116.

[104] P. Atkins, J. de Paula, Chemical equilibrium, in: Atkin's Phys. Chem., 8th ed., Oxford University Press, 2006: pp. 200–239.

[105] C. Aparicio, M.-P. Ginebra, Biomineralization and Biomaterials: Fundamentals and Applications, 1st ed., Woodhead Publishing, 2016. doi:10.1016/B978-1-78242-338-6.00014-4.

[106] A. Dhanapal, S. Rajendraboopathy, V. Balasubramanian, S.R. Rao, A.R.T. Zaman, Effect of pH values, chloride ion concentration and exposure time on pitting corrosion rates of friction stir welded AZ61A magnesium alloy in sodium chloride solution using surface response methodology, Corros. Eng. Sci. Technol. 47 (2012) 425–440. doi:10.1179/1743278212Y.0000000021.

[107] N.T. Kirkland, J. Waterman, N. Birbilis, G. Dias, T.B.F. Woodfield, R.M. Hartshorn, M.P. Staiger, Buffer-regulated biocorrosion of pure magnesium, J. Mater. Sci. Mater. Med. 23 (2012) 283–291. doi:10.1007/s10856-011-4517-y.

[108] R.-C. Zeng, X.-T. Li, S.-Q. Li, F. Zhang, E.-H. Han, In vitro degradation of pure Mg in response to glucose, Sci. Rep. 5 (2015) 13026. doi:10.1038/srep13026.

[109] Y. Wang, L.Y. Cui, R.C. Zeng, S.Q. Li, Y.H. Zou, E.H. Han, In vitro degradation of pure magnesium-The effects of glucose and/or amino acid, Materials (Basel). 10 (2017). doi:10.3390/ma10070725.

[110] R.-Q. Hou, N. Scharnagl, F. Feyerabend, R. Willumeit-Römer, Exploring the effects of organic molecules on the degradation of magnesium under cell culture conditions, Corros. Sci. (2017) 0–1. doi:10.1016/j.corsci.2017.12.023.

[111] H. Ashassi-Sorkhabi, M.R. Majidi, K. Seyyedi, Investigation of inhibition effect of some amino acids against steel corrosion in HCl solution, Appl. Surf. Sci. 225 (2004) 176–185. doi:10.1016/j.apsusc.2003.10.007.

[112] H. Ashassi-Sorkhabi, Z. Ghasemi, D. Seifzadeh, The inhibition effect of some amino acids towards the corrosion of aluminum in 1 M HCl + 1 M H2SO4solution, Appl. Surf. Sci. 249 (2005) 408–418. doi:10.1016/j.apsusc.2004.12.016.

[113] S. Höhn, S. Virtanen, A.R. Boccaccini, Protein adsorption on magnesium and its alloys: A review, Appl. Surf. Sci. 464 (2019) 212–219. doi:10.1016/j.apsusc.2018.08.173.

[114] J. D. Andrade, V. Hlady, Protein Adsorption and Materials Biocompatibility: A Tutorial Review and Suggested Hypotheses, Biopolym. HPLC. Adv. Polym. Sci. 79 (1986). doi:10.1007/3-540-16422-7_6.

[115] R. Hou, R. Willumeit-Römer, V.M. Garamus, M. Frant, J. Koll, F. Feyerabend, Adsorption of Proteins on Degradable Magnesium—Which Factors are Relevant?, ACS Appl. Mater. Interfaces. (2018) acsami.8b17507. doi:10.1021/acsami.8b17507.

[116] C.L. Liu, Y.J. Wang, R.C. Zeng, X.M. Zhang, W.J. Huang, P.K. Chu, In vitro corrosion degradation behaviour of Mg-Ca alloy in the presence of albumin, Corros. Sci. 52 (2010) 3341–3347. doi:10.1016/j.corsci.2010.06.003.

[117] P. Roach, D. Farrar, C.C. Perry, Interpretation of protein adsorption: Surface-induced conformational changes, J. Am. Chem. Soc. 127 (2005) 8168–8173. doi:10.1021/ja042898o.

[118] A. Yamamoto, S. Hiromoto, Effect of inorganic salts, amino acids and proteins on the degradation of pure magnesium in vitro, Mater. Sci. Eng. C. 29 (2009) 1559–1568. doi:10.1016/j.msec.2008.12.015.

[119] S. Virtanen, Biodegradable Mg and Mg alloys: Corrosion and biocompatibility, Mater. Sci. Eng. B. 176 (2011) 1600–1608. doi:10.1016/j.mseb.2011.05.028.

[120] M.A. Khan, R.L. Williams, D.F. Williams, The corrosion behaviour of Ti-6Al-4V, Ti-6Al-7Nb and Ti-13Nb-13Zr in protein solutions, Biomaterials. 20 (1999) 631–637. doi:10.1016/S0142-9612(98)00217-8.

[121] J. Walker, S. Shadanbaz, N.T. Kirkland, E. Stace, T. Woodfield, M.P. Staiger, G.J. Dias, Magnesium alloys: Predicting in vivo corrosion with in vitro immersion testing, J. Biomed. Mater. Res. - Part B Appl. Biomater. 100 B (2012) 1134–1141. doi:10.1002/jbm.b.32680.

[122] C.-L. Liu, Y. Zhang, C.-Y. Zhang, W. Wang, W.-J. Huang, P.K. Chu, Synergistic effect of chloride ion and albumin on the corrosion of pure magnesium, Front. Mater. Sci. 8 (2014) 244–255. doi:10.1007/s11706-014-0251-y.

[123] Y. Hedberg, X. Wang, J. Hedberg, M. Lundin, E. Blomberg, I. Odnevall Wallinder, Surface-protein interactions on different stainless steel grades: Effects of protein adsorption, surface changes and metal release, J. Mater. Sci. Mater. Med. 24 (2013) 1015–1033. doi:10.1007/s10856-013-4859-8.

[124] R. Willumeit, J. Fischer, F. Feyerabend, N. Hort, U. Bismayer, S. Heidrich, B. Mihailova, Chemical surface alteration of biodegradable magnesium exposed to corrosion media, Acta Biomater. 7 (2011) 2704–2715. doi:10.1016/j.actbio.2011.03.004.

[125] Y. Wang, C.S. Lim, C.V. Lim, M.S. Yong, E.K. Teo, L.N. Moh, In vitro degradation behavior of M1A magnesium alloy in protein-containing simulated body fluid, Mater. Sci. Eng. C. 31 (2011) 579–587. doi:10.1016/j.msec.2010.11.017.

[126] L. Wu, F. Feyerabend, A.F. Schilling, R. Willumeit-Römer, B.J.C. Luthringer, Effects of extracellular magnesium extract on the proliferation and differentiation of human osteoblasts and osteoclasts in coculture, Acta Biomater. 27 (2015) 294–304. doi:10.1016/j.actbio.2015.08.042.

[127] W.R. Zhou, Y.F. Zheng, M.A. Leeflang, J. Zhou, Mechanical property, biocorrosion and in vitro biocompatibility evaluations of Mg-Li-(Al)-(RE) alloys for future cardiovascular stent application, Acta Biomater. 9 (2013). doi:10.1016/j.actbio.2013.01.032.

[128] S. Yoshizawa, A. Brown, A. Barchowsky, C. Sfeir, Magnesium ion stimulation of bone

marrow stromal cells enhances osteogenic activity, simulating the effect of magnesium alloy degradation, Acta Biomater. 10 (2014) 2834–2842. doi:10.1016/j.actbio.2014.02.002.

[129] M.E. Iskandar, A. Aslani, Q. Tian, H. Liu, Nanostructured calcium phosphate coatings on magnesium alloys: characterization and cytocompatibility with mesenchymal stem cells, J. Mater. Sci. Mater. Med. 26 (2015). doi:10.1007/s10856-015-5512-5.

[130] N. Zhao, B. Workman, D. Zhu, Endothelialization of novel magnesium-rare earth alloys with fluoride and collagen coating, Int. J. Mol. Sci. 15 (2014) 5263–5276. doi:10.3390/ijms15045263.

[131] F. Feyerabend, J. Fischer, J. Holtz, F. Witte, R. Willumeit, H. Drücker, C. Vogt, N. Hort, Evaluation of short-term effects of rare earth and other elements used in magnesium alloys on primary cells and cell lines, Acta Biomater. 6 (2010) 1834–1842. doi:10.1016/j.actbio.2009.09.024.

[132] F. Feyerabend, H.-P. Wendel, B. Mihailova, S. Heidrich, N.A. Agha, U. Bismayer, R. Willumeit-Römer, Blood compatibility of magnesium and its alloys., Acta Biomater. 25 (2015) 384–94. doi:10.1016/j.actbio.2015.07.029.

[133] M.B. Kannan, A. Yamamoto, H. Khakbaz, Influence of living cells (L929) on the biodegradation of magnesium–calcium alloy, Colloids Surfaces B Biointerfaces. 126 (2015) 603–606. doi:10.1016/j.colsurfb.2015.01.015.

[134] N. Ahmad Agha, R. Willumeit-Römer, D. Laipple, B. Luthringer, F. Feyerabend, The Degradation Interface of Magnesium Based Alloys in Direct Contact with Human Primary Osteoblast Cells, PLoS One. 11 (2016) e0157874. doi:10.1371/journal.pone.0157874.

[135] Y. Shih, J.M. Prausnitz, H.W. Blanch, Some Characteristics of Protein Precipitation by Salts, Biotechnology. 40 (1992) 1155–1164. doi:10.1002/bit.260401004.

[136] C. Liu, Y. Xin, X. Tian, P.K. Chu, Degradation susceptibility of surgical magnesium alloy in artificial biological fluid containing albumin, J. Mater. Res. 22 (2007) 1806–1814. doi:10.1557/jmr.2007.0241.

[137] S. Omanovic, S.G. Roscoe, Electrochemical studies of the adsorption behavior of bovine serum albumin on stainless steel, Langmuir. 15 (1999) 8315–8321. doi:10.1021/la990474f.

[138] J.J. MacFarlane, Diffusion, Boundary Layers and the Uptake of Nutrients by Aquatic Macrophytes, University of Adelaide, 1985.

[139] D. Landolt, Corrosion and surface chemistry of metals, CRC Press, 2007. doi:10.1016/S1369-7021(07)70081-0.

[140] N. Erdmann, N. Angrisani, J. Reifenrath, A. Lucas, F. Thorey, D. Bormann, A. Meyer-Lindenberg, Biomechanical testing and degradation analysis of MgCa0.8 alloy screws: A comparative in vivo study in rabbits, Acta Biomater. 7 (2011) 1421–1428. doi:10.1016/j.actbio.2010.10.031.

[141] C. Rössig, N. Angrisani, P. Helmecke, S. Besdo, J.-M. Seitz, B. Welke, N. Fedchenko, H. Kock, J. Reifenrath, In vivo evaluation of a magnesium-based degradable intramedullary nailing system in a sheep model., Acta Biomater. 25 (2015) 369–83. doi:10.1016/j.actbio.2015.07.025.

[142] Y. Jang, B. Collins, J. Sankar, Y. Yun, Effect of biologically relevant ions on the corrosion products formed on alloy AZ31B: An improved understanding of magnesium corrosion, Acta Biomater. 9 (2013) 8761–8770. doi:10.1016/j.actbio.2013.03.026.

[143] Y.F. Zhang, B. Hinton, G. Wallace, X. Liu, M. Forsyth, On corrosion behaviour of magnesium alloy AZ31 in simulated body fluids and influence of ionic liquid pretreatments, Corros. Eng. Sci. Technol. 47 (2012) 374–382. doi:10.1179/1743278212Y.0000000032.

[144] ASTM G31-72(2004), Standard Practice for Laboratory Immersion Corrosion Testing of Metals, West Conshohocken, PA, 2004. doi:10.1520/G0031-72R04.

[145] ISO, DIN EN ISO 10993:2012-10. Biological evaluation of medical devices - Part 12: Sample preparation and reference materials, 4th ed., 2012. doi:10.31030/1860096.

[146] K. Lips, P. Schmutz, M. Heer, P.J. Uggowitzer, S. Virtanen, Electrochemical corrosion investigation on Mg alloy AZ91: Description of critical parameters and their influence on the mechanisms of attack on NRC type alloys, Mater. Corros. 55 (2004) 5–17. doi:10.1002/maco.200303689.

[147] L. Yang, E. Zhang, Biocorrosion behavior of magnesium alloy in different simulated fluids for biomedical application, Mater. Sci. Eng. C. 29 (2009) 1691–1696. doi:10.1016/j.msec.2009.01.014.

[148] N. Rodríguez-Laguna, A. Rojas-Hernández, M.T. Ramírez-Silva, Estudio y comportamiento de la capacidad buffer de mezclas de especies de un mismo sistema polidonador de protones, Educ. Quim. 25 (2014) 210–222. doi:10.1016/S0187-893X(14)70560-9.

[149] G. Williams, H. Neil McMurray, Localized Corrosion of Magnesium in Chloride-Containing Electrolyte Studied by a Scanning Vibrating Electrode Technique, J. Electrochem. Soc. 155 (2008) C340. doi:10.1149/1.2918900.

[150] D. Tie, F. Feyerabend, N. Hort, R. Willumeit, D. Hoeche, XPS Studies of Magnesium Surfaces after Exposure to Dulbecco's Modified Eagle Medium, Hank's Buffered Salt Solution, and Simulated Body Fluid, Adv. Eng. Mater. 12 (2010) B699–B704. doi:10.1002/adem.201080070.

[151] M. Kieke, F. Feyerabend, J. Lemaitre, P. Behrens, R. Willumeit-Römer, Degradation rates and products of pure magnesium exposed to different aqueous media under physiological conditions, BioNanoMaterials. 0 (2016). doi:10.1515/bnm-2015-0020.

[152] M.J.J.M. van Kemenade, P.L. de B. Bruyn, A Kinetic Study of Precipitation from Supersaturated Calcium Phosphate Solutions, J. Colloid Interface Sci. 118 (1987) 564–585. doi:10.1016/0021-9797(87)90490-5.

[153] A. Ferreira, C. Oliveira, F. Rocha, The different phases in the precipitation of dicalcium phosphate dihydrate, J. Cryst. Growth. 252 (2003) 599–611. doi:10.1016/S0022-0248(03)00899-6.

[154] R. Pörtner, C. Giese, An Overview on Bioreactor Design, Prototyping and Process Control for Reproducible Three-Dimensional Tissue Culture, Drug Test. Vitr. Break. Trends Cell Cult. Technol. (2006) 53–78. doi:10.1002/9783527609611.ch2.

[155] I. Marco, O. Van der Biest, Polarization measurements from a rotating disc electrode for characterization of magnesium corrosion, Corros. Sci. 102 (2016) 384–393. doi:10.1016/j.corsci.2015.10.031.

[156] A.P. Md. Saad, N. Jasmawati, M.N. Harun, M.R. Abdul Kadir, H. Nur, H. Hermawan, A. Syahrom, Dynamic degradation of porous magnesium under a simulated environment of human cancellous bone, Corros. Sci. 112 (2016) 495–506. doi:10.1016/j.corsci.2016.08.017.

[157] J. Wang, Y. Jang, G. Wan, V. Giridharan, G.-L. Song, Z. Xu, Y. Koo, P. Qi, J. Sankar, N. Huang, Y. Yun, Flow-induced corrosion of absorbable magnesium alloy: In-situ and real-time electrochemical study, Corros. Sci. 104 (2016) 277–289. doi:10.1016/j.corsci.2015.12.020.

[158] J.A. Grogan, D. Gastaldi, M. Castelletti, F. Migliavacca, G. Dubini, P.E. McHugh, A novel flow chamber for biodegradable alloy assessment in physiologically realistic environments, Rev. Sci. Instrum. 84 (2013). doi:10.1063/1.4821498.

[159] J. Lévesque, H. Hermawan, D. Dubé, D. Mantovani, Design of a pseudo-physiological test bench specific to the development of biodegradable metallic biomaterials, Acta Biomater. 4 (2008) 284–295. doi:10.1016/j.actbio.2007.09.012.

[160] B. Zeller-Plumhoff, H. Helmholz, F. Feyerabend, T. Dose, F. Wilde, A. Hipp, F. Beckmann, R. Willumeit-Römer, J.U. Hammel, Quantitative characterization of degradation processes in situ by means of a bioreactor coupled flow chamber under physiological conditions using time-lapse SRμCT, Mater. Corros. (2017) 1–9. doi:10.1002/maco.201709514.

[161] Y. Chen, S. Zhang, J. Li, Y. Song, C. Zhao, X. Zhang, Dynamic degradation behavior of MgZn alloy in circulating m-SBF, Mater. Lett. 64 (2010) 1996–1999. doi:10.1016/j.matlet.2010.06.011.

[162] A.P. Md Saad, R.A. Abdul Rahim, M.N. Harun, H. Basri, J. Abdullah, M.R. Abdul Kadir, A. Syahrom, The influence of flow rates on the dynamic degradation behaviour of porous magnesium under a simulated environment of human cancellous bone, Mater. Des. 122 (2017) 268–279. doi:10.1016/j.matdes.2017.03.029.

[163] J. Wang, C.E. Smith, J. Sankar, Y. Yun, N. Huang, Absorbable magnesium-based stent: physiological factors to consider for in vitro degradation assessments, Regen. Biomater. 2 (2015) 59–69. doi:10.1093/rb/rbu015.

[164] A. Chaya, S. Yoshizawa, K. Verdelis, N. Myers, B.J. Costello, D.-T. Chou, S. Pal, S. Maiti, P.N. Kumta, C. Sfeir, In vivo study of magnesium plate and screw degradation and bone fracture healing., Acta Biomater. 18 (2015) 262–9. doi:10.1016/j.actbio.2015.02.010.

[165] D.B. Burr, M.R. Allen, Basic and Applied Bone Biology, Elsevier, 2014. doi:10.1016/C2011-0-05817-9.

[166] Stephen C. Cowin, Bone mechanics, CRC Press, 2001. doi:10.1016/0268-0033(90)90036-6.

[167] N. Kohli, S. Ho, S.J. Brown, P. Sawadkar, V. Sharma, M. Snow, E. García-Gareta, Bone remodelling in vitro: Where are we headed?: A review on the current understanding of physiological bone remodelling and inflammation and the strategies for testing biomaterials in vitro, Bone. 110 (2018) 38–46. doi:10.1016/j.bone.2018.01.015.

[168] C. Combes, S. Cazalbou, C. Rey, Apatite Biominerals, Minerals. 6 (2016) 34. doi:10.3390/min6020034.

[169] A. Dey, P.H.H. Bomans, F.A. Müller, J. Will, P.M. Frederik, G. De With, N.A.J.M. Sommerdijk, The role of prenucleation clusters in surface-induced calcium phosphate crystallization, Nat. Mater. 9 (2010) 1010–1014. doi:10.1038/nmat2900.

[170] F. Nudelman, K. Pieterse, A. George, P.H.H. Bomans, H. Friedrich, L.J. Brylka, P.A.J. Hilbers, G. De With, N.A.J.M. Sommerdijk, The role of collagen in bone apatite formation in the presence of hydroxyapatite nucleation inhibitors, Nat. Mater. 9 (2010) 1004–1009. doi:10.1038/nmat2875.

[171] M.J. Olszta, X. Cheng, S.S. Jee, R. Kumar, Y.Y. Kim, M.J. Kaufman, E.P. Douglas, L.B. Gower, Bone structure and formation: A new perspective, Mater. Sci. Eng. R Reports. 58 (2007) 77–116. doi:10.1016/j.mser.2007.05.001.

[172] E.E. Golub, Role of Matrix Vesicles in Biomineralization, Biochim Biophys Acta. 1790 (2009) 14–21. doi:10.1016/j.bbagen.2009.09.006.

[173] T. Hasegawa, T. Yamamoto, E. Tsuchiya, H. Hongo, K. Tsuboi, A. Kudo, M. Abe, T. Yoshida, T. Nagai, N. Khadiza, A. Yokoyama, K. Oda, H. Ozawa, P.H.L. de Freitas, M. Li, N. Amizuka, Ultrastructural and biochemical aspects of matrix vesicle-mediated mineralization, Jpn. Dent. Sci. Rev. 53 (2017) 34–45. doi:10.1016/j.jdsr.2016.09.002.

[174] A.C. Guyton, J.E. Hall, Textbook of Medical Physiology, 13th ed., Elsecier Saunders, 2016. doi:10.4103/sni.sni_327_17.

[175] S. Johnston, Z. Shi, J. Venezuela, C. Wen, M.S. Dargusch, A. Atrens, Investigating Mg Biocorrosion In Vitro: Lessons Learned and Recommendations, Jom. (2019). doi:10.1007/s11837-019-03327-9.

[176] W. Yao, Z. Shen, G. Ding, Simulation of interstitial fluid flow in ligaments: Comparison among Stokes, Brinkman and Darcy models, Int. J. Biol. Sci. 9 (2013) 1050–1056. doi:10.7150/ijbs.7242.

[177] T. Kokubo, H. Takadama, How useful is SBF in predicting in vivo bone bioactivity?, Biomaterials. 27 (2006) 2907–2915. doi:10.1016/j.biomaterials.2006.01.017.

[178] J.E.L. Buddy D. Ratner, Allan S. Hoffman, Frederick J. Schoen, Biomaterials Science: An Introduction to Materials in Medicine, 3rd ed., Academic Press, 2013. doi:10.1016/C2009-0-02433-7.

[179] J.M. Rutkowski, M.A. Swartz, A driving force for change: interstitial flow as a morphoregulator, Trends Cell Biol. 17 (2007) 44–50. doi:10.1016/j.tcb.2006.11.007.

[180] J. Mcnamara, L.I.G. Worthley, Acid-Base Balance : Part I . Physiology, Crit. Care Resusc. 5042 (2001) 181–187. https://ccr.cicm.org.au/journal-search.

[181] S. V. Lamaka, G. Knörnschild, D. V. Snihirova, M.G. Taryba, M.L. Zheludkevich, M.G.S. Ferreira, Complex anticorrosion coating for ZK30 magnesium alloy, Electrochim. Acta. 55 (2009) 131–141. doi:10.1016/j.electacta.2009.08.018.

[182] J. Izquierdo, L. Nagy, I. Bitter, R.M. Souto, G. Nagy, Potentiometric scanning electrochemical microscopy for the local characterization of the electrochemical behaviour of magnesium-based materials, Electrochim. Acta. 87 (2013) 283–293. doi:10.1016/j.electacta.2012.09.029.

[183] J. Izquierdo, B.M. Fernandez-Perez, D. Filotas, Imaging of Concentration Distributions and Hydrogen Evolution on Corroding Magnesium Exposed to Aqueous Environments Using Scanning Electrochemical Microscopy, Electroanalysis. 28 (2016) 2354–2366.

https://onlinelibrary.wiley.com/doi/abs/10.1002/elan.201600265.

[184] D. Mareci, G. Bolat, J. Izquierdo, C. Crimu, C. Munteanu, I. Antoniac, R.M. Souto, Electrochemical characteristics of bioresorbable binary MgCa alloys in Ringer’s solution: Revealing the impact of local pH distributions during in-vitro dissolution, Mater. Sci. Eng. C. 60 (2016) 402–410. doi:10.1016/j.msec.2015.11.069.

[185] S.S. Jamali, S.E. Moulton, D.E. Tallman, M. Forsyth, J. Weber, G.G. Wallace, Applications of scanning electrochemical microscopy (SECM) for local characterization of AZ31 surface during corrosion in a buffered media, Corros. Sci. 86 (2014) 93–100. doi:10.1016/j.corsci.2014.04.035.

[186] Y. Pan, S. He, D. Wang, D. Huang, T. Zheng, S. Wang, P. Dong, C. Chen, In vitro degradation and electrochemical corrosion evaluations of microarc oxidized pure Mg, Mg-Ca and Mg-Ca-Zn alloys for biomedical applications, Mater. Sci. Eng. C. 47 (2015) 85–96. doi:10.1016/j.msec.2014.11.048.

[187] Y. Liu, S. Zheng, N. Li, H. Guo, Y. Zheng, J. Peng, Study on the in vitro degradation behavior of pure Mg and WE43 in human bile for 60 days for future usage in biliary, Mater. Lett. 179 (2016) 100–103. doi:10.1016/j.matlet.2016.05.042.

[188] N. Li, C. Guo, Y.H. Wu, Y.F. Zheng, L.Q. Ruan, Comparative study on corrosion behaviour of pure Mg and WE43 alloy in static, stirring and flowing Hank’s solution, Corros. Eng. Sci. Technol. 47 (2012) 346–351. doi:10.1179/1743278212Y.0000000006.

[189] H. Kalb, A. Rzany, B. Hensel, Impact of microgalvanic corrosion on the degradation morphology of WE43 and pure magnesium under exposure to simulated body fluid, Corros. Sci. 57 (2012) 122–130. doi:10.1016/j.corsci.2011.12.026.

[190] Z. Li, X. Gu, S. Lou, Y. Zheng, The development of binary Mg-Ca alloys for use as biodegradable materials within bone., Biomaterials. 29 (2008) 1329–44. doi:10.1016/j.biomaterials.2007.12.021.

[191] D. Annur, A. Suhardi, M.I. Amal, M.S. Anwar, I. Kartika, Powder metallurgy preparation of Mg-Ca alloy for biodegradable implant application, J. Phys. Conf. Ser. 817 (2017) 012062. doi:10.1088/1742-6596/817/1/012062.

[192] S.E. Harandi, M. Mirshahi, S. Koleini, M.H. Idris, H. Jafari, M.R.A. Kadir, Effect of calcium content on the microstructure, hardness and in-vitro corrosion behavior of biodegradable Mg-Ca binary alloy, Mater. Res. 16 (2013) 11–18. doi:10.1590/S1516-14392012005000151.

[193] M. Salahshoor, Y. Guo, Biodegradable orthopedic magnesium-calcium (MgCa) alloys, processing, and corrosion performance, Materials (Basel). 5 (2012) 135–155. doi:10.3390/ma5010135.

[194] H. Somekawa, T. Mukai, High strength and fracture toughness balance on the extruded Mg–Ca–Zn alloy, Mater. Sci. Eng. A. 459 (2007) 366–370. doi:10.1016/j.msea.2007.01.021.

[195] D. Tie, F. Feyerabend, W.D. Müller, R. Schade, K. Liefeith, K.U. Kainer, R. Willumeit, Antibacterial biodegradable Mg-Ag alloys, Eur. Cells Mater. 25 (2012) 284–298. doi:10.22203/eCM.v025a20.

[196] P. Maier, F. Zimmermann, M. Rinne, G. Szakács, N. Hort, C. Vogt, Solid solution treatment on strength and corrosion of biodegradable Mg6Ag wires, Mater. Corros. 69

(2018) 178–190. doi:10.1002/maco.201709502.

[197] N. Hort, Y. Huang, D. Fechner, M. Störmer, C. Blawert, F. Witte, C. Vogt, H. Drücker, R. Willumeit, K.U. Kainer, F. Feyerabend, Magnesium alloys as implant materials-Principles of property design for Mg-RE alloys, Acta Biomater. 6 (2010) 1714–1725. doi:10.1016/j.actbio.2009.09.010.

[198] P. Maier, C. Mendis, G. Tober, N. Hort, Tailoring properties of cast Mg10Gd by alloying Nd and heat treatment, Emerg. Mater. Res. 2 (2013) 229–238. doi:10.1680/emr.13.00021.

[199] F. Feyerabend, H. Drücker, D. Laipple, C. Vogt, M. Stekker, N. Hort, R. Willumeit, Ion release from magnesium materials in physiological solutions under different oxygen tensions, J. Mater. Sci. Mater. Med. 23 (2012) 9–24. doi:10.1007/s10856-011-4490-5.

[200] S. V. Lamaka, B. Vaghefinazari, D. Mei, R.P. Petrauskas, D. Höche, M.L. Zheludkevich, Comprehensive screening of Mg corrosion inhibitors, Corros. Sci. 128 (2017) 224–240. doi:10.1016/j.corsci.2017.07.011.

[201] D. Ammann, Ion-Selective Microelectrodes, 1st ed., Springer-Verlag Berlin Heidelberg, 1986. doi:10.1007/978-3-642-52507-0.

[202] M. Taryba, Boosting the application of local potentiometric probe technique for corrosion research, Universidade de Lisboa, 2016.

[203] A.J. Bard, M. V. Mirkin, Scanning Electrochemical Microscopy, 2nd ed., CRC Press, 2012.

[204] O. Karavai, Mapping local corrosion parameters by SVET and SIET, Universidade de Aveiro, 2017.

[205] Merk Ion Sensor Materials, Merck KGaA, Darmstadt, Ger. and/or Its Affil. (2020). https://www.sigmaaldrich.com/analytical-chromatography/analytical-products.html?TablePage=8670762.

[206] P. Bühlmann, E. Pretsch, E. Bakker, Carrier-based ion-selective electrodes and bulk optodes. 2. Ionophores for potentiometric and optical sensors, Chem. Rev. 98 (1998) 1593–1688. doi:10.1021/cr970113+.

[207] S. Lamaka, R.M. Souto, M.G.S. Ferreira, In-situ visualization of local corrosion by Scanning Ion-selective Electrode Technique (SIET), in: A. Méndez-Vilas, J. Díaz (Eds.), Microsc. Sci. Technol. Appl. Educ. Vol. 3, Formatex Research Center, Badajoz, 2010: pp. 2162–2173. https://www.semanticscholar.org/paper/In-situ-visualization-of-local-corrosion-by-(SIET)-Souto-Ferreira/338ded8ceb84c9ac87d70f530b663bdcc3d5aab9#citing-papers.

[208] E.A. Zdrachek, A.G. Karotkaya, V.A. Nazarov, K.A. Andronchyk, L.S. Stanishevskii, V. V. Egorov, M.G. Taryba, D. Snihirova, M. Kopylovich, S. V. Lamaka, H+-selective microelectrodes with optimized measuring range for corrosion studies, Sensors Actuators, B Chem. 207 (2015) 967–975. doi:10.1016/j.snb.2014.07.106.

[209] S. V. Lamaka, O. V. Karavai, A.C. Bastos, M.L. Zheludkevich, M.G.S. Ferreira, Monitoring local spatial distribution of Mg2+, pH and ionic currents, Electrochem. Commun. 10 (2008) 259–262. doi:10.1016/j.elecom.2007.12.003.

[210] R.-S. Huang, C.-J. Lin, H.S. Isaacs, A Difference-Imaging Technique Used to Study Streaking Corrosion of Aluminum Alloys AA7075 and AA8006 in Chloride Solution,

Electrochem. Solid-State Lett. 9 (2006) B11–B14. doi:10.1149/1.2140503.

[211] H.S. Isaacs, Y.M. Looi, J.H.W. de Wit, Behavior of laser welded steel in chloride solution studied using difference imaging, Corros. Sci. 49 (2007) 53–62. doi:10.1016/j.corsci.2006.05.022.

[212] D.C. Bell, N. Erdman, Low Voltage Electron Microscopy: Principles and Applications, John Wiley & Sons, Inc., 2012. doi:10.1002/9781118498514.

[213] M. Nauer, K. Ernst, W. Kautek, M. Neumann-Spallart, Depth profile characterization of electrodeposited multi-thin-film structures by low angle of incidence X-ray diffractometry, Thin Solid Films. 489 (2005) 86–93. doi:10.1016/j.tsf.2005.05.008.

[214] M. Bouroushian, T. Kosanovic, Characterization of Thin Films by Low Incidence X-Ray Diffraction, Cryst. Struct. Theory Appl. 01 (2012) 35–39. doi:10.4236/csta.2012.13007.

[215] G. Lefèvre, T. Preo, J. Lützenkirchen, Attenuated Total Reflection – Infrared Spectroscopy Applied to the Study of Mineral – Aqueous Electrolyte Solution Interfaces : A General Overview and a Case Study, in: T. Theophanides (Ed.), Infrared Spectrosc. - Mater. Sci. Eng. Technol., InTech, 2011: pp. 979-953-307-362–9. doi:10.5772/2055.

[216] F.M. Mirabella, Internal Reflection Spectroscopy: Theory and Aplications, Marcel Dekker, Inc., 1993. doi:|https://doi.org/10.1002/0470027320.s2301.

[217] L.D. Tickanen, M.I. Tejedor-Tejedor, M.A. Anderson, Quantitative characterization of aqueous suspensions using attenuated total reflection Fourier transform infrared spectroscopy: Influence of internal reflection element-particle interactions on spectral absorbance values, Langmuir. 7 (1991) 451–456. doi:10.1021/la00051a006.

[218] John P. Coates, The Industrial Applications of Infrared Internal Reflectance Spectroscopy, in: Intern. Reflect. Spectrosc. Theory Appl., Mercel Dekker, Inc, 1992. doi:10.1002/0470027320.s2301.

[219] Ignasi Puigdomenech, Hydra-Medusa. 32-bit Windows interface, (2019). https://sites.google.com/site/chemdiagr/.

[220] D. Tie, F. Feyerabend, W.D. Müller, R. Schade, K. Liefeith, K.U. Kainer, R. Willumeit, Antibacterial biodegradable Mg-Ag alloys, Eur. Cells Mater. 25 (2012) 284–298.

[221] T.Z. Si, L. Han, Y.T. Li, D.M. Liu, Q.A. Zhang, L.Z. Ouyang, M. Zhu, Achieving highly efficient hydrogen generation and uniform Ag nanoparticle preparation via hydrolysis of Mg9Ag alloy milled under hydrogen gas, Int. J. Hydrogen Energy. 39 (2014) 11867–11872. doi:10.1016/j.ijhydene.2014.06.021.

[222] X. Liu, Z. Zhang, Q. Le, L. Bao, Effects of Nd/Gd value on the microstructures and mechanical properties of Mg–Gd–Y–Nd–Zr alloys, J. Magnes. Alloy. 4 (2016) 214–219. doi:10.1016/j.jma.2016.06.002.

[223] K.Y. Zheng, J. Dong, X.Q. Zeng, W.J. Ding, Microstructural characterisation of as cast and homogenised Mg–Gd–Nd–Zr alloys, Mater. Sci. Technol. 24 (2008) 320–326. doi:10.1179/174328408X275991.

[224] W. Gan, Y. Huang, L. Yang, K.U. Kainer, M. Jiang, H.G. Brokmeier, N. Hort, Identification of unexpected hydrides in Mg-20 wt% Dy alloy by high-brilliance synchrotron radiation, J. Appl. Crystallogr. 45 (2012) 17–21.

doi:10.1107/S0021889811053088.

[225] S.S. Jamali, S.E. Moulton, D.E. Tallman, M. Forsyth, J. Weber, G.G. Wallace, Applications of scanning electrochemical microscopy (SECM) for local characterization of AZ31 surface during corrosion in a buffered media, Corros. Sci. 86 (2014) 93–100. doi:10.1016/j.corsci.2014.04.035.

[226] J. Walker, S. Shadanbaz, N.T. Kirkland, E. Stace, T. Woodfield, M.P. Staiger, G.J. Dias, Magnesium alloys: Predicting in vivo corrosion with in vitro immersion testing, J. Biomed. Mater. Res. - Part B Appl. Biomater. 100 B (2012) 1134–1141. doi:10.1002/jbm.b.32680.

[227] M. Schinhammer, J. Hofstetter, C. Wegmann, F. Moszner, J.F. Löffler, P.J. Uggowitzer, On the immersion testing of degradable implant materials in simulated body fluid: Active pH regulation using CO2, Adv. Eng. Mater. 15 (2013) 434–441. doi:10.1002/adem.201200218.

[228] I.F. Gow, Measurement of ionised magnesium in HEPES-buffered serum samples, Anal. Chim. Acta. 432 (2001) 143–149. doi:10.1016/S0003-2670(00)01345-3.

[229] M.B. Kannan, H. Khakbaz, A. Yamamoto, Understanding the influence of HEPES buffer concentration on the biodegradation of pure magnesium: An electrochemical study, Mater. Chem. Phys. 197 (2017) 47–56. doi:10.1016/j.matchemphys.2017.05.024.

[230] S. Naddaf Dezfuli, Z. Huan, J.M.C. Mol, M.A. Leeflang, J. Chang, J. Zhou, Influence of HEPES buffer on the local pH and formation of surface layer during in vitro degradation tests of magnesium in DMEM, Prog. Nat. Sci. Mater. Int. 24 (2014) 531–538. doi:10.1016/j.pnsc.2014.08.009.

[231] M. Cihova, P. Schmutz, R. Schäublin, J.F. Löffler, Biocorrosion Zoomed In: Evidence for Dealloying of Nanometric Intermetallic Particles in Magnesium Alloys, Adv. Mater. 1903080 (2019) 1903080. doi:10.1002/adma.201903080.

[232] H.E. Friedrich, B.L. Mordike, Magnesium technology: Metallurgy, design data, applications, Springer, 2006. doi:10.1007/3-540-30812-1.

[233] P. Dawson, C.D. Hadfield, G.R. Wilkinson, The polarized infra-red and Raman spectra of Mg(OH)2 and Ca(OH)2, J. Phys. Chem. Solids. 34 (1973) 1217–1225. doi:10.1016/S0022-3697(73)80212-4.

[234] M.B. Kruger, Q. Williams, R. Jeanloz, Vibrational spectra of $Mg(OH)_2$ and $Ca(OH)_2$ under pressure, J. Chem. Phys. 91 (1989) 5910–5915. doi:10.1063/1.457460.

[235] M.A. Salter, Phase heterogeneity in carbonate production by marine fish influences their roles in sediment generation and the inorganic carbon cycle- Suplementary information, Sci. Rep. 7 (2017). doi:10.1038/s41598-017-00787-4.

[236] J. Forsgren, S. Frykstrand, K. Grandfield, A. Mihranyan, M. Strømme, A Template-Free, Ultra-Adsorbing, High Surface Area Carbonate Nanostructure, PLoS One. 8 (2013). doi:10.1371/journal.pone.0068486.

[237] A. Paz, D. Guadarrama, M. López, J.E. González, N. Brizuela, J. Aragón, A Comparative Study of Hydroxyapatite Nanoparticles Synthesized By Different Routes, Quim. Nov. 35 (2012) 1724–1727. doi:10.1590/S0100-40422012000900004.

[238] C. Drouet, Apatite formation: Why it may not work as planned, and how to

conclusively identify apatite compounds, Biomed Res. Int. 2013 (2013). doi:10.1155/2013/490946.

[239] J. Aufort, L. SÃ©galen, C. Gervais, C. Brouder, E. Balan, Modeling the attenuated total reflectance infrared (ATR-FTIR) spectrum of apatite, Phys. Chem. Miner. 43 (2016) 615–626. doi:10.1007/s00269-016-0821-x.

[240] L. Berzina-Cimdina, N. Borodajenko, Research of Calcium Phosphates Using Fourier Transform Infrared Spectroscopy, Infrared Spectrosc. - Mater. Sci. Eng. Technol. (2012). doi:10.5772/36942.

[241] R. Willumeit-Römer, The Interface Between Degradable Mg and Tissue, Jom. (2019). doi:10.1007/s11837-019-03368-0.

[242] M. Nordsveen, S. Nešić, R. Nyborg, A. Stangeland, A mechanistic model for carbon dioxide corrosion of mild steel in the presence of protective iron carbonate films - Part 1: Theory and verification, Corrosion. 59 (2003) 443–456. doi:10.5006/1.3277576.

[243] M.Z. Southard, L.J. Dias, K.J. Himmelstein, V.J. Stella, Experimental Determinations of Diffusion Coefficients in Dilute Aqueous Solution Using the Method of Hydrodynamic Stability, Pharm. Res. An Off. J. Am. Assoc. Pharm. Sci. 8 (1991) 1489–1494. doi:10.1023/A:1015886131198.

[244] G. Song, Control of biodegradation of biocompatable magnesium alloys, Corros. Sci. 49 (2007) 1696–1701. doi:10.1016/j.corsci.2007.01.001.

[245] D. Mei, S. V. Lamaka, J. Gonzalez, F. Feyerabend, R. Willumeit-Römer, M.L. Zheludkevich, The role of individual components of simulated body fluid on the corrosion behavior of commercially pure Mg, Corros. Sci. 147 (2019) 81–93. doi:10.1016/j.corsci.2018.11.011.

[246] D. Tie, F. Feyerabend, N. Hort, R. Willumeit, D. Hoeche, XPS studies of magnesium surfaces after exposure to Dulbecco's modified eagle medium, Hank's buffered salt solution, and simulated body fluid, Adv. Eng. Mater. 12 (2010) 699–704. doi:10.1002/adem.201080070.

[247] C.L. Christ, P.B. Hostetler, Studies in the system MgO-SiO2 -CO2 -H2O (II): the activity-product constant of magnesite, Am J Sci. 268 (1970) 439–453. doi:10.2475/ajs.268.5.439.

[248] M. Hänchen, V. Prigiobbe, R. Baciocchi, M. Mazzotti, Precipitation in the Mg-carbonate system-effects of temperature and CO2 pressure, Chem. Eng. Sci. 63 (2008) 1012–1028. doi:10.1016/j.ces.2007.09.052.

[249] M. Dong, W. Cheng, Z. Li, G.P. Demopoulos, Solubility and Stability of Nesquehonite (MgCO3 · 3H2O) in NaCl, KCl, MgCl2, and NH4Cl Solutions, J. Chem. Eng. Data. 53 (2008). doi:10.1039/tf9595502203.

[250] Y. Yoo, D. Kang, E. Choi, J. Park, I.S. Huh, Morphology control of magnesium carbonate for CO2 utilization using Mg2+ ions in industrial wastewater depending on length of alkyl chain of primary alkanolamine, reaction temperature, CO2 concentration, and Mg2+ /Na+ ratio, Chem. Eng. J. 370 (2019) 237–250. doi:10.1016/j.cej.2019.03.209.

[251] J. Yang, Y. Han, J. Luo, K. Leifer, M. Strømme, K. Welch, Synthesis and characterization of amorphous magnesium carbonate nanoparticles, Mater. Chem. Phys. 224 (2019) 301–307. doi:10.1016/j.matchemphys.2018.12.037.

[252] A.L. Harrison, V. Mavromatis, E.H. Oelkers, P. Bénézeth, Solubility of the hydrated Mg-carbonates nesquehonite and dypingite from 5 to 35 °C: Implications for CO 2 storage and the relative stability of Mg-carbonates, Chem. Geol. 504 (2019) 123–135. doi:10.1016/j.chemgeo.2018.11.003.

[253] P.J. Davies, B. Bubela, The transformation of nesquehonite into hydromagnesite, Chem. Geol. 12 (1973) 289–300. doi:10.1016/0009-2541(73)90006-5.

[254] J. Lanas, J.I. Alvarez, Dolomitic lime: Thermal decomposition of nesquehonite, Thermochim. Acta. 421 (2004) 123–132. doi:10.1016/j.tca.2004.04.007.

[255] F. Tamimi, D. Le Nihouannen, D.C. Bassett, S. Ibasco, U. Gbureck, J. Knowles, A. Wright, A. Flynn, S. V. Komarova, J.E. Barralet, Biocompatibility of magnesium phosphate minerals and their stability under physiological conditions, Acta Biomater. 7 (2011) 2678–2685. doi:10.1016/j.actbio.2011.02.007.

[256] S.R. Knigge, B. Glasmacher, Comparison between three in vitro methods to measure magnesium degradation and their suitability for predicting in vivo degradation, Int. J. Artif. Organs. 41 (2018) 772–778. doi:10.1177/0391398818772777.

[257] M. Grabowski, D. Bluecher, M. Korte, S. Virtanen, Influence of Ca2+ in deicing salt on the corrosion behavior of AM50 magnesium alloy, Corrosion. 70 (2014) 1008–1023. doi:10.5006/1268.

[258] M. Grabowski, D. Bluecher, M. Korte, S. Virtanen, The influence of Ca^{2+}in deicing salt on the chemistry of corrosion products formed on AM50 magnesium alloy - Calcareous deposition, Corrosion. 71 (2015) 703–725. doi:10.5006/1539.

[259] C. Ning, L. Zhou, Y. Zhu, Y. Li, P. Yu, S. Wang, T. He, W. Li, G. Tan, Y. Wang, C. Mao, Influence of Surrounding Cations on the Surface Degradation of Magnesium Alloy Implants under a Compressive Pressure, Langmuir. 31 (2015) 13561–13570. doi:10.1021/acs.langmuir.5b03699.

[260] E. Ghali, Corrosion and Protection of Magnesium Alloys, Mater. Sci. Forum. 1120–1121 (2000) 261–272. doi:10.4028/www.scientific.net/AMR.1120-1121.1078.

[261] J. Hofstetter, E. Martinelli, S. Pogatscher, P. Schmutz, E. Povoden-Karadeniz, A.M. Weinberg, P.J. Uggowitzer, J.F. Löffler, Influence of trace impurities on the in vitro and in vivo degradation of biodegradable Mg–5Zn–0.3Ca alloys, Acta Biomater. 23 (2015) 0–6. doi:10.1016/j.actbio.2015.05.004.

[262] P.K. Bowen, J. Drelich, J. Goldman, Magnesium in the murine artery: probing the products of corrosion, Acta Biomater. 10 (2014) 1475–83. doi:10.1016/j.actbio.2013.11.021.

[263] J. Zhang, X. Zhou, C. Dong, Y. Sun, J. Yu, Investigation of amorphous calcium carbonate ' s formation under high concentration of magnesium : The prenucleation cluster pathway, J. Cryst. Growth. 494 (2018) 8–16. doi:10.1016/j.jcrysgro.2018.05.001.

[264] U.-N. Berninger, G. Jordan, M. Lindner, A. Reul, J. Schott, E.H. Oelkers, On the effect of aqueous Ca on magnesite growth – Insight into trace element inhibition of carbonate mineral precipitation, Geochim. Cosmochim. Acta. 178 (2016) 195–209. doi:10.1016/j.gca.2016.01.019.

[265] E. Loste, R.M. Wilson, R. Seshadri, F.C. Meldrum, The role of magnesium in stabilising amorphous calcium carbonate and controlling calcite morphologies, J.

Cryst. Growth. 254 (2003) 206–218. doi:10.1016/S0022-0248(03)01153-9.

[266] F. Konrad, B. Purgstallera, F. Gallien, V. Mavromatis, P. Gane, M. Dietzel, Influence of aqueous Mg concentration on the transformation of amorphous calcium carbonate, J. Cryst. Growth. 498 (2018) 381–390. doi:10.1016/j.jcrysgro.2018.07.018.

[267] N. Cam, T. Georgelin, M. Jaber, J.-F. Lambert, K. Benzerara, In vitro synthesis of amorphous Mg-, Ca-, Sr- and Ba-carbonates: what do we learn about intracellular calcification by cyanobacteria?, Geochim. Cosmochim. Acta. 161 (2015) 36–49. doi:10.1016/j.gca.2015.04.003.

[268] B. Myszka, M. Schüßler, K. Hurle, B. Demmert, R. Detsch, A.R. Boccaccini, S.E. Wolf, Phase-specific bioactivity and altered Ostwald ripening pathways of calcium carbonate polymorphs in simulated body fluid, RSC Adv. 9 (2019) 18232–18244. doi:10.1039/C9RA01473J.

[269] R. Gelli, F. Ridi, P. Baglioni, The importance of being amorphous: calcium and magnesium phosphates in the human body, Adv. Colloid Interface Sci. 269 (2019) 219–235. doi:10.1016/j.cis.2019.04.011.

[270] Cao X, Harris W., Carbonate and magnesium interactive effect on calcium phosphate precipitation, Environ. Sci. Technol. 42 (2008) 436–442. doi:10.1021/es0716709.

List of Figures

List of Tables

List of abbreviations

µ-CT	Micro citotomography
µXRF	Micro x-ray Fluorescence
AAS	Atomic Absorption Spectroscopy
ACP	Amorphous calcium phosphate
a_i	Ionic activity of the species i
BEF	Bone Extracellular fluid
BLC	Bone-lining cells
BMGs	Bulk metallic glasses
BMU	Basic multicellular units
BSE	Back-scattered electrons
CaPs	Calcium Phosphates phases
CBD	Critical bone defects
CCD	Charge-coupled device
D	Diffusion coefficient
DCPD	Dicalcium phosphate dihydrate
DL	Degradation products layer
DVIT	Difference Viewer Imaging Technique
E	Young´s modulus
E°	Normal potential
ECAP	Equal Channel Angular Pressing
ECMV	Extracellular matrix vesicles
E_{cor}	Corrosion potential
EDX	Energy dispersive x-ray
EDXRF	Energy dispersive X-ray spectrometer
ESB:	European Society for Biomaterials
FET	Field-effect transistor
FISS	Flow-Induced shear stress
FRAP	Fluorescence recovery after photobleaching
FTIR-ATR	Fourier Transform Infrared Spectroscopy Attenuated Total Reflectance
G	Gibbs free energy
GAXRD	Grazing Angle X-ray Diffraction
HA	Hydroxyapatite
HBSS	Hank´s Balanced Salt Solution
HEPES	4-(2-hydroxyethyl)-1-piperazineethanesulfonic acid
HPT	High-Pressure-Torsion
IAP	Product of the free ion species in solution
$i_{corr:}$	Corrosion intensity
IHP	Inner Helmholtz Plane
J_L	Lymphatic flow
J_V	Net flux
K_{sp}	Solubility product constant
L_p	Hydraulic permeability
MM	Mineralised extracellular matrix
NFP	Net filtration pressure
NMR	Nuclear magnetic resonance

OB	Osteoblast
OCP	Octacalcium phosphate
OCT	Osteoclast
OHP	Outer Helmholtz Plane
OPS	Oxide polishing suspension
PBS	Phosphate-buffered saline
PEEK	Polyether ether ketone
Ph	Phenolphthalein
pK_{hyd}	- log (hydration constant)
POCT	pre-Osteoclasts
SDD	Silicon-drift detector
SEM	Scanning electron microscopy
SHE	Standard hydrogen electrode
SI	Saturation Index
SIET	Scanning Ion-selective Electrode Technique
SVET	Scanning Vibrating Electrode Technique
UM	Unmineralised extracellular matrix
UTS	Ultimate tensile strength
V/A ratio	Volume per sample surface area ratio
WLI	Wight Light Interferometry
δ_0	Diffusion layer
δ_N	Approximation of the diffusion layer by Nernst
Πc	Capillary colloid osmotic pressures
Πi	Interstitial colloid osmotic pressures

List of Publications and conferences

Published Papers

J. Gonzalez, R.Q. Hou, E.P.S. Nidadavolu, R. Willumeit-Römer, F. Feyerabend, *Magnesium degradation under physiological conditions – Best practice*, Bioact. Mater. 3 (2018) 174–185. doi:10.1016/j.bioactmat.2018.01.003.

Lamaka, S. V.,**Gonzalez, J**.,Mei, D.,Feyerabend, F.,Willumeit-Römer, R.,Zheludkevich, M. L., *Local pH and Its Evolution Near Mg Alloy Surfaces Exposed to Simulated Body Fluids*, Adv. Mater. Interfaces 2018, 5, 1800169.https://doi.org/10.1002/admi.201800169

Di Mei, Sviatlana V. Lamaka, **Jorge Gonzalez**, Frank Feyerabend, Regine Willumeit-Römer, Mikhail L. Zheludkevich, *The role of individual components of simulated body fluid on the corrosion behavior of commercially pure Mg*, Corrosion Science, Volume 147, 2019, Pages 81-93, ISSN 0010-938X, https://doi.org/10.1016/j.corsci.2018.11.011.

Gawlik, M.M.; Steiner, M.; Wiese, B.; **González, J**.; Feyerabend, F.; Dahms, M.; Ebel, T.; Willumeit-Römer, R. *The Effects of HAc Etching on the Degradation Behaviour of Mg-5Gd*. J. Med. Mater. Tech. 2017, 1, 22–25. https://doi.org/10.24354/medmat.v1i2.17.

Gawlik, M.M.; Wiese, B.; Welle, A.; **González, J**.; Desharnais, V.; Harmuth, J.; Ebel, T.; Willumeit-Römer, R. *Acetic Acid Etching of Mg-xGd Alloys*. Metals 2019, 9, 117. https://doi.org/10.3390/met9020117.

Conference abstracts

Posters

D. Porchetta, **J. González**, F. Feyerabend, R. Willumeit-Romer, M. Behbahani, C. Ptock, A. Kopp. Comparative study on degradation behaviour of magnesium alloys Mg-Y-RE and Mg-Ca-Zn in a dynamic bioreactor testing set-up. 7th Biometal. Symposium on Biodegradable Metals for Biomedical Applications. Aug. 23 – Sept. 28, Carovingio, Italy (2015).

Jorge González, Sviatlana Lamaka, Frank Feyerabend, Regine Willumeit-Römer. *In vitro* environment Influence on magnesium biodegradable materials. 9th Biometal. Symposium on Biodegradable Metals for Biomedical Applications. Aug. 27 – Sept. 1, Bertinoro, Italy (2017).

Gawlik, M.M.; Steiner, M.; Wiese, B.; **González, J.**; Feyerabend, F.; Dahms, M.; Ebel, T.; Willumeit-Römer, R. The Effects of HAc Etching on the Degradation Behaviour of Mg-5Gd, 4th Euro BioMAT - European Symposium and Exhibition on Biomaterials and Related Areas, May 2017, Weimar, Germany.

Talks

Jorge González, Dr. Nezha Ahmad, Dr. Frank Feyerabend, Prof. Dr. Regine Willumeit, *Influences of in vitro conditions in magnesium biomaterials degradation*. 4th Euro BioMAT 2017. European Symposium on Biomaterials and Related Areas. 9 – 10 May, Weimar, Germany (2015.)

Awards

1st ranking place for best posters presented in the 9th Biometal. Symposium on Biodegradable Metals for Biomedical Applications. Aug. 27 – Sept. 1, Bertinoro, Italy (2017). **Jorge González**, Sviatlana Lamaka, Frank Feyerabend, Regine Willumeit-Römer. *In vitro* environment Influence on *magnesium biodegradable materials*.